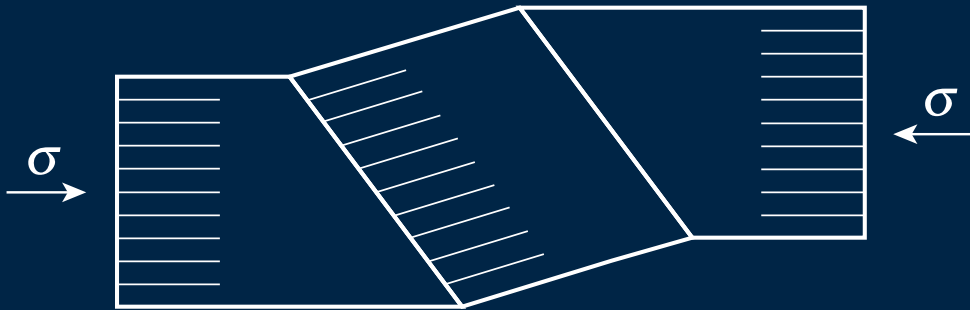


FAILURE OF COMPOSITE MATERIALS BY KINK BAND FORMATION



Simon Peter Hald Skovsgård
Department of Engineering
Aarhus University

This dissertation is submitted for the degree of

PhD

April, 2019

Dissertation title: Failure of composite materials by kink band formation

Dissertation submitted: April 12, 2019
for the degree of PhD

Author: MSc Simon Peter Hald Skovsgård
Department of Engineering
Aarhus University, Denmark
E-mail: sphs@eng.au.dk

Supervisor: Professor, dr. techn. Henrik Myhre Jensen
Department of Engineering
Aarhus University, Denmark
E-mail: hmj@eng.au.dk

© Copyright by Simon Peter Hald Skovsgård

ISBN: 978-87-7507-456-3
DOI: 10.7146/aulsps-e.337

Abstract

Fibre-reinforced composites and layered materials have a heterogeneous composition of two or more constituents and have anisotropic material behaviour. This heterogeneous structure enables numerous failure mechanisms. One of the dominant compressive failure mechanisms of the latter composites is composed of so-called kink bands. These are bands of material where the fibres inside the band have rotated relative to the fibres outside.

This dissertation mainly concerns the examination of kink band formation in fibre composites and layered materials using several different methodologies. Five publications on the latter topic have arisen based on the work done in this project. The four introductory chapters in the dissertation are devoted to explanations and elaborations of the methods used and developed during the project. Several finite element models are developed specifically to examine either the peak strength of the composite or the post-buckling kink band behaviour. Two novel constitutive formulations are developed that can be used in a general framework to investigate the elastic-plastic behaviour of composites, including the study of kink bands.

The following results and conclusions are drawn from the project results. Compressive kinking strength is affected by:

- Fibre-misalignments
- Insufficient fibre-to-matrix bonding
- Matrix yield strength
- Multi-axial loading

The stress at steady-state kink band broadening can be seen as the lower bound of the compressive strength and is lowered by:

- Increasing band inclinations to a certain limit
- Decreasing matrix Poisson's ratio
- Decreasing maximum tangent modulus of the matrix

As part of my visit to the Department of Engineering at the University of Cambridge, contributions are made to the field of joint mechanics, particular regarding composites made from ultra-high molecular weight polyethylene. The latter study is a secondary focus of this dissertation. The research questions, problems, methodologies, results and conclusions appear in an attached article.

Resumé

Fiberforstærkede kompositter og lagdelte materialer har en heterogen sammensætning af to eller flere bestanddele og har en anisotropisk materialeopførsel. Denne heterogene struktur muliggør adskillige fejlmekanismer. En af de dominerende fejlmekanismer i kompression for sidstnævnte kompositter er ved såkaldte kinkbånd. Disse er bånd af materiale, hvor fibre inde i båndet har roteret relativt i forhold til fibre udenfor.

Denne afhandling vedrører primært undersøgelsen af kinkbåndsbildning i fiberkompositter og lagdelte materialer ved anvendelse af flere forskellige metoder. Fem publikationer om sidstnævnte emne er opstået på baggrund af arbejdet i projektet. De fire indledende kapitler i afhandlingen er afsat til forklaringer og uddybninger af de anvendte og udviklede metoder under projektet. Der er udviklet adskillige finite element modeller, der er specielt designet til at undersøge enten topstyrken eller post-buckling adfærden af kompositter. To nye konstitutive formuleringer er udviklet, der kan anvendes til generelle formål ifm. undersøgelsen af kompositters elastisk-plastiske adfærd, heriblandt undersøgelsen af kinkbånd.

Følgende resultater og konklusioner blev draget gennem projektet. Den kompressive kinkbåndstyrke påvirkes af:

- Vinkelimperfektioner af fibre
- Utilstrækkelig binding mellem fiber og matrix
- Faldende matrix flydestyrke
- Multiaksial belastning

Spændingen ved kinkbåndsudvidelse kan ses som den nedre grænse af kompressionsstyrken og sænkes ved:

- Stigende båndhældninger til en vis grænse
- Faldende matrix Poissons forhold
- Faldende maksimal tangentmodul for matrixen

Som en del af besøget ved ingeniørafdelingen ved Cambridge universitet blev der udført forskning indenfor mekanikken for samlinger lavet af kompositter lavet af polyethylen med ultrahøj molekylvægt. Sidstnævnte studie er et sekundært fokus ved denne afhandling. Forskningsspørgsmålene, problemerne, metoderne, resultaterne og konklusionerne fremgår i en vedhæftet artikel.

Preface

This dissertation is submitted in partial fulfilment of the requirements for the degree of PhD from Aarhus University (AU). The research herein was conducted at the Department of Engineering in the Section of Mechanical Engineering, at AU in the period of 1st May 2016 to 12th April 2019 under the supervision of Professor Henrik Myhre Jensen. The dissertation is written as a collection of articles according to the guidelines within the Section of Mechanical Engineering. Furthermore, the dissertation follows the official rules and regulations stated by the Graduate School of Science and Technology (GSST) at AU. The work was funded by the *Thomas B. Thriges Fond*, which is greatly appreciated.

Declaration

I hereby declare that except where specific reference is made to the work of others, the contents of this dissertation are original and have not been submitted in whole or in part for consideration for any other degree or qualification.

Acknowledgements

It has been a great journey and privilege to study at Aarhus University during my PhD. During my time as a student, I have worked with and received support from several people, to whom I am deeply grateful. First and foremost, I am grateful to my supervisor Prof Henrik M. Jensen for considering me for the PhD project. I owe him deep gratitude for his guidance and help through the years. His inspiring and calm method of supervision has inspired me to strive for new discoveries and he was one of the main reasons why I looked forward to work on early Monday mornings.

My fellow PhD students and other colleagues in the office have always been a source of happiness and joy. I have benefited a lot from their wisdom through valuable discussions. I acknowledge my lovely colleagues Kasper Ringgard, Joakim Vester-Petersen, Dan Thomsen, Oliver Tierdad Filsoof, Emil Madsen and Frederik Foldager for making my time enjoyable. I

am grateful to my colleague and friend Simon Heide-Jørgensen for several discussions about mechanics of materials. I would like to thank Vedad Tojaga, who was a master's student in 2017, for a great collaboration on the simulations of kink bands in open-hole composites. In addition, I must thank Jens Lycke Wind, a previous PhD student who worked on kink bands, I have benefited a lot from the foundation that he established.

Furthermore, I am grateful to Professor Norman Fleck for hosting me as a visiting PhD student at the University of Cambridge. I learned a lot from him, including the need to be cautious about my assumptions and conclusions and be precise in the dissemination of my research. I would like to thank all the lovely people in the Oatley Lab for making my stay enjoyable.

Last but not least, I would like to thank my family and friends for their love and support. I am especially grateful to my girlfriend, Katrine, who has given me unconditional love and support and had to do without me during my long stay in Cambridge. She listened patiently to many of my research frustrations throughout my time, although they probably did not make much sense.

To each and every one of you, thank you.

Simon Peter Hald Skovsgård
April, 2019

Table of contents

| | |
|--|------------|
| Abstract | iii |
| Resumé | iv |
| Publications and conference presentations | ix |
| Nomenclature | xi |
| 1 Introduction | 1 |
| 1.1 Compressive failure modes | 4 |
| 1.2 Kink band formation | 6 |
| 1.3 Scope of work | 11 |
| 2 Finite element models | 13 |
| 2.1 Geometries | 14 |
| 2.2 Imperfection | 16 |
| 2.3 Boundary conditions | 19 |
| 2.4 Discretisation | 20 |
| 2.5 Interaction | 22 |
| 3 Semi-analytical kink band model | 24 |
| 3.1 General relations | 24 |
| 3.2 Homogenisation of constituents | 30 |
| 3.3 Kink band bifurcation | 40 |
| 3.4 Kink band model and numerical scheme | 42 |
| 3.5 Kink band broadening | 49 |

| | |
|---|------------|
| 4 Analytical kink band model | 51 |
| 4.1 Stresses and equilibrium | 51 |
| 4.2 Strains and continuity | 52 |
| 4.3 Kink band broadening | 54 |
| 5 Summary and outlook | 57 |
| 5.1 Contributions | 57 |
| 5.2 Perspective | 58 |
| 5.3 Recommendations for further work | 59 |
| 6 P1 | 60 |
| 7 P2 | 75 |
| 8 P3 | 88 |
| 9 P4 | 101 |
| 10 P5 | 112 |
| 11 C1 | 123 |
| Appendix A Jaumann rate of Cauchy stresses | 133 |
| Appendix B Nominal stresses | 136 |
| Appendix C Constitutive formulation | 141 |
| Bibliography | 149 |

Publications

- [P1] Skovsgaard S.P.H., Jensen H.M., 2018. Three-dimensional constitutive model for elastic-plastic behaviour of fibre-reinforced composites. *International Journal of Solids and Structures*. Vol. 139-140, p. 150-162
- [P2] Skovsgaard S.P.H., Jensen H.M., 2018. Constitutive model for imperfectly bonded fibre-reinforced composites. *Composite Structures*. Vol. 192, p. 82-92
- [P3] Skovsgaard S.P.H., Jensen H.M., 2018. Steady-State Kink Band Propagation in Layered Materials. *Journal of Applied Mechanics*. Vol. 85 / 061005-1
- [P4] Skovsgaard S.P.H., Jensen H.M., 2019. A general approach for the study of kink band broadening in fibre composites and layered materials. *European Journal of Mechanics / A Solids*. Vol. 74, p. 394-402
- [P5] Skovsgaard S.P.H., Fleck, N.A., 2019. Load transfer at a bolted joint of a laminate made from ultra high molecular-weight polyethylene fibres. Under review at the *International Journal of Solids and Structures*

Contribution to other work:

- [C1] Tojaga V., Skovsgaard S.P.H., Jensen H.M., 2018. Micromechanics of kink band formation in open-hole fibre composites under compressive loading. *Composites Part B*. Vol. 149, p. 66-73

Oral conference presentations:

- I** DCAMM 16th Internal Symposium, February 2017 Middelfart, Denmark
Title: Modelling of failure in fiber composite materials

- II** 14th U.S. National Congress for Computational Mechanics, July 2017 Montreal, Canada
Title: Kink band instabilities in layered media

- III** 2017 Society of Engineering Science Conference, July 2017 Boston, Massachusetts, USA
Title: Instability in fiber composites by kink band formation

- IV** 18th U.S. National Congress for Theoretical and Applied Mechanics, June 2018 Chicago, Illinois, USA
Title: Kink band instability in fiber composites

- V** 21st International Conference on Composite Structures, September 2018 Bologna, Italy
Title: Steady-state kink band broadening in fibre-reinforced composites and layered materials

- VI** 2018 Society of Engineering Science Conference, October 2018 Madrid, Spain
Title: Kink band failure in fibre composites and layered materials

- VII** DCAMM 17th Internal Symposium, March 2019 Børkop, Denmark
Title: Compressive failure of fibre-reinforced and layered composites initiated by the development of kink bands

Nomenclature

Roman Symbols

| | |
|------------|---|
| A | Area |
| a | Wave amplitude |
| b | Kink band width |
| c | Volume fraction |
| C_{ijkl} | Tensor of incremental nominal moduli |
| E | Young's modulus |
| f_α | Arbitrary function describing a vector field |
| F_{ij} | Deformation gradient tensor |
| F_i | Force vector |
| G | Shear modulus |
| H_{ij} | Inverse of help factor M_{ij} |
| J | Jacobian determinant, volume ratio |
| J_2 | Second invariant of the stress deviator tensor |
| L_0 | Initial geometry length |
| L_{ijkl} | Incremental stiffness tensor |
| M_{ij} | Help factor used in homogenisation formulations |
| N_i | Surface normal in initial state |

| | |
|-------------------|--|
| n_i | Surface normal in deformed state |
| R_{ij} | Directional cosines |
| $E_{\alpha\beta}$ | Green-Lagrange strain tensor |
| $S_{\alpha\beta}$ | Second Piola-Kirchhoff stress tensor |
| S_i | Surface vector in initial state |
| s_i | Surface vector in deformed state |
| t | Time |
| t_0 | Initial geometry thickness |
| t_{ij} | Nominal stress tensor |
| T_i | Traction vector in initial state |
| t_i | Traction vector in deformed state |
| V | Volume |
| $v_{i,j}$ | Velocity gradients |
| v_i | Velocity vector |
| W^E | External work per unit volume |
| W^I | Internal work per unit volume |
| w_0 | Initial geometry width |
| $w_{i,j}$ | Velocity gradients, stationary coordinate system |
| u | Displacement |
| u_i | Displacements tensor |
| X_i | Initial coordinates of spatial field |
| x_i | Deformed coordinates of spatial field |

Greek Symbols

| | |
|----------|----------------------------------|
| α | Fibre misalignments outside band |
|----------|----------------------------------|

| | |
|-----------------------|---------------------------------------|
| β | Kink band orientation |
| δ_{ij} | Kronecker delta |
| $\dot{\epsilon}_{ij}$ | Strain increment tensor |
| λ | Wavelength |
| κ | Fibre-matrix dependent bonding factor |
| μ | Fibre-matrix bonding factor |
| ν | Poisson's ratio |
| ϕ | Fibre misalignment |
| ϕ_0 | Largest initial imperfection angle |
| ρ | Density |
| σ | Stress |
| σ_{ij} | Cauchy stress tensor |
| τ_{ij} | Kirchhoff stress tensor |
| ω_{ij} | Spin tensor |

Superscripts

| | |
|------------------|-----------------------|
| $(\bullet)^{-1}$ | Inverse |
| $(\bullet)^{cr}$ | Critical value |
| $(\bullet)^c$ | Arbitrary constituent |
| $(\bullet)^c$ | Common material state |
| $(\bullet)^f$ | Fibre constituent |
| $(\bullet)^i$ | Inner material state |
| $(\bullet)^m$ | Matrix constituent |
| $(\bullet)^o$ | Outer material state |
| $(\bullet)^{ss}$ | Steady-state value |

$(\bullet)^y$ Yield value

Subscripts

$(\bullet)_0$ Quantity associated with initial state

$(\bullet)_\alpha$ Greek indices that take values 1 or 2

$(\bullet)_i$ Latin indices that take values 1,2 or 3

$(\bullet)_{,i}$ Comma notation denotes partial derivative with respect to x_i

Other Symbols

$\det(\bullet)$ Determinant

$d(\bullet)$ Infinitesimal piece

$\overset{\circ}{(\bullet)}$ Co-rotational Jaumann rate

$\dot{(\bullet)}$ Material time derivative

$d/dt(\bullet)$ Material time derivative

Acronyms / Abbreviations

2D **2 (Two) Dimensional**

3D **3 (Three) Dimensional**

FE **Finite Element**

PBC **Periodic Boundary Conditions**

Q4 **Bilinear Rectangular element**

Q8 **Biquadratic Rectangular element**

RVE **Representative Volume Element**

UHMWPE **Ultra-High Molecular Weight PolyEthylene**

Chapter 1

Introduction

Throughout human evolution, humans have striven to find the ideal materials for a given application. During the prehistoric periods, the Stone Age, Bronze Age and Iron Age, humans developed tools made from different materials to achieve desired properties such as increased stiffness and strength.

In the modern world of structural mechanics efforts to find and develop new materials is still ongoing and particularly materials with low density and high strength are desirable in many applications. One way to achieve these properties is to make a composition of different constituent materials, leading to the material term, composite materials. A composite material is composed of two or more constituents on the macroscopic level i.e. the constituents can be observed with the naked eye.

Besides high stiffness and low density it is possible to obtain other tailored properties that are different from the properties of the individual constituents in their bulk form. Jones (1975) identified some of the properties that can be improved: strength, stiffness, corrosion resistance, wear resistance, attractiveness, weight, fatigue life, temperature-dependent behaviour, thermal insulation, thermal conductivity and acoustical insulation.

One of the earliest uses of composite materials made by humans was wattle and daub, which is a woven lattice of wooden strips embedded in clay (Shaffer, 2006). Wattle and daub were initially used in the Neolithic era i.e. the late Stone Age. When talking about composites today, concrete, glass- and fibre-reinforced polymer composites are among the most widely known composite materials. Fibre-reinforced composites find wide application and examples of industries where composites materials are used are shown in Fig. 1.1.

In the 1970s, fibre composites were used in aerospace and defence-related industries due to their superior properties. Like many other technologies, the use of fibre composites in everyday products was initially limited due to price. Today, prices are reduced and composites



(a)



(b)



(c)



(d)



(e)



(f)

Figure. 1.1 Examples of industries where composites are used. (a) TAHOE 700 Sport boat (b) Bulletproof vest (c) F-35 Lightning II combat aircraft (d) Ferrari's Formula one car 2018 (e) the International Space Station (ISS) (f) Vestas 8 MW Wind turbine

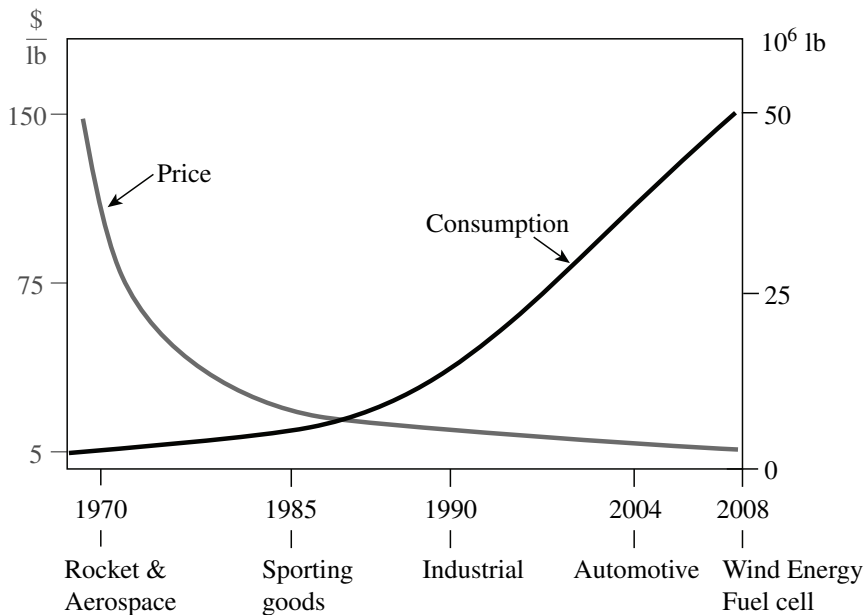


Figure. 1.2 Consumption of composites in million of pounds versus time, and price of composites in dollars per pounds versus time. Shown in a reconstructed edition. Source: The University of Tennessee Space Institute (<https://www.utsi.edu/>)

are increasingly used in the automotive, construction and sport-industries, as indicated in Fig. 1.2, taken from the University of Tennessee Space Institute. The price of composites is still relatively high due to the complexity of producing these materials e.g. laminated structures composed of fibre plies are still mainly hand-laid.

Composite materials are divided into four categories:

- Fibre composites
- Laminated composites
- Particulate composites
- Combinations of the above

Fibre composites, as the name suggests, are composed of fibres embedded in a resin material also known as a matrix. **Laminated composites** are materials composed of two or more layers of material and can be composed of layers of the same material where the individual layers have anisotropic properties e.g. carbon fibre laminated composites. A sandwich structure is another example of a laminated composite. **Particulate composites** are composed of particles of one or more materials embedded in a matrix material e.g. concrete or rocket

propellants consisting of aluminium powder in polyurethane. The current dissertation focuses on fibre composites and laminated composites (also known as layered materials).

As mentioned earlier, fibre-reinforced composites are widely used due to their high strength and stiffness together with their low density. Most commonly, stiff and strong fibres are embedded in a soft and ductile matrix material. Fibres in one layer are primarily oriented in a given direction e.g. uni-directional fibre composites. In these materials, high stiffness is only achieved in the direction of the fibres. Moreover, the high strength is mainly in tension in the direction of the fibres. The strength in compression is often only 60% of the strength in tension (Fleck, 1997). Many structures are prone to bending where the structure, and therefore the material, is exposed to both tension and compression e.g. a wind turbine blade that acts like a cantilever beam. Therefore, understanding how fibre-composites react to compression is of great importance. The study of fibre composites on the micro-mechanical level is rather complex due to the heterogeneous structure leading to anisotropic material behaviour. The heterogeneities can lead to several different compressive failure mechanisms, presented in the subsequent section.

1.1 Compressive failure modes

Compressive failure can occur due to the initiation of different mechanisms. Rosen (1965) was one of the first to investigate the mechanism of compressive failure in fibre composites. Fleck (1997) provided a thorough review of the different failure modes of fibre composites prone to compressive loading in the direction of the fibres. In his work, he distinguishes between six failure modes as presented in Fig. 1.3 and as described below:

- a) **Elastic micro-buckling** is a shear buckling instability initially studied by Rosen (1965).
- b) **Plastic micro-buckling** or kink band formation is a plastic shear instability that occurs with large shearing of the matrix and was initially studied by Argon (1972).
- c) **Fibre crushing** is a failure of the fibres prior to matrix failure and can occur due to several mechanisms, e.g. fibre yielding, longitudinal splitting and microscopic fibre kinking.
- d) **Splitting** is a fracture failure of the matrix along the fibres similar to the tensile mode I cracking and was studied by Sammis and Ashby (1986).
- e) **Buckle-delamination** is an out-of-plane buckling mode that is seen when a surface layer has insufficient bonding and was studied by Hutchinson and Suo (1991).
- f) **Shear band formation** is yielding of the matrix that occurs in a band oriented at approximately at 45° with respect to the loading axis.

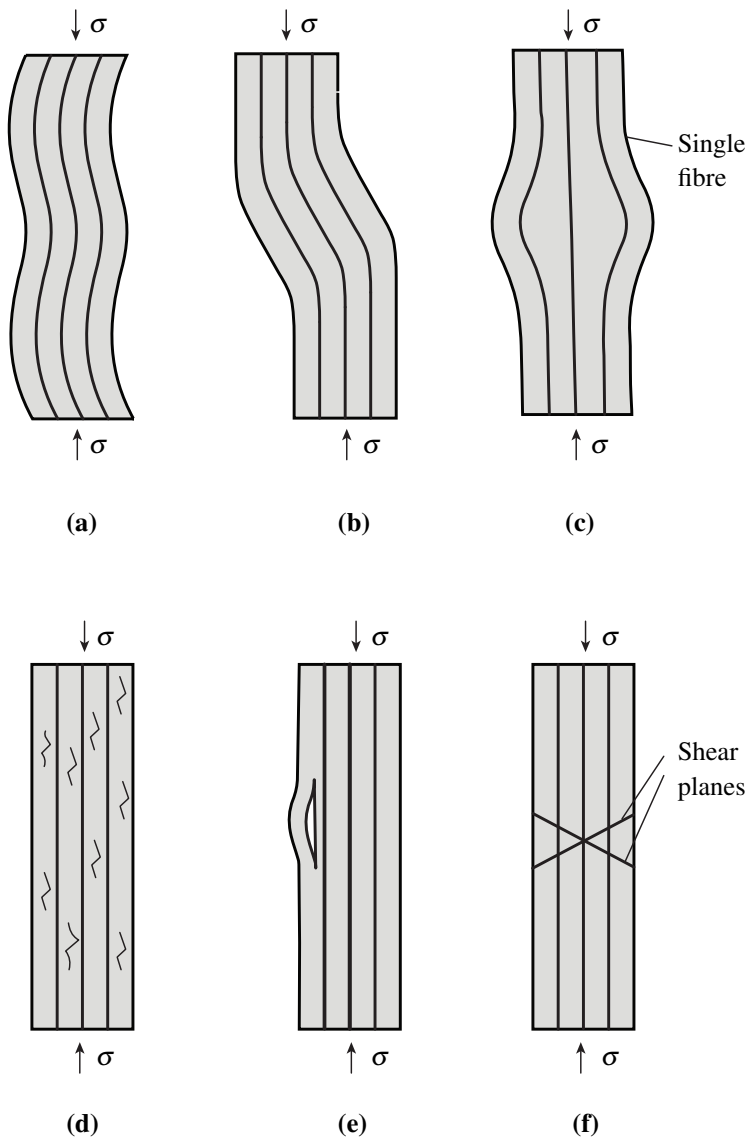


Figure. 1.3 Failure modes in fibre composites under compressive loading. Shown in a reconstructed edition (Fleck, 1997). (a) Elastic micro-buckling (b) Plastic micro-buckling (c) Fibre crushing (d) Splitting (e) Buckle-delamination (f) Shear band formation

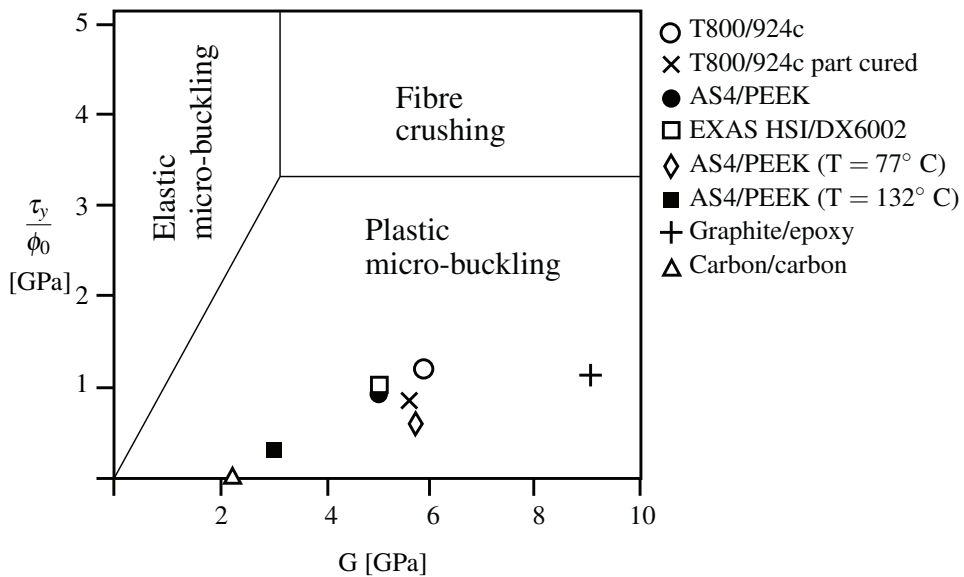


Figure. 1.4 Compressive failure map showing three competing modes of failure. The failure map has the axis of composite shear modulus G and the ratio between in-plane shear strength τ^y and fibre misalignment ϕ_0 . Shown in a reconstructed edition (Fleck, 1997)

Fleck (1997) created several failure maps with appropriate axes to graphically observe the competition between the different failure modes by using simple upper bound solutions for the compressive failures. One of the failure maps constructed by Fleck (1997) is presented in Fig. 1.4. The map has the in-plane composite shear modulus G as the first axis and the second axis is the ratio between in-plane shear strength τ^y and fibre misalignment ϕ_0 . The two-dimensional failure map distinguishes between three final failures: elastic micro-buckling, plastic micro-buckling and fibre crushing. Material data for eight different carbon fibre-reinforced composites is included in the map and for these materials, plastic micro-buckling or kink band formation is the dominant mode of failure in compression. The following section will further clarify the mechanisms of kink band formation.

1.2 Kink band formation

Kink band failure is also known as plastic micro-buckling or fibre kinking. In the current dissertation, the failure will mainly be referred to as kink band formation. Two experiments showing the formation of kink bands are shown in Fig. 1.5 for two different materials. Vogler and Kyriakides (1997) considered the initiation and propagation of kink bands in a carbon

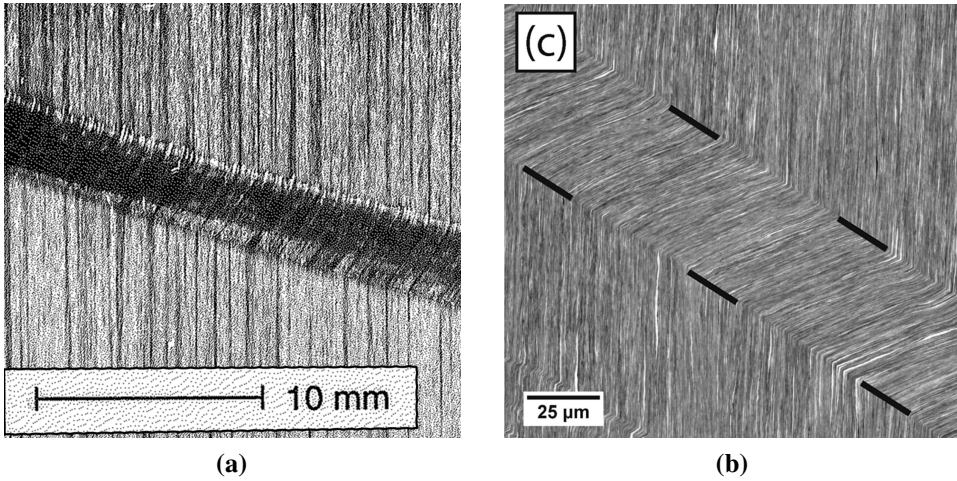


Figure 1.5 Kink band formation in two different fibre composites. (a) AS4/PEEK composite (Vogler and Kyriakides, 1997). (b) Cu/Nb nanolaminate composite (Nizolek et al., 2017).

fibre-reinforced PEEK composite shown in Fig. 1.5a. At the former stage, the kink band width is approximately $b \approx 2000 \mu\text{m}$: see Fig. 1.6. In an experiment conducted by Nizolek et al. (2017) on a Cu/Nb nanolaminate composite, the kink band width is approximately $b \approx 50 \mu\text{m}$ (Fig. 1.5b). The two orders of magnitude difference in kink band width is due to the difference in fibre and layer sizes. Based on experimental findings (e.g. Fig. 1.5), an idealised kink band geometry can be introduced, such as the one demonstrated in Fig. 1.6. The idealised kink band geometry is composed of two material states: a kinked state and an unkinked state. The kinked material, which is localised within a narrow band of width b , has rotated an amount of ϕ relative to the base material. The localisation band is oriented at angle β with respect to the x_2 -axis, as presented in the figure. The material state within the kink band has undergone large shear straining.

One of the studies earliest studies in which kink band formation was observed was conducted by Paterson and Weiss (1966) on a phyllite that is a type of foliated metamorphic rock. In his early work, Rosen (1965) derived an analytical expression based on the compressive bifurcation load of beams surrounded by an elastic matrix. He suggested two bifurcation modes: a tension and a shear mode. The shear mode gave the lowest compressive strength σ_{11}^{cr} at bifurcation and was equal to

$$\sigma_{11}^{cr} = G \quad (1.1)$$

where G is the in-plane elastic shear modulus of the composite. The estimate by Rosen (1965) overpredicts the compressive strength (Lager and June, 1969). Experiments show

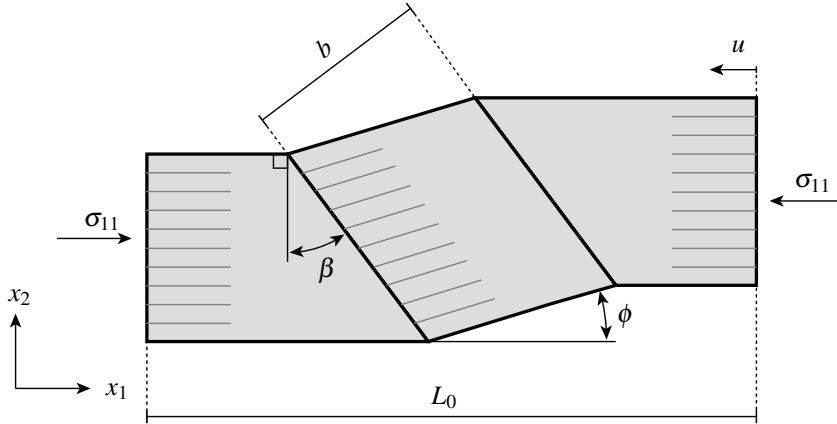


Figure. 1.6 Idealised kink band geometry

compressive strengths down to 1/4 of the prediction by Rosen (1965). Later, Argon (1972) suggested an upper bound solution concerning a composite with rigid plastic properties in shear with a shear yield strength of τ^y . He showed that the compressive strength was influenced by initial fibre misalignments equal to

$$\sigma_{11}^{cr} = \frac{\tau_y}{\phi_0} \quad (1.2)$$

The estimate by Argon (1972) explains the knock-down in compressive strength compared to the estimate by Rosen (1965). The two estimates by Rosen (1965) and Argon (1972) given by Eqs. (1.1) and (1.2) were used by Fleck (1997) to create the two-dimensional failure map presented in Fig. 1.4. Several other attempts have been made to develop analytical expressions of the compressive strength of fibre composites and layered materials due to kink band formation. Budiansky (1983) investigated the elastic-plastic shear behaviour of a composite with rigid fibres. Fleck and Budiansky (1991) examined the influence of shear stresses and later, Slaughter et al. (1993) considered transverse stresses. In all of the above analytical expressions the kink band angle β is assumed to be zero. Christoffersen and Jensen (1996) provided a method for finding the compressive bifurcation stress of a composite with an arbitrary non-linear composite behaviour where the constituents can be described by two independent constitutive relations. Furthermore, the formulation could take nonzero values of the kink band angle β . Christoffersen and Jensen (1996) derived an analytical expression of the bifurcation strength in the case of rigid fibres and found that the lowest compressive strength was achieved with a kink band angle $\beta = 0$.

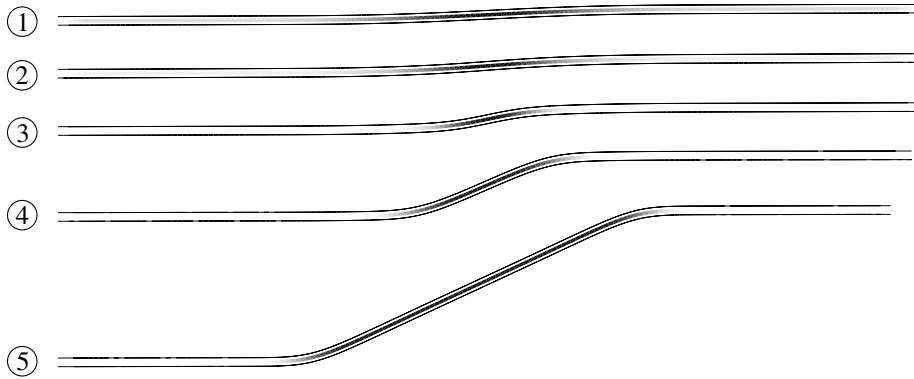


Figure. 1.7 Shear strain in matrix constituent, ϵ_{12} , for five deformed stages of a unit cell. The geometry has an initial imperfection $\phi_0 = 2^\circ$ and a band orientation $\beta = 10^\circ$

To further enhance the reader's understanding of kink band instability, a compressive response from a representative finite element (FE) simulation is presented. Instead of showing the deformation pattern of a full kink band geometry, the deformations of a single unit cell strip with periodic boundary conditions are shown in Fig. 1.7. The model set-up is described in Chapter 2. A compressive displacement is applied in the direction of the fibres. The FE-model is composed of two layers of fibre and a single matrix layer. In the current example, material parameters for an AS4/PEEK composite are used, taken from Kyriakides et al. (1995). Five deformed stages of the geometry are presented in Fig. 1.7. The normalised compressive stress $-\sigma_{11}/G$ as a function of end-displacement is shown in Fig. 1.8, and the normalised compressive stress as a function of fibre rotation ϕ is shown in Fig. 1.9. The geometric quantities L_0 , u and ϕ are designated in Fig. 1.6. The dark regions in Fig. 1.7 correspond to zones of large shear strain.

As described by Liu et al. (1996), the formation of kink bands can be divided into different stages: the linear response and incipient kinking ①, peak stress ②, transient kinking ③ and steady-state kink band broadening ④ and ⑤. Initially, a linear response is observed. With increasing displacement, the stress in the matrix approaches the yield strength at stage ①. At stage ② the matrix has undergone adequate material softening, so that the composite becomes unstable and a kink band initiates. Following the peak load ②, the load drops and the compressive displacement decreases due to elastic relaxation at stage ③. The snap-back phenomenon can not be captured in experiments; rather a dynamic response will follow the peak-load in a real experiment for this particular choice of initial imperfection. The load drops further and asymptotically approaches a constant stress at stage ④, known as the steady-state kink band broadening stress σ_{11}^{ss} or Maxwell stress. Going from stage ④ to ⑤

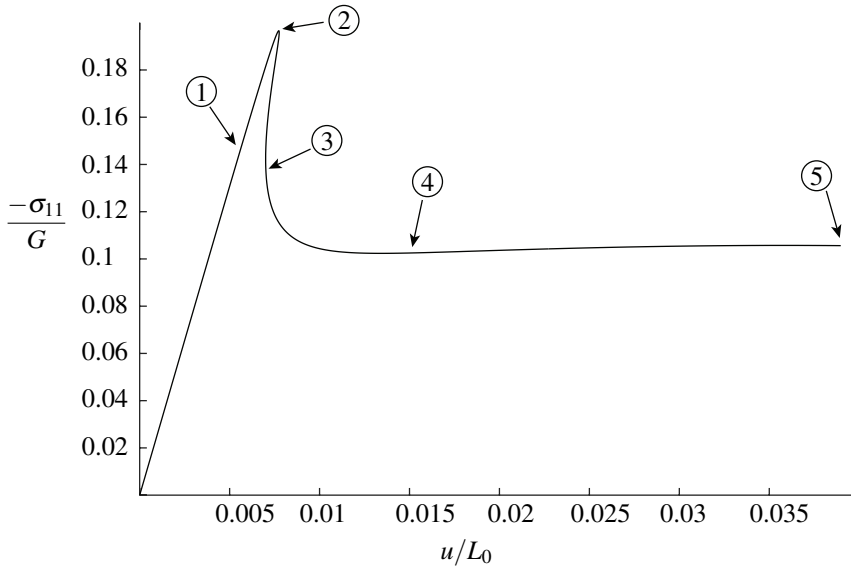


Figure 1.8 Applied normalised stress $-\sigma_{11}/G$ as a function of normalised end shortening u/L_0 for a simulation with a band orientation $\beta = 10^\circ$. The five deformation stages are designated in Fig. 1.7.

the end-displacement has increased and the kink band has broadened or propagated under the constant applied stress σ_{11}^{ss} . Moreover, by focusing on Fig. 1.9 shows almost, nearly no further fibre rotation is observed going from stage ④ to ⑤.

The instability phenomenon, kink band formation, discussed in the current dissertation is similar to a number of other physical phenomena seen on both structural and material scales. Common to several of these phenomena is that a critical load is followed by a steady-state. Examples of instabilities on the material scale include neck propagation in the drawing of polymers, e.g. Hutchinson and Neale (1983); crushing of metal foams, e.g. Ashby et al. (2000); and instabilities in elastic bars, e.g. Ericksen (1975). Other examples of propagating phenomena include channelling of cracks (e.g. Beuth (1992); Jensen and Thouless (1995)) and phase transformation of mediums, e.g. Guggenheim (1959).

Similar instabilities on the structural level were discussed in the review by Kyriakides (1998) and include bulging of internally pressured rubber cylinders (e.g. Kyriakides and Yu-Chung (1991); Corneliussen and Shield (1961); Chater and Hutchinson (1984)), buckling and propagation of externally loaded undersea pipelines (e.g. Mesloh et al. (1973); Palmer and Martin (1972); Jensen (1988)), and buckling of long shallow arches (e.g. Timoshenko and Young (1962); Schreyer and Masur (1966); Kyriakides (1993)).

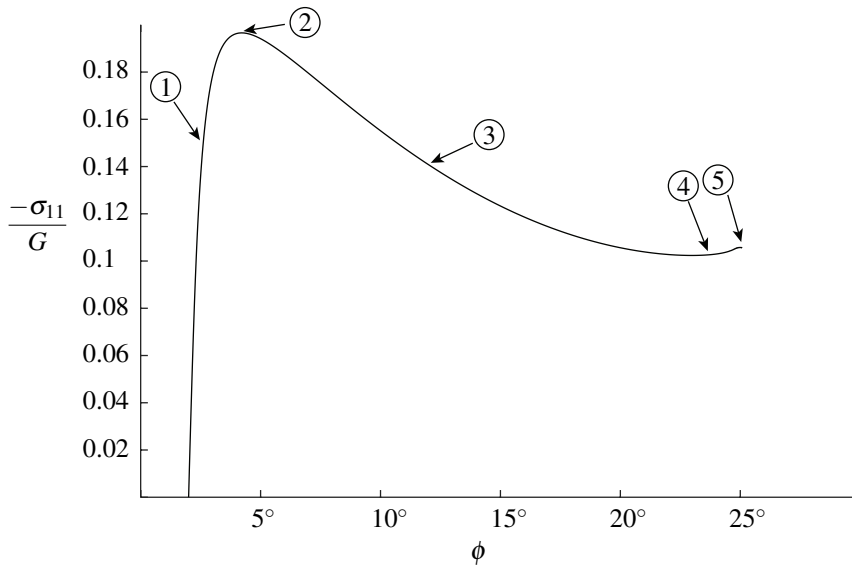


Figure 1.9 Applied normalised stress $-\sigma_{11}/G$ as a function of fibre rotation ϕ for a simulation with a band orientation $\beta = 10^\circ$. The five deformation stages are designated in Fig. 1.7.

1.3 Scope of work

The current dissertation is written and structured based on the 'Guidelines for writing a cumulative PhD thesis' set out by the Department of Engineering, Aarhus University. The three subsequent chapters include the methods and the theoretical foundation behind the articles written during the PhD. Brief descriptions of the articles are attached prior to the articles themselves and include the motivation, methods, contributions and main findings for the given article. The dissertation includes the following chapters:

Chapter 2 presents the inspiration, assumptions and implementation of the finite element models used and presents appropriate equations and illustrations. The chapter does not include the results obtained using the models since these are presented in the articles.

Chapter 3 describes an idealised kink band model used in the publications [P1-P4]. The kink band model was initially developed by Jensen and Christoffersen (1997). Variations of the model were developed during the PhD so a substantial amount of time was spent understanding, modifying and developing the models.

Chapter 4 describes an analytical model used to study the kink band broadening phenomenon. The model was initially developed in [P3] and was used in a similar form in [P4].

Chapter 5 summarises the work done during the PhD. Furthermore, the chapter puts the contributions in perspective and suggestions for further work are given.

Chapter 6 includes the first article and deals with the development of a three-dimensional constitutive model that can predict strain localisation in fibre-reinforced composites. The constitutive model is implemented within a kink band model that is presented in Chapter 3.

Chapter 7 includes the second article, which deals with the development of a constitutive model for a fibre composite that takes imperfect fibre/matrix interfacial bonding into account. The constitutive model is used together with a kink band model that is presented in Chapter 3.

Chapter 8 includes the third article and deals with the study of steady-state kink band propagation using the three different models presented in Chapters 2, 3 and 4.

Chapter 9 includes the fourth article, which again deals with kink band broadening. This publication includes two case studies, of different length scales, and involves different materials.

Chapter 10 presents the fifth article. This article is written based on the work done during my visit to the Department of Mechanical Engineering in Cambridge, UK. It deals with the study of load transfer in a bolted joint in a laminate made from ultra-high molecular weight polyethylene.

Chapter 11 includes an article, mainly written by the master's student Vedad Tojaga, for which I am a co-author. The article deals with the development of kink bands in open-hole fibre composites under compressive loading.

Chapter 2

Finite element models

This chapter will describe the finite element models used to study fibre-kinking during the project. Different FE-models of varying complexity have been developed for the study of kink band formation in the last couple of decades. The FE-models presented in this chapter are comparable to the models by Kyriakides et al. (1995) and Hsu et al. (1999). Either two- or three-dimensional models can be used. In the current work, both two- and three-dimensional models were used when appropriate.

The models are further divided into discrete and homogenised models. In the discrete models, the composite constituents are modelled explicitly as different geometry parts, where different material behaviours are given to the constituents e.g. fibre and matrix. For the homogenised models, the average properties of a representative volume element are used. There are advantages and disadvantages to each method. The advantages of using discrete models are: details about the fibre geometry and distribution can be included; the interaction with the surrounding matrix can be studied. If commercial software such as Abaqus/CAE is used, the built-in material behaviour can be utilised. When the constituents are modelled separately, the interaction between the parts can be modelled explicitly by e.g. using cohesive elements or contact friction. Moreover, using X-ray tomography, a real fibre configuration can be built. Based on the X-ray scan, discrete FE-models can be built by reconstruction followed by segmentation into fibre and matrix parts. Some disadvantages of using discrete models can be the computational time due to the level of detail. It can be rather difficult to build the fibre-matrix layout explicitly, even for simple geometries, which gives a key advantage to the use of homogenised models.

Most of the composites of interest exhibit non-linear material behaviour in the form of plastic deformation, at the deformations required for kink band formation. Furthermore, by using the common geometrical configurations used to study fibre-kinking, snap-back and

snap-through, instabilities occur in the equilibrium path when using an implicit finite element code. This leads to the use of non-linear arc-length solvers. In all of the FE-simulations, time-independent formation of kink bands is studied using Abaqus/CAE.

2.1 Geometries

A typical composite structure consists of multiple layers. A popular choice is to use uni-directional fibre plies (or lamina) and stack them together with different fibre orientations, as seen in Fig. 2.1. An assembly of plies is called a composite laminate, or simply a laminate. The average anisotropic constitutive behaviour of a laminate is used on a larger scale to predict the overall structural behaviour. A representative volume element (RVE) of a laminate structure will in the general case be exposed to a three-dimensional stress and strain state. Classical laminated plate theory is frequently used in connection with composite laminates. Using the theory, assumptions about the continuity of displacements are made. Therefore, if the deformation of a ply is known based on the deformation of the laminate, and if the constitutive relation is also known, the stress state can be determined. Multiple authors have developed failure criteria for composite plies for different loading conditions e.g. shear-, tensile-, compressive-, fatigue failure and others. In the current study, the focus is given to compressive failure in the fibre direction

Fig. 2.1 shows a laminate together with an exploded view of the same laminate. The principal strains at a point can be determined based on the general strain state. The direction of maximum compressive strains is of interest when considering a laminate composed of uni-directional plies. The plies with fibre orientations closest to the direction of the maximum principal compressive strain will be exposed to the highest compressive stresses due to higher stiffness in the fibre direction. The blue highlighted plies in Fig. 2.1 will be exposed to the highest stresses and will therefore fail first. Thus, it is a valid simplification to study a single ply when regarding the compressive failure of laminates.

A section of a ply is illustrated in Fig. 2.2 to the left. A hexagonal distribution of the fibres is assumed based on the assumption of equal spacing between fibres and an even distribution of the matrix. The effect of variations in the layout of fibre distribution upon the constitutive behaviour was studied by e.g. Huang (2018). A full model as displayed in Fig. 2.2 can be very computationally expensive to solve when with regard to the study of kink band formation. Naya et al. (2017) considered a full model using approximately 50 fibres that were randomly distributed. In the simulations, they included cohesive elements between the fibre and matrix components. Furthermore, finite deformation and material non-linearities were included. Using a cluster, the full model studied by Naya et al. (2017) took more than 72 hours to solve. This high computational time has led to the use of simplified models,

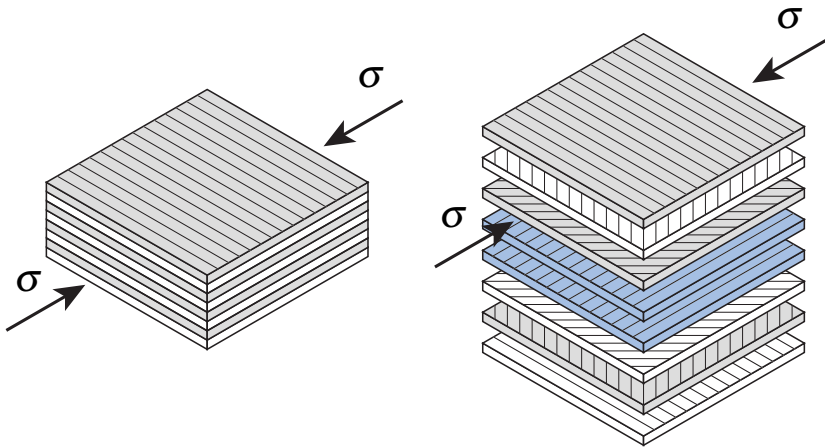


Figure. 2.1 Illustration of a laminate section (left) and an exploded view (right) of the same laminate. The lamina that have the same fibre directions as the direction of loading are highlighted with blue.

either by simplifying the FE-problem or by using alternative computational methods, e.g. the constitutive models presented in Chapters 3 and 4.

Examples of possible simplifications of the full FE-model are demonstrated in Fig. 2.2. Here the simplifications are divided into two- or three-dimensional versions. Moreover, two levels of simplification are shown: a layered model and a unit cell model. The layered models make it possible to study variations of the geometry in the plane i.e. both initial geometry and post-buckling configuration. As an example, Fleck and Shu (1995) identified the influence of imperfections confined within an elliptically-shaped domain in the plane upon kink band formation. Hsu et al. (1998) used a three-dimensional layered model and compared it with a two-dimensional version; only small variations between the results were observed. Wind et al. (2014) used a two-dimensional layered model, inspired by the one introduced by Kyriakides et al. (1995).

The next level of simplification after layered models is unit cell models. A three-dimensional unit cell model is used in [P2] in order to study the influence of bonding between the fibre and matrix. Prabhakar and Waas (2013) used a two-dimensional model to study the influence of fibre-to-matrix bonding; however when using a two-dimensional model and when low or no bonding is present, the shear straining in the matrix becomes unrealistic. This fact led to the use of a three-dimensional model in [P2]. The model was simplified into a unit cell model to decrease the computational time. A two-dimensional unit cell model is the most computationally efficient discrete kink band FE-model and was used in [P3] and [P4] to study kink band broadening. When using the unit cell models to study kink bands,

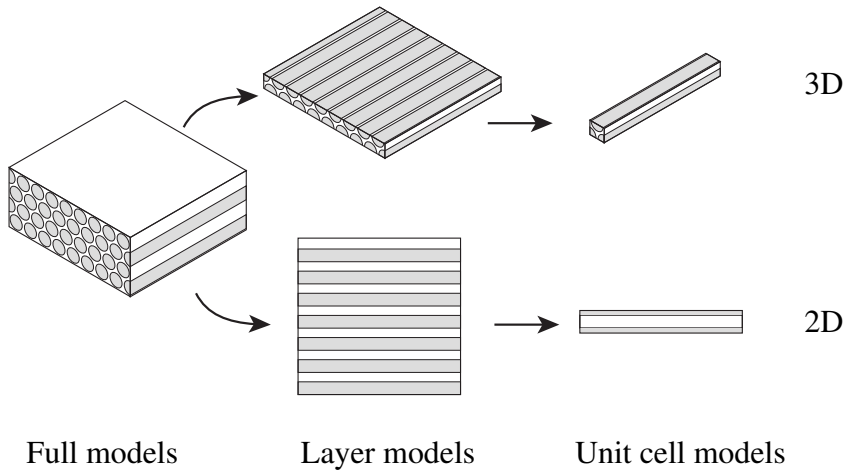


Figure. 2.2 An illustration of a section from an uni-directional lamina (left). Two simplification levels, **Layer models** and **Unit cell models**, are illustrated from **Full models** for both 2D and 3D models.

periodic boundary conditions (PBC) are required, which will be described in Section 2.3, to avoid structural Euler buckling.

An alternative simplification from the full model is to use a homogenised model. An example of a homogenised FE-model is presented in Fig. 2.3. As described earlier, the overall constitutive behaviour is needed for these models. An example of a constitutive formulation that was developed by Christoffersen and Jensen (1996) will be presented in Chapter 3. The latter constitutive formulation was implemented in an FE-model and was used in [C1] to study the compressive response of fibre composites with open-holes.

2.2 Imperfection

The critical compressive stress at the initiation of kink bands is highly sensitive to geometrical imperfections as confirmed in the review by Fleck (1997). There are several ways to introduce imperfections into the analyses. One choice of initial imperfection is to use a superposition of deformations obtained from a linear buckling analysis. Alternatively, an assumed imperfect geometry can be implemented; e.g. Kyriakides et al. (1995) introduced a uniform sinusoidal waviness of the fibres and Fleck and Shu (1995) considered an area of fibre imperfections confined to an ellipse. Sørensen et al. (2009) studied kink band formation using a homogenised model with the constitutive formulation developed by Christoffersen and Jensen (1996). In the FE-model by Sørensen et al. (2009), an imperfection in the form of

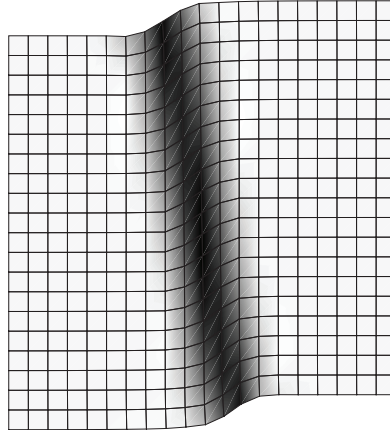


Figure. 2.3 An example of an FE kink band simulation using a homogenised constitutive model. The dark zone is an area of high plastic strain.

an infinitesimal kink band was used where the directions of fibres ϕ were described by the analytical expression

$$\phi(X_1, X_2) = \begin{cases} \frac{1}{2} \phi_0 \left[\cos \left(\frac{2\pi \cos \beta}{b} (X_1 + X_2 \tan \beta) \right) + 1 \right] + \alpha & \text{if } X_{1,min} < X_1 < X_{1,max} \\ \alpha & \text{otherwise} \end{cases} \quad (2.1)$$

where ϕ_0 is the largest imperfection angle, β is the angle of the band, b is the band width and α is the fibre angle outside the band. The equation above was presented in Sørensen et al. (2009) and can also be presented in the equivalent form

$$\phi(X_1, X_2) = \begin{cases} \phi_0 \cos^2 \left(\frac{\pi \cos \beta}{b} (X_1 + X_2 \tan \beta) \right) + \alpha & \text{if } X_{1,min} < X_1 < X_{1,max} \\ \alpha & \text{otherwise} \end{cases} \quad (2.2)$$

The geometric quantities are presented in Fig. 2.4. Hutchinson and Koiter (1970) wrote a review on the bifurcation and post-buckling of plates and shells. According to Hutchinson and Koiter (1970), an imperfection in the shape of the buckling mode results in the largest reduction in buckling load. An imperfection in the form of a kink band will therefore be the most critical imperfection. By assuming that the fibre imperfection angle ϕ , described by Eq. (2.1) or (2.2), is equal to the derivative $\phi = dx_2/dx_1$, the deformed coordinates x_2 can be determined. Small letters x_α refer to deformed coordinates while capital letters X_α are initial

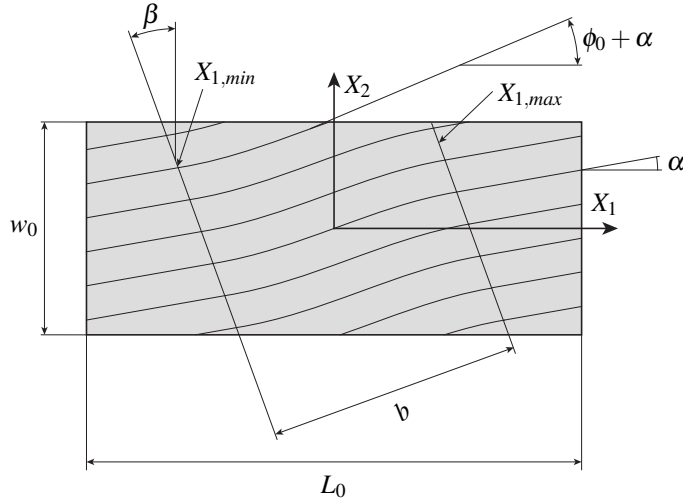


Figure. 2.4 Illustration of initial imperfection in the form of fibre misalignments. Sørensen et al. (2009) introduced the current imperfection and is used in the simulation presented in Fig. 2.3.

coordinates. It is assumed that the deformed coordinate x_1 is equal to the initial coordinate ($x_1 = X_1$). The deformed coordinate x_2 can be integrated into the form

$$x_2(X_1, X_2) = \begin{cases} X_2 + \frac{1}{2} \phi_0 \left(\frac{-b}{2 \cos \beta} - X_2 \tan \beta \right) + \alpha X_1 & \text{if } X_1 < X_{1,min} \\ X_2 + \frac{1}{2} \phi_0 \left[\frac{b}{2 \pi \cos \beta} \sin \left(\frac{2 \pi \cos \beta}{b} (X_1 + X_2 \tan \beta) \right) + X_1 \right] + \alpha X_1 & \text{if } X_{1,min} < X_1 < X_{1,max} \\ X_2 + \frac{1}{2} \phi_0 \left(\frac{b}{2 \cos \beta} - X_2 \tan \beta \right) + \alpha X_1 & \text{if } X_{1,max} < X_1 \end{cases} \quad (2.3)$$

where the boundaries $X_{1,min}$ and $X_{1,max}$ are introduced, which are simply two equations for the two boundary lines

$$X_{1,min}(X_2) = \frac{-b}{2 \cos \beta} - X_2 \tan \beta \quad X_{1,max}(X_2) = \frac{b}{2 \cos \beta} - X_2 \tan \beta \quad (2.4)$$

The imperfection, Eq. (2.3), is used in [P2], [P3] and [P4]. A geometrical representation of an initial geometry and the corresponding imperfect geometry are illustrated in Fig. 2.5. The imperfection angle used in the figure is $\phi_0 = 15^\circ$ where the initial imperfection angles used in the simulations are in the range $\phi_0 \approx 0^\circ - 5^\circ$. In both Fig. 2.4 and Fig. 2.5, the initial geometry width w_0 and length L_0 are presented.

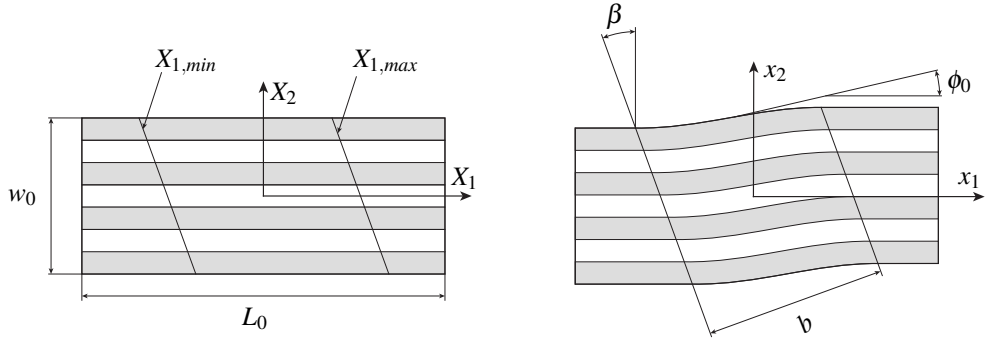


Figure. 2.5 Illustration of an uni-directional lamina before (left) and after (right) the imperfection is used given by Eq. (2.3). The fibre angle outside the band is $\alpha = 0^\circ$ in the current illustration.

2.3 Boundary conditions

The most simple boundary conditions are applied to the geometries that still capture the kink band phenomenon. The displacements u_i are, introduced which are the displacements along the corresponding axes X_i . In all of the simulations, the left boundary is simply supported and the lower left corner is fully fixed. With a coordinate system placed in the geometry centre, the boundary condition can be described by

$$\begin{aligned} u_1 &= 0 \quad \text{on} \quad X_1 = -\frac{L_0}{2} \\ u_2 &= 0 \quad \text{on} \quad (X_1, X_2) = \left(-\frac{L_0}{2}, -\frac{w_0}{2}\right) \end{aligned} \quad (2.5)$$

The boundary conditions are graphically displayed in Fig. 2.6. Furthermore, in the FE-simulations where a three-dimensional model is used, the front and back are simply supported as well:

$$\begin{aligned} u_3 &= 0 \quad \text{on} \quad X_3 = -\frac{t_0}{2} \\ u_3 &= 0 \quad \text{on} \quad X_3 = \frac{t_0}{2} \end{aligned} \quad (2.6)$$

where t_0 is the initial thickness of the geometry. Besides the boundary conditions, loading is applied in the form of applied stress or displacement. In [P2], [P3] and [P4], loading in the form of an applied displacement u is used. When using an applied displacement field, the stress can be calculated based on the reaction forces in the corresponding nodes.

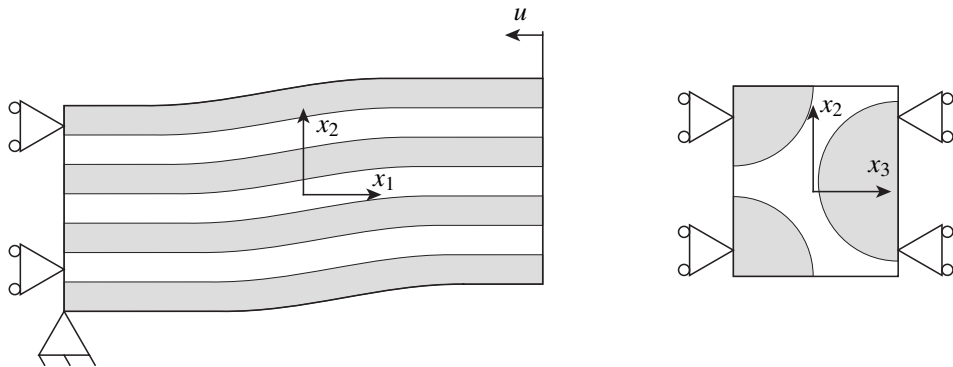


Figure. 2.6 Visualisation of the boundary conditions used for the FE kink band model. The BCs on the right does only apply for the 3D models.

In the simulations where a unit cell model is used (as in [P2], [P3] and [P4]), periodic boundary conditions are used between the top and bottom boundary. The PBCs are applied such that a single unit cell model represents an infinite array of fibres. The PBCs are enforced using constraint equations in the form

$$u_i^{(A)} - u_i^{(B)} = 0 \quad (2.7)$$

where $(\bullet)^{(A)}$ and $(\bullet)^{(B)}$ correspond to nodes on the top and bottom boundaries. An example of the coupling between two nodes is presented in Fig. 2.7. When using PBCs, it is common to use nodes that share some coordinates, e.g. $X_1^{(A)} = X_1^{(B)}$ and $X_3^{(A)} = X_3^{(B)}$, as in the model used in [P2]. An alternative node coupling is introduced in [P3] to account for the band inclination. In [P3] the coupled nodes are oriented with an angle β prior to deformation. This forces the band to initiate and to propagate in a specified angle β .

2.4 Discretisation

In the FE-model presented in [P3], the influence of the number of elements per constituent layer was investigated. It was concluded that a single element in the height per layer is sufficient. The material behaviour of the constituents, presented in [P1]-[P4], is taken from Kyriakides et al. (1995). The constituents in the latter study were AS4-carbon fibres embedded in a PEEK matrix. In this composite, Young's modulus of the fibres is 35 times the modulus of the matrix. In a kink band simulation using the latter constituents, the fibres will take most of the bending and the matrix will almost be in a state of pure shear.

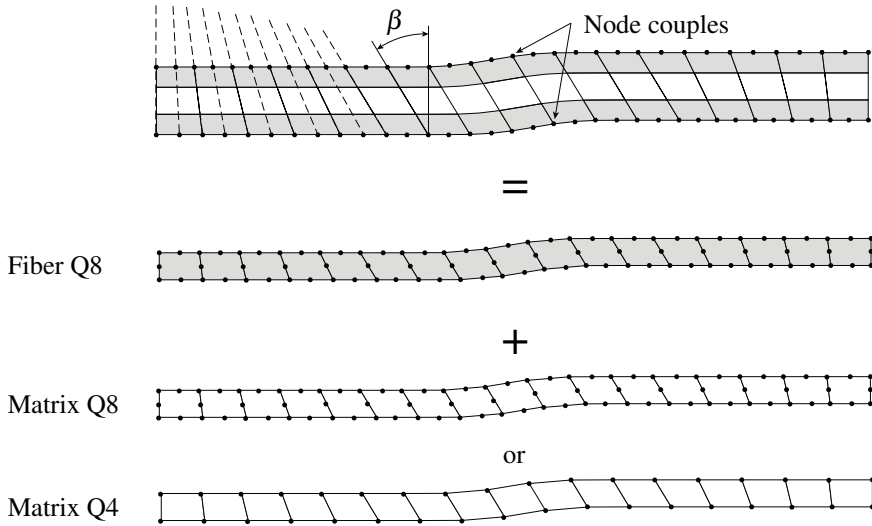


Figure. 2.7 Illustration of the discretisation of the kink band geometry into separate elements. In the top geometry, the node couplings are presented when using periodic boundary conditions. Furthermore, the combination of elements are illustrated.

In the two-dimensional models plane-strain, 8-node biquadratic elements (Q8) with full integration were used for the fibres. Biquadratic elements were chosen for the fibre geometry instead of bilinear elements since Q8 elements give a more realistic response during bending. The influence of using either 8-node biquadratic elements or 4-node bilinear elements (Q4) with full integration for the matrix constituent was investigated in [P3]. The idea of combining two incompatible elements (biquadratic and bilinear) was inspired by the micro-mechanical model used by Sutcliffe and Fleck (1997). The discretisation scenarios are presented graphically for a unit cell model in Fig. 2.7. No observable differences were seen in the applied stress versus end-displacement curve when converting the elements from biquadratic to bilinear. One of the primary benefits of using bilinear elements for the matrix layer is a lower computational time; however more importantly, it was possible to obtain a larger part of the post-bifurcation response. In [P3] and [P4] the propagating instability known as kink band broadening was investigated and here the late post-buckling response is of high importance.

In the three-dimensional unit cell model from [P2], a combination of 20-node quadratic bricks and 15-node triangular prism elements with full integration was used for the fibre constituents, while 20-node quadratic bricks with full integration were used for the matrix. Again, the influence of mesh refinement was investigated for the three-dimensional model

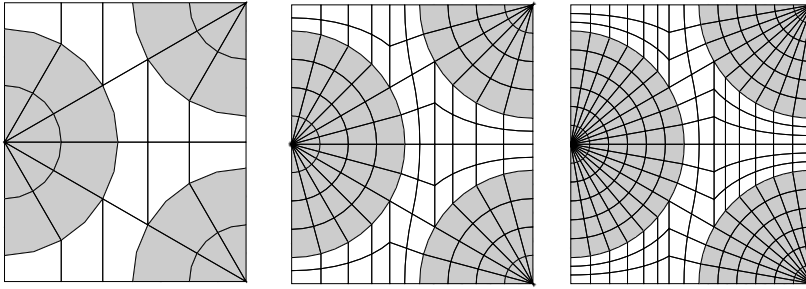


Figure. 2.8 Illustration of the cross-section of the three-dimensional unit cell model showing the different mesh refinements used.

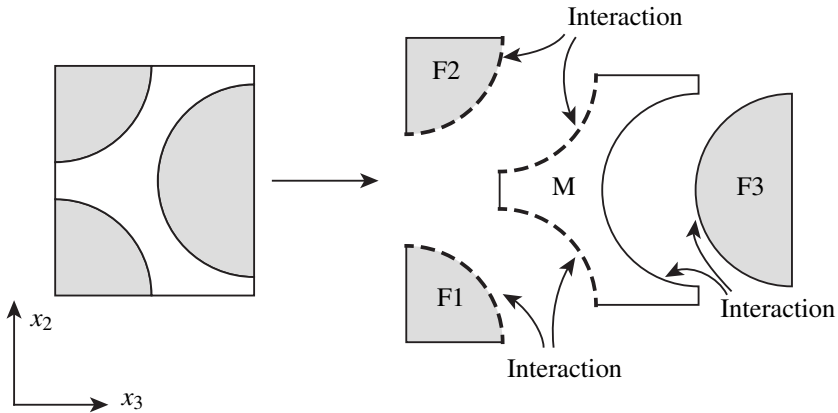


Figure. 2.9 The cross-section of the three-dimensional unit cell model (left) and an exploded view (right) of the same section. The surfaces are designated where fibre-to-matrix interaction can occur.

and three examples of refinement of the cross-section are shown in Fig. 2.8. Visualisations of the nodes is omitted for clarity. The coarsest mesh presented in Fig. 2.8 was used due to negligible differences in the critical compressive stress and due to the lower computational time.

2.5 Interaction

In [P2], the influence of fibre-to-matrix bonding upon the critical compressive strength was investigated. A normal and an exploded view of the cross-section of the unit cell model are presented in Fig. 2.9. The unit cell was composed of four parts: three fibre parts and one matrix part. In the FE-model, the four parts were formulated as four different parts with

the possibility of exploiting the fibre-to-matrix interaction by using e.g. contact friction or cohesive elements. The FE-model in [P2] was compared with a constitutive model that will be presented in Chapter 3. For simplicity's sake, two simple interaction scenarios were used: a tie constraint and a frictionless hard contact interaction. Based on the two interaction possibilities, three bonding scenarios were created: a case of perfect bonding; a case of no bonding; and a case of intermediate bonding. In the case of perfect bonding, tie constraints were applied between the relevant parts and in the case of no bonding, the frictionless contacts were used. In the case of intermediate bonding, tie constraints were used for half of the surfaces (dashed lines in Fig. 2.9), while for the remaining surfaces, frictionless contacts were used.

Chapter 3

Semi-analytical kink band model

This chapter will describe an idealised kink band model, which will be referred to as the semi-analytical model. The kink band is idealised to consist of two material states: a state inside the kink band and a state outside. However, in contrast to the FE-model, the current model does not consider the transition from unknicked to the knicked configuration. The kink band model that will be presented in the current chapter was developed by Jensen and Christoffersen (1997) using a homogenised constitutive formulation introduced in Christoffersen and Jensen (1996). The model requires continuity of displacements and traction equilibrium between the base and knicked material and is solved incrementally. Full elastic-plastic constitutive formulations can be used with the model without initial requirements of e.g. rigid fibres or incompressibility.

The constitutive model is used in several of the publications [P1-P4] and variations of the model so a substantial amount of time was needed during the project to understand, modify and develop the models. Therefore, the assumptions and theories behind the models will be described in detail in the current chapter. It is assumed that the reader has knowledge about index notation and fundamental continuum mechanics (such as the equilibrium- and compatibility equations).

3.1 General relations

In the current section, the continuum mechanics foundation is presented. Throughout the chapter, the index notation and the summation convention are adopted. Latin indices i.e. i, j, k take values 1, 2, 3 and Greek indices α, β, γ take values 1, 2. In general, the Latin and Greek indices are used with three- and two-dimensional problems, respectively. A comma

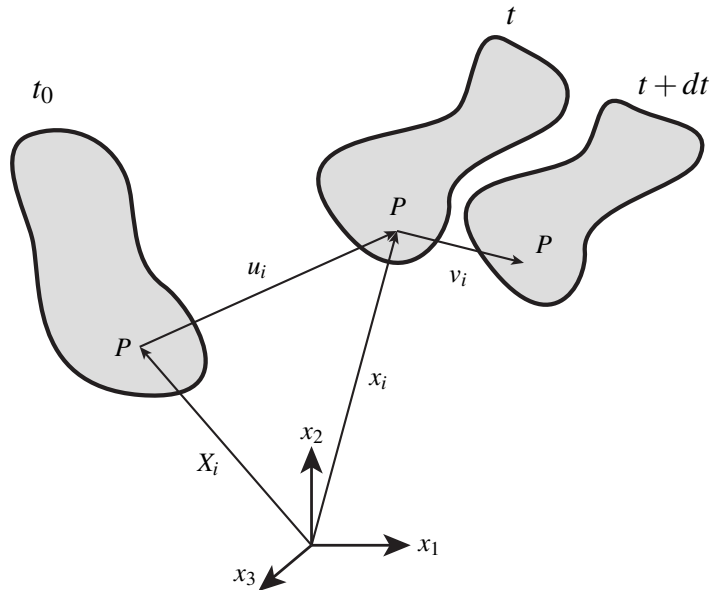


Figure. 3.1 Illustration of an arbitrary continuum body at three instants of time. The illustration shows the important vectors founding the basis of the kinematics.

$(\bullet)_{,i}$ denotes a partial derivative with respect to the x_i coordinate. A general continuum body is illustrated in Fig. 3.1 in a three-dimensional Euclidean space with a Cartesian coordinate system containing the three orthonormal directions x_1, x_2 and x_3 . The initial state of the body at time $t = 0$ is described by the coordinates X_i with capital letters. The body may include residual stresses σ_{ij} prior to deformation. The body in the current or deformed configuration at time t is described by the coordinates x_i . The displacement vector $u_i(X_i)$ describes the displacements of every point going from the initial to the current configuration. The configuration subsequent to a small time increment $t = t + dt$ is illustrated as well. In both time-dependent and -independent continuum mechanics the velocity vector $v_i = \dot{x}_i$ is used, where the dot ($\dot{\bullet}$) refers to the material time derivative. In the current study, time-independent constitutive formulations are used and here v_i are regarded as infinitesimal displacement increments taking place during a pseudo-time increment dt . In the proceeding derivations, deformation gradients are used. The deformation gradients relate infinitesimal vector elements in the initial to the current configuration

$$dx_i = F_{ij} dX_j \quad (3.1)$$

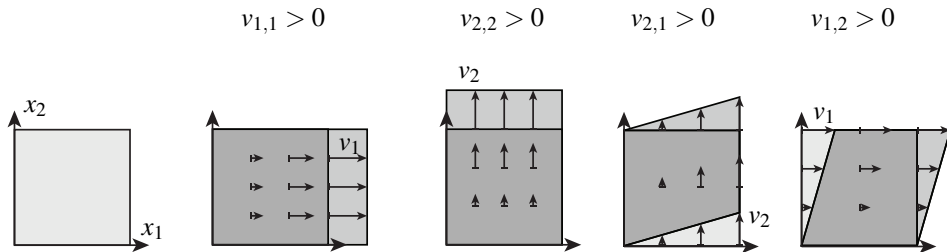


Figure. 3.2 Five configurations for a square are shown: one initial state to the left and four deformed configurations.

where the definition of the deformation gradients is

$$F_{ij} = \frac{\partial x_i}{\partial X_j} \quad (3.2)$$

Furthermore, the velocity gradients $v_{i,j}$ are used in the constitutive model. The velocity gradients give information about how the velocities change in the vicinity of a point in the direction of the basis x_i . Simple illustrations of squares undergoing homogeneous deformations are shown in Fig. 3.2 with the relevant velocity gradients marked on the figure above the deformations. The deformed configuration (dark area) is superimposed upon the initial configuration (light area). The strain increment tensor $\dot{\epsilon}_{ij}$ and the spin tensor ω_{ij} are used in the model and are the symmetric and the anti-symmetric parts of the velocity gradients

$$\dot{\epsilon}_{ij} = \frac{1}{2} (v_{i,j} + v_{j,i}) \quad \omega_{ij} = \frac{1}{2} (v_{i,j} - v_{j,i}) \quad (3.3)$$

Here $\dot{\epsilon}_{ij}$ give the pure deformation increments and can be used with physical constitutive formulations and ω_{ij} gives the local rotation or spin of the points.

When setting up constitutive formulations of continuum bodies that include residual stresses, it is important to distinguish between stress increments that arise from deformations and those that arrive from the rotations of the local basis. The Cauchy stress tensor σ_{ij} is used and gives the force per unit surface area in a given configuration. Furthermore, the Kirchhoff stress tensor τ_{ij} is used and is related to the Cauchy stresses by

$$\tau_{ij} = J \sigma_{ij} \quad (3.4)$$

where J is the Jacobian, giving the volume ratio $J = V/V_0$ or density ratio $J = \rho_0/\rho$ between the current and initial configuration. The models assume that the relation between the rate of Kirchhoff stresses and strain increments is described by

$$\dot{\tau}_{ij} = L_{ijkl} \dot{\epsilon}_{kl} \quad (3.5)$$

where L_{ijkl} are components of the elastic-plastic tangent moduli and $\dot{\tau}_{ij}$ are the Jaumann rate of Kirchhoff stresses and are the work-conjugate of the strain rate tensor $\dot{\epsilon}_{kl}$ as confirmed by Ji et al. (2013). The moduli L_{ijkl} must satisfy the symmetries

$$L_{ijkl} = L_{jikl} = L_{ijlk} \quad (3.6)$$

due to the symmetries of the Kirchhoff stress ($\dot{\tau}_{ij} = \dot{\tau}_{ji}$) and strain increment tensor ($\dot{\epsilon}_{kl} = \dot{\epsilon}_{lk}$). The only restriction to the constitutive formulations giving the moduli L_{ijkl} is that time-independent material behaviour is used, whether the formulations are elastic or elastic-plastic e.g. J_2 -deformation theories or J_2 -flow theories. For incompressible materials $\dot{\tau}_{ij} = \dot{\sigma}_{ij}$ where $\dot{\sigma}_{ij}$ is the Jaumann rate of Cauchy stresses. Both $\dot{\sigma}_{ij}$ and $\dot{\tau}_{ij}$ are objective stress rates that are independent of the local material rotation. As mentioned earlier, it is important to distinguish between stress increments that have geometrical or physical origins. The stresses after deformation in a coordinate system that stays stationary during an increment are $\sigma_{ij}(t + dt) = \sigma_{ij}(t) + \dot{\sigma}_{ij}$. The relation between the Cauchy stress increments $\dot{\sigma}_{ij}$ and $\dot{\tau}_{ij}$ is

$$\dot{\sigma}_{ij} = \underbrace{\dot{\sigma}_{ij}}_{\text{Physical origin}} + \underbrace{\omega_{jk} \sigma_{ik} + \omega_{ik} \sigma_{kj}}_{\text{Geometrical origin}} \quad (3.7)$$

The Jaumann rate of Cauchy stresses $\dot{\sigma}_{ij}$ describes the stress increments in a coordinate system that rotates with the deformation; for a more comprehensive explanation see Appendix A. In the same manner the Jaumann rate of Kirchhoff stresses is given by

$$\dot{\tau}_{ij} = \underbrace{\dot{\tau}_{ij}}_{\text{Physical origin}} + \underbrace{\omega_{jk} \tau_{ik} + \omega_{ik} \tau_{kj}}_{\text{Geometrical origin}} \quad (3.8)$$

Alternative stress quantities (nominal stresses or Second Piola-Kirchhoff stresses) occur when considering finite deformations. They are frequently used in connection with total Lagrangian formulations where the state of strain is described based on the initial configuration. The alternative stresses arrive as the work-conjugate of the choice of finite strain measurements. The nominal stress tensor t_{ij} is used to set up the constitutive models presented in this chapter even though the models are formulated with an updated Lagrangian approach. In Fig. 3.3 the concept of the nominal stress tensor t_{ij} vs Cauchy stress σ_{ij} is

illustrated using a simple example. In Fig 3.3a a dog bone specimen is displayed in its initial and deformed states. In this example, it is assumed that no residual stresses are present. The surface area of the cross-sections before and after deformation is designated on the figure. In Fig. 3.3b, two cuboids are presented, where the one to the left is a unit cube. The force acting per unit surface area in the deformed configuration is given by $\sigma_{11} = F_1/s_1$, which is the Cauchy stress or true stress. The nominal stress is the force per initial unit surface area $t_{11} = F_1/S_1$. The nominal stresses can be seen as the forces acting on a cuboid's faces (or in the general case, a parallelepiped) that was initially a unit cube in the reference state.

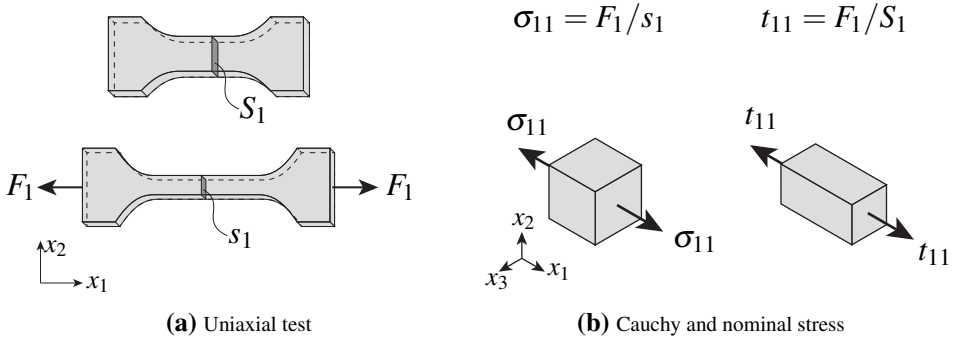


Figure. 3.3 Illustration that shows the difference between Cauchy stresses σ_{ij} and nominal stresses t_{ij} from a simple uniaxial loading example.

A more general case is illustrated in Fig. 3.4. In the figure, an initial and a deformed configuration are displayed. From the deformed configuration, an infinitesimal cube and an infinitesimal parallelogram are drawn from the same point. The cube represents the forces acting per unit area. The parallelogram represents an infinitesimal piece that was initially a unit cube in the reference configuration. The relation between nominal stresses and Cauchy stresses is

$$t_{ij} = J \frac{\partial X_i}{\partial x_k} \sigma_{kj} = J F_{ik}^{-1} \sigma_{kj} \tag{3.9}$$

The relation between the Cauchy stresses and nominal stresses can be obtained by considering an infinitesimal force vector acting on an area in the current and reference configurations with the equality $df_i = t_i ds = T_i dS$, where t_i and ds are a traction and an infinitesimal area around a point in the current configuration. Furthermore T_i and dS are the corresponding nominal traction vector and infinitesimal area in the reference configuration. Cauchy's stress theorem states that the tractions can be determined based on $t_i = \sigma_{ji} n_j$ and $T_i = t_{ji} N_j$. Nanson's formula $ds_i = J F_{ij}^{-1} dS_j$ relates surface areas in the deformed configuration to those in the

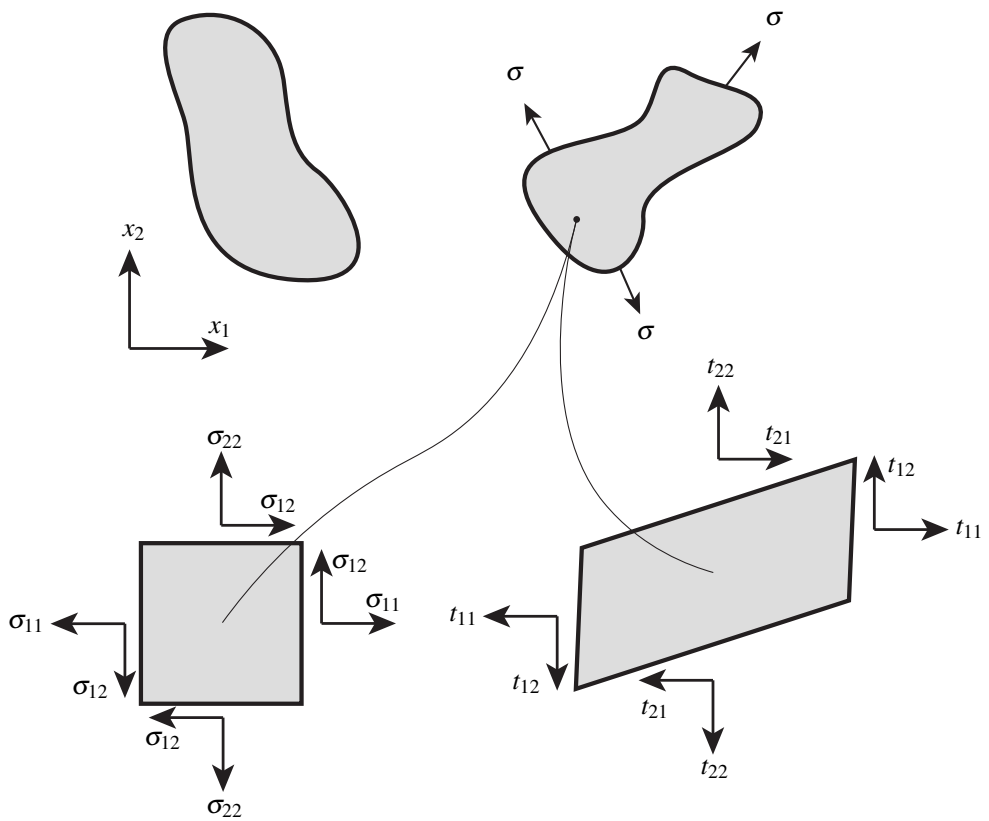


Figure. 3.4 An initial and a deformed configuration. A single point showing the Cauchy- and nominal stress tensor on an infinitesimal piece.

reference configuration. The relation given by Eq. (3.9) can be derived by combining the latter equalities. For a more comprehensive derivation see Appendix B. In addition, the nominal stresses can be expressed with respect to Kirchhoff stresses:

$$t_{ij} = \frac{\partial X_i}{\partial x_k} \tau_{kj} = F_{ik}^{-1} \tau_{kj} \quad (3.10)$$

As mentioned earlier, the kink band model is formulated with an updated Lagrangian formulation. The rate of nominal stresses \dot{t}_{ij} are used in the models. Taking the material time derivative $d/dt(\bullet)$ of Eq. (3.10) yields the rate of nominal stresses as a function of the rate of Kirchhoff stresses:

$$\dot{t}_{ij} = \dot{\tau}_{ij} - \tau_{jk} v_{i,k} \quad (3.11)$$

where $\dot{\tau}_{ij}$ are the rates of Kirchhoff stresses when following a point seen from a coordinate system that does not rotate. The rate of Kirchhoff stresses can be written as a function of the Jaumann rate of Kirchhoff stresses using Eq. (3.8), which is needed in constitutive formulations.

$$\dot{t}_{ij} = \overset{\circ}{\tau}_{ij} + \omega_{jk} \tau_{ik} + \omega_{ik} \tau_{kj} - \tau_{jk} v_{i,k} \quad (3.12)$$

Expanding the spin tensor using Eqs. (3.3) and (3.5), the velocity gradients can be isolated in the latter equation:

$$\dot{t}_{ij} = \underbrace{\left(L_{ijkl} - \frac{1}{2} \delta_{il} \tau_{kj} - \frac{1}{2} \delta_{ik} \tau_{lj} - \frac{1}{2} \tau_{il} \delta_{kj} + \frac{1}{2} \tau_{ik} \delta_{lj} \right)}_{C_{ijkl}} v_{l,k} \quad (3.13)$$

where δ_{ij} is Kronecker delta and C_{ijkl} are components of the tensor of nominal moduli relating nominal stress increments to velocity gradients through the Kirchhoff stress tensor. Details behind the derivations resulting in Eq. (3.13) can be studied in Appendix B. The moduli C_{ijkl} are used in the model set-up since they account for the deformations and tractions in the updated deformed configuration. The following form will be used to set up the constitutive models:

$$\dot{t}_{ij} = C_{ijkl} v_{l,k} \quad (3.14)$$

3.2 Homogenisation of constituents

In the current section, three models for homogenising the properties of fibre-reinforced composites and layered materials will be described. First, a two-dimensional homogenised model developed by Christoffersen and Jensen (1996) is described, followed by a three-

dimensional version developed in [P1]. Lastly, a model taking account of imperfect bonding between fibres and the surrounding matrix is presented and developed in [P2]. The models result in constitutive formulations in the form given by Eq. (3.14). In the current dissertation, the focus is on kink band formation; however, the constitutive formulations can be used in general for e.g. FE-analyses where there is a need for elastic-plastic composite behaviour. The common factor and the unique point of the three formulations are that independent constitutive equations are given to the constituents. This differs from regular constitutive formulations used for composites, where the composite behaviour is determined based on the overall response.

3.2.1 2D model

In Fig. 3.5, a general piece of a fibre-reinforced or layered composite is shown to the left. When setting up the constitutive behaviour, a representative volume element (RVE) is needed, as depicted on the right-hand side of the figure. The size of the RVE is determined based on the phenomenon requiring attention. In kink band formation the localisation of deformation needs information on the size of the fibres. In the two-dimensional model developed by Christoffersen and Jensen (1996), volume fractions of the two constituents are needed. The current formulation does not include a length scale which requires strain gradients (higher order strains) as in the formulation developed by Poullos and Niordson (2016). The two-dimensional formulation can be used for fibre-reinforced composites and assumes that the composite behaviour can be adequately described with a layered material as indicated in Fig. 3.5. The homogenisation assumes that the wavelengths λ of the fibre waviness are much larger than the amplitudes $\lambda \gg a$. Unit-thickness of the composite is assumed, meaning the volume V and area A of the composite are equal: $V = A$. Two constituents are introduced, indicated with superscripts $(\bullet)^f$ and $(\bullet)^m$, indicating a fibre and matrix constituent, respectively. Omission of superscripts refers to overall composite properties. The volume fraction of fibres is $c^f = V^f/V$ where V^f is the fibre volume of the RVE. With regard to two-dimensional models, the fibre volume fraction is given by $c^f = A^f/A$ where A^f is the area of fibres as indicated in Fig. 3.5. The relation

$$c^f + c^m = 1 \quad (3.15)$$

is required for the fibre and matrix volume fractions.

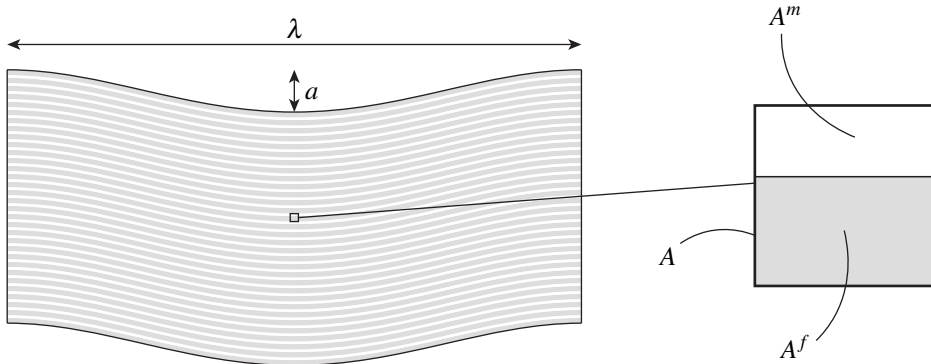


Figure. 3.5 A general piece from a two-dimensional layered composite (left) and a representative volume element from the composite (right).

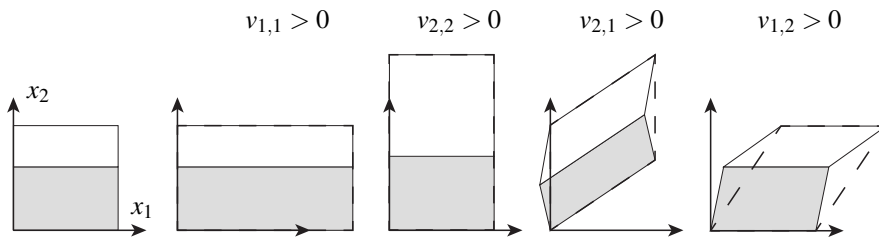


Figure. 3.6 A representative volume element of a layered composite in one undeformed and four deformed configurations. The figure clarifies the kinematic equalities used in the homogenisation formulation.

The constitutive formulation requires that the fibres of the RVE are aligned with the x_1 axis prior to deformation. The homogenisation of the constituents is based on the assumptions

1. Material lines parallel with the fibres are subject to a common stretching and rotation.
2. Planes parallel with the fibres transmit identical tractions.
3. The material behaviour of the constituents is time-independent.

Five configurations of an RVE are presented in Fig. 3.6: one undeformed and four deformed configurations. The first requirement, that lines parallel with the fibres are subject to a common stretching and rotation, is illustrated through the second and fourth configurations. The kinematic requirements are presented mathematically through the velocity gradients

$$\begin{aligned} v_{1,1} &= v_{1,1}^f = v_{1,1}^m \\ v_{2,1} &= v_{2,1}^f = v_{2,1}^m \end{aligned} \quad (3.16)$$

which can be written with a compact notation using the index notation

$$v_{\alpha,1} = v_{\alpha,1}^f = v_{\alpha,1}^m \quad (3.17)$$

Here, Greek indices are used since the indices take values 1 and 2. Furthermore, the two kinematic requirements

$$\begin{aligned} v_{1,2} &= c^f v_{1,2}^f + c^m v_{1,2}^m \\ v_{2,2} &= c^f v_{2,2}^f + c^m v_{2,2}^m \end{aligned} \quad (3.18)$$

are required for overall compatibility. The equalities simply state that the overall deformations $v_{1,2}$ and $v_{2,2}$ are average strains of the constituent deformations. The latter requirement can be presented using index notation:

$$v_{\alpha,2} = c^f v_{\alpha,2}^f + c^m v_{\alpha,2}^m \quad (3.19)$$

The second requirement states that planes parallel with the fibres transmit identical tractions. The requirement sets a restriction upon the stresses prior to deformation

$$\begin{aligned} \sigma_{12} &= \sigma_{12}^f = \sigma_{12}^m \\ \sigma_{22} &= \sigma_{22}^f = \sigma_{22}^m \end{aligned} \quad (3.20)$$

as indicated in Fig. 3.7 to the left. The rate of nominal stresses can be used to enforce the required equilibrium during the increments through

$$\begin{aligned} i_{21} &= i_{21}^f = i_{21}^m \\ i_{22} &= i_{22}^f = i_{22}^m \end{aligned} \quad (3.21)$$

which states that the traction increments, on the plane with outward normal parallel to the x_2 -axis, are identical for the overall composite and for the constituents (Fig. 3.7 on the right). The requirements presented with indices

$$i_{2\alpha} = i_{2\alpha}^f = i_{2\alpha}^m \quad (3.22)$$

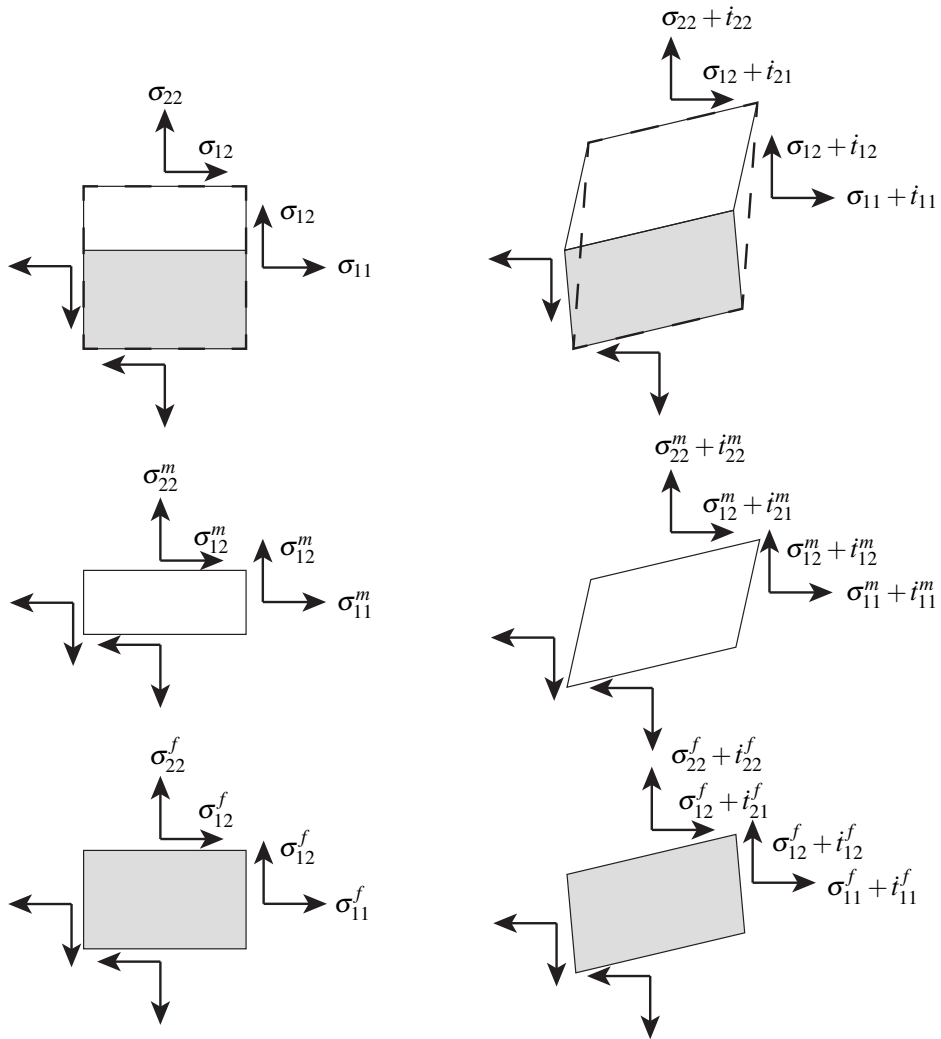


Figure 3.7 An initial state with stress equilibrium of a representative volume element is shown (left) and a (exaggerated) deformed configuration after an increment with equilibrium of tractions is shown (right).

Overall equilibrium of stresses prior to deformation requires

$$\boldsymbol{\sigma}_{11} = c^f \boldsymbol{\sigma}_{11}^f + c^m \boldsymbol{\sigma}_{11}^m \quad (3.23)$$

The requirements of the traction increments are

$$\begin{aligned} i_{11} &= c^f i_{11}^f + c^m i_{11}^m \\ i_{12} &= c^f i_{12}^f + c^m i_{12}^m \end{aligned} \quad (3.24)$$

and presented with indices

$$i_{1\alpha} = c^f i_{1\alpha}^f + c^m i_{1\alpha}^m \quad (3.25)$$

Based on the latter equalities a constitutive equation in the form

$$i_{\alpha\beta} = C_{\alpha\beta\gamma\delta} v_{\delta,\gamma} \quad (3.26)$$

can be derived, where the homogenised moduli $C_{\alpha\beta\gamma\delta}$ are functions of the constituent moduli $C_{\alpha\beta\gamma\delta}^c$ and the volume fractions. Using Eqs. (3.17), (3.19), (3.22) and (3.25), Christoffersen and Jensen (1996) identified that the moduli can be calculated using

$$\begin{aligned} C_{\alpha\beta\gamma\delta} &= c^f C_{\alpha\beta\gamma\delta}^f + c^m C_{\alpha\beta\gamma\delta}^m - c^f c^m \left(C_{\alpha\beta 2\varepsilon}^f - C_{\alpha\beta 2\varepsilon}^m \right) H_{\varepsilon\zeta} \left(C_{2\zeta\gamma\delta}^f - C_{2\zeta\gamma\delta}^m \right) \\ M_{\alpha\beta} &= c^m C_{2\alpha 2\beta}^f + c^f C_{2\alpha 2\beta}^m \end{aligned} \quad (3.27)$$

where $H_{\alpha\beta}$ is the inverse of $M_{\alpha\beta}$, complying to

$$H_{\alpha\gamma} M_{\gamma\beta} = \delta_{\alpha\beta} \quad (3.28)$$

where $\delta_{\alpha\beta}$ is the Kronecker delta. The moduli $C_{\alpha\beta\gamma\delta}^c$ for the constituents are calculated using Eq. (3.13). The velocity gradients $v_{\alpha,2}^c$ for the constituents can be calculated using the velocity gradients $v_{\alpha,\beta}$ for the composite

$$\begin{aligned} v_{\varepsilon,2}^f &= -c^m H_{\varepsilon\zeta} \left(C_{2\zeta 1\delta}^f - C_{2\zeta 1\delta}^m \right) v_{\delta,1} + H_{\varepsilon\zeta} C_{2\zeta 2\delta}^m v_{\delta,2} \\ v_{\varepsilon,2}^m &= c^f H_{\varepsilon\zeta} \left(C_{2\zeta 1\delta}^f - C_{2\zeta 1\delta}^m \right) v_{\delta,1} + H_{\varepsilon\zeta} C_{2\zeta 2\delta}^f v_{\delta,2} \end{aligned} \quad (3.29)$$

Due to differences in bulk moduli between the fibre and matrix constituent, the volume fractions will change during deformation. The change in fibre volume fraction can be

calculated using the velocity gradients

$$\dot{c}^f = c^f c^m \left(v_{2,2}^f - v_{2,2}^m \right) \quad (3.30)$$

The derivations of Eqs. (3.27) and (3.30) are demonstrated in Appendix C using a vector notation. The constitutive formulation presented in Eq. (3.27) was used in Christoffersen and Jensen (1996) to study kink band formation at bifurcation. Furthermore, the relation was used in Jensen and Christoffersen (1997) to study kink band formation with initial fibre imperfections in the form of fibre misalignments. The kink band model is presented in Section 3.4.

3.2.2 3D model

A three-dimensional version of the model was developed in [P1]. The assumptions behind the model are described briefly; the article can be read for an extended explanation. In the article, the emphasis is on fibre-reinforced composites, where fibres are surrounded by or embedded in a resin material. Instead of simplifying an RVE into a two-dimensional domain with two constituents, a three-dimensional cube with three constituents is introduced. An example of one of the RVEs introduced in the article, is displayed in Fig. 3.8. Two matrices and one fibre constituent were used. A methodology was developed to homogenise the properties between two arbitrary constituents $(\bullet)^a$ and $(\bullet)^b$ with a shared plane that was parallel with either the x_1 - x_2 or the x_1 - x_3 plane. The homogenisation of the fibre-matrix model was obtained through two homogenisation steps as indicated in Fig. 3.8. Three assumptions are used for the homogenisation between two arbitrary materials in 3D:

1. Material lines lying on the common plane between two materials are subjected to a common stretching and rotation.
2. Planes on the intersection between two materials transmit identical tractions.
3. The material of the constituents is elastic or elastic-plastic.

When the shared plane between the constituents lies in the x_1 - x_3 plane, the first assumption leads to the restriction of the velocity gradients

$$\begin{aligned} v_{i,1} &= v_{i,1}^a = v_{i,1}^b \\ v_{i,3} &= v_{i,3}^a = v_{i,3}^b \end{aligned} \quad (3.31)$$

where the Latin indices $(\bullet)_i$ are used, indicating that they take values 1, 2 or 3. To have overall compatibility, the average of the strains in the x_2 direction requires

$$v_{i,2} = c^a v_{i,2}^a + c^b v_{i,2}^b \quad (3.32)$$

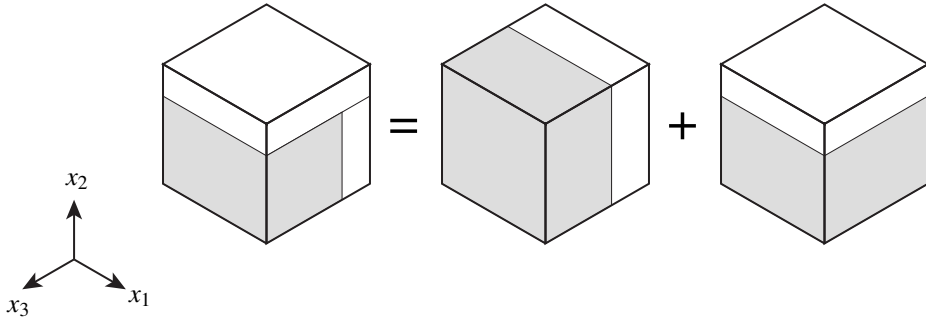


Figure. 3.8 A representative volume element of a three-dimensional cube consisting of two homogenisations.

The second assumption leads to the stress equilibrium

$$\begin{aligned}\sigma_{12} &= \sigma_{12}^a = \sigma_{12}^b \\ \sigma_{22} &= \sigma_{22}^a = \sigma_{22}^b \\ \sigma_{23} &= \sigma_{23}^a = \sigma_{23}^b\end{aligned}\quad (3.33)$$

prior to a deformation increment and the equilibrium of tractions on the shared plane requires

$$t_{2i} = t_{2i}^a = t_{2i}^b \quad (3.34)$$

Overall equilibrium on the two other planes prior to deformation requires

$$\begin{aligned}\sigma_{11} &= c^a \sigma_{11}^a + c^b \sigma_{11}^b \\ \sigma_{33} &= c^a \sigma_{33}^a + c^b \sigma_{33}^b \\ \sigma_{13} &= c^a \sigma_{13}^a + c^b \sigma_{13}^b\end{aligned}\quad (3.35)$$

and during an increment, the rate of nominal stresses

$$\begin{aligned}\dot{t}_{1i} &= c^a \dot{t}_{1i}^a + c^b \dot{t}_{1i}^b \\ \dot{t}_{3i} &= c^a \dot{t}_{3i}^a + c^b \dot{t}_{3i}^b\end{aligned}\quad (3.36)$$

is required. Using the latter equalities, [P1] demonstrates that the rate of nominal moduli can be written in a form similar to

$$\begin{aligned} C_{ijkl} &= c^a C_{ijkl}^a + c^b C_{ijkl}^b - c^a c^b \left(C_{ij2m}^a - C_{ij2m}^b \right) H_{mn} \left(C_{2nkl}^a - C_{2nkl}^b \right) \\ M_{ij} &= c^a C_{2i2j}^b + c^b C_{2i2j}^a \end{aligned} \quad (3.37)$$

where H_{ij} is the inverse of M_{ij} complying to the equality:

$$H_{ik} M_{kj} = \delta_{ij} \quad (3.38)$$

In [P1], the equations were presented using a matrix format similar to the one used in Christoffersen and Jensen (1996) to simplify the derivations. The moduli given by Eq. (3.37) give the homogenised properties between two materials that share a common plane with outward normals parallel with the x_2 axis. Similarly, the homogenised moduli can be formulated for two arbitrary materials that share planes with outward normals parallel with the x_3 axis. In this case the moduli are given by

$$\begin{aligned} C_{ijkl} &= c^a C_{ijkl}^a + c^b C_{ijkl}^b - c^a c^b \left(C_{ij3m}^a - C_{ij3m}^b \right) H_{mn} \left(C_{3nkl}^a - C_{3nkl}^b \right) \\ M_{ij} &= c^a C_{3i3j}^b + c^b C_{3i3j}^a \end{aligned} \quad (3.39)$$

By using a combination of the homogenisation equations Eqs. (3.37) and (3.39), the overall homogenised properties of a fibre-reinforced composite can be obtained as presented in [P1]. It is emphasised that general time-independent elastic-plastic material behaviour can be given to the constituents using the current three-dimensional constitutive formulations. The models are formulated in a rate form and can be used in formulations with large deformations and rotations.

3.2.3 Imperfect bonding

The article [P2] presents the development of a two-dimensional constitutive formulation accounting for imperfect bonding between fibre and matrix. The formulation is inspired by the two-dimensional model by Christoffersen and Jensen (1996) assuming perfect bonding, and the version introduced in Jensen (1999b) assuming complete decohesion. In the constitutive formulation presented in [P2] a variable μ is introduced to control the amount of bonding where $\mu = 1$ is a case of perfect bonding and $\mu = 0$ is a completely debonded case.

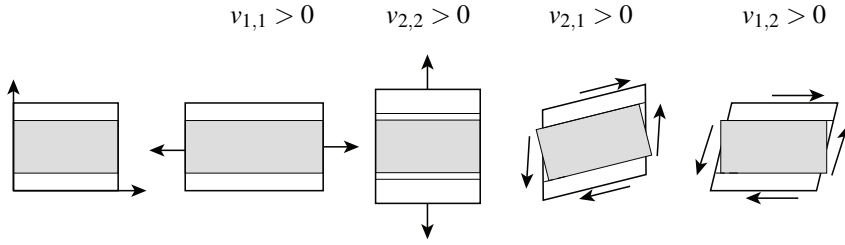


Figure. 3.9 A representative volume element of a layered composite with imperfect bonding in one undeformed and four deformed configurations. The figure clarifies the kinematic assumptions used in the formulation.

In Fig. 3.9 an initial undeformed configuration together with four deformed configurations of an RVE are displayed. The figure is presented in [P2] to show how the deformations vary between the matrix and fibre constituent in composites with poor bonding.

Once again, the constitutive formulation assumes that material lines parallel with the fibres are subject to a common stretching and rotation. In contrast, the strains in the x_2 direction are not simply averages of the strains as in the formulation by Christoffersen and Jensen (1996). In the extreme case of complete debonding, the shear strains in the matrix are equal to the overall shear strains and no shear strains are transmitted to the fibres. Similarly, the shear tractions are not transmitted to the fibres in the case of complete debonding. In [P2] it is shown that the constitutive formulation given by

$$\begin{aligned}
 C_{\alpha\beta\gamma\delta} &= c^f C_{\alpha\beta\gamma\delta}^f + c^m C_{\alpha\beta\gamma\delta}^m - c^f c^m \left(\kappa C_{\alpha\beta 2\varepsilon}^f - \mu C_{\alpha\beta 2\varepsilon}^m \right) H_{\varepsilon\zeta} \left(\kappa C_{2\zeta\gamma\delta}^f - \mu C_{2\zeta\gamma\delta}^m \right) \\
 M_{\alpha\beta} &= c^m \kappa^2 C_{2\alpha 2\beta}^f + c^f \mu^2 C_{2\alpha 2\beta}^m
 \end{aligned}
 \tag{3.40}$$

gives the relation for an imperfect composite, where the variables μ and κ are introduced to control the amount of bonding. The variable κ is dependent on μ according to

$$\kappa(\mu) = \left(1 - \frac{1}{c^m} \right) \mu + \frac{1}{c^m}
 \tag{3.41}$$

In the case of perfect bonding $\mu = 1$, the constitutive formulation, Eq. (3.40), equals the two-dimensional version from Christoffersen and Jensen (1996), Eq. (3.27). In the case of

complete debonding $\mu = 0$, the formulation simplifies to

$$\begin{aligned} \mu = 0 \rightarrow \\ C_{\alpha\beta\gamma\delta} &= c^f C_{\alpha\beta\gamma\delta}^f + c^m C_{\alpha\beta\gamma\delta}^m - c^f C_{\alpha\beta 2e}^f H_{e\zeta} C_{2\zeta\gamma\delta}^f \\ M_{\alpha\beta} &= C_{2\alpha 2\beta}^f \end{aligned} \quad (3.42)$$

The latter form of the constitutive formulation was proposed by Jensen (1999b). Details behind the derivations and the use of the constitutive formulation can be explored in [P2]. The use of the constitutive formulation is explored in [P2] using a kink band model. The model predictions are compared with a three-dimensional unit-cell model with different amounts of bonding as presented in Section 2.5.

3.3 Kink band bifurcation

The constitutive formulations presented for fibre-reinforced and layered composites are used studying kink band formation. Initially, a methodology is introduced to investigate kink band formation at bifurcation, i.e. no initial fibre misalignment. In Section 3.4, a numerical formulation is introduced to enable the study of post-bifurcation behaviour, e.g. initial fibre imperfections.

Kink band formation in the absence of fibre misalignments can be predicted as localisation of deformation at bifurcation where ellipticity of the incremental equilibrium equations is lost as explained in Jensen and Christoffersen (1997). A similar approach was used by Hutchinson and Neale (1978) to study the localisation phenomenon known as sheet necking that can form under tensile loading. They were inspired by the fundamental work by Rice (1976) regarding localisation of plastic deformation. The current bifurcation formulation within kink band formation was initially used by Christoffersen and Jensen (1996) together with the two-dimensional constitutive formulation. The methodology is used in [P2] to study fibre kinking in imperfect composites.

Fig. 3.10 depicts a perfect composite. The fibres are aligned in the x_1 -direction. A general stress field $\sigma_{\alpha\beta}$ can be present prior to localisation. An alternative velocity field is searched for where the fibres localise in a band according to

$$v_\alpha = f_\alpha(n_1 x_1 + n_2 x_2) = f_\alpha(n_\beta x_\beta) \quad (3.43)$$

where v_α are the velocity components and f_α are functions describing the velocity field and are dependent on the normal n_β to an assumed band and the coordinates x_β . In this way

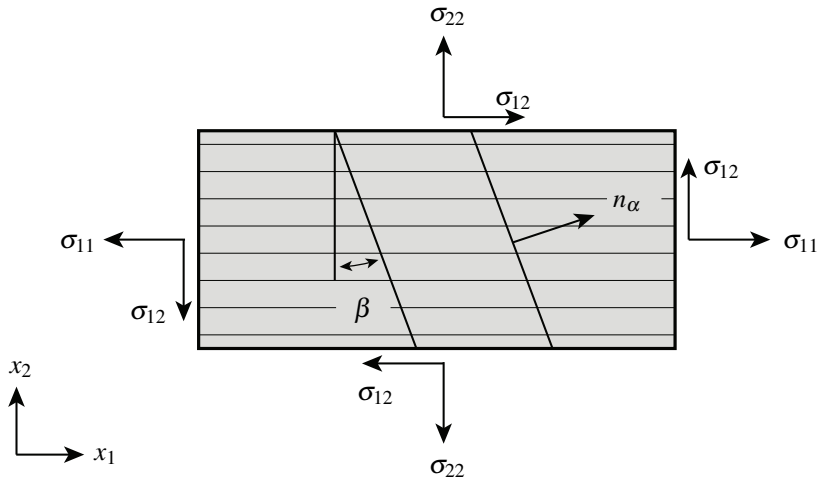


Figure. 3.10 Kink band geometry before localisation. The angle β is the orientation of the localisation band searched for in the bifurcation analysis.

the velocity fields are constrained to vary across the band. The state at bifurcation requires equilibrium of the nominal stress rates

$$\dot{i}_{\alpha\beta,\alpha} = 0 \quad (3.44)$$

Replacing the rate of nominal stresses \dot{i}_{ij} with the form given by Eq. (3.14) yields

$$C_{\alpha\beta\gamma\delta} v_{\delta,\gamma\alpha} = 0 \quad (3.45)$$

and when using the assumed velocity field, Eq. (3.43), the equilibrium equation can be rewritten using the product rule of differentiation

$$C_{\alpha\beta\gamma\delta} n_\alpha n_\gamma \frac{\partial^2 f_\delta(n_\epsilon x_\epsilon)}{\partial (n_\zeta x_\zeta)^2} = 0 \quad (3.46)$$

The equation above gives two equations since β is the only free index. Thus, bifurcation is possible when a non-trivial solution to the latter equation exists (where the equation loses ellipticity), i.e. when the determinant of the coefficient matrix of the function f_δ vanishes.

$$\det(C_{\alpha\beta\gamma\delta} n_\alpha n_\gamma) = 0 \quad (3.47)$$

No assumptions were made regarding the constitutive behaviour of the solid. By using the two-dimensional constitutive equation Eq. (3.27), and by assuming rigid fibres, Christoffersen and Jensen (1996) showed that the state at kink band bifurcation is

$$0 = \sigma_{11} - \sigma_{22} + \frac{1}{c^m} C_{2121}^m + \frac{2}{c^m} (L_{1222}^m - c^f \sigma_{12}) \tan \beta + \frac{1}{c^m} C_{2222}^m \tan^2 \beta \quad (3.48)$$

As [P2] shows, the localisation of fibres at bifurcation for an imperfect composite with rigid fibres is

$$0 = \sigma_{11} - \sigma_{22} + \frac{1}{c^m \kappa^2} \left(L_{1212}^m - \frac{\sigma_{11}^m - \kappa \sigma_{22}}{2} \right) + \frac{2}{c^m \kappa^2} (L_{1222}^m - c^f \kappa \mu \sigma_{12}) \tan \beta + \frac{1}{c^m \kappa^2} (L_{2222}^m - \kappa \sigma_{22}) \tan^2 \beta \quad (3.49)$$

Furthermore, [P2] shows that the latter equation is identical to Eq. (3.48) with $\mu = 1$. In contrast to the results in the proceeding sections, the current formulation can result in a closed form solution. The solutions give valuable information regarding the effect of the stress field, constituent volume fractions and kink angle β upon the critical stress σ_{11}^{cr} at bifurcation.

3.4 Kink band model and numerical scheme

The constitutive formulations introduced in Section 3.2 can be used in a numerical scheme to study kink band formation. This scheme is presented in the current section. The numerical formulation is developed by Jensen and Christoffersen (1997) (two-dimensional) and is used in [P2], [P3] and [P4]. The formulation is extended to a three-dimensional version in [P1] and is used to validate the constitutive formulation presented in Section 3.2.

Common to both the two- and three-dimensional numerical formulations is that a kink band forms either by bifurcation or due to the presence of an initial imperfection ϕ_0 . The kink band develops by prescribing a rotation increment ϕ to the fibres within the kink band. Two material states are present: a state inside the kink band (band material) and a state outside the kink band (base material). Equilibrium of stresses prior to deformation together with equilibrium of traction increments is required on the band boundary between the base and kinked material. Furthermore, displacement continuities are required across the band during deformation.

3.4.1 2D model

An illustration of a two-dimensional kink band is presented in Fig. 3.11. Two material states are shown. The superscripts $(\bullet)^o$ and $(\bullet)^i$ are associated with the outer base and inner kink band material, respectively. Furthermore, a superscript $(\bullet)^c$ is introduced which in this section refers to the common system located at the band. The stress states in the three systems can be observed in the bottom part of Fig. 3.11.

A rotation increment $\dot{\phi}$ is prescribed to the kink material system. The constitutive formulations require that the x_1 -axis of the coordinate systems are aligned with the fibres prior to the deformation increment. Rotation of the coordinate systems is therefore required during deformation. There are two ways of implementing the rotation: the coordinate systems stay stationary during the rotation increment; the coordinate systems follow the rotation. Both implementations are explored by Jensen and Christoffersen (1997) and give identical results. The implementation where the coordinate systems follow the rotation is used in [P1 - P4]. Using this approach, rotation of the stresses and instantaneous moduli is avoided. When the coordinate systems follow the rotation of the fibres, then

$$v_{2,1}^o = 0 \quad v_{2,1}^i = 0 \quad (3.50)$$

are the consequences upon the velocity gradients. The velocity gradients $w_{i,j}^i$ observed in a system that stays stationary during a rotation increment are

$$w_{i,j}^i = v_{i,j}^i + \omega_{ij} \quad (3.51)$$

where ω_{ij} is the relative spin tensor with the components

$$\omega_{21} = -\omega_{12} = \dot{\phi} \quad \omega_{11} = \omega_{22} = 0 \quad (3.52)$$

In the latter equation, the prescribed spin increment $\dot{\phi}$ is introduced. Two tensors R_{ij}^i and R_{ij}^o that contain the directional cosines are introduced

$$R_{ij}^i = \cos(\angle(Ox_i^c, Ox_j^i)) \quad R_{ij}^o = \cos(\angle(Ox_i^c, Ox_j^o)) \quad (3.53)$$

where R_{ij}^i and R_{ij}^o give the directional cosines between the inner kink band system x_i^i or outer system x_i^o to the common system x_i^c . Continuity of velocities across the band requires that a line element lying on the band is stretched $v_{2,2}^c$ and rotated $v_{2,1}^c$ equally, when it is calculated from the two systems. The directional cosines can be used to evaluate the velocity gradients

in another system. Continuity of velocities requires

$$w_{i,j}^i R_{2i}^i R_{2j}^i = v_{i,j}^o R_{2i}^o R_{2j}^o \quad w_{i,j}^i R_{1i}^i R_{2j}^i = v_{i,j}^o R_{1i}^o R_{2j}^o \quad (3.54)$$

In addition, the equalities can be expressed using the normal and tangent to the band

$$w_{i,j}^i t_i^i t_j^i = v_{i,j}^o t_i^o t_j^o \quad w_{i,j}^i n_i^i t_j^i = v_{i,j}^o n_i^o t_j^o \quad (3.55)$$

where n_i^o and t_i^o are the unit normal and tangent expressed in the outer base material system. Equilibrium of traction increments require the tractions t_{11}^c and t_{12}^c , expressed in the two systems to be equal

$$t_{ij}^i R_{1i}^i R_{1j}^i = t_{ij}^o R_{1i}^o R_{1j}^o \quad t_{ij}^i R_{1i}^i R_{2j}^i = t_{ij}^o R_{1i}^o R_{2j}^o \quad (3.56)$$

which can be expressed with velocity gradients using Eq. (3.14)

$$C_{ijkl}^i w_{l,k}^i R_{1i}^i R_{1j}^i = C_{ijkl}^o v_{l,k}^o R_{1i}^o R_{1j}^o \quad C_{ijkl}^i w_{l,k}^i R_{1i}^i R_{2j}^i = C_{ijkl}^o v_{l,k}^o R_{1i}^o R_{2j}^o \quad (3.57)$$

When shear strains or stresses are present in the base material, the band will rotate. The band rotation increments are

$$\dot{\beta}^o = -v_{i,j}^o R_{1i}^o R_{2j}^o \quad \dot{\beta}^i = -v_{i,j}^i R_{1i}^i R_{2j}^i \quad (3.58)$$

The necessary constraints are given by Eqs. (3.50), (3.54) and (3.57), which gives six equations. The velocity gradients of the inner and outer material contain eight components in total that need to be specified in every increment. Furthermore, two boundary conditions are required. In the majority of the simulations presented in [P1 - P4], the following two boundary conditions are used: no shear and transverse stresses are present in the base material

$$\dot{\sigma}_{22}^o = 0 \quad \dot{\sigma}_{12}^o = 0 \quad (3.59)$$

The Cauchy stress increments $\dot{\sigma}_{\alpha\beta}$ are calculated based on

$$\dot{\sigma}_{\alpha\beta} = C_{\alpha\beta\gamma\delta} v_{\delta,\gamma} - \sigma_{\alpha\beta} v_{\gamma,\gamma} + v_{\alpha,\gamma} \sigma_{\gamma\beta} \quad (3.60)$$

Using the model, σ_{11}^o in the outer base material can be determined in every increment. The maximum value obtained for σ_{11}^o during the fibre increments $\dot{\phi}$ is the critical compressive stress σ_{11}^{cr} .

3.4.2 3D model

A three-dimensional numerical formulation is developed in [P1] to study kink band formation and to validate the developed three-dimensional homogenised constitutive equation. The numerical scheme is inspired by the two-dimensional version and is generalised. An illustration of a developed three-dimensional kink band is presented in Fig. 3.12. Again, two material states are present and a common system lies on the band. The stresses in the systems are illustrated at the bottom of the figure.

The velocity gradients $v_{i,j}$ in 3D contain nine components. Since two material states are present, 18 components need to be determined in every increment and therefore 18 equations are required. For simplicity and for the comparison with the two-dimensional formulation, in [P1] we chose to let the kink band develop in the x_1 - x_2 plane. Furthermore, the x_3^o and x_3^i bases coincide before and during deformation. A formulation where the coordinate systems follow the rotation is once again chosen:

$$v_{2,1}^o = 0 \quad v_{2,1}^i = 0 \quad (3.61)$$

Continuity of velocities across the band require six equations in 3D and again, the directional cosines are used to relate the velocity gradients to the common system

$$\begin{aligned} w_{i,j}^i R_{2i}^i R_{2j}^i &= v_{i,j}^o R_{2i}^o R_{2j}^o & w_{i,j}^i R_{3i}^i R_{3j}^i &= v_{i,j}^o R_{3i}^o R_{3j}^o \\ w_{i,j}^i R_{1i}^i R_{2j}^i &= v_{i,j}^o R_{1i}^o R_{2j}^o & w_{i,j}^i R_{1i}^i R_{3j}^i &= v_{i,j}^o R_{1i}^o R_{3j}^o \\ w_{i,j}^i R_{3i}^i R_{2j}^i &= v_{i,j}^o R_{3i}^o R_{2j}^o & w_{i,j}^i R_{2i}^i R_{3j}^i &= v_{i,j}^o R_{2i}^o R_{3j}^o \end{aligned} \quad (3.62)$$

The first two equations ensure stretching continuity on the band. The third and fourth equations ensure continuity of out-of-plane rotations of the kink band plane. The fifth and sixth equations ensure continuity of shear straining and rotation of the kink band plane. Continuity of traction increments requires three equations:

$$\begin{aligned} C_{ijkl}^i w_{l,k}^i R_{1i}^i R_{1j}^i &= C_{ijkl}^o v_{l,k}^o R_{1i}^o R_{1j}^o \\ C_{ijkl}^i w_{l,k}^i R_{1i}^i R_{2j}^i &= C_{ijkl}^o v_{l,k}^o R_{1i}^o R_{2j}^o \\ C_{ijkl}^i w_{l,k}^i R_{1i}^i R_{3j}^i &= C_{ijkl}^o v_{l,k}^o R_{1i}^o R_{3j}^o \end{aligned} \quad (3.63)$$

The equalities given by Eqs. (3.61), (3.62) and (3.63) are necessary and give eleven equations. The last seven equations set the boundary conditions. Five boundary conditions are used in [P1] to enforce plane strain conditions

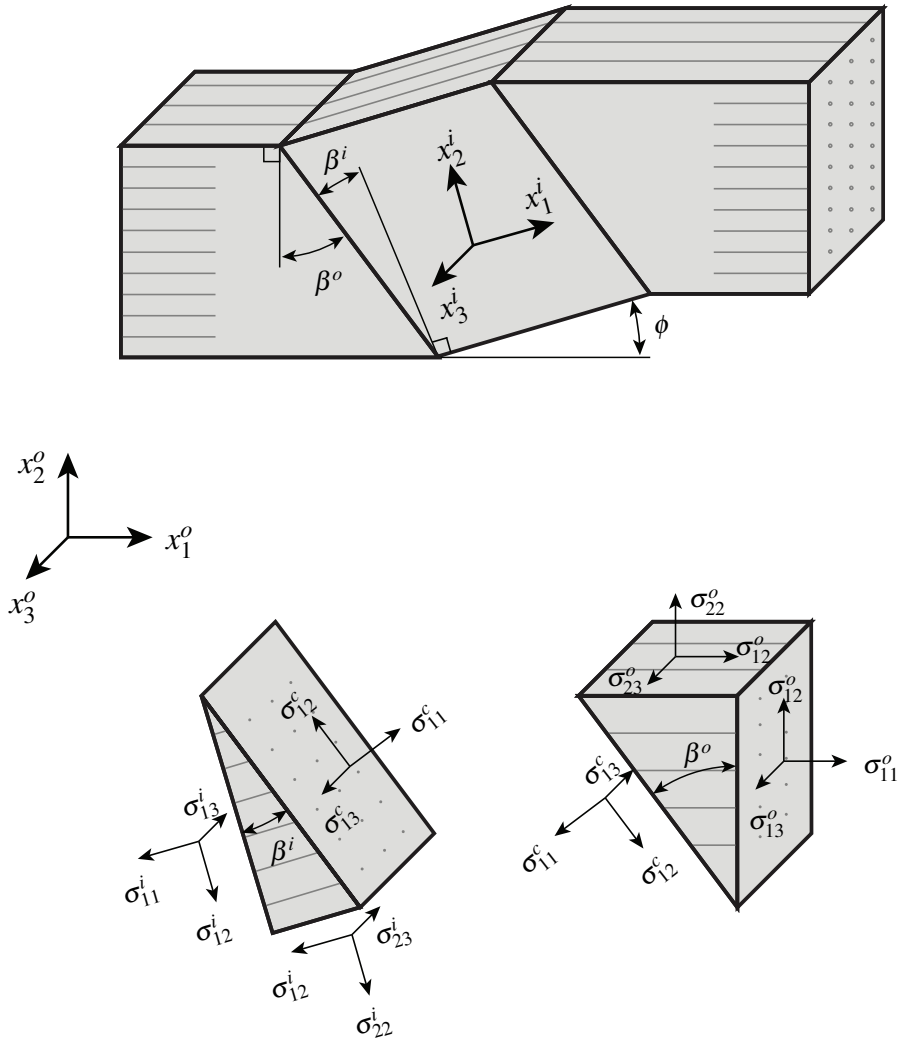


Figure. 3.12 Kink band geometry showing the two material states with two coordinate systems in a three-dimensional case (top). Two small pieces of the material states together with the stresses on the common plane (bottom).

$$\begin{aligned} v_{3,1}^o = 0 & & v_{3,2}^o = 0 & & v_{1,3}^o = 0 \\ & & v_{2,3}^o = 0 & & v_{3,3}^o = 0 \end{aligned} \quad (3.64)$$

In [P1], the influence of multi-axial loading is explored. Two variables ρ and ψ are introduced, to control the proportional amount of multi-axial loading.

$$\rho = \frac{\dot{\sigma}_{22}^o}{\dot{\sigma}_{11}^o} \quad \psi = \frac{\dot{\sigma}_{12}^o}{\dot{\sigma}_{11}^o} \quad (3.65)$$

The last two boundary conditions for the three-dimensional scheme are

$$\dot{\sigma}_{22}^o - \rho \dot{\sigma}_{11}^o = 0 \quad \dot{\sigma}_{12}^o - \psi \dot{\sigma}_{11}^o = 0 \quad (3.66)$$

The Cauchy stress increments $\dot{\sigma}_{ij}$ are calculated based on

$$\dot{\sigma}_{ij} = C_{ijkl} v_{l,k} - \sigma_{ij} v_{k,k} + v_{i,k} \sigma_{kj} \quad (3.67)$$

With the introduced formulation, it is possible to compare the two- and three-dimensional kink band models using the homogenised constitutive formulations.

3.4.3 Numerical scheme

Many equations were presented and to enhance the transparency of the implementations, the steps within the numerical scheme are outlined here. The relative spin increment $\dot{\phi}$ is prescribed. The simulations progress from an initial fibre imperfection ϕ_0 to an end rotation ϕ decided by the user. The following steps are required for every increment:

1. Update instantaneous moduli for the constituents L_{ijkl}^c using an elastic or elastic-plastic time-independent material law.
2. Calculate the nominal moduli for the constituents C_{ijkl}^c using Eq. (3.13).
3. Calculate the nominal moduli for the composite $C_{\alpha\beta\gamma\delta}$ or C_{ijkl} based on Eq. (3.27), Eq. (3.40) or Eq. (3.39).
4. A linear system in the form $[\mathbf{A}]\mathbf{V} = \mathbf{R}$ is created, where \mathbf{V} is a vector containing the unknown velocity gradients for the band and base material $v_{i,j}^i, v_{i,j}^o$ and $[\mathbf{A}]$ is a matrix containing the coefficients. The linear system is solved with respect to the unknown vector \mathbf{V} . The linear system is based on
 - (a) In 2D – 8 equations given by Eqs. (3.50), (3.54), (3.57) and (3.59) using Eq. (3.60).

- (b) In 3D – 18 equations given by Eqs. (3.61), (3.62), (3.63), (3.64) and (3.66) using Eq. (3.67).
5. Calculate the velocity gradients for the constituents $v_{i,j}^c$ within the band and base material based on the overall velocity gradients $v_{i,j}$ using Eq. (3.29) in 2D. The velocity gradients in the 3D case are presented in [P1].
 6. Update the stresses $\sigma_{ij} = \sigma_{ij} + \dot{\sigma}_{ij}$ where the stress increments $\dot{\sigma}_{ij}$ are calculated using Eq. (3.60) or (3.67).
 7. Update the geometric quantities β , ϕ and c^f using Eq. (3.58) and Eq. (3.30).

3.5 Kink band broadening

The propagating instability known as kink band broadening or steady-state kink band propagation is investigated in [P3] and [P4]. In the publications, the semi-analytical model presented in this chapter is used. Propagating instabilities initiate from local imperfections and propagate under a constant applied load, that can be several magnitudes lower than the load required to initiate the instability as explained by Kyriakides (1993). Within the framework of fibre-kinking, a kink band will initiate and rotate until a steady-state is reached where the fibres stop rotating and broadening of the kink band is energetically preferable.

In the current section, a method is introduced to study kink band broadening using the semi-analytical model that is developed by Jensen (1999a). The methodology is based on a Maxwell construction of work equilibrium. Chater and Hutchinson (1984) proposed a similar methodology to study steady-state propagation in structural applications. The internal work W^I and external work W^E per unit volume are calculated in every increment and when the equilibrium $W^I = W^E$ is obtained, the steady-state is obtained. The external work per unit volume is calculated according to

$$W^E = S_{\alpha\beta}^o \Delta E_{\alpha\beta}^o \quad (3.68)$$

where $\Delta E_{\alpha\beta}^o$ are the differences in Lagrangian strains inside and outside the kink band evaluated in the base material system. $S_{\alpha\beta}^o$ are stress components of the work-conjugate of the Lagrangian strain i.e. Second Piola Kirchhoff stresses. The internal work per unit volume is calculated based on the integral

$$W^I = \int_{\epsilon^o}^{\epsilon^i} \sigma_{\alpha\beta} d\epsilon_{\alpha\beta} \quad (3.69)$$

where ε^o and ε^i are strain states in the base and kink band material. The simulations initiate from a small fibre imperfection $\phi_0 \approx 0$ and progress with fibre rotation increments $\dot{\phi}$. The simulations run until the work equilibrium $W^I = W^E$ is reached. Further details and illustrations are presented in [P3] and [P4].

Chapter 4

Analytical kink band model

The phenomenon known as kink band broadening was briefly introduced in the previous chapter. The concept will be further discussed in the current chapter using an analytical model developed in [P3] and is used in a similar form in [P4]. Regarding an idealised kink band, the analytical model assumes stress equilibrium on the band and displacement continuity across the band. In the current chapter, it is formulated using the total stress and strain states instead of a rate formulation. Similarly, a Maxwell construction of work equilibrium is assumed, resulting in one transcendental equation with the fibre rotation ϕ being the unknown variable. Moran et al. (1995) derived a similar analytical expression of kink band broadening where they used the experimentally observed relation $\phi = 2\beta$ from Evans and Adler (1978). Furthermore, Moran et al. (1995) assumed incompressibility of the composite. In contrast, the analytical model developed in [P3] does not assume $\phi = 2\beta$ but does account for compressibility. In the current formulation the kink band inclination β is seen as a free parameter. The final value of β during kink band broadening is discussed in [P4] with the hypothesis that β is influenced by the boundary conditions. In contrast to the semi-analytical model (Chapter 3), the analytical model makes several prior assumptions regarding e.g. the fibre and matrix material behaviour and the overall stress state in the base material.

4.1 Stresses and equilibrium

Two material states are considered: an outer base material and an inner kink band material. This is equivalent to the assumptions introduced for the semi-analytical model. Equilibrium of stresses is required on the band between the base and band material, which gives a statically

admissible stress field. To have equilibrium of stresses, both stress states are evaluated in the same coordinate system as shown in Fig. 3.11. The directional cosines are used once again:

$$\sigma_{ij}^i R_{1i}^i R_{1j}^i = \sigma_{ij}^o R_{1i}^o R_{1j}^o \quad \sigma_{ij}^i R_{1i}^i R_{2j}^i = \sigma_{ij}^o R_{1i}^o R_{2j}^o \quad (4.1)$$

where the first equation gives the stress σ_{11}^c , expressed through the stress field from the band material (left of equality) and the outer material (right of equality). Similarly, the second equation equals the shear stress σ_{12}^c in the common system. In the analytical model, it is assumed that only σ_{11}^o is present (stress along the fibres) in the base material. In [P3] it is demonstrated that the stress σ_{11}^o can be expressed as a function of the inner stresses σ_{12}^i and σ_{22}^i according to

$$\sigma_{11}^o = -\sigma_{12}^i [\cot \phi + \tan \beta] - \sigma_{22}^i [\cot \phi \tan \beta - 1] \quad (4.2)$$

where the band inclination β is regarded as a free parameter that needs to be specified. In [P3], simple assumptions are made regarding the constitutive behaviour and are inspired by the stress-strain response in the semi-analytical model. It is assumed that the stress σ_{22} can be determined from the total strain ϵ_{22} alone and that the response is linear-elastic. The expression

$$\sigma_{22} = \frac{E(1-\nu)}{(1+\nu)(1-2\nu)} \epsilon_{22} \quad (4.3)$$

is used with the assumption of plane strain conditions, where E is the transverse composite Young's modulus and ν is the Poisson's ratio. A simple bilinear relation is assumed for the shear stress-strain behaviour:

$$\sigma_{12} = \begin{cases} 2G_1 \epsilon_{12} & \text{for } \epsilon_{12} < \epsilon_{12}^y \\ \sigma_{12} = 2G_2 \epsilon_{12} + \sigma_{12}^y \left(1 - \frac{G_2}{G_1}\right) & \text{otherwise} \end{cases} \quad (4.4)$$

where G_1 is the initial shear modulus prior to yielding and G_2 is the shear modulus beyond yielding. σ_{12}^y and ϵ_{12}^y are the shear yield stress and shear yield strain.

4.2 Strains and continuity

In the current section, the strain state ϵ_{ij} in the base and band material is determined as a function of fibre rotation ϕ . Fig. 4.1 will be used to illustrate the kinematic requirements on the kink band boundary. Initially, the focus is given to the two points lying on the band boundary (black circles in Fig. 4.1). It is assumed that there is a compatible strain field prior

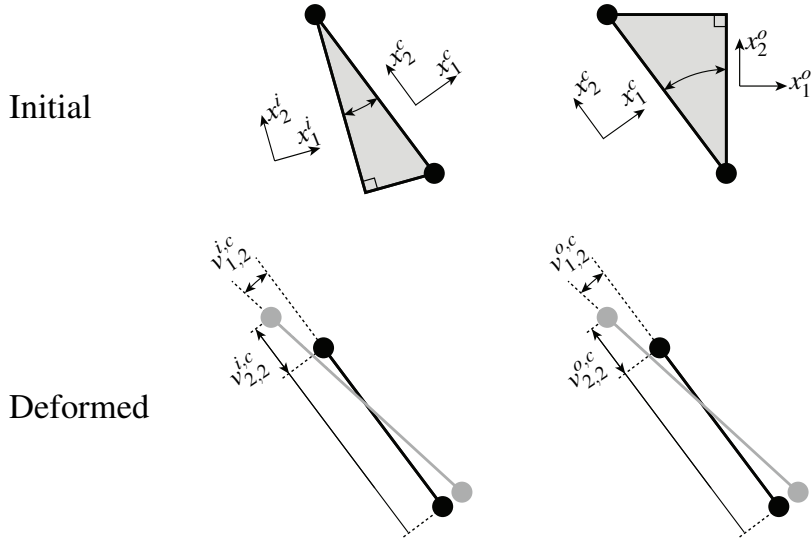


Figure. 4.1 Two points on kink band boundary seen from the two material states (top). Initial (black) and deformed configuration (grey) of the two points on the band boundary seen from the two states (bottom).

to deformation i.e. material lines lying on the band boundary have stretched and rotated the same amount when expressed through the inner and outer strains. To have compatibility during a deformation increment, material lines on the band boundary need to have the same stretch and rotation increment when expressed through the strains in the two systems. This requirement is illustrated in Fig. 4.1, where the grey circles represent a material piece lying on the boundary after a deformation increment.

The velocity gradient $v_{1,2}^{o,c}$ represents a velocity gradient in the common system (x^c) and is calculated based on the velocity gradients $v_{i,j}^o$ in the outer material system. In the analytical model, the fibres are assumed to be inextensible and when the fibres are aligned with the x_1 -axis during deformation, this entails $v_{1,1}^o = v_{1,1}^i = 0$. Furthermore, only σ_{11} stress is applied along the fibres in the base material, which implicitly yields no transverse and shear straining $v_{i,j}^o = 0$ in the base material. Continuity of displacements across the band is formulated using velocity gradients

$$w_{i,j}^i R_{2i}^i R_{2j}^i = 0 \quad w_{i,j}^i R_{1i}^i R_{2j}^i = 0 \quad (4.5)$$

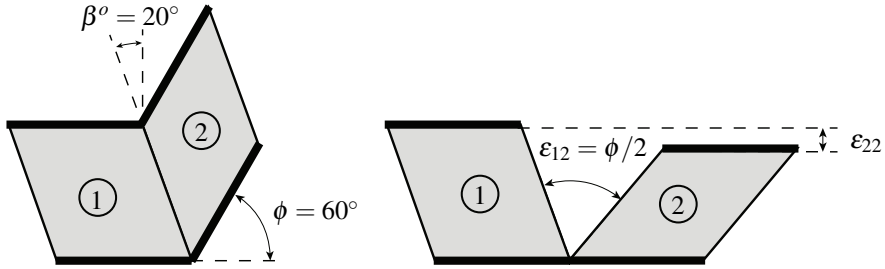


Figure. 4.2 Strain state in outer material ① and inside kink band ② (left). The strain state inside the kink band is rotated 60° to show the total strains (right).

where the velocity gradients $w_{i,j}^i$ are given by Eq. (3.51). In [P3] it is demonstrated that the finite strains in the band material can be derived based on the latter equations, and are equal to

$$\varepsilon_{12}^i = \frac{\phi}{2} \quad \varepsilon_{22}^i = \ln \left(\frac{\cos(\beta - \phi)}{\cos \beta} \right) \quad (4.6)$$

The same expressions of the strains were obtained by Budiansky and Fleck (1993). To enhance understanding of the final strain states, Fig. 4.2 is introduced in [P3]. A material piece of the base material is designated as ① and a piece in the band material is designated as ②. In the initial configuration, the material piece ② is equal to ①. To illustrate the total deformation going from ① to ②, the piece ② is rotated an amount of ϕ in the right-hand illustration in Fig. 4.2. By inserting the kinematic relation $\phi = 2\beta$ into Eq. (4.6) for ε_{22}^i , zero transverse straining $\varepsilon_{22}^i = 0$ is obtained.

4.3 Kink band broadening

An illustration of a kink band that has undergone broadening is displayed in Fig. 4.3. It is assumed that a steady-state is obtained when the work done by external forces equals the work required to deform an infinitesimal piece into the band. The externally applied stress σ_{11} works on an area A . The specimen boundary displaces at the uniform rate $-u$. Positive values work in the direction of the basis. The work done by the external force is

$$W^E = -uA\sigma_{11} \quad (4.7)$$

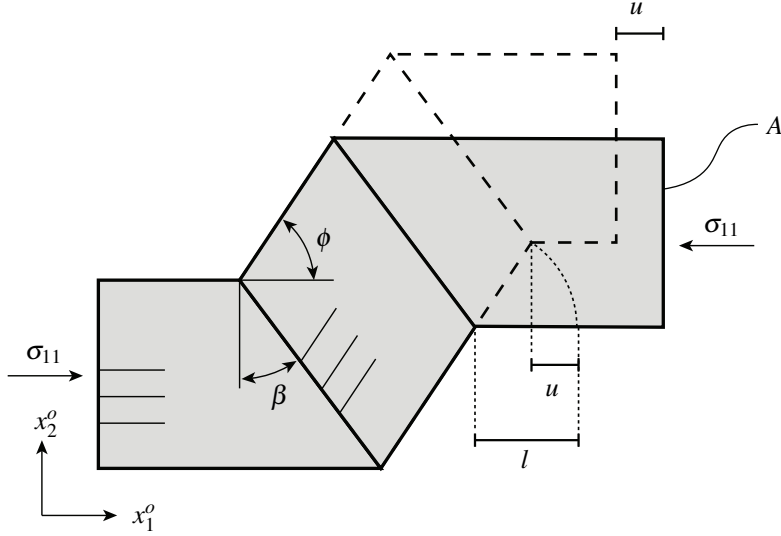


Figure. 4.3 Illustration of the model of kink band broadening. A propagated configuration is illustrated with dashed lines.

Using the geometric relation $u = l(1 - \cos \phi)$, see Fig. 4.3, the relation can be written in the form:

$$W^E = -lA \sigma_{11} (1 - \cos \phi) \quad (4.8)$$

During the uniform rate $-u$, a material volume of lA undergoes internal work equal to

$$W^I = lA \int_{\epsilon^o}^{\epsilon^i} \sigma_{\alpha\beta} d\epsilon_{\alpha\beta} \quad (4.9)$$

When comparing the internal and external work, the volume lA is present in both equations. The stresses and strains within the equations of work can be substituted by the expressions presented in the two previous sections. [P3] demonstrates that the internal and external work per unit volume can be expressed by

$$W^E = (2C_2 \phi + C_3) [\cot \phi + \tan \beta] (1 - \cos \phi) + 2C_4 \ln \left(\frac{\cos(\beta - \phi)}{\cos \beta} \right) [\cot \phi \tan \beta - 1] (1 - \cos \phi) \quad (4.10)$$

$$W^I = C_1 (\phi^y)^2 + C_2 (\phi^2 - (\phi^y)^2) + C_3 (\phi - \phi^y) + C_4 \ln \left(\frac{\cos(\beta - \phi)}{\cos \beta} \right)^2 \quad (4.11)$$

where constants are introduced as follows:

$$C_1 = \frac{G_1}{2} \quad C_2 = \frac{G_2}{2} \quad C_3 = \sigma_{12}^y \left(1 - \frac{G_2}{G_1} \right) \quad C_4 = \frac{E(1-\nu)}{2(1+\nu)(1-2\nu)} \quad (4.12)$$

The latter constants are based on material properties of the composite and as mentioned, the band inclination β is a free parameter. The only unknown variable upon evaluating the work balance $W^E = W^I$ is the fibre angle ϕ . The work balance during steady-state kink band broadening is determined numerically.

Chapter 5

Summary and outlook

The dissertation is chiefly concerned with the study of kink band formation, which is the dominant compressive failure mechanism for many fibre-reinforced composites loaded in the direction of the fibres. The study covers both numerical and analytical approaches. Several numerical models and constitutive relations were developed during the project.

Secondly, contributions to the field of joint mechanics within composites were made and were carried out at the Department of Engineering at the University of Cambridge.

The contributions to the field are elaborated in the following section.

5.1 Contributions

Regarding the failure mechanism, kink band formation, this project has contributed with:

- An exploration of kink bands using an idealised three-dimensional, semi-analytical, kink band model.
- Investigations of the effect of multi-axial loading upon the critical peak strength for a case study involving a carbon fibre-reinforced composite.
- An investigation of the influence of fibre-to-matrix bonding quality upon the critical peak strength at kink band formation.
- A developed understanding of the propagating instability known as kink band broadening, including the influence of relevant material parameters upon the lock-up angle and propagating stress.
- An investigation of size effects upon kink band broadening using an FE-model.

- An investigation of kink band formation in open-hole fibre-composites, including the sensitivity of loading direction upon compressive strength.

As part of the project, the following models were developed:

- A three-dimensional constitutive model that can be used to explore plastic deformation with large rotations and deformations for fibre-reinforced composites. The model is based on two independently described constitutive formulations for the constituents.
- A two-dimensional constitutive model that includes information about fibre-to-matrix bonding. Once again, this model is based on two independently described constitutive relations of the constituents.
- A three-dimensional, unit-cell finite element model where the fibre and matrix constituents are modelled explicitly. The model makes it possible to investigate the effect of the fibre-to-matrix interaction upon kink band formation.
- A two-dimensional finite element model with periodic boundary conditions on a skewed mesh, used to study kink band broadening.
- An analytical model for the estimation of kink band broadening. The model was based on a Maxwell condition for the steady-state.

As part of the visit to the Department of Engineering at the University of Cambridge, the following contributions were made regarding the investigation of the load transfer mechanism in a Dyneema composite:

- Construction of an experimental set-up to study the load transfer mechanism.
- Identification of the dominant failure mechanism through X-ray tomography and optical images. It was found that the failure was dominated by inter-laminar shearing between the 0° and 90° fibre layers.
- Development of a simple analytical model of the dominant failure.
- Construction of a failure mechanism map with the specimen geometries as the independent variables.

5.2 Perspective

In the previous section, all the contributions were stated as bullet points and in the following, the contributions are put into perspective for real applications.

The development of the three-dimensional constitutive model makes it possible to simulate the failure of real three-dimensional structures made from composite materials. Previous 3D models were based on the measured homogenised response of the overall composite. The

current model takes two independently described materials and homogenises the properties instead of taking the overall measured properties. Furthermore, no information is lost with respect to the stress and strain states of the individual constituents during deformation.

The results obtained using the two-dimensional constitutive model taking imperfect bonding into account can be used to give an upper and lower bound for the actual compressive strength of fibre composites. The actual strength lies between the two boundaries of perfect and no bonding. The latter model can be implemented as a user subroutine in Abaqus/CAE. This gives the possibility of having areas of imperfect bonding as e.g. around drilled open-holes in composite laminates where the composite will be damaged in the vicinity of the hole due to the machining process.

A laminated composite structure will, in general, be exposed to different multi-axial stress states throughout the material. Previous studies have mainly focused on idealised cases with only stresses acting in the direction of the fibres. The results obtained with respect to multi-axial loading can be used to estimate the actual compressive strength of a composite with a realistic stress state.

As mentioned previously, the stress at steady-state kink band broadening can be seen as the lower bound of the compressive strength. In structures where the design needs to be insensitive to fibre-imperfections, parametric studies with respect to kink band broadening can be used to develop new composite materials with improved properties with compressive failure in mind.

5.3 Recommendations for further work

The three-dimensional constitutive model developed in [P1] was used to study kink band formation using an idealised model. The constitutive relation is formulated in a general framework and can be implemented as a user subroutine in a finite element software as e.g. a UMAT into Abaqus/CAE. This enables the study of failures of complex structures and fibre layouts where plasticity plays a crucial role.

The constitutive formulation developed in [P2] uses a phenomenological parameter μ going from zero to unity to specify the quality of fibre-to-matrix bonding. A connection is missing between the phenomenological parameter μ and the measured fracture toughness obtained from single-fibre push-out experiments e.g. Jäger et al. (2015).

Hybrid composites are currently being developed i.e. composites with more than two constituents; for example, glass and carbon fibres embedded in a resin material. The company Owens Corning has produced glass fibre laminates since 1944 and has recently started producing hybrid laminate composites composed of glass and carbon fibres. Limited work has been done within the field of compressive failure of hybrid composites.

Chapter 6

P1

Three-dimensional constitutive model for elastic-plastic behaviour of fibre-reinforced composites

6.1 Motivation

As described in the Introduction, the estimation of the behaviour of fibre composites under large deformations, including plasticity, can be challenging due to the heterogeneous structure of the composites. Both discrete and homogeneous finite element models can be used to study the deformation as explained in Chapter 2. The use of discrete models, where the fibre and matrix constituents are modelled explicitly, is limited to simple and small geometries. When the fibre layout becomes complex, the use of homogeneous models become advantageously. Previous developed homogeneous, elastic-plastic, formulations have mainly been based on the composite response instead of the constitutive response of the constituents.

The current publication regards the development of a three-dimensional constitutive formulation for fibre-reinforced composites. The formulation takes as input, two constitutive relations of two constituents and the volume fractions of the constituents. The formulation can be used in a general elastic-plastic framework with large displacements and rotations. The formulation is inspired by the two-dimensional constitutive model developed by Christoffersen and Jensen (1996). The original source of the publication is: (Skovsgaard and Jensen, 2018b).

6.2 Method

The homogenization of the constituents is based on three assumptions

- Material lines on the common plane between two materials are subjected to common stretching and rotation.
- Planes on the intersection between two materials transmit identical tractions.
- The material of the constituents is elastic or elastic-plastic.

The thoughts and theory behind the formulation were described in Chapter 3 and the essence is repeated here for completeness. The model is formulated in an updated Lagrangian framework using velocity gradients and rates of nominal stresses. The final three-dimensional constitutive relation is based on two homogenisations to obtain a fibre that is embedded in a matrix. The relation is implemented and used in a semi-analytical kink band simulation using Fortran 77 programming. The model implementation is described in Section 3.4.

6.3 Contribution

The contributions to the publication comprise: the development of a novel constitutive formulation; expansion of a two-dimensional kink band model to a three-dimensional version; conducting kink band simulations with and without multi-axial loading and writing the paper.

6.4 Main findings

One of the main findings is the development of the constitutive formulation itself. Several different versions of the three-dimensional relations are proposed and results from a kink band simulations using the models are compared with the results from a two-dimensional model introduced by Jensen and Christoffersen (1997). The influence of initial fibre imperfection upon the critical compressive strength is investigated using the different models. Furthermore, the influence of transverse and shear loading upon the critical compressive stress is investigated using the two- and three-dimensional relations.

The developed constitutive formulation is used in a kink band study using a semi-analytical approach, but is far from limited to this application. The formulation can e.g. be implemented as a user subroutines into Abaqus/CAE and be used to study the response and failure of complex fibre domains.



Contents lists available at ScienceDirect

International Journal of Solids and Structures

journal homepage: www.elsevier.com/locate/ijsolstr

Three-dimensional constitutive model for elastic-plastic behaviour of fibre-reinforced composites



Simon P.H. Skovsgaard*, Henrik Myhre Jensen

Department of Engineering, Aarhus University, Inge Lehmanns Gade 10, Aarhus C 8000, Denmark

ARTICLE INFO

Article history:
Received 8 August 2017
Revised 23 January 2018
Available online 2 February 2018

Keywords:
Fibre reinforced
Anisotropic
Constitutive laws
Finite deformation
Instability

ABSTRACT

A formulation of a three-dimensional homogenized constitutive model is developed that can predict strain localization in fibre-reinforced composites. A constitutive equation for the model is developed in a general rate form based on independent constituent behaviour which can be either elastic or elastic-plastic. The performance of the constitutive model is investigated by performing an infinite kink band analysis. The development of a kink band is investigated for several initial imperfections and compared with previously published results.

© 2018 Elsevier Ltd. All rights reserved.

1. Introduction

The increased use of fibre composites has given rise to a thorough investigation of the behaviour and failure of composites based on several load types. Especially the compressive failure has received attention due to its sudden instability which can cause a catastrophic failure. Compressive failure of fibre composites is caused by several competing failure mechanisms. Several experiments show that a frequently observed failure is due to plastic micro-buckling which leads to the development of kink bands. Wadee et al. (2004) observed plastic micro-buckling in a compression experiment and compared the results with a simple mechanical model. Liu et al. (2014) investigated the collapse of composite beams made from ultra-high molecular polyethylene fibres where they observed kink band formation. Zhou et al. (2013) investigated the compressive response of unidirectional fibres under axial and off-axis compressive loading and kink band formation dominated the failure for small off-axis angles. Nizolek et al. (2017) investigated stable kink band propagation in Cu-Nb nanolaminates. They observed that kink bands were initiated and propagated from local imperfections.

In the early work of micro-buckling (Rosen, 1965) investigated the compressive strength of a polymer matrix composite where the fibres were treated as beams on an elastic foundation. Budiansky (1983) introduced a composite with elastic ideally plas-

tic matrix material. The failure was caused by kink band formation in a geometry with an initial fibre imperfection. As a continuation, Budiansky and Fleck (1993) included the effects of finite fibre stiffness. They concluded that the assumption of rigid fibres could be justified for many kinking problems. It is now commonly accepted that the micro-buckling compression failure is primarily dominated by fibre imperfections and the elastic-plastic shear behaviour of the composite.

Numerical investigations of the failure of long fibre-reinforced composites can roughly be divided into two categories. The first approach is by creating a finite element analysis where fibre and matrix are treated individually. This approach is commonly known as discretized models or individual fibre models. The approach was initially used by Guynn et al. (1992) and several authors have used a similar approach, including: Vogler et al. (2001a) who investigated the compressive response due to local imperfection near a free edge and was compared with own experiments presented in Vogler et al. (2001b). Romanowicz (2013) investigated both uniform and non-uniform sinusoidal imperfections. Wind et al. (2014) compared a discretized and homogenized model in a kink band study. Hsu et al. (1999a) conducted an experiment where they investigated steady-state axial propagation of kink bands and compared their findings with a three-dimensional discretized finite element model presented in Hsu et al. (1999b). Recent investigations using the current approach with random fibre distribution were performed by Zhang et al. (2016). More comprehensive methods including damage and cohesive friction elements were studied by Naya et al. (2017). The use of discretized finite element models can be challenging and time consuming when concerning large or complex geometries. Especially the deci-

* Corresponding author.

E-mail addresses: sphs@eng.au.dk (S.P.H. Skovsgaard), hmj@eng.au.dk (H.M. Jensen).

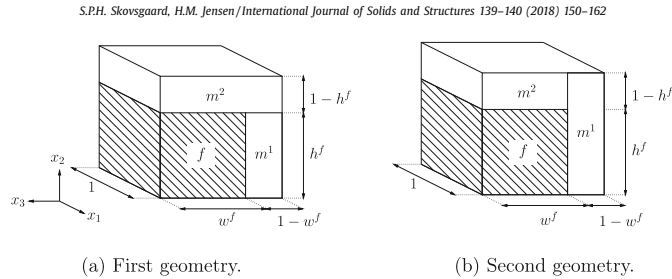


Fig. 1. Geometries for the constitutive formulations.

sions on how the direction should be varied for every single fibre are complicated when the geometry becomes comprehensive. The method, where the fibres are discretized and are embedded in a matrix material, is limited to simple geometries.

A second approach is by homogenizing or smear out the properties of the fibre and matrix constituents. Early formulations of two-dimensional constitutive models were presented by Fleck and Shu (1995) and Christoffersen and Jensen (1996). Fleck and Shu (1995) formulated their constitutive model using Cosserat couple stress theory, where they were able to include fibre bending effects. Christoffersen and Jensen (1996) formulated a general rate constitutive equation where the homogenized properties were based on independent constitutive laws for both constituents (matrix and fibre). Poullos and Niordson (2016) combined the qualities of the two latter models. They developed a two-dimensional constitutive model which is described by two independent constitutive laws for the constituents and is able to include intrinsic size effects using higher order strain gradients.

The present paper introduces a general three-dimensional constitutive model which is largely inspired by the formulation done by Christoffersen and Jensen (1996). Only few attempts have been done to introduce three-dimensional effects into a general framework to simulate the compressive failure of composites. Grandidier et al. (1992) introduced three-dimensional effects to investigate elastic micro-buckling by introducing a non-uniform distribution of the displacements through the thickness. Gutkin et al. (2016) investigated kink bands under 3D stress states using a damage model created in Gutkin and Pinho (2015).

Three-dimensional constitutive models including plasticity is needed to investigate the failure of more complex geometries and fibre layouts created by fibre-reinforced composites. The current paper introduces a three-dimensional homogenized constitutive model which is based on independent constitutive laws for the constituents. The model is created in a rate form using nominal stresses. The model is based on kinematic and static continuities and are averaged over a representative volume element. Lastly, the constitutive model is investigated using an infinite kink band analysis and is compared with results obtained by Jensen and Christoffersen (1997) and Jensen (1999).

The paper is organized in nine sections. Initially in Section 2, an overview of the representative volume elements is presented which the constitutive model is based on. The general relations are introduced in Section 3. Section 4 together with Section 5 derives the constitutive model. Section 6 presents the formulation of the infinite kink band simulation. In Section 7, the constitutive law used for the constituents is presented. Section 8 gives an overview of the steps required in the numerical simulation. Section 9 shows results for kink band formation where different constitutive models are compared. Section 10 concludes the paper.

2. Geometrical representation of constitutive model

In this section, a geometric representation of the representative volume elements is shown and described. The constitutive model is based on similar assumptions used to derive the model used in Christoffersen and Jensen (1996). Their constitutive model was based on a two-dimensional domain of fibres and matrix and was formulated based on three assumptions outlined here for completeness

1. Material lines parallel with the fibres are subject to a common stretching and rotation.
2. Planes parallel with the fibres transmit identical tractions.
3. The material of the constituents is elastic or elastic-plastic.

The first assumption correspond to a Voigt estimate in the fibre direction and is commonly accepted for fibre-reinforced composites. The second assumption implies that the shared plane between the fibre and matrix transmit the same traction and thereby is in equilibrium across the boundaries. The third assumption is a specification of the time-independent materials for the constituents. The current model uses both the first and third assumption directly and partially the second assumption which will be outlined later. An illustration of the representative volume elements (RVE) is shown in Fig. 1. Two different geometries are shown which the derivations are based on. Common for both geometries is a fibre constituent f and two matrix constituents m^1 and m^2 , representing a fibre surrounded by a resin material. Two length scales are introduced w^f and h^f which is the width and height of the simplified fibre geometry. In the case of a uniform distribution of fibre and matrix, the length scales can be calculated based on

$$w^f = h^f = \sqrt{c^f} \quad (1)$$

where c^f is the volume fraction of fibres. The fibre and matrix volume fraction c^f and c^m comply to the identities

$$\begin{aligned} c^f &= w^f h^f \\ c^m &= (1 - w^f)h^f + (1 - h^f) = (1 - w^f) + (1 - h^f)w^f \\ 1 &= c^f + c^m \end{aligned} \quad (2)$$

The only difference between the two geometries shown in Fig. 1 is the volume fractions of m^1 and m^2 . When the models are derived, they behave orthotropically. Unidirectional fibre composites with fibres aligned in the x_1 direction are usually assumed to have transverse isotropic behaviour. To obtain a transverse isotropic behaviour of the constitutive model, a combination of the properties between the two geometries, illustratively shown in Fig. 2, is used.

The constitutive models are constructed based on a homogenization in two steps. For the first geometry shown in Fig. 1(a), the

152

S.P.H. Skovgaard, H.M. Jensen / International Journal of Solids and Structures 139–140 (2018) 150–162

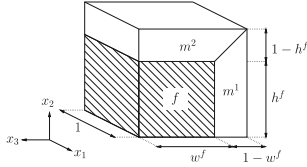


Fig. 2. Geometric interpretation of the average constitutive properties.

initial homogenization is done between f and m^1 . After the homogenization, the lower part of the geometry is treated as a homogeneous constituent which is illustrated in Fig. 3(a). In the same manner, the second geometry is initially homogenized between f and m^2 as shown in Fig. 3(b).

3. General relations

The constitutive model is based on a rate form of the constitutive behaviour of the three constituents. A formulation in the following form is pursued

$$\dot{t}_{ij} = C_{ijkl} v_{l,k} \quad i, j, k, l = \{1, 2, 3\} \quad (3)$$

where \dot{t}_{ij} are components of the rate of nominal stresses, $v_{l,k}$ are components of the velocity gradients and C_{ijkl} are components of the tensor of nominal moduli. The summation convention is adopted for repeated index. Knowing the constitutive relations and the velocity gradients for the individual constituents, similar relations can be set up

$$\dot{t}_{ij}^c = C_{ijkl}^c v_{l,k}^c \quad i, j, k, l = \{1, 2, 3\} \quad (4)$$

here $(\cdot)^c$ represent either $(\cdot)^f$, $(\cdot)^{m^1}$ or $(\cdot)^{m^2}$. The relation between the nominal stress rate and the Cauchy stress rate is given by

$$\dot{t}_{ij}^c = \dot{\sigma}_{ij}^c + \sigma_{ij}^c v_{k,k}^c - \sigma_{jk}^c v_{i,k}^c \quad (5)$$

It is assumed that the elastic-plastic relation between the rate of Cauchy stress and strain rate are given in the form

$$\dot{\sigma}_{ij}^c = L_{ijkl}^c \dot{\epsilon}_{kl}^c \quad (6)$$

here $\dot{\sigma}_{ij}^c$ are components of the Jaumann rate of Cauchy stresses which follows the local rotated coordinate system during deformation. L_{ijkl}^c are components of the elastic-plastic tangent moduli which satisfies the symmetries

$$L_{ijkl}^c = L_{jikl}^c = L_{jilk}^c \quad (7)$$

which is required by objectivity. The strain rates can be calculated using the velocity gradients

$$\dot{\epsilon}_{ij}^c = \frac{1}{2} (v_{i,j}^c + v_{j,i}^c) \quad (8)$$

Eq. (6) can be rewritten using the symmetries of L_{ijkl}^c combined with the latter equation

$$\dot{\sigma}_{ij}^c = L_{ijkl}^c v_{l,k}^c \quad (9)$$

The relation between the Jaumann rate of Cauchy stress and the Cauchy stress rate seen from a stationary coordinate system is given by

$$\dot{\sigma}_{ij}^c = \dot{\sigma}_{ij}^c + \omega_{jk}^c \sigma_{ik}^c + \omega_{ik}^c \sigma_{kj}^c \quad (10)$$

where ω_{ij}^c is the spin tensor given by

$$\omega_{ij}^c = \frac{1}{2} (v_{i,j}^c - v_{j,i}^c) \quad (11)$$

Combining Eq. (5) and Eqs. (9)–(11) yields the relation between nominal stress rate and velocity gradients

$$\dot{t}_{ij}^c = \left(L_{ijkl}^c + \frac{1}{2} \sigma_{ik}^c \delta_{jl} - \frac{1}{2} \sigma_{ij}^c \delta_{kl} - \frac{1}{2} \sigma_{kj}^c \delta_{il} - \frac{1}{2} \sigma_{li}^c \delta_{jk} + \sigma_{ij}^c \delta_{ik} \right) v_{l,k}^c \quad (12)$$

where δ_{ij} is Kronecker's delta. Comparing the latter equation with Eq. (4) results in the desired moduli

$$C_{ijkl}^c = L_{ijkl}^c + \frac{1}{2} \sigma_{ik}^c \delta_{jl} - \frac{1}{2} \sigma_{ij}^c \delta_{kl} - \frac{1}{2} \sigma_{kj}^c \delta_{il} - \frac{1}{2} \sigma_{li}^c \delta_{jk} + \sigma_{ij}^c \delta_{ik} \quad (13)$$

Using the nominal moduli C_{ijkl}^c gives the opportunity to include residual stresses which were investigated in a two-dimensional kink band study by Jensen (2002). In the derivations below, it is convenient to represent the stress rates and velocities in vectors. The nine components of the nominal stress rates are represented in the three vectors

$$\mathbf{t}_1 = \begin{pmatrix} \dot{t}_{11} \\ \dot{t}_{12} \\ \dot{t}_{13} \end{pmatrix} \quad \mathbf{t}_2 = \begin{pmatrix} \dot{t}_{21} \\ \dot{t}_{22} \\ \dot{t}_{23} \end{pmatrix} \quad \mathbf{t}_3 = \begin{pmatrix} \dot{t}_{31} \\ \dot{t}_{32} \\ \dot{t}_{33} \end{pmatrix} \quad (14)$$

Each of the stress vectors represents the traction increment acting on the deformed configuration which initially was a unit cube. The vector \mathbf{v} will denote the velocity vector

$$\mathbf{v} = \begin{pmatrix} v_1 \\ v_2 \\ v_3 \end{pmatrix} \quad (15)$$

Using the vectors above, the constitutive relation Eq. (4) for the composite and the constituents may be written as

$$\mathbf{t}_i = \mathbf{C}_{ij} \mathbf{v}_j \quad i, j = \{1, 2, 3\} \\ \mathbf{t}_i^c = \mathbf{C}_{ij}^c \mathbf{v}_j^c \quad i, j = \{1, 2, 3\} \quad (16)$$

Where \mathbf{C}_{ij} and \mathbf{C}_{ij}^c represents matrices of the size 3×3 . The matrices includes the constitutive moduli C_{ijkl} and C_{ijkl}^c .

4. Homogenization between arbitrary materials

The homogenization between two material planes are based on the assumptions:

1. Material lines lying on the common plane between two materials are subjected to a common stretching and rotation.
2. Planes on the intersection between two materials transmit identical tractions.
3. The material of the constituents is elastic or elastic-plastic.

The first assumption results in 3 stretching continuities and 3 rotation continuities. The second assumption expresses local equilibrium.

To obtain the homogenized models presented in Section 2, two homogenization operations are performed. The homogenization is done for two materials who share a plane parallel with the $x_1 - x_2$ plane and another situation where they share a plane parallel with the $x_1 - x_3$ plane.

On Fig. 4 two materials a and b are shown who share a plane parallel with the $x_1 - x_3$ plane. As a consequence of the first assumption, the velocity gradients $\mathbf{v}_{,1}^a$ and $\mathbf{v}_{,3}^b$ are common for both constituents based on the geometry shown in Fig. 4

$$\mathbf{v}_{,1}^a = \mathbf{v}_{,1}^b = \mathbf{v}_{,1} \\ \mathbf{v}_{,3}^a = \mathbf{v}_{,3}^b = \mathbf{v}_{,3} \quad (17)$$

where superscripts $(\cdot)^a$ and $(\cdot)^b$ represents the two arbitrary materials, and velocity gradients with no superscript are overall quantities. For overall compatibility of the representative volume element

$$c^a \mathbf{v}_{,2}^a + c^b \mathbf{v}_{,2}^b = \mathbf{v}_{,2} \quad (18)$$

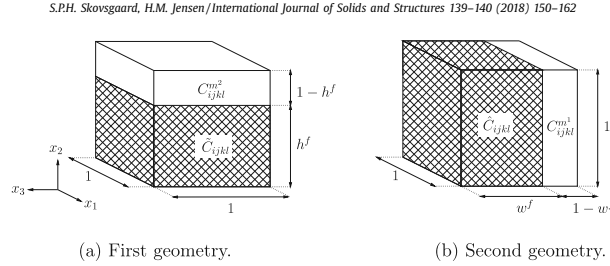
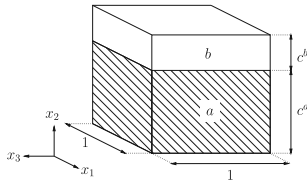


Fig. 3. Geometries after first homogenization.

Fig. 4. Representative volume element, where two arbitrary materials share a common plane with outward normals which are parallel with the x_2 -axis.

where c^a and c^b are the length scales presented in Fig. 4 which also are the volume fractions of the two materials.

The second assumption leads to the equality

$$\mathbf{t}_2^a = \mathbf{t}_2^b = \mathbf{t}_2 \quad (19)$$

Overall equilibrium of the RVE entails

$$\begin{aligned} c^a \mathbf{t}_1^a + c^b \mathbf{t}_1^b &= \mathbf{t}_1 \\ c^a \mathbf{t}_3^a + c^b \mathbf{t}_3^b &= \mathbf{t}_3 \end{aligned} \quad (20)$$

Based on Eqs. (17)–(20) the representative volume element will comply to equilibrium and compatibility. Combining Eqs. (17)–(20) together with Eq. (16), as detailed in Appendix A, yields the following expressions for \mathbf{v}_2^a

$$\begin{aligned} \mathbf{v}_2^a &= -c^b \mathbf{C}_{22}^{a-1} \left((\mathbf{C}_{21}^a - \mathbf{C}_{21}^b) \mathbf{v}_1 + \left(\mathbf{C}_{22}^a - \mathbf{C}_{22}^b - \frac{1}{c^b} \mathbf{C}_{22}^a \right) \mathbf{v}_2 + (\mathbf{C}_{23}^a - \mathbf{C}_{23}^b) \mathbf{v}_3 \right) \\ \mathbf{v}_2^b &= c^a \mathbf{C}_{22}^{b-1} \left((\mathbf{C}_{21}^b - \mathbf{C}_{21}^a) \mathbf{v}_1 + \left(\mathbf{C}_{22}^b - \mathbf{C}_{22}^a + \frac{1}{c^a} \mathbf{C}_{22}^b \right) \mathbf{v}_2 + (\mathbf{C}_{23}^b - \mathbf{C}_{23}^a) \mathbf{v}_3 \right) \end{aligned} \quad (21)$$

Using Eq. (16) the velocity gradients for the constituents can be determined based on the traction forces. Initially, the focus is on the tractions \mathbf{t}_1^a

$$\begin{aligned} \mathbf{t}_1^a &= \mathbf{C}_{11}^a \mathbf{v}_1 + \mathbf{C}_{12}^a \mathbf{v}_2 + \mathbf{C}_{13}^a \mathbf{v}_3 \\ \mathbf{t}_1^b &= \mathbf{C}_{11}^b \mathbf{v}_1 + \mathbf{C}_{12}^b \mathbf{v}_2 + \mathbf{C}_{13}^b \mathbf{v}_3 \end{aligned} \quad (22)$$

Inserting the results for \mathbf{v}_2^a and \mathbf{v}_2^b yields

$$\begin{aligned} \mathbf{t}_1^a &= \left(\mathbf{C}_{11}^a - c^b \mathbf{C}_{12}^a \mathbf{C}_{22}^{a-1} (\mathbf{C}_{21}^a - \mathbf{C}_{21}^b) \right) \mathbf{v}_1 \\ &\quad + \left(\mathbf{C}_{12}^a - c^b \mathbf{C}_{12}^a \mathbf{C}_{22}^{a-1} (\mathbf{C}_{22}^a - \mathbf{C}_{22}^b) \right) \mathbf{v}_2 \\ &\quad + \left(\mathbf{C}_{13}^a - c^b \mathbf{C}_{12}^a \mathbf{C}_{22}^{a-1} (\mathbf{C}_{23}^a - \mathbf{C}_{23}^b) \right) \mathbf{v}_3 \\ \mathbf{t}_1^b &= \left(\mathbf{C}_{11}^b + c^a \mathbf{C}_{12}^b \mathbf{C}_{22}^{b-1} (\mathbf{C}_{21}^b - \mathbf{C}_{21}^a) \right) \mathbf{v}_1 \\ &\quad + \left(\mathbf{C}_{12}^b + c^a \mathbf{C}_{12}^b \mathbf{C}_{22}^{b-1} (\mathbf{C}_{22}^b - \mathbf{C}_{22}^a) \right) \mathbf{v}_2 \\ &\quad + \left(\mathbf{C}_{13}^b + c^a \mathbf{C}_{12}^b \mathbf{C}_{22}^{b-1} (\mathbf{C}_{23}^b - \mathbf{C}_{23}^a) \right) \mathbf{v}_3 \end{aligned} \quad (23)$$

Combining the latter equation with the first part of Eq. (20)

$$\begin{aligned} \mathbf{t}_1 &= \left(c^a \mathbf{C}_{11}^a + c^b \mathbf{C}_{11}^b - c^a c^b (\mathbf{C}_{12}^a - \mathbf{C}_{12}^b) \mathbf{C}_{22}^{a-1} (\mathbf{C}_{21}^a - \mathbf{C}_{21}^b) \right) \mathbf{v}_1 \\ &\quad + \left(c^a \mathbf{C}_{12}^a + c^b \mathbf{C}_{12}^b - c^a c^b (\mathbf{C}_{12}^a - \mathbf{C}_{12}^b) \mathbf{C}_{22}^{a-1} (\mathbf{C}_{22}^a - \mathbf{C}_{22}^b) \right) \mathbf{v}_2 \\ &\quad + \left(c^a \mathbf{C}_{13}^a + c^b \mathbf{C}_{13}^b - c^a c^b (\mathbf{C}_{12}^a - \mathbf{C}_{12}^b) \mathbf{C}_{22}^{a-1} (\mathbf{C}_{23}^a - \mathbf{C}_{23}^b) \right) \mathbf{v}_3 \end{aligned} \quad (24)$$

Using the same arguments for the tractions \mathbf{t}_3^a using the second part of Eq. (20) yields

$$\begin{aligned} \mathbf{t}_3 &= \left(c^a \mathbf{C}_{31}^a + c^b \mathbf{C}_{31}^b - c^a c^b (\mathbf{C}_{32}^a - \mathbf{C}_{32}^b) \mathbf{C}_{22}^{a-1} (\mathbf{C}_{21}^a - \mathbf{C}_{21}^b) \right) \mathbf{v}_1 \\ &\quad + \left(c^a \mathbf{C}_{32}^a + c^b \mathbf{C}_{32}^b - c^a c^b (\mathbf{C}_{32}^a - \mathbf{C}_{32}^b) \mathbf{C}_{22}^{a-1} (\mathbf{C}_{22}^a - \mathbf{C}_{22}^b) \right) \mathbf{v}_2 \\ &\quad + \left(c^a \mathbf{C}_{33}^a + c^b \mathbf{C}_{33}^b - c^a c^b (\mathbf{C}_{32}^a - \mathbf{C}_{32}^b) \mathbf{C}_{22}^{a-1} (\mathbf{C}_{23}^a - \mathbf{C}_{23}^b) \right) \mathbf{v}_3 \end{aligned} \quad (25)$$

By inserting the velocity gradients given by Eq. (21) into Eq. (19) results in two expressions for the traction \mathbf{t}_2

$$\begin{aligned} \mathbf{t}_2 &= \left(\mathbf{C}_{21}^a - c^b \mathbf{C}_{22}^a \mathbf{C}_{22}^{a-1} (\mathbf{C}_{21}^a - \mathbf{C}_{21}^b) \right) \mathbf{v}_1 \\ &\quad + \left(\mathbf{C}_{22}^a - c^b \mathbf{C}_{22}^a \mathbf{C}_{22}^{a-1} (\mathbf{C}_{22}^a - \mathbf{C}_{22}^b) \right) \mathbf{v}_2 \\ &\quad + \left(\mathbf{C}_{23}^a - c^b \mathbf{C}_{22}^a \mathbf{C}_{22}^{a-1} (\mathbf{C}_{23}^a - \mathbf{C}_{23}^b) \right) \mathbf{v}_3 \\ \mathbf{t}_2 &= \left(\mathbf{C}_{21}^b + c^a \mathbf{C}_{22}^b \mathbf{C}_{22}^{b-1} (\mathbf{C}_{21}^b - \mathbf{C}_{21}^a) \right) \mathbf{v}_1 \\ &\quad + \left(\mathbf{C}_{22}^b + c^a \mathbf{C}_{22}^b \mathbf{C}_{22}^{b-1} (\mathbf{C}_{22}^b - \mathbf{C}_{22}^a) \right) \mathbf{v}_2 \\ &\quad + \left(\mathbf{C}_{23}^b + c^a \mathbf{C}_{22}^b \mathbf{C}_{22}^{b-1} (\mathbf{C}_{23}^b - \mathbf{C}_{23}^a) \right) \mathbf{v}_3 \end{aligned} \quad (26)$$

Since the two previous solutions for \mathbf{t}_2 yield identical results, a combination of the two, multiplied by c^a and c^b will also give an identical solution

$$\mathbf{t}_2 = c^a \mathbf{t}_2 + c^b \mathbf{t}_2 \quad (27)$$

Using the latter property, the tractions \mathbf{t}_2 can be written as

$$\begin{aligned} \mathbf{t}_2 &= \left(c^a \mathbf{C}_{21}^a + c^b \mathbf{C}_{21}^b - c^a c^b (\mathbf{C}_{22}^a - \mathbf{C}_{22}^b) \mathbf{C}_{22}^{a-1} (\mathbf{C}_{21}^a - \mathbf{C}_{21}^b) \right) \mathbf{v}_1 \\ &\quad + \left(c^a \mathbf{C}_{22}^a + c^b \mathbf{C}_{22}^b - c^a c^b (\mathbf{C}_{22}^a - \mathbf{C}_{22}^b) \mathbf{C}_{22}^{a-1} (\mathbf{C}_{22}^a - \mathbf{C}_{22}^b) \right) \mathbf{v}_2 \\ &\quad + \left(c^a \mathbf{C}_{23}^a + c^b \mathbf{C}_{23}^b - c^a c^b (\mathbf{C}_{22}^a - \mathbf{C}_{22}^b) \mathbf{C}_{22}^{a-1} (\mathbf{C}_{23}^a - \mathbf{C}_{23}^b) \right) \mathbf{v}_3 \end{aligned} \quad (28)$$

Comparing the coefficients from Eqs. (24), (25) to (28) with the desired relation given by Eq. (16), the matrices may be written in the form

$$\mathbf{C}_{ij} = c^a \mathbf{C}_{ij}^a + c^b \mathbf{C}_{ij}^b - c^a c^b (\mathbf{C}_{i2}^a - \mathbf{C}_{i2}^b) \mathbf{C}_{22}^{a-1} (\mathbf{C}_{2j}^a - \mathbf{C}_{2j}^b) \quad i, j = \{1, 2, 3\} \quad (29)$$

The constitutive equation gives the homogenized properties of the overall nominal tractions and overall velocity gradients. In an incremental scheme, the velocity gradients for the constituents can be obtained based on Eqs. (17) and (21). The previous derivations

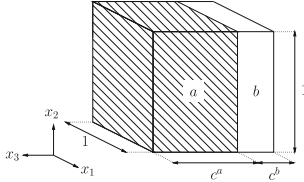


Fig. 5. Representative volume element, where two arbitrary materials share a common plane with outward normals which are parallel with the x_3 -axis.

were based on a representative volume with two arbitrary materials sharing a plane with an outward normal parallel to the x_2 -axis. In Fig. 5, two materials share a common plane with outward normal parallel to the x_3 -axis. The derivation of the homogenized properties of such a geometry is similar to the previous and therefore details are omitted.

In this case the velocity gradients \mathbf{v}_1^c and \mathbf{v}_2^c are common for both constituents

$$\begin{aligned} \mathbf{v}_1^c &= \mathbf{v}_1^b = \mathbf{v}_1 \\ \mathbf{v}_2^c &= \mathbf{v}_2^b = \mathbf{v}_2 \end{aligned} \quad (30)$$

For overall compatibility of the representative volume element

$$c^a \mathbf{v}_3^a + c^b \mathbf{v}_3^b = \mathbf{v}_3 \quad (31)$$

The second assumption leads to the equality

$$\mathbf{t}_3^a = \mathbf{t}_3^b = \mathbf{t}_3 \quad (32)$$

By overall equilibrium

$$\begin{aligned} c^a \mathbf{t}_1^a + c^b \mathbf{t}_1^b &= \mathbf{t}_1 \\ c^a \mathbf{t}_2^a + c^b \mathbf{t}_2^b &= \mathbf{t}_2 \end{aligned} \quad (33)$$

Based on the assumptions and the equalities for the current geometry, the constitutive relations between nominal tractions and velocity gradients is given by

$$\mathbf{C}_{ij} = c^a \mathbf{C}_{ij}^a + c^b \mathbf{C}_{ij}^b - c^a c^b (\mathbf{C}_{i3}^a - \mathbf{C}_{i3}^b) \mathbf{C}_{33}^{a-1} (\mathbf{C}_{3j}^a - \mathbf{C}_{3j}^b) \quad i, j = \{1, 2, 3\} \quad (34)$$

The only difference between the latter constitutive equation and Eq. (29) is the last part which is a consequence of the direction of the outward normal of the shared plane between the constituents. The velocity gradients \mathbf{v}_3^c can be calculated based on the overall velocity gradients

$$\begin{aligned} \mathbf{v}_3^c &= -c^b \mathbf{C}_{33}^{a-1} \left((\mathbf{C}_{31}^a - \mathbf{C}_{31}^b) \mathbf{v}_1 + (\mathbf{C}_{32}^a - \mathbf{C}_{32}^b) \mathbf{v}_2 \right) \\ &\quad + \left(\mathbf{C}_{33}^a - \mathbf{C}_{33}^b - \frac{1}{c^b} \mathbf{C}_{33}^a \right) \mathbf{v}_3 \\ \mathbf{v}_3^b &= c^a \mathbf{C}_{33}^{b-1} \left((\mathbf{C}_{31}^b - \mathbf{C}_{31}^a) \mathbf{v}_1 + (\mathbf{C}_{32}^b - \mathbf{C}_{32}^a) \mathbf{v}_2 \right) \\ &\quad + \left(\mathbf{C}_{33}^b - \mathbf{C}_{33}^a + \frac{1}{c^a} \mathbf{C}_{33}^b \right) \mathbf{v}_3 \end{aligned} \quad (35)$$

5. Constitutive models

To derive the constitutive properties of the geometries shown in Fig. 1, a combination of the constitutive formulations Eqs. (29) and (34) is to be used. Initially, the focus is on the first geometry shown in Fig. 1(a).

5.1. Constitutive model 1

An initial homogenization is performed between f and m^1 as shown in Fig. 3(a), where the symbol \odot is used. The materials

share a common plane with outward normal parallel with the x_3 -axis and for this reason Eq. (34) is used

$$\begin{aligned} \tilde{\mathbf{C}}_{ij} &= w^f \mathbf{C}_{ij}^f + (1 - w^f) \mathbf{C}_{ij}^{m^1} - w^f (1 - w^f) (\mathbf{C}_{i3}^f - \mathbf{C}_{i3}^{m^1}) \mathbf{C}_{33}^{* -1} (\mathbf{C}_{3j}^f - \mathbf{C}_{3j}^{m^1}) \\ i, j &= \{1, 2, 3\} \end{aligned} \quad (36)$$

where \mathbf{C}_{33}^* is given by

$$\mathbf{C}_{33}^* = w^f \mathbf{C}_{33}^{m^1} + (1 - w^f) \mathbf{C}_{33}^f \quad (37)$$

Based on the homogenized velocity gradients $\tilde{\mathbf{v}}_j$ for the initial homogenization the velocity gradients for the constituents can be calculated as

$$\begin{aligned} \mathbf{v}_1^f &= \mathbf{v}_1^{m^1} = \tilde{\mathbf{v}}_1 \\ \mathbf{v}_2^f &= \mathbf{v}_2^{m^1} = \tilde{\mathbf{v}}_2 \\ \mathbf{v}_3^f &= -(1 - w^f) \mathbf{C}_{33}^{* -1} \left((\mathbf{C}_{31}^f - \mathbf{C}_{31}^{m^1}) \tilde{\mathbf{v}}_1 + (\mathbf{C}_{32}^f - \mathbf{C}_{32}^{m^1}) \tilde{\mathbf{v}}_2 \right) \\ &\quad + \left(\mathbf{C}_{33}^f - \mathbf{C}_{33}^{m^1} - \frac{1}{1 - w^f} \mathbf{C}_{33}^* \right) \tilde{\mathbf{v}}_3 \\ \mathbf{v}_3^{m^1} &= w^f \mathbf{C}_{33}^{* -1} \left((\mathbf{C}_{31}^{m^1} - \mathbf{C}_{31}^f) \tilde{\mathbf{v}}_1 + (\mathbf{C}_{32}^{m^1} - \mathbf{C}_{32}^f) \tilde{\mathbf{v}}_2 \right) \\ &\quad + \left(\mathbf{C}_{33}^{m^1} - \mathbf{C}_{33}^f + \frac{1}{w^f} \mathbf{C}_{33}^* \right) \tilde{\mathbf{v}}_3 \end{aligned} \quad (38)$$

The last homogenization is between \odot and m^2 . The current constituents share a common plane with an outward normal parallel with the x_2 -axis and therefore Eq. (29) is used

$$\begin{aligned} \mathbf{C}_{ij}^1 &= h^f \mathbf{C}_{ij}^f + (1 - h^f) \mathbf{C}_{ij}^{m^2} - h^f (1 - h^f) (\tilde{\mathbf{C}}_{i2}^f - \mathbf{C}_{i2}^{m^2}) \tilde{\mathbf{C}}_{22}^{* -1} (\tilde{\mathbf{C}}_{2j}^f - \mathbf{C}_{2j}^{m^2}) \\ i, j &= \{1, 2, 3\} \end{aligned} \quad (39)$$

where $\tilde{\mathbf{C}}_{22}^*$ is

$$\tilde{\mathbf{C}}_{22}^* = h^f \mathbf{C}_{22}^{m^2} + (1 - h^f) \tilde{\mathbf{C}}_{22} \quad (40)$$

Based on the overall velocity gradients \mathbf{v}_j the velocity gradients for the constituents can be calculated.

$$\begin{aligned} \mathbf{v}_1^f &= \mathbf{v}_1^{m^2} = \mathbf{v}_1 \\ \mathbf{v}_3^f &= \mathbf{v}_3^{m^2} = \mathbf{v}_3 \\ \mathbf{v}_2^f &= -(1 - h^f) \tilde{\mathbf{C}}_{22}^{* -1} \left((\tilde{\mathbf{C}}_{21}^f - \mathbf{C}_{21}^{m^2}) \mathbf{v}_1 + \left(\tilde{\mathbf{C}}_{22}^f - \mathbf{C}_{22}^{m^2} - \frac{1}{1 - h^f} \mathbf{C}_{22}^* \right) \mathbf{v}_2 \right) \\ &\quad + (\tilde{\mathbf{C}}_{23}^f - \mathbf{C}_{23}^{m^2}) \mathbf{v}_3 \\ \mathbf{v}_2^{m^2} &= h^f \tilde{\mathbf{C}}_{22}^{* -1} \left((\tilde{\mathbf{C}}_{21}^{m^2} - \mathbf{C}_{21}^f) \mathbf{v}_1 + \left(\tilde{\mathbf{C}}_{22}^{m^2} - \mathbf{C}_{22}^f + \frac{1}{h^f} \mathbf{C}_{22}^* \right) \mathbf{v}_2 \right) \\ &\quad + (\tilde{\mathbf{C}}_{23}^{m^2} - \mathbf{C}_{23}^f) \mathbf{v}_3 \end{aligned} \quad (41)$$

Combining the latter expression for the velocity gradients with Eq. (38), the velocity gradients for the constituents can be obtained.

$$\begin{aligned} \mathbf{v}_1^f &= \mathbf{v}_1 \\ \mathbf{v}_2^f &= -(1 - h^f) \tilde{\mathbf{C}}_{22}^{* -1} \left((\tilde{\mathbf{C}}_{21}^f - \mathbf{C}_{21}^{m^2}) \mathbf{v}_1 + \left(\tilde{\mathbf{C}}_{22}^f - \mathbf{C}_{22}^{m^2} - \frac{1}{1 - h^f} \mathbf{C}_{22}^* \right) \mathbf{v}_2 \right) \\ &\quad + (\tilde{\mathbf{C}}_{23}^f - \mathbf{C}_{23}^{m^2}) \mathbf{v}_3 \\ \mathbf{v}_3^f &= -(1 - w^f) \mathbf{C}_{33}^{* -1} \left((\mathbf{C}_{31}^f - \mathbf{C}_{31}^{m^1}) \mathbf{v}_1 - (1 - h^f) (\mathbf{C}_{32}^f - \mathbf{C}_{32}^{m^1}) \mathbf{C}_{22}^{* -1} \right. \\ &\quad \left. \left((\tilde{\mathbf{C}}_{21}^f - \mathbf{C}_{21}^{m^2}) \mathbf{v}_1 + \left(\tilde{\mathbf{C}}_{22}^f - \mathbf{C}_{22}^{m^2} - \frac{1}{1 - h^f} \mathbf{C}_{22}^* \right) \mathbf{v}_2 \right) \right. \\ &\quad \left. + (\mathbf{C}_{33}^f - \mathbf{C}_{33}^{m^1} - \frac{1}{1 - w^f} \mathbf{C}_{33}^*) \mathbf{v}_3 \right) \end{aligned}$$

$$+ (\tilde{\mathbf{C}}_{23} - \mathbf{C}_{23}^{m^2}) \mathbf{v}_{.3} + \left(\mathbf{C}_{33}^f - \mathbf{C}_{33}^{m^1} - \frac{1}{1-w^f} \mathbf{C}_{33}^* \right) \mathbf{v}_{.3} \quad (42)$$

$$\mathbf{v}_{.1}^{m^1} = \mathbf{v}_{.1}$$

$$\mathbf{v}_{.2}^{m^1} = -(1-h^f) \mathbf{C}_{22}^{*^{-1}} \left((\tilde{\mathbf{C}}_{21} - \mathbf{C}_{21}^{m^2}) \mathbf{v}_{.1} + \left(\tilde{\mathbf{C}}_{22} - \mathbf{C}_{22}^{m^2} - \frac{1}{1-h^f} \mathbf{C}_{22}^* \right) \mathbf{v}_{.2} + (\tilde{\mathbf{C}}_{23} - \mathbf{C}_{23}^{m^2}) \mathbf{v}_{.3} \right)$$

$$\mathbf{v}_{.3}^{m^1} = w^f \mathbf{C}_{33}^{*^{-1}} \left((\mathbf{C}_{31}^f - \mathbf{C}_{31}^{m^1}) \mathbf{v}_{.1} - (1-h^f) (\mathbf{C}_{32}^f - \mathbf{C}_{32}^{m^1}) \mathbf{C}_{22}^{*^{-1}} \left((\tilde{\mathbf{C}}_{21} - \mathbf{C}_{21}^{m^2}) \mathbf{v}_{.1} + \left(\tilde{\mathbf{C}}_{22} - \mathbf{C}_{22}^{m^2} - \frac{1}{1-h^f} \mathbf{C}_{22}^* \right) \mathbf{v}_{.2} + (\tilde{\mathbf{C}}_{23} - \mathbf{C}_{23}^{m^2}) \mathbf{v}_{.3} \right) + \left(\mathbf{C}_{33}^f - \mathbf{C}_{33}^{m^1} - \frac{1}{1-w^f} \mathbf{C}_{33}^* \right) \mathbf{v}_{.3} \right) \quad (43)$$

$$\mathbf{v}_{.1}^{m^2} = \mathbf{v}_{.1}$$

$$\mathbf{v}_{.2}^{m^2} = h^f \mathbf{C}_{22}^{*^{-1}} \left((\tilde{\mathbf{C}}_{21} - \mathbf{C}_{21}^{m^2}) \mathbf{v}_{.1} + \left(\tilde{\mathbf{C}}_{22} - \mathbf{C}_{22}^{m^2} + \frac{1}{h^f} \mathbf{C}_{22}^* \right) \mathbf{v}_{.2} + (\tilde{\mathbf{C}}_{23} - \mathbf{C}_{23}^{m^2}) \mathbf{v}_{.3} \right)$$

$$\mathbf{v}_{.3}^{m^2} = \mathbf{v}_{.3} \quad (44)$$

5.2. Constitutive model 2

The second constitutive model shown in Fig. 1(b) is derived in a similar manner, where the first plane for performing homogenization is shifted. The initial homogenization is done between f and m^2 as shown in Fig. 3(b), where the symbol (\bullet) is used. The materials share a common plane with outward normal parallel with the x_2 -axis and for this reason Eq. (29) is used

$$\hat{\mathbf{C}}_{ij} = h^f \mathbf{C}_{ij}^f + (1-h^f) \mathbf{C}_{ij}^{m^2} - h^f (1-h^f) (\mathbf{C}_{i2}^f - \mathbf{C}_{i2}^{m^2}) \mathbf{C}_{22}^{*^{-1}} (\mathbf{C}_{2j}^f - \mathbf{C}_{2j}^{m^2}) \quad (45)$$

where \mathbf{C}_{22}^* is given by

$$\mathbf{C}_{22}^* = h^f \mathbf{C}_{22}^{m^2} + (1-h^f) \mathbf{C}_{22}^f \quad (46)$$

Based on the homogenized velocity gradients $\hat{\mathbf{v}}_j$ for the initial homogenization, the velocity gradients for the constituents can be obtained as

$$\mathbf{v}_{.1}^f = \mathbf{v}_{.1}^{m^2} = \hat{\mathbf{v}}_{.1}$$

$$\mathbf{v}_{.3}^f = \mathbf{v}_{.3}^{m^2} = \hat{\mathbf{v}}_{.3}$$

$$\mathbf{v}_{.2}^f = -(1-h^f) \mathbf{C}_{22}^{*^{-1}} \left((\mathbf{C}_{21}^f - \mathbf{C}_{21}^{m^2}) \hat{\mathbf{v}}_{.1} + \left(\mathbf{C}_{22}^f - \mathbf{C}_{22}^{m^2} - \frac{1}{1-h^f} \mathbf{C}_{22}^* \right) \hat{\mathbf{v}}_{.2} + (\mathbf{C}_{23}^f - \mathbf{C}_{23}^{m^2}) \hat{\mathbf{v}}_{.3} \right)$$

$$\mathbf{v}_{.2}^{m^2} = h^f \mathbf{C}_{22}^{*^{-1}} \left((\mathbf{C}_{21}^f - \mathbf{C}_{21}^{m^2}) \hat{\mathbf{v}}_{.1} + \left(\mathbf{C}_{22}^f - \mathbf{C}_{22}^{m^2} + \frac{1}{h^f} \mathbf{C}_{22}^* \right) \hat{\mathbf{v}}_{.2} + (\mathbf{C}_{23}^f - \mathbf{C}_{23}^{m^2}) \hat{\mathbf{v}}_{.3} \right) \quad (47)$$

The last homogenization for the model is done between (\bullet) and m^1 . The current constituents share a common plane with an outward normal parallel with the x_3 -axis and therefore Eq. (34) is

used

$$\mathbf{C}_{ij}^2 = w^f \hat{\mathbf{C}}_{ij} + (1-w^f) \mathbf{C}_{ij}^{m^1} - w^f (1-w^f) (\hat{\mathbf{C}}_{i3} - \mathbf{C}_{i3}^{m^1}) \hat{\mathbf{C}}_{33}^{*^{-1}} (\hat{\mathbf{C}}_{3j} - \mathbf{C}_{3j}^{m^1}) \quad (48)$$

where $\hat{\mathbf{C}}_{33}^*$ is given as

$$\hat{\mathbf{C}}_{33}^* = w^f \mathbf{C}_{33}^{m^1} + (1-w^f) \hat{\mathbf{C}}_{33} \quad (49)$$

Based on the overall velocity gradients $\mathbf{v}_{.j}$, the velocity gradients for the constituents can be obtained

$$\hat{\mathbf{v}}_{.1} = \mathbf{v}_{.1}^{m^1} = \mathbf{v}_{.1}$$

$$\hat{\mathbf{v}}_{.2} = \mathbf{v}_{.2}^{m^1} = \mathbf{v}_{.2}$$

$$\hat{\mathbf{v}}_{.3} = -(1-w^f) \hat{\mathbf{C}}_{33}^{*^{-1}} \left((\hat{\mathbf{C}}_{31} - \mathbf{C}_{31}^{m^1}) \mathbf{v}_{.1} + (\hat{\mathbf{C}}_{32} - \mathbf{C}_{32}^{m^1}) \mathbf{v}_{.2} + \left(\hat{\mathbf{C}}_{33} - \mathbf{C}_{33}^{m^1} - \frac{1}{1-w^f} \hat{\mathbf{C}}_{33}^* \right) \mathbf{v}_{.3} \right) + w^f \hat{\mathbf{C}}_{33}^{*^{-1}} \left((\hat{\mathbf{C}}_{31} - \mathbf{C}_{31}^{m^1}) \mathbf{v}_{.1} + (\hat{\mathbf{C}}_{32} - \mathbf{C}_{32}^{m^1}) \mathbf{v}_{.2} + \left(\hat{\mathbf{C}}_{33} - \mathbf{C}_{33}^{m^1} + \frac{1}{w^f} \hat{\mathbf{C}}_{33}^* \right) \mathbf{v}_{.3} \right) \quad (50)$$

Combining the latter expression with Eq. (47), the velocity gradients for the constituents can be determined.

$$\mathbf{v}_{.1}^f = \mathbf{v}_{.1}$$

$$\mathbf{v}_{.2}^f = -(1-h^f) \mathbf{C}_{22}^{*^{-1}} \left((\mathbf{C}_{21}^f - \mathbf{C}_{21}^{m^2}) \mathbf{v}_{.1} + \left(\mathbf{C}_{22}^f - \mathbf{C}_{22}^{m^2} - \frac{1}{1-h^f} \mathbf{C}_{22}^* \right) \mathbf{v}_{.2} - (1-w^f) (\mathbf{C}_{23}^f - \mathbf{C}_{23}^{m^2}) \hat{\mathbf{C}}_{33}^{*^{-1}} \left((\hat{\mathbf{C}}_{31} - \mathbf{C}_{31}^{m^1}) \mathbf{v}_{.1} + (\hat{\mathbf{C}}_{32} - \mathbf{C}_{32}^{m^1}) \mathbf{v}_{.2} + \left(\hat{\mathbf{C}}_{33} - \mathbf{C}_{33}^{m^1} - \frac{1}{1-w^f} \hat{\mathbf{C}}_{33}^* \right) \mathbf{v}_{.3} \right) \right)$$

$$\mathbf{v}_{.3}^f = -(1-w^f) \hat{\mathbf{C}}_{33}^{*^{-1}} \left((\hat{\mathbf{C}}_{31} - \mathbf{C}_{31}^{m^1}) \mathbf{v}_{.1} + (\hat{\mathbf{C}}_{32} - \mathbf{C}_{32}^{m^1}) \mathbf{v}_{.2} + \left(\hat{\mathbf{C}}_{33} - \mathbf{C}_{33}^{m^1} - \frac{1}{1-w^f} \hat{\mathbf{C}}_{33}^* \right) \mathbf{v}_{.3} \right) \quad (51)$$

$$\mathbf{v}_{.1}^{m^1} = \mathbf{v}_{.1}$$

$$\mathbf{v}_{.2}^{m^1} = \mathbf{v}_{.2}$$

$$\mathbf{v}_{.3}^{m^1} = w^f \hat{\mathbf{C}}_{33}^{*^{-1}} \left((\hat{\mathbf{C}}_{31} - \mathbf{C}_{31}^{m^1}) \mathbf{v}_{.1} + (\hat{\mathbf{C}}_{32} - \mathbf{C}_{32}^{m^1}) \mathbf{v}_{.2} + \left(\hat{\mathbf{C}}_{33} - \mathbf{C}_{33}^{m^1} + \frac{1}{w^f} \hat{\mathbf{C}}_{33}^* \right) \mathbf{v}_{.3} \right) \quad (52)$$

$$\mathbf{v}_{.1}^{m^2} = \mathbf{v}_{.1}$$

$$\mathbf{v}_{.2}^{m^2} = h^f \mathbf{C}_{22}^{*^{-1}} \left((\mathbf{C}_{21}^f - \mathbf{C}_{21}^{m^2}) \mathbf{v}_{.1} + \left(\mathbf{C}_{22}^f - \mathbf{C}_{22}^{m^2} + \frac{1}{h^f} \mathbf{C}_{22}^* \right) \mathbf{v}_{.2} - (1-w^f) (\mathbf{C}_{23}^f - \mathbf{C}_{23}^{m^2}) \hat{\mathbf{C}}_{33}^{*^{-1}} \left((\hat{\mathbf{C}}_{31} - \mathbf{C}_{31}^{m^1}) \mathbf{v}_{.1} + (\hat{\mathbf{C}}_{32} - \mathbf{C}_{32}^{m^1}) \mathbf{v}_{.2} + \left(\hat{\mathbf{C}}_{33} - \mathbf{C}_{33}^{m^1} - \frac{1}{1-w^f} \hat{\mathbf{C}}_{33}^* \right) \mathbf{v}_{.3} \right) \right)$$

$$\mathbf{v}_{.3}^{m^2} = -(1-w^f) \hat{\mathbf{C}}_{33}^{*^{-1}} \left((\hat{\mathbf{C}}_{31} - \mathbf{C}_{31}^{m^1}) \mathbf{v}_{.1} + (\hat{\mathbf{C}}_{32} - \mathbf{C}_{32}^{m^1}) \mathbf{v}_{.2} + \left(\hat{\mathbf{C}}_{33} - \mathbf{C}_{33}^{m^1} - \frac{1}{1-w^f} \hat{\mathbf{C}}_{33}^* \right) \mathbf{v}_{.3} \right) \quad (53)$$

5.3. Average constitutive model

By examination of the entries in the matrices given by Eqs. (39) and (48) it was observed that the models did not result

156

S.P.H. Skovsgaard, H.M. Jensen / International Journal of Solids and Structures 139–140 (2018) 150–162

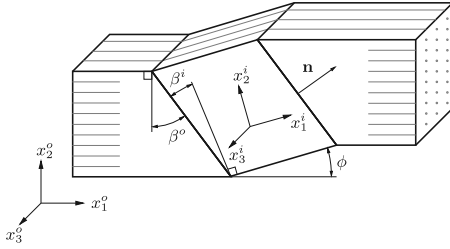


Fig. 6. Geometric representation of kink band formation.

in transverse isotropic moduli. An average of the two models was observed to give the wanted transverse isotropic properties

$$\mathbf{C}_{ij} = \frac{1}{2} (\mathbf{C}_{ij}^f + \mathbf{C}_{ij}^m) \quad (54)$$

The constitutive expression shown above is the key expression proposed for three-dimensional simulations. In addition, the velocity gradients for the constituents should be the average quantities based on Eqs. (42)–(44) and (51)–(53)

$$\mathbf{v}_{ij}^c = \frac{1}{2} (\mathbf{v}_{ij}^{c(1)} + \mathbf{v}_{ij}^{c(2)}) \quad (55)$$

If the length scale w^f is set to unity in the first, second and average constitutive equation, given by Eqs. (39), (48) and (54), then the constitutive equations simplifies to

$$\mathbf{C}_{ij} = c^f \mathbf{C}_{ij}^f + c^m \mathbf{C}_{ij}^m - c^f c^m (\mathbf{C}_{12}^f - \mathbf{C}_{12}^m) \mathbf{C}_{22}^{-1} (\mathbf{C}_{2j}^f - \mathbf{C}_{2j}^m) \quad (56)$$

where the equality given by Eq. (2) is used. The matrix \mathbf{C}_{22}^m is given by Eq. (46). The latter constitutive equation has similarities with the formulation derived by Christoffersen and Jensen (1996), where in their formulation the free index i, j varies between the integers 1 and 2 and their matrices \mathbf{C}_{ij}^m have dimensions 2×2 and not 3×3 as in the present study.

6. Localization of deformation

To validate the constitutive equation given by Eq. (54), a kink band simulation is set-up. The analysis is created as a numerical simulation similar to the one done by Jensen and Christoffersen (1997) with some changes in the formulation to account for the three-dimensional boundary conditions.

In the analysis, two composite states are introduced: A material inside the kink band and a surrounding base material as illustrated in Fig. 6. In the figure $(\cdot)^o$ represents quantities associated with the outer base material and $(\cdot)^i$ is associated with the material inside the kink band. The relative rotation of the fibres within the kink band is given by the angle ϕ . The rotated fibres are located in a localized band with an outward normal \mathbf{n} . The angle between the first axis x_1^o of the base material and the outward normal \mathbf{n} is given by β^o and the angle β^i is the angle from the first axis of the inner material x_1^i to the normal.

To compare the analysis with the two-dimensional simulation done by Jensen and Christoffersen (1997) the third axis x_3^o and x_3^i coincide initially and during the simulation. This is done for the purpose of illustration, and is not a restriction in general. The outward normal \mathbf{n} lies in the $x_1^o - x_2^o$ plane which entails that it also lies in the $x_1^i - x_2^i$ plane. The angle ϕ is formed during the simulation either by bifurcation (for $\phi_0 = 0$) or as a consequence of an initial imperfection ϕ_0 . The simulation is performed by prescribing

either a stress- or velocity gradient increment and the rest of the unknown quantities can be calculated based on equilibrium and displacement continuities across the localized band. The velocity gradients $v_{i,j}^o$ and $v_{i,j}^i$ need to be fully determined for every increment, this is a total of 18 velocity gradients, therefore 18 equations are to be determined.

In Jensen and Christoffersen (1997) two different formulations for the simulation were introduced. One where the coordinate systems followed the rotation of the fibres during an increment, and a second where the coordinate system inside the kink band was stationary during the increment. The two formulations were shown to give identical results. In the current simulation, the first approach is adapted due to its convenience when implemented in a numerical scheme. When the coordinate systems rotate, with the fibres, this entails

$$v_{2,1}^o = v_{2,1}^i = 0 \quad (57)$$

the velocity gradient $v_{2,1}$ represents the rotation of the fibres and since the coordinate systems rotates with the fibres no relative rotation is seen. In a coordinate system that initially coincides with the band coordinate system but stays stationary during an increment, seen from the outer coordinate system, has the velocity gradients $v_{i,j}^o + \Omega_{ij}$. Here, Ω_{ij} is the relative spin tensor between the band and base material, where

$$\Omega_{21} = -\Omega_{12} = \dot{\phi} \quad (58)$$

and all other components of Ω_{ij} are zero. The quantity $\dot{\phi}$ is the relative spin increment. In the simulation, $\dot{\phi}$ will be a prescribed quantity and based on this increment, the velocity gradients and stresses are to be determined. To ensure continuity across the band, the second-order tensors (tractions and velocity gradients) need to be rotated into a common coordinate system. The tensors R_{ij}^o and R_{ij}^i are introduced which gives the directional cosines into a common coordinate system where their first axis will coincide with the outward normal \mathbf{n} . The components of the rotation tensor R_{ij}^o can be illustrated in a matrix format

$$\begin{pmatrix} R_{11}^o & R_{12}^o & R_{13}^o \\ R_{21}^o & R_{22}^o & R_{23}^o \\ R_{31}^o & R_{32}^o & R_{33}^o \end{pmatrix} = \begin{pmatrix} \cos(\beta^o) & \sin(\beta^o) & 0 \\ -\sin(\beta^o) & \cos(\beta^o) & 0 \\ 0 & 0 & 1 \end{pmatrix} \quad (59)$$

where the orientation β^o is shown in Fig. 6. The calculation of R_{ij}^i is equivalent using the orientation β^i . Displacement continuity across the band entails six equations

$$\begin{aligned} (v_{i,j}^i + \Omega_{ij}) R_{2i}^i R_{2j}^i &= v_{i,j}^o R_{2i}^o R_{2j}^o & (v_{i,j}^i + \Omega_{ij}) R_{3i}^i R_{3j}^i &= v_{i,j}^o R_{3i}^o R_{3j}^o \\ (v_{i,j}^i + \Omega_{ij}) R_{1i}^i R_{2j}^i &= v_{i,j}^o R_{1i}^o R_{2j}^o & (v_{i,j}^i + \Omega_{ij}) R_{1i}^i R_{3j}^i &= v_{i,j}^o R_{1i}^o R_{3j}^o \\ (v_{i,j}^i + \Omega_{ij}) R_{3i}^i R_{2j}^i &= v_{i,j}^o R_{3i}^o R_{2j}^o & (v_{i,j}^i + \Omega_{ij}) R_{2i}^i R_{3j}^i &= v_{i,j}^o R_{2i}^o R_{3j}^o \end{aligned} \quad (60)$$

The first two equations are stretching continuities of the material on the kink band plane. The third and fourth equation are continuities of the band plane rotation. The last two equation describe the shear strain and rotation of the material on the kink band plane. Continuity of tractions entails three equations

$$\begin{aligned} C_{ijkl}^i (v_{i,k}^i + \Omega_{ik}) R_{1i}^i R_{1j}^i &= C_{ijkl}^o v_{i,k}^o R_{1i}^o R_{1j}^o \\ C_{ijkl}^i (v_{i,k}^i + \Omega_{ik}) R_{1i}^i R_{2j}^i &= C_{ijkl}^o v_{i,k}^o R_{1i}^o R_{2j}^o \\ C_{ijkl}^i (v_{i,k}^i + \Omega_{ik}) R_{1i}^i R_{3j}^i &= C_{ijkl}^o v_{i,k}^o R_{1i}^o R_{3j}^o \end{aligned} \quad (61)$$

Where the first equation is the force normal to the band plane and the last two equations are shear stresses. In the simulations done by Jensen and Christoffersen (1997), different boundary conditions were investigated including plane stress, plane strain, no $\dot{\sigma}_{22}$ increments and no $v_{2,2}^o$ velocity gradient. The simulations are performed

with plane strain condition and unless stated otherwise, $\sigma_{22}^o = 0$, which entails the boundary condition

$$\dot{\sigma}_{22}^o = 0 \quad (62)$$

Some simulations are performed with biaxial loading e.g. combined σ_{11} and σ_{22} stresses. In those simulations the biaxial loading ratio, ρ , is introduced

$$\rho = \frac{\dot{\sigma}_{22}^o}{\dot{\sigma}_{11}^o} \quad (63)$$

In the simulations with biaxial loading the boundary condition

$$\dot{\sigma}_{22}^o - \rho \dot{\sigma}_{11}^o = 0 \quad (64)$$

is used. Furthermore, simulations with combined compression and shear stresses in the base material are performed, where the loading ratio, ψ , is introduced

$$\psi = \frac{\dot{\sigma}_{12}^o}{\dot{\sigma}_{11}^o} \quad (65)$$

together with the boundary condition

$$\dot{\sigma}_{12}^o - \psi \dot{\sigma}_{11}^o = 0 \quad (66)$$

The rate of Cauchy stress for the composite can be calculated based on the nominal stress rates and the velocity gradients using

$$\dot{\sigma}_{ij} = C_{ijkl} v_{l,k} - \sigma_{ij} v_{k,k} + v_{i,k} \sigma_{kj} \quad (67)$$

Furthermore, five boundary conditions are applied to the base material to obtain plan strain conditions

$$\begin{aligned} v_{3,1}^o &= 0, & v_{3,2}^o &= 0, & v_{1,3}^o &= 0 \\ v_{2,3}^o &= 0, & v_{3,3}^o &= 0 \end{aligned} \quad (68)$$

Using the continuity- and boundary conditions presented, the velocity gradients and stresses can be calculated for the base and band material numerically. The relative rotation of the kink band is updated according to

$$\dot{\beta}^o = -v_{i,j}^o R_{11}^o R_{2j}^o \quad \dot{\beta}^i = -v_{i,j}^i R_{11}^i R_{2j}^i \quad (69)$$

In line with the formulation done by Jensen and Christoffersen (1997), the fibre volume fraction c^f inside and outside the kink band is different. The number of fibres penetrating a unit area $A = A^f/c^f$ of an arbitrary section with the unit normal n_i is

$$N = n_i e_i \frac{c^f}{A^f} \quad (70)$$

where e_i is a unit vector parallel with the fibres, A^f is the area of a single fibre. In any region not containing fibre ends the latter equation entails

$$n_i^o e_i^o \frac{c^{fo}}{A^{fo}} = n_i^i e_i^i \frac{c^{fi}}{A^{fi}} \quad (71)$$

Based on the latter equation the volume fraction inside the band can be determined based on the volume fraction in the base material. The length scales w^f and h^f are updated according to

$$\begin{aligned} \dot{h}^f &= h^f (1 - h^f) (v_{2,2}^f - v_{2,2}^{m2}) \\ \dot{w}^f &= w^f (1 - w^f) (v_{3,3}^f - v_{3,3}^{m3}) \end{aligned} \quad (72)$$

Jensen and Christoffersen (1997) used a similar formulation with the main difference that two length scales w^f and h^f are needed in the current formulation.

7. Elastic-plastic behaviour of the constituents

In Jensen (1999) three constitutive formulations for the incremental stiffness tensor L_{ijkl}^c for the constituents were compared.

Only small differences were seen in the post-buckling regime between the formulations. The Stören and Rice (1975) version of J_2 -deformation theory is presently adapted for all constituents. The formulation is outlined here for completeness. The components of the tensor of instantaneous moduli are given by

$$L_{ijkl} = G_s (\delta_{ik} \delta_{jl} + \delta_{il} \delta_{jk}) + \left(K - \frac{2}{3} G_s \right) \delta_{ij} \delta_{kl} - \frac{4}{3} (G_s - G_t) m_{ij} m_{kl} \quad (73)$$

m_{ij} is given in terms of Cauchy stresses

$$m_{ij} = \frac{1}{2\sigma_{eq}} \left(\sigma_{ij} - \frac{1}{3} \delta_{ij} \sigma_{kk} \right) \quad (74)$$

where σ_{eq} is the equivalent von Mises stress

$$\sigma_{eq} = \sqrt{\frac{3}{2} \sigma_{ij} \sigma_{ij} - \frac{1}{2} \sigma_{ii} \sigma_{jj}} \quad (75)$$

The remaining terms introduced in Eq. (73) is the bulk modulus, K , the secant shear modulus, G_s , and the tangent shear modulus, G_t . The two latter moduli can be calculated based on the secant and tangent moduli E_s and E_t

$$\frac{1}{G_s} = \frac{3}{E_s} - \frac{1-2\nu}{E} \quad \frac{1}{G_t} = \frac{1}{E_t} - \frac{1-2\nu}{E} \quad K = \frac{E}{3(1-2\nu)} \quad (76)$$

where ν is Poisson's ratio and E is Young's modulus. The nonlinear relationship between the equivalent uniaxial logarithmic strain ε_{eq} and equivalent uniaxial stress σ_{eq} is given by a Ramberg-Osgood relation

$$\varepsilon_{eq} = \frac{\sigma_{eq}}{E} + \frac{3\sigma_y}{7E} \left(\frac{\sigma_{eq}}{\sigma_y} \right)^n \quad (77)$$

where σ_y is a reference yield stress and n is a hardening exponent. Both the secant modulus E_s and tangent modulus E_t can be determined based on the Ramberg-Osgood curve using the relations

$$\frac{1}{E_s} = \frac{\varepsilon_{eq}}{\sigma_{eq}} \quad \frac{1}{E_t} = \frac{\partial \varepsilon_{eq}}{\partial \sigma_{eq}} \quad (78)$$

8. Numerical scheme

The steps required in the numerical scheme are presented in this section. The relative spin increment ϕ is prescribed. The simulation goes from an initial fibre imperfection ϕ_0 to an end rotation ϕ decided by the user. The following steps are required in every increment:

1. Update instantaneous moduli for the constituents L_{ijkl}^c using Eq. (73).
2. Calculate nominal moduli for the constituents C_{ijkl}^c using Eq. (13).
3. Form the matrices C_{ij}^c for the constituents based on C_{ijkl}^c so they fulfil the form $\mathbf{t}_i^c = C_{ij}^c \mathbf{v}_j^c$ given by Eq. (16).
4. Calculate the nominal moduli for the composite C_{ij} based on Eq. (54) using Eqs. (39) and (48).
5. Set-up a linear system of equations based on the 18 equations given by Eq. (57), (60), (61), (64), (66) and (68). A linear system in the form $[\mathbf{A}]\mathbf{V} = \mathbf{R}$ can be set up where \mathbf{V} is a vector containing the unknown velocity gradients for the band and base material $v_{i,j}^i, v_{i,j}^o$. The linear system is solved with respect to the unknown vector \mathbf{V} .
6. Calculate the velocity gradients for the band and base constituents $v_{i,j}^c$ based on the overall velocity gradients $v_{i,j}$ using Eqs. (42)–(44), (51)–(53) and (55).

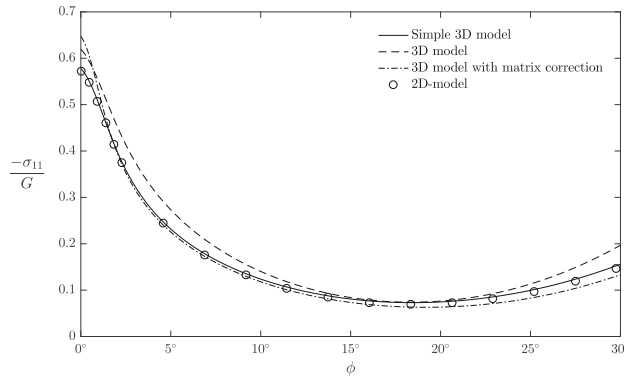


Fig. 7. Applied stress $-\sigma_{11}^a$ in base material normalised with the elastic shear modulus G , as a function of fibre rotation ϕ , shown for four different homogenized formulations. Initial imperfection $\phi_0 \approx 0^\circ$ and initial orientation $\beta_0 = 10^\circ$.

Table 1
Material parameters.

| | |
|------------------|-------|
| ν^m | 0.356 |
| σ_p^m/E^m | 0.013 |
| n^m | 4 |
| E^f/E^m | 35 |
| ν^f | 0.263 |
| σ_f^f/E^f | 0.019 |
| n^f | 1.9 |
| c^f | 0.6 |

- Update the stresses $\sigma_{ij} = \sigma_{ij} + \dot{\sigma}_{ij}$ where the stress increments $\dot{\sigma}_{ij}$ is calculated using Eq. (67).
- Update the geometric quantities β , ϕ , h^f and w^f using Eqs. (69) and (72).

9. Results

The material parameters used in the present study and also used in Jensen (1999), are taken based on experimental results on APC-2/AS4 carbon fibre composite from Kyriakides et al. (1995). The parameters are summarized in Table 1. Aligned with studies done by previous authors, then the composite behaviour is described through a rate independent J_2 -deformation theory, even though the matrix constituent is a polymer. Authors who have investigated the influence of the rate and pressure dependency in fibre-reinforced polymers include: Vogler and Kyriakides (1999a) experimentally investigated the nonlinear behaviour of AS4/PEEK under combined transverse compression and shear and they compared it with simulations with different constitutive models in Vogler and Kyriakides (1999b).

The results presented are used to investigate the performance of the present three-dimensional constitutive model.

In Figs. 7 and 8, results are shown for simulations with an initial imperfection of $\phi_0 \approx 0^\circ$ and $\phi_0 = 3^\circ$, respectively. For both simulations, the initial kink band angle is set to $\beta_0 = 10^\circ$. In the figures, four different results are presented. The first result, which is presented as a solid line, is a simplified version of the three-dimensional constitutive model, where $w^f = 1$. In the case where the length scale $w^f = 1$, the three-dimensional formulation converges towards Eq. (56). This model will be denoted the *Simple 3D model*. The results obtained by Jensen (1999) is presented as circles

and will be referred to as the *2D model*. The results obtained using the *Simple 3D model* and the *2D model* show results that coincides. The reason for the coinciding results can be explained by the simplified constitutive equation given by Eq. (56) and the similarities to the constitutive equation developed by Christoffersen and Jensen (1996). The main difference between the two mentioned constitutive equation is the size of the matrices, which is 3×3 in the present study and not 2×2 as in the equation derived by Christoffersen and Jensen.

The results obtained using the three-dimensional model given by Eq. (54) will be denoted the *3D model* which is illustrated as a dashed line. The *3D model* shows the same characteristics during deformation based on the results shown in Figs. 7 and 8. The *3D model* gives slightly higher bifurcation stress and higher stresses during deformation. The higher stresses can be explained by the slightly stiffer shear response observed in the current three-dimensional model. Several authors including Budiansky (1983), Budiansky and Fleck (1993) and Christoffersen and Jensen (1996) have shown that kink band formation is dominated by the shear response of the composite interacting with fibre misalignments. Skovsgaard and Jensen (2017) investigated the kink band response for a three-dimensional discretized finite element model and a constitutive model. In that study a comparison between the shear response was conducted initially. The matrix material was softened in the finite element model so the shear response between the models was similar. The material characteristics of the matrix material (AS4-PEEK) change during the curing process, due to this fact the matrix characteristics are in several cases predicted based on the composite response (Hsu et al., 1998; Ng et al., 2010). Since the shear response of the *3D model* and *2D model* differs, a new calibration of the material parameters of the matrix material is proposed. A fourth model is illustrated in the figures and will be referred to as the *3D model with matrix correction*. This is a model where the elastic modulus of the matrix material E^m is changed. The modulus E^m is calculated so the elastic shear response of the composite is identical to the elastic shear response of the *2D model*.

The *3D model with matrix correction* is illustrated as a dashed-dotted line. The simulations with an initial imperfection of $\phi_0 = 3^\circ$ show that the present model, where the shear response is aligned, yield results closer to the response obtained by the two-

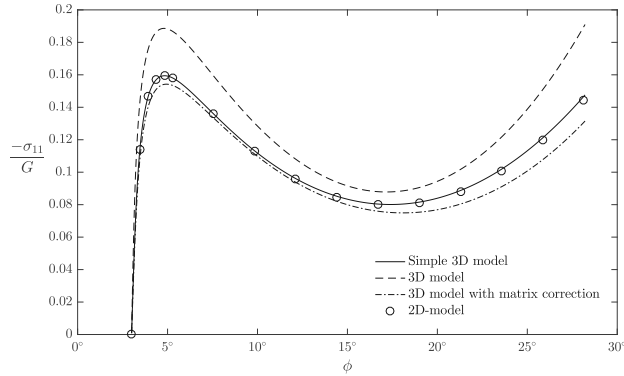


Fig. 8. Applied stress $-\sigma_{11}^a$ in base material normalised with the elastic shear modulus G , as a function of fibre rotation ϕ , shown for four different homogenized formulations. Initial imperfection $\phi_0 = 3^\circ$ and initial orientation $\beta_0 = 10^\circ$.

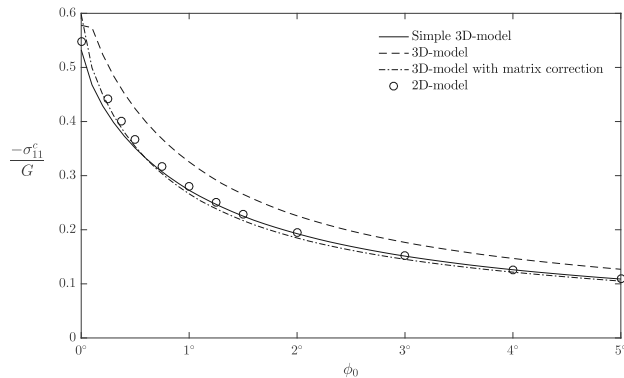


Fig. 9. Critical kink band stress $-\sigma_{11}^c$ in base material normalised with the elastic shear modulus G , versus initial imperfection ϕ_0 , shown for four different homogenized formulations. The critical stress is presented for the most critical initial kink band orientation β_0 .

dimensional model. Hsu et al. (1998) made a comparison between a two- and three-dimensional micro-mechanical kink band model where they simulated the buckling response using a finite element model in ABAQUS. They arrived at the same conclusion that the three-dimensional model showed similar response as the two-dimensional model. Equivalently, they also used different elastic-plastic parameters for the two-dimensional and three-dimensional model.

In Fig. 9, the critical stress is shown as function of the initial fibre imperfection ϕ_0 . In line with the simulations performed by Jensen and Christoffersen (1997), the critical stress is illustrated for the most critical initial kink band orientation β_0 . The *Simple 3D model*, the *3D model with matrix correction* and the *2D model* show similar results. The *3D model*, with the same material parameters as used for the two-dimensional model, shows higher critical stresses for all initial imperfections. As mentioned earlier, the in-situ material parameters of the matrix material are in several cases fitted so the overall shear response of the composite match exper-

imental data. In the current results, a simulation was created with the enhanced elastic response of the matrix material. Since kink band formation is highly sensitive to the plastic shear response (Budiansky, 1983), the elastic and plastic parameters should be calibrated to match the composite shear response for strains relevant for the simulation. In the current simulation, only the elastic parameter E^m was changed in the *3D model with matrix correction*.

Furthermore, different simulation cases have been conducted with biaxial loading (combined compression and tension and combined compression and compression) and cases of combined compression and shear with different sign of shear. In the simulations to come both the *2D model* and the *3D model with matrix correction* have been used. In Figs. 10 and 11 the normalized critical stress $-\sigma_{11}^c/G$ is shown as function of initial fibre imperfection, ϕ_0 , for different biaxial loading ratios. Fig. 10 gives the results from the *2D model* and Fig. 10 are results from the *3D model with matrix correction*.

160

S.P.H. Skovsgaard, H.M. Jensen / International Journal of Solids and Structures 139–140 (2018) 150–162

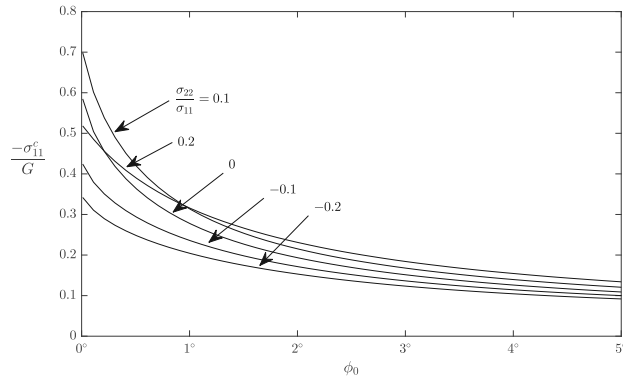


Fig. 10. Normalized critical kink band stress $-\sigma_{11}^c/G$ versus initial imperfection ϕ_0 for different ratios of biaxial loading. The critical stress is presented for the most critical initial kink band orientation β_0 . The results are generated based on the 2D-model.

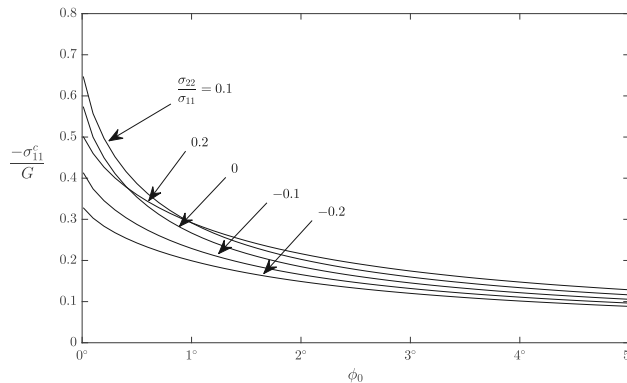


Fig. 11. Normalized critical kink band stress $-\sigma_{11}^c/G$ versus initial imperfection ϕ_0 for different ratios of biaxial loading. The critical stress is presented for the most critical initial kink band orientation β_0 . The results are generated based on the 3D-model with matrix correction.

Positive values of the biaxial loading ratio, $\sigma_{22}^o/\sigma_{11}^o > 0$, represents a case of combined compression and compression. With the current material parameters, then the loading ratio $\sigma_{22}^o/\sigma_{11}^o = 0.1$ leads to an increase in the critical stress for all imperfection angles compared to the case of $\sigma_{22} = 0$. The loading ratio $\sigma_{22}^o/\sigma_{11}^o = 0.2$ leads to a reduction in the critical stress for imperfection angles $\phi_0 < 1^\circ$, which is due to matrix yielding due to the increased stress level. In all cases of combined compression and tension, e.g. $\sigma_{11} < 0$ and $\sigma_{22} > 0$, a decrease in the critical stress is obtained. The current findings are in line with the analytical expression for kink band bifurcation found by Christoffersen and Jensen (1996) and Slaughter et al. (1993). By comparing the results obtained using the two-dimensional and three-dimensional constitutive model then good correlation is seen.

The critical stress as function of initial fibre imperfection in the case of combined compression and shear is shown in Figs. 12 and 13. Fig. 11 shows the results from the 2D model and Fig. 13 gives

the results obtained from the 3D model with matrix correction. The boundary condition $\dot{\sigma}_{22}^o = 0$ is used in the simulations including shear stresses in the base material.

For fibre imperfections $\phi_0 > 1^\circ$ a clear tendency is seen between the critical stresses and the compression-shear ratio. Positive ratios $\sigma_{12}^o/\sigma_{11}^o > 0$ lead to an increase in the critical compressive stress, e.g. negative shear stresses $\sigma_{12}^o < 0$. The result that negative shear stresses increase the compressive strength is in line with the expression derived in Christoffersen and Jensen (1996). For small fibre imperfections a cross-over is seen between the results with positive ratios $\sigma_{12}^o/\sigma_{11}^o > 0$ e.g. the bifurcation stress for $\sigma_{12}^o/\sigma_{11}^o = 0.02$ is smaller than in the case of pure compression. The yield surface is based on a von Mises yield criterion and the equivalent von Mises stress is higher in the case combined compression and shear. It has been observed that very small positive ratios (e.g. $\sigma_{12}^o/\sigma_{11}^o = 0.001$) will lead to an infinitesimal increase in bifurcation stress, but this is not shown in the figure.

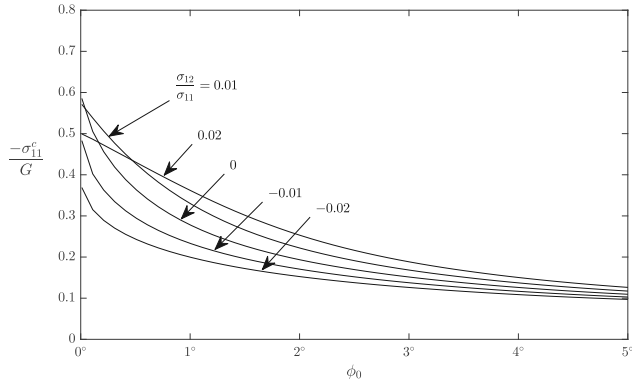


Fig. 12. Normalized critical kink band stress $-\sigma_{11}^c/G$ versus initial imperfection ϕ_0 for different ratios of combined compression and shear. The critical stress is presented for the most critical initial kink band orientation β_0 . The results are generated based on the 2D-model.

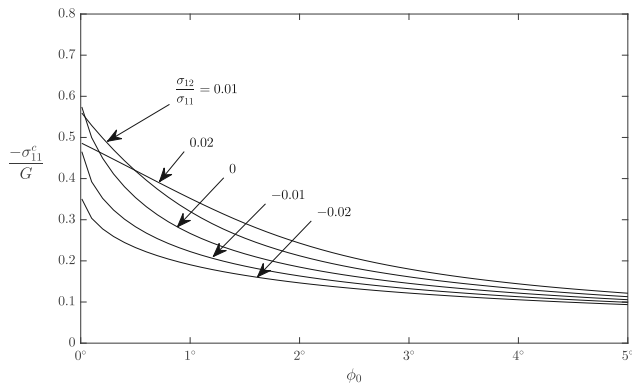


Fig. 13. Normalized critical kink band stress $-\sigma_{11}^c/G$ versus initial imperfection ϕ_0 for different ratios of combined compression and shear. The critical stress is presented for the most critical initial kink band orientation β_0 . The results are generated based on the 3D-model with matrix correction.

By comparing Figs. 10 and 11 for biaxial loading and by comparing Figs. 12 and 13 for combined compression and shear, these results further validates the present three-dimensional constitutive model.

10. Conclusion

A three-dimensional constitutive model has been proposed which give the material response of a fibre-reinforced composite in a general framework. The model is based on independent constitutive relations for the constituents where the constituents can behave either elastic or elastic-plastic. The model is formulated in a rate form using nominal stress rates and velocity gradients which gives the model opportunity to be used in the finite strain regime with large deformations and rotations. The present paper emphasises the derivations behind the model, where homogenizations are based on continuum mechanical continuities and averages. The

constitutive model is built up using three material blocks: one fibre and two matrix.

The current constitutive model can be used to predict strain localization of fibre composites including the localization phenomenon known as kink band formation. The constitutive model is used in a simple kink band simulation where the response is compared with results obtained by previous authors. Similar results for plane strain are observed in the post-buckling regime when comparing the constitutive models. The critical stress is seen to be sensitive to fibre imperfections and to the shear response of the composite which is consistent with previously published results. The same elastic-plastic parameters are used for the present three-dimensional model and higher stresses are observed in general. The higher stresses observed, can be explained by the stiffer shear response in the present model. The three-dimensional effects from the constitutive model due not alter the critical values predicted by previous two-dimensional models when the shear responses for the two models are aligned with the present bound-

162

S.P.H. Skovsgaard, H.M. Jensen / International Journal of Solids and Structures 139–140 (2018) 150–162

ary conditions. This is consistent with conclusions done by other authors (Hsu et al., 1998), who have compared three-dimensional and two-dimensional models. To fit the full elastic-plastic shear response of the proposed constitutive model to experimental data has not been in the scope of the current research. Instead, focus is given to the overall tendencies and performance of a new three-dimensional constitutive model.

The simulations performed verifies the derived three-dimensional constitutive model. The current infinite kink band simulation only includes plane strain conditions and in-plane rotations. Future simulations can include three-dimensional effects e.g. deformation out-of-plane and inclined kink bands through thickness in a similar set-up.

Acknowledgement

This work was supported by the Thomas B. Thriges fund.

Appendix A. Velocity gradients \mathbf{v}_2^a

Noting Eqs. (16) and (17) together with Eq. (19) yields

$$\mathbf{C}_{21}^a \mathbf{v}_1 + \mathbf{C}_{22}^a \mathbf{v}_2 + \mathbf{C}_{23}^a \mathbf{v}_3 = \mathbf{C}_{21}^b \mathbf{v}_1 + \mathbf{C}_{22}^b \mathbf{v}_2 + \mathbf{C}_{23}^b \mathbf{v}_3 \quad (\text{A.1})$$

Isolating the term related \mathbf{v}_2^b

$$\mathbf{C}_{22}^b \mathbf{v}_2 = (\mathbf{C}_{21}^a - \mathbf{C}_{21}^b) \mathbf{v}_1 + \mathbf{C}_{22}^a \mathbf{v}_2 + (\mathbf{C}_{23}^a - \mathbf{C}_{23}^b) \mathbf{v}_3 \quad (\text{A.2})$$

Using the equality given by Eq. (18) and isolating the term related to \mathbf{v}_2^b yields

$$\mathbf{c}^b \mathbf{v}_2 = \mathbf{v}_2 - \mathbf{c}^a \mathbf{v}_2^a \quad (\text{A.3})$$

Multiplying the latter equation with \mathbf{C}_{22}^b yields

$$\mathbf{c}^b \mathbf{C}_{22}^b \mathbf{v}_2 = \mathbf{C}_{22}^b \mathbf{v}_2 - \mathbf{c}^a \mathbf{C}_{22}^b \mathbf{v}_2^a \quad (\text{A.4})$$

Comparing the equation with Eq. (A.2) yields

$$\mathbf{c}^b (\mathbf{C}_{21}^a - \mathbf{C}_{21}^b) \mathbf{v}_1 + \mathbf{c}^b \mathbf{C}_{22}^a \mathbf{v}_2 + \mathbf{c}^b (\mathbf{C}_{23}^a - \mathbf{C}_{23}^b) \mathbf{v}_3 = \mathbf{C}_{22}^b \mathbf{v}_2 - \mathbf{c}^a \mathbf{C}_{22}^b \mathbf{v}_2^a \quad (\text{A.5})$$

Isolating the term \mathbf{v}_2^a yields

$$\begin{aligned} & (\mathbf{c}^a \mathbf{C}_{22}^b + \mathbf{c}^b \mathbf{C}_{22}^a) \mathbf{v}_2^a \\ & = -\mathbf{c}^b (\mathbf{C}_{21}^a - \mathbf{C}_{21}^b) \mathbf{v}_1 + \mathbf{C}_{22}^b \mathbf{v}_2 - \mathbf{c}^b (\mathbf{C}_{23}^a - \mathbf{C}_{23}^b) \mathbf{v}_3 \end{aligned} \quad (\text{A.6})$$

Introducing the matrix \mathbf{C}_{22}^c

$$\mathbf{C}_{22}^c = \mathbf{c}^a \mathbf{C}_{22}^b + \mathbf{c}^b \mathbf{C}_{22}^a \quad (\text{A.7})$$

The velocity gradients \mathbf{v}_2^a can be calculated as

$$\mathbf{v}_2^a = -\mathbf{c}^b \mathbf{C}_{22}^{c-1} \left((\mathbf{C}_{21}^a - \mathbf{C}_{21}^b) \mathbf{v}_1 - \frac{1}{\mathbf{c}^b} \mathbf{C}_{22}^b \mathbf{v}_2 + (\mathbf{C}_{23}^a - \mathbf{C}_{23}^b) \mathbf{v}_3 \right) \quad (\text{A.8})$$

In a similar manner the velocity gradients \mathbf{v}_2^b can be determined as

$$\mathbf{v}_2^b = \mathbf{c}^a \mathbf{C}_{22}^{c-1} \left((\mathbf{C}_{21}^a - \mathbf{C}_{21}^b) \mathbf{v}_1 + \frac{1}{\mathbf{c}^a} \mathbf{C}_{22}^a \mathbf{v}_2 + (\mathbf{C}_{23}^a - \mathbf{C}_{23}^b) \mathbf{v}_3 \right) \quad (\text{A.9})$$

It is convenient to rewrite the velocity gradients to the form presented in Eq. (21).

References

Budiansky, B., 1983. Micromechanics. *Comput. Struct.* 16 (1–4), 3–12. doi:10.1016/0045-7949(83)90141-4.
 Budiansky, B., Fleck, N., 1993. Compressive failure of fibre composites. *J. Mech. Phys. Solids* 41 (1), 183–211. doi:10.1016/0022-5096(93)90068-Q.
 Christoffersen, J., Jensen, H.M., 1996. Kink band analysis accounting for the microstructure of fiber reinforced materials. *Mech. Mater.* 24 (4), 305–315. doi:10.1016/S0167-6636(96)00052-X.

Fleck, N.A., Shu, J.Y., 1995. Microbuckle initiation in fibre composites: affine element study. *J. Mech. Phys. Solids* 43 (12), 1887–1918. doi:10.1016/0022-5096(95)00057-P.
 Granddier, J.C., Ferron, G., Potier-Ferry, M., 1992. Microbuckling and strength in long-fiber composites: theory and experiments. *Int. J. Solids Struct.* 29 (14–15), 1753–1761. doi:10.1016/0020-7683(92)90168-5.
 Gutkin, R., Costa, S., Olsson, R., 2016. A physically based model for kink-band growth and longitudinal crushing of composites under 3D stress states accounting for friction. *Compos. Sci. Technol.* doi:10.1016/j.compscitech.2016.09.002.
 Gutkin, R., Pinho, S.T., 2015. Combining damage and friction to model compressive damage growth in fibre reinforced composites. *J. Compos. Mater.* 49 (20), 2183–2495. doi:10.1177/0021998314549614.
 Guynn, E.G., Ochoa, O.O., Bradley, W.L., 1992. A parametric study of variables that affect fiber microbuckling initiation in composite laminates: part I—analyses. *J. Compos. Mater.* 26 (11), 1594–1616. doi:10.1177/002199839202601103.
 Hsu, S.-Y., Vogler, T., Kyriakides, S., 1999. On the axial propagation of kink bands in fiber composites: part I experiments. *Int. J. Solids Struct.* 36, 575–595. doi:10.1016/S0020-7683(98)00030-4.
 Hsu, S.-Y., Vogler, T., Kyriakides, S., 1999. On the axial propagation of kink bands in fiber composites: part II analysis. *Int. J. Solids Struct.* 36, 575–595. doi:10.1016/S0020-7683(98)00030-4.
 Hsu, S.-Y., Vogler, T.J., Kyriakides, S., 1998. Compressive strength predictions for fiber composites. *J. Appl. Mech.* 65 (1), 7. doi:10.1115/1.2789050.
 Jensen, H.M., 1999. Analysis of compressive failure of layered materials by kink band broadening. *Int. J. Solids Struct.* 36 (23), 3427–3441. doi:10.1016/S0020-7683(98)00158-9.
 Jensen, H.M., 2002. Residual stress effects on the compressive strength of uni-directional fibre composites. *Acta Mater.* 50, 2895–2904. doi:10.1016/S1359-6464(02)00114-3.
 Jensen, H.M., Christoffersen, J., 1997. Kink band formation in fiber reinforced materials. *J. Mech. Phys. Solids* 45 (7), 1121–1136. doi:10.1016/S0022-5096(96)00126-3.
 Kyriakides, S., Arseculeratne, R., Perry, E.J., Liechti, K.M., 1995. On the compressive failure of fiber reinforced composites. *Int. J. Solids Struct.* 32 (6–7), 689–738. doi:10.1016/0020-7683(94)00157-R.
 Liu, G., Thouless, M.D., Deshpande, V.S., Fleck, N.A., 2014. Collapse of a composite beam made from ultra high molecular-weight polyethylene fibres. *J. Mech. Phys. Solids* 63 (1), 320–335. doi:10.1016/j.jmps.2013.08.021.
 Naya, F., Herraiz, M., Gonzalez, C., Lopes, C., der Veen, S.V., Pons, F., 2017. Computational micromechanics of fiber kinking in unidirectional FRP under different environmental conditions. *Compos. Sci. Technol.* 144, 26–35. doi:10.1016/j.compscitech.2017.03.014.
 Ng, W.H., Salvi, A.G., Waas, A.M., 2010. Characterization of the in-situ non-linear shear response of laminated fiber-reinforced composites. *Compos. Sci. Technol.* 70 (7), 1126–1134. doi:10.1016/j.compscitech.2010.02.024.
 Nizolek, T., Begley, M., McCabe, R., Avallone, J., Mara, N., Beyerlein, I., Pollock, T., 2017. Strain fields induced by kink band propagation in Cu-Nb nanolaminate composites. *Acta Mater.* 133, 303–315. doi:10.1016/j.actamat.2017.04.050.
 Poullos, K., Nirdson, C.F., 2016. Homogenization of long fiber reinforced composites including fiber bending effects. *J. Mech. Phys. Solids* 94, 433–452. doi:10.1016/j.jmps.2016.04.010.
 Romanowicz, M., 2013. Initiation of kink bands from regions of higher misalignment in carbon fiber-reinforced polymers. *J. Compos. Mater.* 0 (0), 1–13. doi:10.1177/0021998313498106.
 Rosen, B.W., 1965. Mechanics of Composite Strengthening in: *Fiber Composite Materials*. American Society for Metals, Metals Park, OH, pp. 37–75.
 Skovsgaard, S.P.H., Jensen, H.M., 2017. Constitutive model for imperfectly bonded fibre-reinforced composites. *Compos. Struct.* 192, 82–92.
 Slaughter, W.S., Fleck, N.A., Budiansky, B., 1993. Compressive failure of fibre composites: the roles of multi-axial loading and creep. *J. Eng. Mater. Technol.* 115 (3), 308–313.
 Støren, S., Rice, J.R., 1975. Localized necking in thin sheets. *J. Mech. Phys. Solids* 23 (6), 421–441. doi:10.1016/0022-5096(75)90004-6.
 Vogler, T., Hsu, S.-Y., Kyriakides, S., 2001. On the initiation and growth of kink bands in fiber composites. Part II: analysis. *Int. J. Solids Struct.* 38 (15), 2653–2682. doi:10.1016/S0020-7683(00)00175-X.
 Vogler, T.J., Hsu, S.Y., Kyriakides, S., 2001. On the initiation and growth of kink bands in fiber composites. Part I: experiments. *Int. J. Solids Struct.* 38 (15), 2653–2682. doi:10.1016/S0020-7683(00)00175-X.
 Vogler, T.J., Kyriakides, S., 1999. Inelastic behavior of an AS4 / PEEK composite under combined transverse compression and shear. Part I: experiments 15 (8), 807–836.
 Vogler, T.J., Kyriakides, S., 1999. Inelastic behavior of an AS4 / PEEK composite under combined transverse compression and shear. Part II: modeling 15.
 Wade, M.A., Hunt, G.W., Peletier, M.A., 2004. Kink band instability in layered structures. *J. Mech. Phys. Solids* 52 (5), 1071–1091. doi:10.1016/j.jmps.2003.09.026.
 Wind, J.L., Steffensen, S., Jensen, H.M., 2014. Comparison of a composite model and an individually fiber and matrix discretized model for kink band formation. *Int. J. Non-Linear Mech.* 67, 319–325. doi:10.1016/j.jnonlinmec.2014.10.005.
 Zhang, L., Zhang, S., Jiang, Y., Tao, J., Chen, X., 2016. Compressive behaviour of fibre reinforced plastic with random fibre packing and a region of fibre waviness. *J. Reinf. Plast. Compos.* doi:10.1177/0731684416674070.
 Zhou, H.W., Yi, H.Y., Gao, L.L., Dai, G.M., Peng, R.D., Wang, H.W., Mishnaevsky, L., 2013. Compressive damage mechanism of GFRP composites under off-axis loading: experimental and numerical investigations. *Compos. Part B* 55, 119–127. doi:10.1016/j.compositesb.2013.06.007.

Chapter 7

P2

Constitutive model for imperfectly bonded fibre-reinforced composites

7.1 Motivation

The behaviour and failure of fibre composites are influenced by the fibre-to-matrix interfacial bonding. Imperfect fibre/matrix bonding will inevitably be present and can be influenced by the fibre treatment when producing the fibres (different sizing). One way of including the behaviour of the interface properties, when doing simulations, is by using a three-dimensional discrete FE-model including interfacial behaviour through e.g. cohesive elements and contact constraints as explained in Section 2.5. The use of micro-mechanical models (discrete models) become inexpedient compared to homogenised constitutive models when advanced fibre layups or complex geometries are considered.

The present publication introduces a novel two-dimensional constitutive formulation that includes information about imperfect fibre-to-matrix bonding, that can be used in a general elastic-plastic framework. The constitutive model is used to study kink band formation that is formed by bifurcation or due to the presence of initial geometric fibre imperfections. The original source of the publication is: (Skovsgaard and Jensen, 2018a).

7.2 Method

The thoughts and theory behind the formulation are described in Chapter 3 and the essence is repeated here for completeness. In the case of perfect bonding, the homogenised properties are based on the assumptions that

- Material lines parallel with the fibres are subject to a common stretching and rotation.
- Planes parallel with the fibres transmit identical tractions.
- The material of the constituents is elastic or elastic plastic.

In the other extreme case of complete debonding, the model assumes that the transverse and shear behaviour is dominated by the matrix properties as if the fibres were not present. The formulation includes a parameter μ taking values between zero and one. Where a value $\mu = 1$ is perfect bonding and $\mu = 0$ is no bonding. The developed constitutive formulation is used together with a semi-analytical kink band model described in Section 3.4, and was solved using Fortran 77. Furthermore, a three-dimensional finite element model was developed that includes different amounts of fibre-to-matrix bonding. The FE-model was developed to investigate the influence of fibre/matrix bonding and to validate the homogenised constitutive formulation.

7.3 Contribution

The contributions to the publication comprise: the development of a novel constitutive formulation including information about fibre/matrix bonding; development of a three-dimensional unit cell finite element model; conducting kink band simulations using the different models and writing the paper.

7.4 Main findings

One of the main findings is the development of the constitutive formulations itself. In the publication, the homogenised constitutive model is compared with the FE-model through a kink band study, and good agreement between the models was observed despite the remarkable difference in the model set-up. The constitutive model was used to investigate the influence of both geometrical fibre imperfections and fibre-to-matrix imperfections upon the critical compressive strength of unidirectional fibre composites and layered materials.

The formulation can furthermore be implemented as a user subroutines into Abaqus/CAE and thereby be used to study the response and failure of complex fibre domains e.g. investigate the influence of open-holes as done in [C1].



Constitutive model for imperfectly bonded fibre-reinforced composites

Simon P.H. Skovsgaard*, Henrik Myhre Jensen

Department of Engineering, Aarhus University, Inge Lehmanns Gade 10, 8000 Aarhus C, Denmark



ARTICLE INFO

Keywords:

Imperfect bonding
Strain localisation
Bifurcation
Constitutive model
Kink band

ABSTRACT

A constitutive model for fibre-reinforced composites has been developed that takes imperfect fibre/matrix interfacial bonding into account. The model can predict the nonlinear material response of a composite in the large strain regime. Independent constitutive laws can be used for the constituents behaving elastic or elastic-plastic. A constitutive equation is derived for the composite moduli relating stresses to strains. The model is used to predict the development of the compressive failure; fibre kinking that is either formed by bifurcation or due to an initial fibre imperfection. A three-dimensional finite element model for kink band formation is used to validate the results obtained using the constitutive model with varying levels of interfacial bonding.

1. Introduction

Fibre-reinforced composites (FRC) are used in many applications where high stiffness and low weight is desirable. These materials are composed of fibres bonded together using a resin material also known as the matrix material. In many of the frequently used FRCs as for example glass- and carbon fibre-reinforced composites, the fibres have high stiffness and strength and the matrix is more ductile and has high toughness but with a lower stiffness. These fibre composites have high strength in the direction of the fibres but when loaded in compression the critical stress can be considerable lower due to instabilities caused by imperfections coupled with matrix yielding. The compressive failure of multidirectional laminates is composed of several competing failure mechanisms including: fibre kinking, fibre splitting, matrix cracking, delamination, fibre/matrix interfacial debonding. In an experimental study conducted by Bishara et al. (2017) [1], together with finite element analyses, they showed that the compressive failure of a laminate with 16 layers initiated due to kink band formation in the 0° ply near an imperfection. The fibre kinking was triggered by matrix yielding. Several of the other mentioned failure mechanisms was seen to occur close to the kink band after the initiation.

The kink band failure has been observed experimentally by several authors including: Kyriakides et al. (1995) [2] who made a thorough investigation of the compressive failure of unidirectional AS4/PEEK composites. Kink band formation were seen both experimentally and in their two-dimensional micromechanical finite element model (FEM). Wadee et al. (2004) [3] conducted a compression test on a FRC and fibre kinking was observed and compared with a simple mechanical model taking bending, friction, membrane and foundation energy into

account. Zhou et al. (2013) [4] investigated the compressive strength of unidirectional glass fibre reinforced-polymers (GFRP) from different angles and fibre kinking was the dominant failure for small angles. Nizolek et al. (2017) [5] observed kink band initiation and stable band broadening in a Cu-Nb nanolaminate exposed to compressive loading. It was observed by Nair et al. (2017) [6] that a 75 % reduction in compressive strength could be achieved by introducing a severe fibre waviness into the unidirectional GFRP and failed by kink band formation.

Several attempts have been done towards developing analytical expressions predicting the kink band initiation. In the early work of Rosen (1965) [7] an analytical expression was derived based on the compressive bifurcation load of beams surrounded by an elastic matrix. Argon (1972) [8] treated the kink band failure as a plastic event, with a composite behaving rigid perfectly plastic with an initial imperfection. Budiansky (1983) [9] extended the expression by assuming rigid fibres and elastic perfectly plastic shear response of the composite. Fleck and Budiansky (1991) [10] included shear stresses and later Slaughter et al. (1993) [11] introduced transverse stresses in an analytical expression. Christoffersen and Jensen (1996) [12] developed a method to find the kink band bifurcation load for a composite including fibre and matrix material nonlinearities and with multiaxial loading. In the case of rigid fibres an analytical equation was developed where the effect of residual stresses could be included. Later Jensen (1999) [13] developed an analytical expression for the kink band bifurcation in the extreme case of no bonding between fibre and matrix. The expression developed in Christoffersen and Jensen (1996) [12] assumed perfect bonding.

The kink band initiation can be investigated numerically either by setting up a simplified kink band analysis as done by Jensen and Christoffersen (1997) [14] and Wadee et al. (2004) [3] or by creating a

* Corresponding author.

E-mail addresses: sphs@eng.au.dk (S.P.H. Skovsgaard), hunj@eng.au.dk (H.M. Jensen).

<https://doi.org/10.1016/j.compstruct.2018.02.053>

Received 28 September 2017; Accepted 19 February 2018

Available online 26 February 2018

0263-8223/ © 2018 Elsevier Ltd. All rights reserved.

finite element model. The FEMs used to study kink bands can roughly be divided into two categories: discretized FEMs also known as micromechanical models or FEMs using homogenised constitutive models. The fibre and matrix constituents are modelled discretely in the micromechanical models. Examples of authors who have used this approach are Hsu et al. (1999) [15] who used a three-dimensional FEM with a hexagonal fibre distribution, and Wind et al. (2014) [16] who compared results obtained using a discretized model and a constitutive model. When advanced fibre layouts or complex geometries are considered then discretized models become inexpedient compared to homogenized constitutive models. Fleck and Shu (1995) [17] developed a constitutive model using finite strain continuum theory combined with Cosserat couple theory. The constitutive model gives the smeared out properties of a composite including fibre bending effects. The constitutive model developed by Christoffersen and Jensen (1996) [12] is based on independent constitutive equations for the constituents instead of smeared out properties of the composite. Poullos and Niordson (2016) [18] developed a two-dimensional constitutive model based on independent constituent behaviour and included intrinsic size effects using higher order strain gradients. Skovsgaard and Jensen (2018) [19] developed a three-dimensional constitutive model for a FRC with independent elastic-plastic behaviour of the constituents similar to the two-dimensional model developed in Christoffersen and Jensen (1996) [12].

Dève (1997) [20] observed in a compression experiment on an aluminium matrix composite reinforced by Al_2O_3 fibres that the interfacial bonding between matrix and fibre has a severe influence on the compressive strength. In the experiment the fibres were coated so the interface was "weak" and lower critical stresses were observed. To the authors' knowledge, this is the only compression experiment of kink band formation done where composites with strong and weak bonding are compared. The longitudinal and transverse response of an aluminium composite was investigated by Zhang et al. (2008) [21] and they concluded that the transverse properties depends strongly on interfacial bonding between matrix and fibre. It is commonly accepted that the kink band instability is sensitive to the composite shear response, and since the shear response is altered by the interfacial bonding then so are the critical kink band stress. Jiang et al. (2014) [22] investigated the composite properties using a finite element representative volume element with different levels of bonding between matrix and fibre and made the same conclusions as Zhang et al. (2008) [21]. The interface was modelled with cohesive contact surfaces. A comprehensive micromechanical kink band analysis with cohesive-frictional interfaces were conducted by Naya et al. (2017) [23].

The interface bonding between fibre and matrix has a severe influence on the critical compressive stress, and the need to have constitutive models to investigate complex geometries and fibre layouts leads to the main focus of this paper. The current paper focuses on the development of a novel constitutive model for imperfectly bonded fibre-reinforced composites. The constitutive model is validated using a kink band analysis and is compared with results obtained using a three-dimensional FE micromechanical kink band model. The paper is organised in 7 sections. The constitutive model and a novel analytical kink band expression is derived in Section 2. A semi-analytical kink band analysis with the constitutive model implemented is introduced in Section 3. The constituent behaviour used in the FE and semi-analytical analysis is presented in Section 4. The FEM together with the boundary conditions are shown in Section 5. Finally the results from the analyses are shown, compared and discussed in Section 6 and Section 7 concludes the paper.

2. Constitutive model

In the following section a constitutive model is derived that can take imperfect cohesion between fibre and matrix into account. The model is inspired by the two constitutive models derived by Christoffersen and

Jensen (1996) [12] and Jensen (1999) [13]. The latter constitutive models are extrema where the model derived in Christoffersen and Jensen (1996) [12] assumes perfect bonding between the constituents and the model in Jensen (1999) [13] assumes complete decohesion. The present constitutive model can display the transition between the two previous mentioned extrema using a factor μ going from zero to unity. The constitutive model is implemented in a kink band analysis and is compared with a three-dimensional micromechanical finite element model for verification.

Simple representations of perfect and imperfect bonding are illustrated in Figs. 1 and 2 to enhance the understanding behind the assumptions used in the constitutive models. The model with perfect bonding is based on the assumptions.

1. Material lines parallel with the fibres are subject to a common stretching and rotation.
2. Planes parallel with the fibres transmit identical tractions.
3. The material of the constituents is elastic or elastic-plastic.

As outlined in Christoffersen and Jensen (1996) these assumptions leads to the restriction on the velocity gradients

$$\begin{aligned} v_{1,1}^m &= v_{1,1}^f = v_{1,1}, & v_{2,1}^m &= v_{2,1}^f = v_{2,1}, \\ c^f v_{1,2}^f + c^m v_{1,2}^m &= v_{1,2}, & c^f v_{2,2}^f + c^m v_{2,2}^m &= v_{2,2}, \end{aligned} \quad (1)$$

where c^m and c^f are volume fractions of matrix and fibre fulfilling $c^f + c^m = 1$. A comma (\bullet), denotes partial derivative. Superscripts $(\bullet)^m$ and $(\bullet)^f$ will refer to quantities associated with the matrix and fibre constituent and omission of superscript refers to overall composite properties. This convention will be adopted in the current article. The second assumption together with overall equilibrium entails

$$\begin{aligned} i_{21}^m &= i_{21}^f = i_{21}, & i_{22}^m &= i_{22}^f = i_{22}, \\ c^f i_{1,1}^f + c^m i_{1,1}^m &= i_{1,1}, & c^f i_{1,2}^f + c^m i_{1,2}^m &= i_{1,2}, \end{aligned} \quad (2)$$

where i_{ij} is the nominal stress rates.

In Fig. 2 shear and transverse deformation of a fibre composite with imperfect bonding is shown. The constitutive model suggested by Jensen (1999) [13] also assumes that material lines parallel with the fibres are subject to a common stretching and rotation. Furthermore it is assumed that the matrix as a whole is subject to the overall strains

$$\begin{aligned} v_{1,1}^m &= v_{1,1}^f = v_{1,1}, & v_{2,1}^m &= v_{2,1}^f = v_{2,1}, \\ v_{1,2}^m &= v_{1,2} & v_{2,2}^m &= v_{2,2}. \end{aligned} \quad (3)$$

Further, the rate of nominal stress was given by

$$\begin{aligned} c^f i_{1,1}^f + c^m i_{1,1}^m &= i_{1,1}, & c^f i_{1,2}^f + c^m i_{1,2}^m &= i_{1,2}, \\ c^m i_{2,1}^m &= i_{2,1}, & i_{2,1}^f &= 0, & c^m i_{2,2}^m &= i_{2,2}, & i_{2,2}^f &= 0. \end{aligned} \quad (4)$$

The suggestion $i_{1\alpha} = c^f i_{1\alpha}^f + c^m i_{1\alpha}^m$ is an average of the tractions where both the fibre and matrix transmit traction. The assumption $c^m i_{2\alpha}^m = i_{2\alpha}$ is an average where only the matrix constituent contributes.

2.1. General relations

The index notation and the summation convention is adopted. Latin indices i.e. i,j,k take values 1,2,3, and Greek indices i.e. α,β,γ take values 1,2. The relation between nominal stress rates and velocity gradients is given by

$$\dot{i}_{ij} = C_{ijkl} v_{l,k}, \quad (5)$$

where \dot{i}_{ij} are components of the nominal stress rate, $v_{l,k}$ are the velocity gradients and C_{ijkl} are components of nominal moduli. The moduli C_{ijkl} can be calculated using

$$C_{ijkl} = L_{ijkl} - \frac{1}{2} \tau_{ij} \delta_{kl} - \frac{1}{2} \tau_{kl} \delta_{ij} - \frac{1}{2} \tau_{ij} \delta_{kl} + \frac{1}{2} \tau_{kl} \delta_{ij}, \quad (6)$$

S.P.H. Skovsgaard, H.M. Jensen

Composite Structures 192 (2018) 82–92

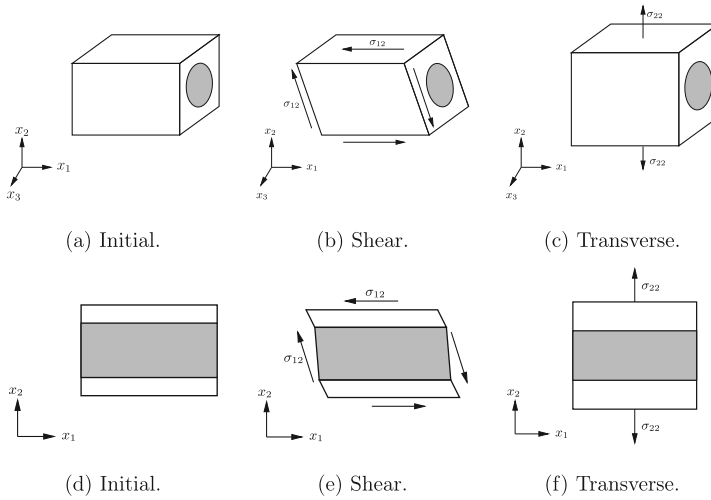


Fig. 1. Perfect bonding between constituents. Three-dimensional (a–c) and two-dimensional (d–f) illustrations of the initial state, shear- and transverse deformation are shown.

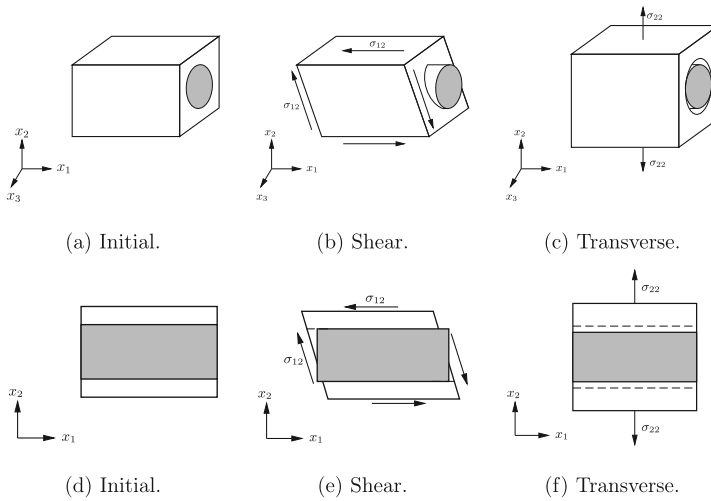


Fig. 2. Imperfect bonding between constituents. Three-dimensional (a–c) and two-dimensional (d–f) illustrations of the initial state, shear- and transverse deformation are shown.

where L_{ijkl} are components of a tensor of elastic–plastic tangent moduli relating the Jaumann rates of Kirchhoff stresses to strain rates $\dot{\tau}_{ij} = L_{ijkl} \epsilon_{kl}$. δ_{ij} is Kronecker's delta and τ_{ij} are Kirchhoff stresses. L_{ijkl} must satisfy the minor and major symmetries

$$L_{ijkl} = L_{jikl} = L_{ijlk}, \quad L_{ijkl} = L_{klij}. \quad (7)$$

When the tangent moduli are used in two dimensions then Latin indices are replaced by Greek indices $L_{\alpha\beta\gamma\delta}$ and so are the moduli $C_{\alpha\beta\gamma\delta}$.

Plane strain conditions is used for the moduli $L_{\alpha\beta\gamma\delta}$. The relation between Kirchhoff stresses and Cauchy stresses is given by

$$\tau_{ij} = J \sigma_{ij}, \quad (8)$$

where σ_{ij} are components of the Cauchy stresses and J is the Jacobian giving the volume ratio $J = V/V_0$.

2.2. Constitutive model with imperfect bonding

Inspired by the assumptions from the latter constitutive models with perfect and imperfect bonding, a transition between the two models is suggested. Introducing the factors μ and κ , where μ takes values between 0 and 1 and κ is calculated based on μ according to

$$\kappa(\mu) = \left(1 - \frac{1}{c^m}\right)\mu + \frac{1}{c^m}, \quad (9)$$

which is a linear relation going from $\kappa(\mu = 0) = 1/c^m$ to $\kappa(\mu = 1) = 1$. The present constitutive model also assumes that material lines parallel with the fibres are subjected to a common stretching and rotation. Further the fibres is aligned with the x_1 -axis prior to deformation this entails

$$v_{\alpha,1}^f = v_{\alpha,1}^m = v_{\alpha,1}, \quad (10)$$

where the index $(\bullet)_{\alpha}$ takes values 1 and 2. Inspired by the assumptions from Eq. (1) and (3) and using the introduced factors μ and κ suggest

$$v_{\alpha,2} = c^f \mu v_{\alpha,2}^f + c^m \kappa v_{\alpha,2}^m. \quad (11)$$

Using the proposed equation yields the case of perfect bonding when $\mu = 1$ and imperfect bonding for $\mu = 0$. Traction on planes parallel with the fibres can be calculated according to

$$\begin{aligned} i_{2\alpha}^f &= \mu i_{2\alpha}, \\ i_{2\alpha}^m &= \kappa i_{2\alpha}, \\ i_{2\alpha} &= c^f i_{2\alpha}^f + c^m i_{2\alpha}^m. \end{aligned} \quad (12)$$

To have overall equilibrium

$$i_{1\alpha} = c^f i_{1\alpha}^f + c^m i_{1\alpha}^m. \quad (13)$$

Using the relation between the Jaumann rate of Cauchy stresses and nominal stress rates

$$\sigma'_{ij} = \dot{i}_{ij} - \omega_{jk} \sigma_{ik} - \omega_{ik} \sigma_{kj} - \sigma_{ij} v_{k,k} + \sigma_{jk} v_{i,k}, \quad (14)$$

where σ'_{ij} are components of the Jaumann rate of Cauchy stresses and ω_{ij} is the spin tensor, then it can be proven that the components of the Cauchy stresses are

$$\begin{aligned} \sigma_{11} &= c^f \sigma_{11}^f + c^m \sigma_{11}^m, \\ \sigma_{12}^f &= \mu \sigma_{12}, & \sigma_{12}^m &= \kappa \sigma_{12}, \\ \sigma_{22}^f &= \mu \sigma_{22}, & \sigma_{22}^m &= \kappa \sigma_{22}, \end{aligned} \quad (15)$$

where moment equilibrium $\sigma_{ij} = \sigma_{ji}$ is satisfied. The relation between rates of nominal stresses and velocity gradients given by Eq. (5) can equivalently be used for the two constituents. The relation given by Eq. (5) together with Eq. (10) can be written as

$$i_{\alpha\beta}^c = C_{\alpha\beta 1\delta}^c v_{\delta,1} + C_{\alpha\beta 2\delta}^c v_{\delta,2}, \quad (16)$$

where the superscript $(\bullet)^c$ indicates one of the constituents. As derived in Appendix A, the velocity gradients $v_{\delta,2}^f$ and $v_{\delta,2}^m$ can be expressed through overall composite velocity gradients

$$\begin{aligned} v_{\delta,2}^f &= -c^m \kappa H_{\alpha\beta}^f (\kappa C_{2\delta 1\delta}^f - \mu C_{2\delta 1\delta}^m) v_{\delta,1} + \mu H_{\alpha\beta}^f C_{2\delta 2\delta}^f v_{\delta,2}, \\ v_{\delta,2}^m &= c^f \mu H_{\alpha\beta}^m (\kappa C_{2\delta 1\delta}^f - \mu C_{2\delta 1\delta}^m) v_{\delta,1} + \kappa H_{\alpha\beta}^m C_{2\delta 2\delta}^m v_{\delta,2}, \end{aligned} \quad (17)$$

where $H_{\alpha\beta}$ denotes

$$H_{\alpha\beta} = \frac{1}{\det(M)} (\delta_{\alpha\beta} \delta_{\gamma\gamma} - \delta_{\alpha\delta} \delta_{\beta\gamma}) M_{\delta\gamma}, \quad (18)$$

which is the inverse of $M_{\alpha\beta}$ given by

$$M_{\alpha\beta} = c^m \kappa^2 C_{2\alpha 2\beta}^f + c^f \mu^2 C_{2\alpha 2\beta}^m, \quad (19)$$

and $\det(M)$ denotes the determinant calculated according to

$$\det(M) = \frac{1}{2} (\delta_{\alpha\gamma} \delta_{\beta\delta} - \delta_{\alpha\delta} \delta_{\beta\gamma}) M_{\gamma\alpha} M_{\delta\beta}. \quad (20)$$

It is convenient to rewrite the velocity gradients $v_{\delta,2}^f$ and $v_{\delta,2}^m$ in the equivalent forms

$$\begin{aligned} v_{\delta,2}^f &= -c^m \kappa H_{\alpha\beta}^f (\kappa C_{2\delta 1\delta}^f - \mu C_{2\delta 1\delta}^m) v_{\delta,1} - c^m \kappa H_{\alpha\beta}^f (\kappa C_{2\delta 2\delta}^f - \mu C_{2\delta 2\delta}^m) v_{\delta,2} + v_{\delta,2}, \\ v_{\delta,2}^m &= c^f \mu H_{\alpha\beta}^m (\kappa C_{2\delta 1\delta}^f - \mu C_{2\delta 1\delta}^m) v_{\delta,1} + c^f \mu H_{\alpha\beta}^m (\kappa C_{2\delta 2\delta}^f - \mu C_{2\delta 2\delta}^m) v_{\delta,2} + v_{\delta,2}. \end{aligned} \quad (21)$$

Using Eq. (13) and (16) the overall nominal stress rates $i_{1\alpha}$ can be determined

$$i_{1\beta} = c^f C_{1\beta 1\delta}^f v_{\delta,1} + c^f C_{1\beta 2\delta}^f v_{\delta,2} + c^m C_{1\beta 1\delta}^m v_{\delta,1} + c^m C_{1\beta 2\delta}^m v_{\delta,2}. \quad (22)$$

Replacing $v_{\delta,2}^f$ and $v_{\delta,2}^m$ using Eq. (21) and collecting terms related to $v_{\alpha,\beta}$ yields

$$\begin{aligned} i_{1\beta} &= [c^f C_{1\beta 1\delta}^f + c^m C_{1\beta 1\delta}^m - c^f c^m (\kappa C_{1\beta 2\delta}^f - \mu C_{1\beta 2\delta}^m) H_{\alpha\beta}^f (\kappa C_{2\delta 1\delta}^f - \mu C_{2\delta 1\delta}^m)] v_{\delta,1} \\ &\quad + [c^f C_{1\beta 2\delta}^f + c^m C_{1\beta 2\delta}^m - c^f c^m (\kappa C_{1\beta 2\delta}^f - \mu C_{1\beta 2\delta}^m) H_{\alpha\beta}^f (\kappa C_{2\delta 2\delta}^f \\ &\quad - \mu C_{2\delta 2\delta}^m)] v_{\delta,2}. \end{aligned} \quad (23)$$

Using the last part of Eq. (12) then $i_{2\alpha}$ can be determined as

$$\begin{aligned} i_{2\beta} &= [c^f C_{2\beta 1\delta}^f + c^m C_{2\beta 1\delta}^m - c^f c^m (\kappa C_{2\beta 2\delta}^f - \mu C_{2\beta 2\delta}^m) H_{\alpha\beta}^f (\kappa C_{2\delta 1\delta}^f - \mu C_{2\delta 1\delta}^m)] v_{\delta,1} \\ &\quad + [c^f C_{2\beta 2\delta}^f + c^m C_{2\beta 2\delta}^m - c^f c^m (\kappa C_{2\beta 2\delta}^f - \mu C_{2\beta 2\delta}^m) H_{\alpha\beta}^f (\kappa C_{2\delta 2\delta}^f \\ &\quad - \mu C_{2\delta 2\delta}^m)] v_{\delta,2}. \end{aligned} \quad (24)$$

The latter two equations may be written in a similar form as Eq. (5) with

$$C_{\alpha\beta\gamma\delta} = c^f C_{\alpha\beta\gamma\delta}^f + c^m C_{\alpha\beta\gamma\delta}^m - c^f c^m (\kappa C_{\alpha\beta 2\delta}^f - \mu C_{\alpha\beta 2\delta}^m) H_{\alpha\beta}^f (\kappa C_{2\delta\gamma\delta}^f - \mu C_{2\delta\gamma\delta}^m). \quad (25)$$

This is the final equation for the constitutive model relating the overall nominal stress rates to velocity gradients. Using the constitutive equation, the overall response of a composite can be determined with information about imperfect bonding based on μ . When the overall deformations are determined in an incremental scheme then the velocity gradients for the constituents can be retrieved using Eqs. (10) and (21). In the case of perfect bonding $\mu = 1, \kappa = 1$ Eq. (25) simplifies to

$$\begin{aligned} \mu = 1 \rightarrow \\ C_{\alpha\beta\gamma\delta} &= c^f C_{\alpha\beta\gamma\delta}^f + c^m C_{\alpha\beta\gamma\delta}^m - c^f c^m (C_{\alpha\beta 2\delta}^f - C_{\alpha\beta 2\delta}^m) H_{\alpha\beta}^f (C_{2\delta\gamma\delta}^f - C_{2\delta\gamma\delta}^m), \\ M_{\alpha\beta\gamma} &= c^m C_{2\alpha 2\beta}^f + c^f C_{2\alpha 2\beta}^m, \end{aligned} \quad (26)$$

which is identical to the expression derived by Christoffersen and Jensen (1996) [12]. In the other extremum of decohesion $\mu = 0, \kappa = 1/c^m$ the constitutive equation simplifies to

$$\begin{aligned} \mu = 0 \rightarrow \\ C_{\alpha\beta\gamma\delta} &= c^f C_{\alpha\beta\gamma\delta}^f + c^m C_{\alpha\beta\gamma\delta}^m - c^f C_{\alpha\beta 2\delta}^f H_{\alpha\beta}^f C_{2\delta\gamma\delta}^f, \\ M_{\alpha\beta\gamma} &= C_{2\alpha 2\beta}^f, \end{aligned} \quad (27)$$

which is identical to the suggested expression presented in Jensen (1999) [13]. In both of the simplified expressions, the inverse $H_{\alpha\beta}$ can be calculated using Eq. (18). The elastic-plastic tangent moduli can be determined using Eq. (6) to be

$$L_{\alpha\beta\gamma\delta} = C_{\alpha\beta\gamma\delta} + \frac{1}{2} \tau_{\gamma\delta} \delta_{\alpha\delta} + \frac{1}{2} \tau_{\delta\delta} \delta_{\alpha\gamma} + \frac{1}{2} \tau_{\delta\delta} \delta_{\beta\delta} - \frac{1}{2} \tau_{\alpha\gamma} \delta_{\beta\delta}. \quad (28)$$

Combining this with the derived constitutive equation (Eq. (25)) and utilizing the properties from Eq. (15) yields the tangent moduli for the composite

$$L_{\alpha\beta\gamma\delta} = c^f L_{\alpha\beta\gamma\delta}^f + c^m L_{\alpha\beta\gamma\delta}^m - c^f c^m (\kappa C_{\alpha\beta 2\delta}^f - \mu C_{\alpha\beta 2\delta}^m) H_{\alpha\beta}^f (\kappa C_{2\delta\gamma\delta}^f - \mu C_{2\delta\gamma\delta}^m). \quad (29)$$

The tangent moduli for the composite satisfy the minor and major

S.P.H. Skovsgaard, H.M. Jensen

Composite Structures 192 (2018) 82–92

symmetries given by Eq. (7).

2.3. Kink band bifurcation

The constitutive equation is now applied in a kink band study, where no initial fibre waviness is present and thereby kink band formation at a bifurcation point is searched for. The applied method for finding the bifurcation load associated with strain localisation was formulated by Rice (1976) [24] and was used in a kink band analysis in Christoffersen and Jensen (1996) [12]. The equilibrium equation can be written in terms of the rate of nominal stresses

$$\dot{\epsilon}_{\alpha\beta,\alpha} = 0. \quad (30)$$

Combining this with Eq. (5) yields

$$C_{\alpha\beta\gamma\delta} v_{\beta,\gamma\alpha} = 0. \quad (31)$$

In the bifurcation analysis a nonhomogeneous and sufficiently smooth velocity field is searched for where the fibres starts to rotate and overall strains localize into a band with orientation β as shown in Fig. 3. The velocity field searched for takes the form

$$v_{\alpha} = f_{\beta}(n_{\beta} x_{\beta}), \quad (32)$$

where $n_{\alpha} = (\cos(\beta), \sin(\beta))$ is the unit normal to the localization band. Using the introduced velocity field in the equilibrium equation yield

$$C_{\alpha\beta\gamma\delta} n_{\alpha} n_{\gamma} \frac{d^2 f_{\beta}(n_{\beta} x_{\beta})}{d(n_{\beta} x_{\beta})^2} = 0. \quad (33)$$

The bifurcation point is when the determinant of the latter equation vanishes

$$\det(C_{\alpha\beta\gamma\delta} n_{\alpha} n_{\gamma}) = 0. \quad (34)$$

Until this point, no assumptions have been made regarding the elastic-plastic behaviour of the constituents. When concerning the idealized situation of infinitely rigid fibres then a closed form solution for the bifurcation point is obtainable. The method to obtain the solution follows the method introduced in Jensen (1999) [13]. The components of the tangent moduli for the fibre constituent are written in the form

$$L_{\alpha\beta\gamma\delta}^f = E^f \tilde{L}_{\alpha\beta\gamma\delta}^f, \quad (35)$$

where the moduli are proportional to the stiffness modulus E^f . Multiplying Eq. (25) with the determinant $\det(M)$ given by Eq. (20) will not change the bifurcation point. By doing so, the constitutive equation can be written as polynomials of E^f

$$\det(M) C_{\alpha\beta\gamma\delta} = (E^f)^3 C_{\alpha\beta\gamma\delta}^{(3)} + (E^f)^2 C_{\alpha\beta\gamma\delta}^{(2)} + E^f C_{\alpha\beta\gamma\delta}^{(1)} + C_{\alpha\beta\gamma\delta}^{(0)}, \quad (36)$$

where the superscripts $C_{\alpha\beta\gamma\delta}^{(i)}$ means the moduli associated with the given polynomial order of E^f . The condition for bifurcation Eq. (34) can be

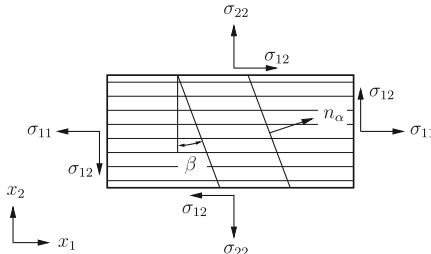


Fig. 3. Geometry of composite model with fibres oriented in the x_1 direction. The angle β is the orientation of the localization band searched for in the bifurcation analysis.

rewritten

$$\det(\det(M) C_{\alpha\beta\gamma\delta} n_{\alpha} n_{\gamma}) = 0. \quad (37)$$

When calculating the determinant in Eq. (37) a polynomial form is thus obtained

$$0 = (E^f)^5 d_5 + (E^f)^4 d_4 + O(E^f)^3. \quad (38)$$

The term d_5 will dominate the solution for high fibre stiffness E^f . The solution to $d_5 = 0$ gives the closed form solution

$$0 = \sigma_{11} - \sigma_{22} + \frac{1}{c^m \kappa^2} \left(L_{1212}^m - \frac{\sigma_{11}^m - \kappa \sigma_{22}}{2} \right) + \frac{2}{c^m \kappa^2} (L_{1222}^m - c^f \kappa \mu \sigma_{12}) \tan \beta + \frac{1}{c^m \kappa^2} (L_{2222}^m - \kappa \sigma_{22}) \tan^2 \beta, \quad (39)$$

which can be compared to the expressions obtained by Christoffersen and Jensen (1996) [12] and Slaughter et al. (1993) [11] with no initial fibre imperfection. Evaluating Eq. (39) for perfect bonding and using Eq. (6) leads to

$$\mu = 1 \rightarrow 0 = \sigma_{11} - \sigma_{22} + \frac{1}{c^m} C_{2121}^m + \frac{2}{c^m} (L_{1222}^m - c^f \sigma_{12}) \tan \beta + \frac{1}{c^m} C_{2222}^m \tan^2 \beta, \quad (40)$$

which is identical to the expression derived by Christoffersen and Jensen (1996) [12] where the symmetry $L_{1222}^m = L_{2212}^m$ has been utilized. In the case of imperfect bonding Eq. (39) yields

$$\mu = 0 \rightarrow 0 = \sigma_{11} - \sigma_{22} + c^m C_{2121}^m + 2 c^m L_{1222}^m \tan \beta + c^m C_{2222}^m \tan^2 \beta, \quad (41)$$

which is nearly identical to the expression derived in Jensen (1999) [13] with the only difference that in the current expression no terms are present in front of σ_{22} . This is due to the assumptions of the stress equality given by Eq. (15). In the current case of imperfect bonding, it is assumed that no shear- and transverse stresses are transmitted to the fibres. The same conclusion can be made as done by Jensen (1999) [13] that the two expressions Eq. (40) and (41) corresponding to the two extreme cases; perfect bonding and no bonding essentially differs by a factor of $(c^m)^2$. In the experiments conducted by Dève (1997) [20] the compressive strength of coated and uncoated fibres were compared. The uncoated fibres had good interfacial bonding and a mean compressive strength of $\sigma_{11}^c \approx -4000$ [MPa] was obtained. Only one experiment with coated fibres (weakly bonded) was conducted where a compressive strength of $\sigma_{11}^c \approx -2600$ [MPa] was obtained. Assuming that the uncoated fibres were perfectly bonded $\mu = 1$, a matrix volume fraction of $c^m = 0.5$ and only σ_{11} stresses were present then this corresponds to an interfacial bonding $\mu = 0.76$ using Eq. (39).

3. Kink band formation with the constitutive model

The developed constitutive model is implemented in a semi-analytical kink band analysis with an initial fibre imperfection. The method was introduced in Jensen and Christoffersen (1997) [14]. Since the implementation is similar to the previous some of the details are skipped. Two material states are introduced, one inside the kink band (band system) and one outside (base system) as illustrated in Fig. 4. The fibres are localized in a band with an inclination β^o and β^i when represented in the base- and band system respectively. The fibres are aligned with the x_1 -axis prior to the deformation increment. A small fibre rotation ϕ_0 is introduced initially as an imperfection. The displacement gradients for the composite is updated numerically due to a prescribed rotation increment of the fibres in the band ϕ . The governing equation for the material states is

$$C_{\alpha\beta\gamma\delta} v_{\beta,\gamma} - \sigma_{\alpha\beta} v_{\gamma,\gamma} + v_{\alpha,\gamma} \sigma_{\gamma,\beta} = \dot{\epsilon}_{\alpha\beta}. \quad (42)$$

Two different numerical implementations in the incremental loading procedure leading to identical predictions were presented by Jensen and Christoffersen (1997) [14]. The first version is utilized here

S.P.H. Skovsgaard, H.M. Jensen

Composite Structures 192 (2018) 82–92

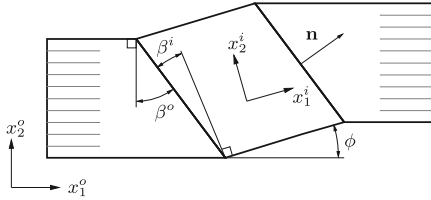


Fig. 4. Kink band geometry.

where the basis rotates with the fibres, leading to

$$v_{2,1}^o = 0, \quad v_{1,1}^i = 0, \quad (43)$$

where superscripts $(\bullet)^o$ and $(\bullet)^i$ refer to quantities described in the base and band system, respectively. A spin tensor is introduced $\Omega_{\alpha\beta}$ with the components

$$\Omega_{21} = -\Omega_{12} = \dot{\phi}, \quad \Omega_{11} = \Omega_{22} = 0. \quad (44)$$

Using the spin tensor then the components of the velocity gradients, seen from a basis in the band system that stays stationary during deformation, are $v_{\alpha,\beta}^i + \Omega_{\alpha\beta}$. The unit normal n_α and unit tangent t_α to the band for the two systems are calculated using

$$\begin{aligned} (n_1^i, n_2^i) &= (\cos\beta^o, \sin\beta^o), & (t_1^i, t_2^i) &= (-\sin\beta^o, \cos\beta^o), \\ (n_1^o, n_2^o) &= (\cos\beta^i, \sin\beta^i), & (t_1^o, t_2^o) &= (-\sin\beta^i, \cos\beta^i). \end{aligned} \quad (45)$$

Continuity of velocities along the boundary of the band requires that

$$(v_{\alpha,\beta}^i + \Omega_{\alpha\beta}) t_\alpha^i t_\beta^i = v_{\alpha,\beta}^o t_\alpha^o t_\beta^o, \quad (v_{\alpha,\beta}^i + \Omega_{\alpha\beta}) n_\alpha^i t_\beta^i = v_{\alpha,\beta}^o n_\alpha^o t_\beta^o. \quad (46)$$

Continuity of tractions across the boundary requires that

$$\begin{aligned} C_{\alpha\beta\gamma\delta}^i (v_{\delta,\gamma}^i + \Omega_{\delta\gamma}) n_\alpha^i n_\beta^i &= C_{\alpha\beta\gamma\delta}^o v_{\delta,\gamma}^o n_\alpha^o n_\beta^o, \\ C_{\alpha\beta\gamma\delta}^i (v_{\delta,\gamma}^i + \Omega_{\delta\gamma}) n_\alpha^i t_\beta^i &= C_{\alpha\beta\gamma\delta}^o v_{\delta,\gamma}^o n_\alpha^o t_\beta^o. \end{aligned} \quad (47)$$

The relative rotation increment of the band seen from the two bases are calculated according to

$$\dot{\beta}^o = -v_{\alpha,\beta}^o n_\alpha^o t_\beta^o, \quad \dot{\beta}^i = -v_{\alpha,\beta}^i n_\alpha^i t_\beta^i. \quad (48)$$

The volume fraction of fibres inside and outside the band change due to transfer deformation according to

$$\dot{c}^f = c^f c^m (v_{2,2}^i - v_{2,2}^o). \quad (49)$$

Plane strain conditions and the boundary condition $v_{1,2}^o = 0$ is used, furthermore $\sigma_{22} = 0$ together with Eq. (46) and (47) give five boundary conditions for the last five unknown velocity gradients.

4. Constituent behaviour

The Stören and Rice (1975) [25] version of J_2 -deformation theory is chosen as the elastic-plastic tangent moduli relating the Jaumann rate of Kirchhoff stresses to strain rates $\tau_{ij} = L_{ijkl} \dot{\epsilon}_{kl}$. The formulation is outlined here for completeness. The components of the tensor of instantaneous moduli are given by

$$L_{ijkl} = G_s (\delta_{ij} \delta_{kl} + \delta_{ij} \delta_{kl}) + \left(K - \frac{2}{3} G_s \right) \delta_{ij} \delta_{kl} - \frac{4}{3} (G_s - G_t) m_{ij} m_{kl}, \quad (50)$$

where m_{ij} is given in terms of Cauchy stresses

$$m_{ij} = \frac{1}{2\sigma_{eq}} \left(\sigma_{ij} - \frac{1}{3} \delta_{ij} \sigma_{kk} \right), \quad (51)$$

where σ_{eq} is the equivalent von Mises stress

$$\sigma_{eq} = \sqrt{\frac{3}{2} \sigma_{ij} \sigma_{ij} - \frac{1}{2} \sigma_{ii} \sigma_{jj}}. \quad (52)$$

The remaining terms introduced in Eq. (50) is the bulk modulus, K , the secant shear modulus, G_s , and the tangent shear modulus, G_t . The two latter moduli can be calculated based on the secant and tangent moduli E_s and E_t

$$\frac{1}{G_s} = \frac{3}{E_s} - \frac{1-2\nu}{E}, \quad \frac{1}{G_t} = \frac{3}{E_t} - \frac{1-2\nu}{E}, \quad K = \frac{E}{3(1-2\nu)}, \quad (53)$$

where ν is Poisson's ratio and E is Young's modulus. The nonlinear relationship between logarithmic strain ϵ_{eq} and the stress σ_{eq} is given by the Ramberg-Osgood relation

$$\epsilon_{eq} = \frac{\sigma_{eq}}{E} + \frac{3\sigma_y}{7E} \left(\frac{\sigma_{eq}}{\sigma_y} \right)^n, \quad (54)$$

where σ_y is a reference yield stress and n is a hardening exponent. Both the secant modulus E_s and tangent modulus E_t can be determined based on the Ramberg-Osgood relation. The J_2 -deformation theory is used for the constitutive model and is also implemented as a UMAT in Abaqus for the finite element model presented in Section 5.

The material parameters used for the constitutive model and partially the FEM are normalised quantities of the parameters obtained by Kyriakides et al. (1995) [2] and are given by

$$\begin{aligned} c^f &= 0.6, \quad E^f/E^m = 35, \quad \nu^f = 0.263, \\ \nu^m &= 0.356, \quad \sigma_y^m/E^m = 0.013, \quad n^m = 4. \end{aligned} \quad (55)$$

The fibres are assumed to behave linear elastic although Kyriakides et al. (1995) [2] observed nonlinear behaviour of the fibres. The fibre nonlinearity have a minor effect on the kink band instability. Kyriakides et al. (1995) [2] used an initial imperfection of $\phi_0 \approx 1.5^\circ$ and compared results obtained using linear and nonlinear fibres. The tendencies were not influenced significantly based on their results. Jensen and Christoffersen (1997) [14] concluded that nonlinear fibres have a significant influence on the bifurcation stress but goes asymptotically towards the same stress for increasing imperfections ϕ_0 .

5. Finite element model

To validate the usability of the constitutive model developed in Section 2, then a three-dimensional finite element model is created. In the FEM the fibre and matrix constituents are discretized and are assumed to be hexagonally distributed comparable to the set-up introduced by Hsu et al. (1998) [26]. Utilizing the symmetries of the assumed fibre distribution, the cross section used in the simulation can be seen in the unit cell shown in Fig. 5. The diameter of the fibres entering the simulation is

$$d = w_0 \sqrt{\frac{6c^f}{\pi\sqrt{3}}}, \quad (56)$$

where w_0 is the width of the cross section, and the thickness is related to the width $t_0 = \sqrt{3/2} w_0$. ABAQUS 6.14 is chosen to solve the finite element problem. 20-node quadratic brick- and 15-node quadratic triangular prism elements are chosen with full integration. Different mesh configurations are investigated for the cross section as seen in Fig. 6. Based on a convergence analysis, it is chosen to use the first mesh presented in Fig. 6a. The starting point for the material parameters was presented in Section 4. The kink band instability is sensitive to the elastic-plastic shear response of the composite as confirmed by Argon (1972) [8], Budiansky (1983) [9], Slaughter et al. (1993) [11] and several others since then. In the FEM created by Hsu et al. (1998) [26] they experienced that the material parameters for the matrix constituent needed to be changed going from two-dimensional to a three-dimensional FEM based on the overall shear response of the composite. A similar investigation of the pure shear response is investigated here

S.P.H. Skovsgaard, H.M. Jensen

Composite Structures 192 (2018) 82–92

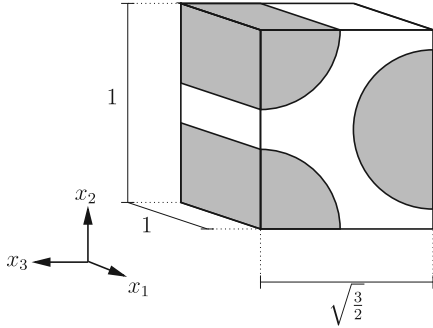


Fig. 5. Unit cell of the 3D finite element model with fibres oriented in the x_1 direction.

where a two-dimensional and three-dimensional model is compared. The unit cell for the three-dimensional model is shown in Fig. 5. The boundary conditions for the two models are shown in Fig. 7. The abbreviation (PBC) stands for periodic boundary conditions. The shear stress vs shear strain response is shown in Fig. 8. Three different curves are presented. The first and second curve show the shear response of the two- and three-dimensional model where the same material parameters are chosen for the constituents from Section 4. The third curve shows the response of the three-dimensional FEM with a Young's modulus $E^{m(3D)}/E^m = 0.5$ which is normalised with the two-dimensional modulus. The shear response for the first and third curve nearly coincide. Based on the current simulation a modified modulus $E^{m(3D)}/E^m = 0.5$ is chosen for the three-dimensional finite element model. The boundary conditions for the FEM for kink band formation is shown in Figs. 9 and 10. Focusing on Fig. 9, the left surface is simple supported and a displacement is applied to the right surface. Periodic boundary conditions between the lower and upper part are utilized to imitate an infinite band and to avoid an extensive amount of degrees of freedom. Out of plane deformation is constrained as shown in Fig. 10. An imperfection is introduced as a fibre waviness where the deformed coordinates are calculated based on

$$\begin{aligned}
 x_2 &= \frac{1}{2} \phi_0 \left(\frac{-b}{2 \cos \beta} - X_2 \tan \beta \right) & \text{for } X_1 < X_{1,min}, \\
 x_2 &= \frac{1}{2} \phi_0 \left[\frac{b}{2 \pi \cos \beta} \sin \left(\frac{2 \pi \cos \beta}{b} (X_1 + X_2 \tan \beta) \right) + X_2 \right] & \text{for } X_{1,min} < X_1 \\
 &< X_{1,max}, \\
 x_2 &= \frac{1}{2} \phi_0 \left(\frac{b}{2 \cos \beta} - X_2 \tan \beta \right) & \text{for } X_{1,max} < X_1,
 \end{aligned}
 \tag{57}$$

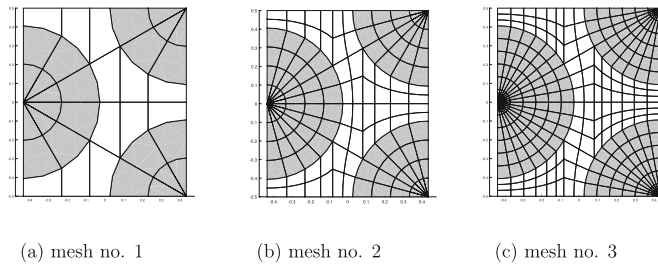


Fig. 6. Illustration of different mesh configurations for the cross section. The meshes are composed of 20-node quadratic brick- and 15-node quadratic triangular prism elements.

where small letters x_i refer to deformed coordinates and capital letters X_i are the undeformed coordinates with a reference coordinate system placed in the centre of the geometry. b is the width of the imperfection, β is the band inclination and ϕ_0 is the largest imperfection angle and is located in the geometry centre. The imperfection is a modified version of the one introduced by Srensen et al. (2008) [27]. The quantities $X_{1,min}$ and $X_{1,max}$ are calculated using

$$X_{1,min} = \frac{-b}{2 \cos \beta} - X_2 \tan \beta, \quad X_{1,max} = \frac{b}{2 \cos \beta} - X_2 \tan \beta.
 \tag{58}$$

The geometrical parameters used in the simulations are

$$L_0 = 1, \quad w_0 = 0.01, \quad b = 1, \quad \beta = 0.
 \tag{59}$$

The band inclination is set to $\beta = 0$ in the simulations which is compatible with the current implementation of the periodic boundary conditions. The width $w_0 = 0.01$ is chosen based on a convergence study where the ratio L_0/w_0 was increased until the fibre bending effects were negligible.

The FEM is composed of four parts: three fibre parts and one matrix part. Two different constraints are used between the parts. In the case of perfect bonding ($\mu = 1$) all the parts are tied together using a surface-based tie constraint. In the case of no bonding ($\mu = 0$) a hard-contact constraint is set-up between the surface normals and a tangential frictionless behaviour is chosen. In the case of an intermediate bonding state ($\mu = 0.5$) half of the fibre surface area is not bonded but is allowed to slide frictionless and the rest is perfectly bonded to the matrix. A time independent kink band analysis is performed using Abaqus Standard. A nonlinear arc-length method (Static, Riks) is used to solve the problem due to snap-back and snap-through behaviour in the equilibrium path.

6. Results

The results presented are a combination of results obtained by the semi-analytical kink band model and the finite element model. The constitutive formulation presented in Section 2 is implemented in the semi-analytical numerical scheme presented in Section 3. The boundary conditions and the assumptions behind the finite element model was presented in Section 5. The behaviour and material parameters of the constituents used in the two models was presented in Section 4. The only deviation between the material parameters is the elastic modulus of the matrix constituent. As explained in Section 5 the Young's modulus for the matrix constituent in the semi-analytical model is normalised by itself and in the FEM it is set to $E^{m(3D)}/E^m = 0.5$. In the semi-analytical model, fibre rotation increments ϕ are specified in the localized band. In the FEM displacement increments is specified on the right side of the structure, Fig. 9 and a solution for the equilibrium path is searched for. Based on the deformed geometry it was possible to calculate the fibre rotation ϕ for a given increment, which was the maximum rotation of the fibres with respect to the x_1 -axis.

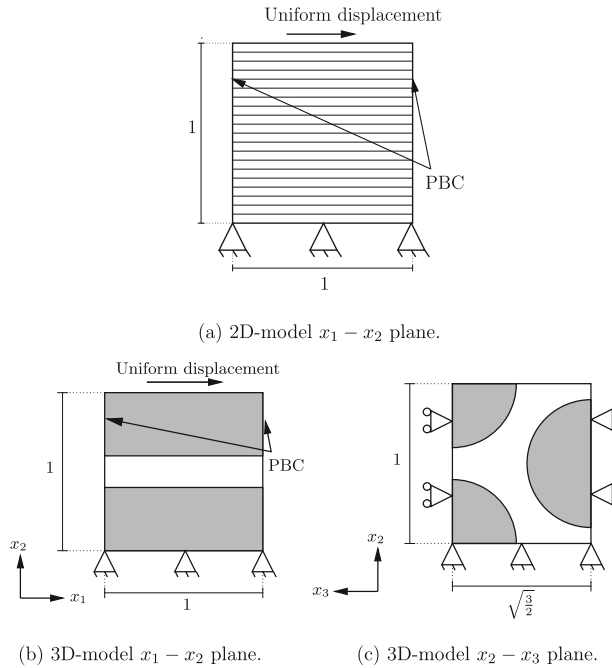


Fig. 7. Boundary conditions for the two-dimensional and three-dimensional FEM used to evaluate the pure shear response.

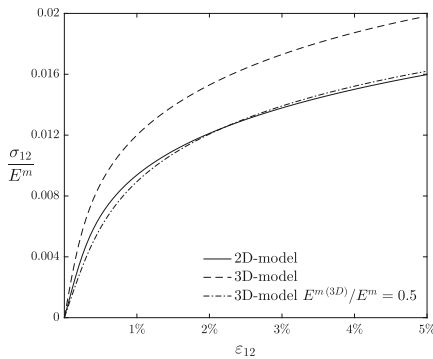


Fig. 8. Shear stress vs shear strain for unit cells exposed to pure shear deformation.

In Figs. 11 and 12 the normalised stress versus fibre rotation is shown for different cohesion levels μ and initial fibre imperfections ϕ_0 . The stress σ_{11} is normalised with the elastic composite shear modulus G calculated according to

$$\frac{1}{G} = \frac{c^f}{G^f} + \frac{c^m}{G^m} \quad (60)$$

where G^f and G^m are the elastic shear moduli of the fibres and matrix, respectively. The shear modulus of the matrix material $G^m = 1/2/(1 + \nu)$ is also normalised by the elastic modulus E^m . The same shear modulus is used for the results from the semi-analytical model as well as the FEM. Results obtained from the analyses with an initial imperfection of $\phi_0 = 0.5^\circ$ are presented in Fig. 11. The results from the FEM are presented in Fig. 11a and from the semi-analytical model in Fig. 11b. Three curves are presented in the figures based on three different cohesion levels μ . The critical stresses obtained for $\mu = 1$ (perfect bonding) and $\mu = 0.5$ (partially bonded) are nearly identical between the two models. For $\mu = 0$ the FEM predicts slightly lower stresses and no stability point is seen on the figure. However, quite good quantitative agreement is seen between the models. In the case of $\mu = 0$ the response of the composite is similar to a model with only matrix and voids. This explains the lower stresses predicted by the FEM where the modulus $E^{m(3D)}/E^m = 0.5$ is used compared to the modulus used for the semi-analytical model which is unity due to the normalisation with E^m . In Fig. 12 the normalised stress versus fibre rotation is shown for an initial imperfection $\phi = 3^\circ$. The same conclusions can be made for the tendencies between the models as for the imperfection $\phi = 0.5^\circ$. There is a good agreement between the FEM and the semi-analytical model for $\mu = 1$ and $\mu = 0.5$. The shear response between the models was aligned in Section 5 for the case of perfect bonding $\mu = 1$. Since the critical kink band stress correlates well between the models it is verified again that the kink band stress depends on the shear response of the composite. Similar tendencies for different cohesion levels are seen between the FEM and semi-analytical model despite the substantial differences in the numerical set-up.

S.P.H. Skovsgaard, H.M. Jensen

Composite Structures 192 (2018) 82–92

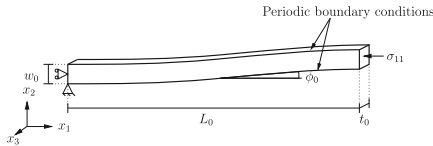


Fig. 9. Three-dimensional visualization of the boundary condition for the finite element kink band model.

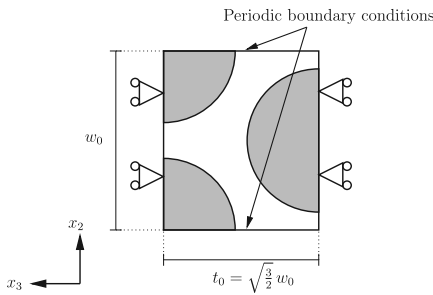


Fig. 10. Boundary condition on the cross section x_2 - x_3 plane for the kink band model.

In Section 2 results obtained by Dève (1997) [20] were presented. Based on the results, an interfacial bonding factor of $\mu = 0.76$ was computed using Eq. (39). The result can be interpreted as that 76% of the fibre surface area was perfectly bonded in the experiment with weakly bonded fibres. The interpretation can be made due to the strong correlation between the FEM and semi-analytical model for values between $\mu = 1$ and $\mu = 0.5$.

In Fig. 13 the critical stress $-\sigma_{11}^c/G$ versus initial fibre imperfection ϕ_0 is shown for different cohesion levels μ . The semi-analytical kink band model is used to generate the results shown. The FEM has not been used to generate comparable results due to the substantial time required per simulation. The critical stresses presented in Fig. 13 are evaluated for the most critical kink band angle β_0 which is found by executing 11 simulations for every imperfection ϕ_0 with different β_0 angles varying from $\beta_0 = 0^\circ$ for $\phi_0 \approx 0^\circ$ to $\beta_0 = 10^\circ$. The critical band inclination varies from $\beta_0 = 0^\circ$ for $\phi_0 \approx 0^\circ$ to $\beta_0 = 7^\circ$ for $\phi_0 = 5^\circ$ in the case of perfect bonding $\mu = 1$. The constitutive model predicts that nearly the same inclinations β_0 is critical for other cohesion levels with the current material parameters. Based on Fig. 13 it can be concluded that the critical stress in the case of imperfect cohesion is also sensitive to fibre imperfections. For all values of μ a steep descent is seen in the beginning going from zero imperfection to increasing initial imperfections. For descending values of μ the curves stabilize around a lower critical value more rapidly.

The time used to solve the semi-analytical- and the finite element simulation is noticeable different. To compare the simulation time then the simulations are run on the same computer: A Lenovo T550 with a i7-5600 Processor (2.6 GHz) with 16 GB of memory (RAM). A typical simulation using the semi-analytical model takes approximately 20 s

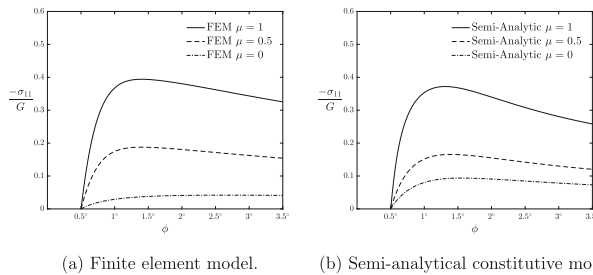


Fig. 11. Non-dimensional stress versus fibre rotation ϕ , for an initial fibre imperfection of $\phi_0 = 0.5^\circ$ with different bonding parameters μ .

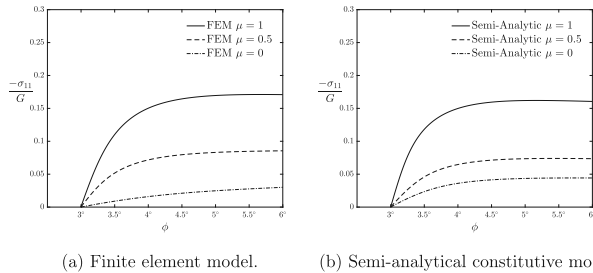


Fig. 12. Non-dimensional stress versus fibre rotation ϕ , for an initial fibre imperfection of $\phi_0 = 3^\circ$ with different bonding parameters μ .

S.P.H. Skovsgaard, H.M. Jensen

Composite Structures 192 (2018) 82–92

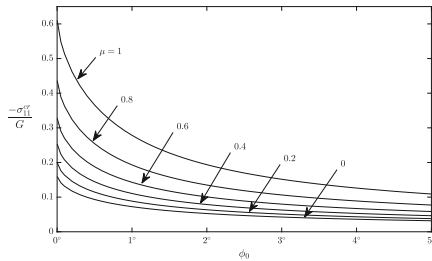


Fig. 13. Normalised critical kink band stress $-\sigma_{II}^c/G$ versus initial fibre imperfection ϕ_0 for different bonding parameters μ . The critical stresses are shown for the most critical band inclination β_0 .

including post processing for a simulation with 400,000 increments. A typical simulation with the FEM takes about 6 h for a simulation with 400 pseudo time increments. The 6 h of simulation was with the mesh presented in Fig. 6a and as mentioned earlier, periodic boundary conditions were utilized to save computation time.

7. Conclusions

A constitutive model for imperfectly bonded fibre-reinforced composites has been developed. Independent constitutive laws can be used

Appendix A. Velocity gradients $v_{\xi,2}^c$

Using Eq. (12) ($\kappa t_{22}^m = \mu t_{22}^m$) together with Eq. (16) yields

$$\kappa C_{2118}^f v_{\delta,1} + \kappa C_{2128}^f v_{\delta,2} = \mu C_{2118}^m v_{\delta,1} + \mu C_{2128}^m v_{\delta,2}, \quad (A.1)$$

where the Greek letter ξ is used as the free index for $t_{\xi,2}^c$. Rearranging the latter equation and multiplying with $c^m \kappa$ yields

$$c^m \kappa (\kappa C_{2118}^f - \mu C_{2118}^m) v_{\delta,1} + c^m \kappa^2 C_{2128}^f v_{\delta,2} = c^m \kappa \mu C_{2128}^m v_{\delta,2}. \quad (A.2)$$

Rearranging Eq. (11) and multiplying with μC_{2128}^m yields

$$c^m \kappa \mu C_{2128}^m v_{\delta,2} = \mu C_{2128}^m v_{\delta,2} + c^l \mu^2 C_{2128}^m v_{\delta,2}. \quad (A.3)$$

The right side of Eq. (A.2) and the left side of Eq. (A.3) is identical. By combining the equations and isolating terms related to $v_{\delta,2}^c$ leads to

$$M_{\delta 2} v_{\delta,2} = -c^m \kappa (\kappa C_{2118}^f - \mu C_{2118}^m) v_{\delta,1} + \mu C_{2128}^m v_{\delta,2}, \quad (A.4)$$

where $M_{\delta 2}$ is given by Eq. (19). The inverse $H_{\delta 2}$ is given by Eq. (18). The terms $M_{\delta 2}$ and the inverse $H_{\delta 2}$ comply to

$$H_{\delta 2} M_{\delta 2} = \delta_{\gamma\gamma}. \quad (A.5)$$

Using the latter identity together with Eq. (A.4) yields the velocity gradients $v_{\xi,2}^c$ expressed through overall homogenized velocity gradients

$$v_{\xi,2}^c = -c^m \kappa H_{\xi 2} (\kappa C_{2118}^f - \mu C_{2118}^m) v_{\delta,1} + \mu H_{\xi 2} C_{2128}^m v_{\delta,2}. \quad (A.6)$$

Similarly the velocity gradients $v_{\xi,3}^m$ can be determined

$$v_{\xi,3}^m = c^l \mu H_{\xi 3} (\kappa C_{2118}^f - \mu C_{2118}^m) v_{\delta,1} + \kappa H_{\xi 3} C_{2128}^f v_{\delta,2}. \quad (A.7)$$

References

- Bishara M, Vogler M, Rolfe R. Revealing complex aspects of compressive failure of polymer composites Part II: Failure interactions in multidirectional laminates and validation. *Compos Struct* 2017;169:116–28. <http://dx.doi.org/10.1016/j.compstruct.2016.10.091>.
- Kyriakides S, Arsecularatne R, Perry EJ, Liechti KM. On the compressive failure of fiber reinforced composites. *Int J Solids Struct* 1995;32(6–7):689–738. [http://dx.doi.org/10.1016/0020-7683\(94\)00157-R](http://dx.doi.org/10.1016/0020-7683(94)00157-R).
- Wadee MA, Hunt GW, Peletier MA. Kink band instability in layered structures. *J Mech Phys Solids* 2004;52(5):1071–91. <http://dx.doi.org/10.1016/j.jmps.2003.09.026>.
- Zhou HW, Yi HY, Gui LL, Dai GM, Peng RD, Wang HW, Mishnaevsky L. Compressive damage mechanism of GFRP composites under off-axis loading: experimental and numerical investigations. *Compos Part B: Eng* 2013;55:119–27. <http://dx.doi.org/10.1016/j.compositesb.2013.06.007>.
- Nizolek T, Begley M, McCabe R, Avallone J, Mara N, Beyerlein I, Pollock T. Strain fields induced by kink band propagation in Cu-Nb nanolaminate composites. *Acta Mater* 2017;133:303–15. <http://dx.doi.org/10.1016/j.actamat.2017.04.050>. URL <http://www.sciencedirect.com/science/article/pii/S1359645417303427>.
- Nair SN, Dasari A, Yue CY, Narasimalu S. Failure behavior of unidirectional composites under compression loading: Effect of fiber waviness. *Materials* 10 (8). <http://dx.doi.org/10.3390/ma10080909>.
- Rosen BW. Mechanics of composite strengthening. In: *Fiber Composite Materials*, American Society for Metals, Metals Park, OH (1965) 37–75.

S.P.H. Skovsgaard, H.M. Jensen

Composite Structures 192 (2018) 82–92

- [8] Argon AS. Fracture of composites. *Treatise Mater Sci Technol* 1972;79–114.
- [9] Budiansky B. Micromechanics. *Comput Struct* 1983;16(1–4):3–12. [http://dx.doi.org/10.1016/0045-7949\(83\)90141-4](http://dx.doi.org/10.1016/0045-7949(83)90141-4).
- [10] Fleck NA, Budiansky B. Compressive failure of fibre composites due to micro-buckling. In: *Proc. 3rd Symp. on Inelastic Deformation of Composite Materials*; 1991. p. 235–73.
- [11] Slaughter WS, Fleck NA, Budiansky B. Compressive failure of fibre composites: the roles of multi-axial loading and creep. *J Eng Mater Technol* 1993;115(3):308–13. URL<http://www.dtic.mil/cgi-bin/GetTRDoc?AD=ADA265398#page=265>.
- [12] Christoffersen J, Jensen HM. Kink band analysis accounting for the microstructure of fiber reinforced materials. *Mech Mater* 1996;24(4):305–15. [http://dx.doi.org/10.1016/S0167-6636\(96\)00052-X](http://dx.doi.org/10.1016/S0167-6636(96)00052-X).
- [13] Jensen HM. Models of failure in compression of layered materials. *Mech Mater* 1999;31:553–64.
- [14] Jensen HM, Christoffersen J. Kink band formation in fiber reinforced materials. *J Mech Phys Solids* 1997;45(7):1121–36. [http://dx.doi.org/10.1016/S0022-5096\(96\)00126-3](http://dx.doi.org/10.1016/S0022-5096(96)00126-3).
- [15] Hsu S-Y, Vogler T, Kyriakides S. On the axial propagation of kink bands in fiber composites: Part II analysis. *Int J Solids Struct* 1999;36:575–95. [http://dx.doi.org/10.1016/S0020-7683\(98\)00030-4](http://dx.doi.org/10.1016/S0020-7683(98)00030-4).
- [16] Wind JL, Steffensen S, Jensen HM. Comparison of a composite model and an individually fiber and matrix discretized model for kink band formation. *Int J Non-Linear Mech* 2014;67:319–25. <http://dx.doi.org/10.1016/j.jnonlinmec.2014.10.005>.
- [17] Fleck NA, Shu JY. Microbuckle initiation in fibre composites: a finite element study. *J Mech Phys Solids* 1995;43(12):1887–918. [http://dx.doi.org/10.1016/0022-5096\(95\)00057-P](http://dx.doi.org/10.1016/0022-5096(95)00057-P).
- [18] Poulos K, Niorrdson CF. Homogenization of long fiber reinforced composites including fiber bending effects. *J Mech Phys Solids* 2016;94:433–52. <http://dx.doi.org/10.1016/j.jmps.2016.04.010>.
- [19] Skovsgaard SPH, Jensen HM. Three-dimensional constitutive model for elastic-plastic behaviour of fibre-reinforced composites. *Int J Solids Struct* 2018;1–13. <http://dx.doi.org/10.1016/j.ijsolstr.2018.01.032>.
- [20] Dève HE. Compressive strength of continuous fiber reinforced aluminum matrix composites. *Acta Mater* 1997;45(12):5041–6. [http://dx.doi.org/10.1016/S1359-6454\(97\)00174-2](http://dx.doi.org/10.1016/S1359-6454(97)00174-2).
- [21] Zhang W, Zhang M, Ochiai S, Gu M. Experimental and simulation investigations of tensile response of (Al₂O₃/Al)/2024Al composite. *Mater Sci Eng. A* 2008;497(1–2):44–50. <http://dx.doi.org/10.1016/j.msea.2008.07.048>.
- [22] Jiang WG, Zhong RZ, Qin QH, Tong YG. Homogenized finite element analysis on effective elastoplastic mechanical behaviors of composite with imperfect interfaces. *Int J Mol Sci* 2014;15(12):23389–407. <http://dx.doi.org/10.3390/jms151223389>.
- [23] Naya F, Herraes M, Gonzalez C, Lopes C, der Veen SV, Pons F. Computational micromechanics of fiber kinking in unidirectional FRP under different environmental conditions. *Compos Sci Technol* 2017;144:26–35. <http://dx.doi.org/10.1016/j.compscitech.2017.03.014>.
- [24] Rice JR. The Localization of plastic deformation. *Theoret Appl Mech* 1976;207–20.
- [25] Stören S, Rice JR. Localized necking in thin sheets. *J Mech Phys Solids* 1975;23(6):421–41. [http://dx.doi.org/10.1016/0022-5096\(75\)90004-6](http://dx.doi.org/10.1016/0022-5096(75)90004-6).
- [26] Hsu S-Y, Vogler TJ, Kyriakides S. Compressive strength predictions for fiber composites. *J Appl Mech* 1998;65(1):7. <http://dx.doi.org/10.1115/1.2789050>. URL<http://appliedmechanics.asmedigitalcollection.asme.org/article.aspx?articleid=1413036>.
- [27] Sørensen KD, Mikkelsen LP, Jensen HM. User subroutine for compressive failure of composites. 2009 Simulia Customer Conference (1965); 2009. p. 618–32.

Chapter 8

P3

Steady-state kink band propagation in layered materials

8.1 Motivation

Kink band formation is the dominant compressive failure mechanism for many fibre-reinforced plastics. As explained in the Introduction, the fibre kinking strength (peak stress) is dominated by the shear yield strength of the composite and fibre misalignments. The formation of a kink band can be divided into different stages; the linear response, incipient kinking, peak stress, transient kinking and steady-state kink band broadening. The fibre misalignments are difficult to estimate for a composite, thereby the exact compressive strength is unknown. As the fibre misalignments increase in a composite, the peak strength decrease and approach the propagation stress at kink band broadening. The stress at steady-state broadening can thereby be seen as a lower bound for the critical compressive stress in composites.

The current publication deals with the investigation of the propagating instability known as kink band broadening using three different methods. A case study is conducted with material parameters from Kyriakides et al. (1995). The original source of the publication is: (Skovsgaard and Jensen, 2018c).

8.2 Method

The phenomenon is investigated using three substantially different methods. A finite element model (Chapter 2), a semi-analytical (Chapter 3) and an analytical model (Chapter 4) are used.

The FE-model consists of three layers; one matrix and two half fibre layers. Periodic boundary conditions are applied on a skewed mesh to get a band inclination β . An arc-length solver in Abaqus/CAE is used to solve the non-linear problem. The semi-analytical approach is based on a kink band model developed by Jensen and Christoffersen (1997) with a homogenised constitutive formulation from Christoffersen and Jensen (1996). The analytical model, as described in Chapter 4, results in one transcendental equation for the steady-state propagation state and is derived by evaluating the internal and external work at the steady-state.

8.3 Contribution

The contributions to the publication comprise: the development of a finite element model with periodic boundary conditions on a skewed mesh; the development of an analytical model for kink band broadening; conducting the simulations and writing the paper.

8.4 Main findings

Initially, two main findings are the analytical model and the FE-model. The three models are in mutually agreement. The models predict that for small band inclinations β , the predictions for the fibre rotation ϕ exceeds the usual assumed linear relation at fibre lock-up $\phi = 2\beta$. Furthermore, it was found that the stress at kink band broadening is largely influenced by the matrix Poisson's ratio and the uni-axial tangent modulus at large strains.

Simon P. H. Skovsgaard

Department of Engineering,
Aarhus University,
Inge Lehmanns Gade 10,
Aarhus C 8000, Denmark
e-mail: sphs@eng.au.dk

Henrik Myhre Jensen

Professor
Department of Engineering,
Aarhus University,
Inge Lehmanns Gade 10,
Aarhus C 8000, Denmark
e-mail: hmj@eng.au.dk

Steady-State Kink Band Propagation in Layered Materials

Failure by steady-state kink band propagation in layered materials is analyzed using three substantially different models. A finite element model and an analytical model are developed and used together with a previously introduced constitutive model. A novel methodology for simulating an infinite kink band is used for the finite element model using periodic boundary conditions on a skewed mesh. The developed analytical model results in a transcendental equation for the steady-state kink band propagation state. The three models are mutually in good agreement and results obtained using the models correlate well with the previous experimental findings. [DOI: 10.1115/1.4039573]

1 Introduction

It is well known that fiber-reinforced composites can have a considerably lower compressive strength compared to the strength in tension. Fleck [1] made a review of different failure modes and stated that the compressive strength of carbon fiber-epoxy laminates are often less than 60% of their tensile strength. Long fiber-reinforced composites with a ductile and tough resin material are prone to fail by plastic microbuckling which leads to the formation of one or several kink bands. A recent investigation of the compressive failure of fiber composites was conducted by Bishara et al. [2]. They investigated the compressive failure of a multidirectional fiber composite experimentally and numerically. They concluded that the failure initiated from the 0deg ply is due to the formation of a kink band. The failure was followed by delamination, fiber-matrix debonding, and fiber cracking and was initiated in the vicinity of the kink band.

The critical compressive strength of fiber composites is sensitive to initial fiber misalignments which is concluded by several authors, e.g., Budiansky [3] and Jensen and Christoffersen [4]. In an experimental kink band study conducted by Vogler and Kyriakides [5] on a AS4/PEEK composite, they showed that a kink band was formed under compressive loading in the direction of the fibers. A kink band was formed with a band orientation of $\beta = 15\text{deg}$ and an initial band width of 250 fibers ($\approx 2\text{mm}$). This initial state was followed by a state, where the band inclination remained constant and the width of the band was broadened under a constant applied stress. This is referred to as the steady-state kink band broadening stress or propagation stress. After the critical stress is reached, an unstable rotation of the fibers within a localized band will begin. Due to the kinematics of the developing kink band, a multi-axial strain state increases with increasing rotation. This unstable rotation stops when it is energetically preferable to increase the bandwidth instead of an increased rotation due to strain hardening.

With increasing fiber imperfections, the compressive strength of composites will tend toward the stress at steady-state kink band broadening. The stress at steady-state is insensitive to fiber imperfections and does only depend on the constitutive behavior of the composite. The steady-state broadening stress can thereby be seen as a lower bound for the critical compressive stress in composites with moderately large or unknown fiber imperfections. This lower bound of critical stress can be used to create fail safe structures and it is thereby valuable to predict the propagation state accurately.

A study of the kink band instability in a carbon fiber composite was conducted by Evans and Adler [6]. They analyzed different steps in the formation of kink bands including the steady-state propagation phenomenon. They observed the relation $\phi \approx 2\beta$, where ϕ is the relative rotation of the fibers within the kink band and β is the kink boundary orientation. The relation $\phi = 2\beta$ was later used by Moran et al. [7] to predict the kink band broadening strength of a carbon fiber-reinforced composite. Furthermore, they assumed inextensible fibers and incompressibility of the composite. Hsu et al. [8] investigated the propagation of kink bands experimentally and these findings were compared with a micro-mechanical finite element model (FE-model) in Hsu et al. [9] and reasonable correlation was seen between the studies as concluded by the authors. Kink band broadening has also been observed in materials other than glass- and carbon fiber-reinforced composites, e.g., Attwood et al. [10] observed broadening in a composite made of ultrahigh molecular weight polyethylene. Poulsen et al. conducted a compression experiment on clear wood and observed kink band broadening. Later, Byskov et al. [11] introduced a semi-analytical and a finite element model to investigate kink band propagation and the emphasis was given to wood and fiber composites. A recent experimental investigation of the propagation state was conducted by Nizolek et al. [12] on a Cu-Nb composite and they also observed the relation $\phi \approx 2\beta$.

An investigation of steady-state kink band propagation is conducted in the present paper using three different models with substantial difference in model configuration. A finite element model and an analytical kink band model are proposed in the present study and are compared with a previously developed semi-analytical kink band model [13]. In contrast to the previous investigations, the relation $\phi = 2\beta$ is not used to obtain the steady-state quantities. Instead, an approach of work balance is utilized for the semi-analytical and the analytical kink band model. Furthermore, the composites are assumed compressible which yields a more realistic estimate of the steady-state quantities. In contrast to the FE-model and semi-analytical model, inextensible fibers are assumed for the analytical model. In the present study, it is assumed that the matrix constituent deforms elastic/plastic in the whole regime, which can be unrealistic for some matrix materials due to the shear strains required for band broadening. Information about imperfect bonding and splitting between the fiber/matrix interface can be included as in the studies conducted by Prabhakar and Waas [14] and Skovsgaard and Jensen [15]. Information about splitting and imperfect bonding has not been included in the current study, but good correlation is still seen between experiments and the results obtained as seen in

Manuscript received January 22, 2018; final manuscript received March 5, 2018; published online March 30, 2018. Assoc. Editor: Shaoxing Qu.

Sec. 5. A case study is conducted with material parameters obtained by Kyriakides et al. [16] for a AS4/PEEK composite.

The paper is organized in six sections. The boundary conditions and material parameters for the proposed FE-model are presented in Sec. 2. Furthermore, a brief introduction into different steps in the formation of kink bands is included in Sec. 2. A constitutive model developed by Christoffersen and Jensen [17] was used to study kink band broadening in Jensen [13]. The latter model will be known as the semi-analytical model and is introduced in Sec. 3. An analytical model is introduced in Sec. 4 with the assumption of inextensible fibers together with simple assumptions for the stress-strain relations. Results generated by the three models are presented in Sec. 5 and Sec. 6 concludes the paper.

2 Finite Element Model

A micromechanical FE-model is developed that can predict the steady-state kink band propagation state for a layered material or fiber-reinforced composite. The FE-model can in general be used to investigate both the critical stress and the kink band propagation stress for arbitrary compositions of two constituents. In the current paper, emphasis will be given to composites with relatively stiff fibers embedded in a ductile resin material with a lower stiffness and yield strength as in the case of glass- and carbon fiber-reinforced polymers.

In Fig. 1, an overview of the geometry and boundary conditions for the developed FE-model is shown. The commercial finite element software ABAQUS 6.14 is used for the simulations. ABAQUS/STANDARD is used, which is an implicit general-purpose finite element program that tracks the equilibrium path during deformation. A nonlinear arc-length method (Static, Riks) is used to solve the problem due to snap-back and snap-through behavior in the equilibrium path. As seen in Fig. 1(a), the model consists of three layers: one matrix or resin layer and two half fiber layers. Periodic boundary conditions are utilized between the upper and the lower part of the geometry to simulate an infinite kink band as illustrated in Fig. 1(b). Inclined periodic boundary conditions are applied using a skewed mesh as shown in Fig. 2. The geometry ends are vertical to accomplish a simple state of uniaxial loading. The

vertical ends are far away from the deformation of interest, which is why the periodicity can be interpreted as shown in Fig. 1(b). The study of an infinite kink band is in line with the classical methodology done by previous authors (Budiansky [3], Moran et al. [7] and Jensen [13]). The fixed geometries used in the simulations are

$$L_0 = 1, \quad w_0 = 0.01, \quad b_0 = 0.5, \quad \phi_0 = 2 \text{ deg} \quad (1)$$

where L_0 and w_0 are the initial length and width of the geometry, respectively. The width $w_0 = 0.01$ was chosen based on a convergence study, where the width was decreased until the fiber bending stiffness became insignificant. The length b_0 controls the extent of the imperfection. Small values of b_0 lead to a localization of the imperfection toward the geometry center and ϕ_0 is the largest misalignment angle in the imperfection. The geometries b_0 , ϕ_0 , and β are used to introduce an initial fiber imperfection according to

$$\begin{aligned} x_2 &= \frac{1}{2} \phi_0 \left(\frac{-b_0}{2 \cos \beta} - X_2 \tan \beta \right) \quad \text{for } X_1 < X_{1,\min}, \\ x_2 &= \frac{1}{2} \phi_0 \left[\frac{b_0}{2 \pi \cos \beta} \sin \left(\frac{2 \pi \cos \beta}{b_0} (X_1 + X_2 \tan \beta) \right) + X_1 \right] \\ &\quad \text{for } X_{1,\min} < X_1 < X_{1,\max}, \\ x_2 &= \frac{1}{2} \phi_0 \left(\frac{b_0}{2 \cos \beta} - X_2 \tan \beta \right) \quad \text{for } X_1 > X_{1,\max} \end{aligned} \quad (2)$$

where x_i are deformed coordinates and X_i are undeformed coordinates described in a coordinate system placed in the geometry center. The imperfection is a modified version of the one introduced by Sørensen et al. [18]. The quantities $X_{1,\min}$ and $X_{1,\max}$ are the X_1 -coordinates where the imperfections begin and end. Since an inclination β is introduced, $X_{1,\min}$ and $X_{1,\max}$ are functions of the X_2 -coordinate and are calculated according to

$$X_{1,\min} = \frac{-b_0}{2 \cos \beta} - X_2 \tan \beta, \quad X_{1,\max} = \frac{b_0}{2 \cos \beta} - X_2 \tan \beta \quad (3)$$

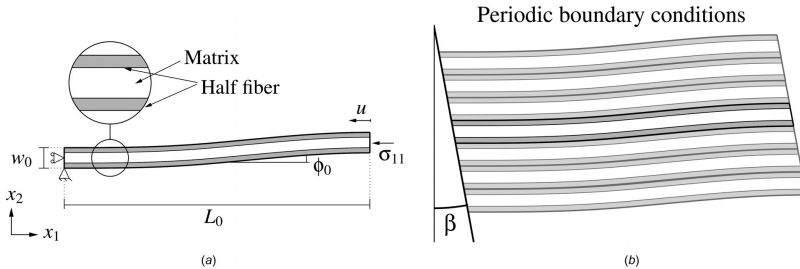


Fig. 1 (a) Geometry of the micromechanical finite element model. The darker regions represent the fiber constituent. (b) Sketch of overall deformation.

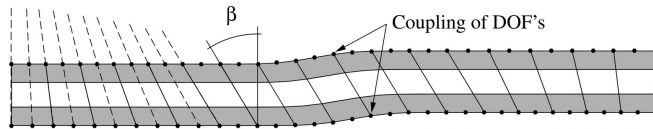


Fig. 2 Illustration of mesh used in the finite element simulations. The coupling of the nodes locks the deformation in an orientation β .

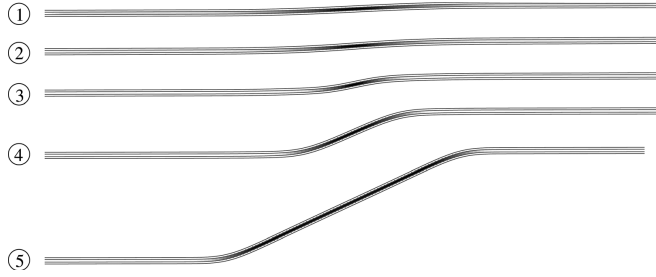


Fig. 3 Shear strain in matrix constituent, ε_{12} , for five deformation stages during simulation for a geometry with an initial imperfection $\phi_0 = 2$ deg and a band orientation $\beta = 10$ deg for a single strip as shown in Fig. 1(a)

The fiber imperfection is introduced as a waviness using trigonometric functions, Eq. (2), where ϕ_0 is the largest angle with respect to the X_1 -axis. Simpler initial imperfections have been introduced earlier with promising results, e.g., Prabhakar and Waas [14] and Davidson and Waas [19]. Simple imperfections as the latter are not feasible in the current study. Both the band inclination, β , and the geometry ends outside $X_{1,\min}$ and $X_{1,\max}$, where the fibers are aligned with the X_1 -axis, are of great importance to obtain the steady-state stress using the current model.

The critical stress is highly sensitive to the initial imperfection (e.g., Wind et al. [20] and Fleck and Budiansky [21]), but the steady-state broadening stress is independent of this imperfection, and therefore, ϕ_0 and b_0 can be chosen arbitrarily. The geometric parameter β is the inclination of the infinite band with respect to the X_2 -axis.

To account for an inclination β of the infinite band at the steady-state, the coupling of the nodes is chosen as seen in Fig. 2. Toward the ends of the geometry, the nodes are aligned with the X_2 -axis, and from here, the mesh gradually becomes more skewed until the coupled nodes are orientated with an angle of β with respect to the X_2 -axis. The displacement degrees-of-freedom are coupled in pairs between the upper and the lower part using the Lagrange multiplier method in ABAQUS. This leads to identical displacements of coupled nodes during deformation. Even though that the band orientation, β , at initiation and at steady-state is in general different, this will not influence the results at kink band propagation when using a deformation theory for the constituent behavior.

The material parameters used in the simulations are normalized values of the one obtained by Kyriakides et al. [16] and are given by

$$\begin{aligned} c^f &= 0.6, & E^f/E^m &= 35, & \nu^f &= 0.263, \\ \nu^m &= 0.356, & \sigma^{y,m}/E^m &= 0.013, & n^m &= 4 \end{aligned} \quad (4)$$

where c^f is the volume fraction of fibers. Superscripts $(\bullet)^m$ and $(\bullet)^f$ correspond to values associated with the matrix and fiber constituents. E^m and E^f are the matrix and fiber Young's moduli, respectively, ν^m and ν^f are Poisson's ratios for the two constituents. The parameters $\sigma^{y,m}$ and n^m are the reference yield stress and hardening exponent for the matrix constituent, respectively. The nonlinear response of the matrix is described using a rate-independent J_2 -deformation theory, where the uni-axial response is described using a Ramberg–Osgood relation according to

$$\varepsilon = \frac{\sigma}{E} + \frac{3\sigma^2}{7E} \left(\frac{\sigma}{\sigma^y} \right)^n \quad (5)$$

where ε and σ are the uni-axial strain and stress, respectively, σ^y is a reference yield stress, and n is a hardening exponent.

Young's modulus of the fibers is 35 times the one for the matrix. Due to this ratio, most of the bending will be carried out by the fibers and the matrix will obtain high shear straining. Eight-noded biquadratic elements are used for the fibers with full integration, and four-noded bilinear elements with full integration are used for the matrix. Even though the elements are incompatible, the errors will be small. The use of both eight- and four-noded elements for the matrix has been compared and showed identical results. It has been possible to obtain a larger part of the post-buckling response using four-noded elements and are therefore chosen.

Five typical deformation stages are shown in Fig. 3, where the darker regions correspond to high shear straining of the matrix. The five stages are designated in Fig. 4, where the stress $-\sigma_{11}$ normalized by the elastic shear modulus for the composite G is shown as a function of the normalized end shortening u/L_0 . Both σ_{11} and u are illustrated in Fig. 1(a). The response is initially linear until the critical stress, σ_{11}^c , is reached at stage (2). The snapback behavior is clearly seen from stages (2) to (3), where both the stress and the end displacement decrease. A large rotation of the fibers is also observed between stages (2) and (3). The fibers rotate further and lock-up at stage (4). From stage (4) to (5), the end shortening keeps increasing under steady-state conditions, at constant loading and the fibers maintain the same steady-state rotation ϕ^{ss} .

The same five stages are shown in Fig. 5, where the normalized stress $-\sigma_{11}/G$ is shown as a function of fiber rotation ϕ . In the current figure, the band orientation is set to $\beta = 10$ deg and the fibers lock-up in an angle approximately $\phi^{ss} \approx 25$ deg. The influence of multiple element layers within the matrix layer has been investigated and is shown in Fig. 6 for two simulations with 1 and 4 element layers, respectively. The results are almost indistinguishable due to an identical initial response. Only a small part of the post-buckling regime was obtainable with the FE-model with multiple element layers due to lack of numerical convergence. Apparently, the simulations tend toward the same steady-state response. One element layer is considered sufficient to obtain the steady-state results presented in Sec. 5.

3 Semi-Analytical Model

Jensen [13] investigated kink band broadening using a constitutive model developed in Christoffersen and Jensen [17]. The model is reused in this paper for comparison with the other models. The current model will be known as the semi-analytical model. The theory behind this approach will be outlined here.

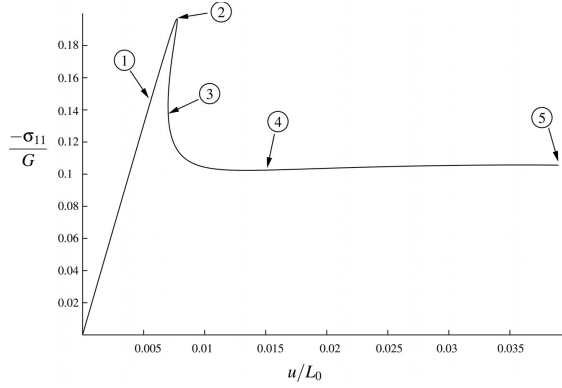


Fig. 4 Applied normalized stress $-\sigma_{11}/G$ as a function of normalized end shortening u/L_0 for simulation with a band orientation $\beta = 10$ deg. The five deformation stages in Fig. 3 are designated.

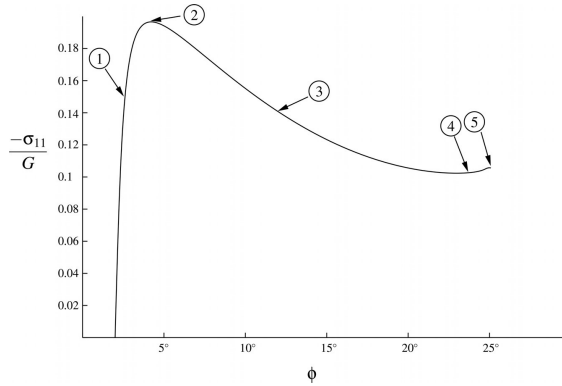


Fig. 5 Applied normalized stress $-\sigma_{11}/G$ as a function of fiber rotation ϕ for simulation with a band orientation $\beta = 10$ deg. The five deformation stages in Fig. 3 are designated.

3.1 General Relations. The index notation is adopted, where Latin indices, i.e., i, j, k , take values 1, 2, 3, and Greek indices, i.e., α, β, γ , take values 1, 2. The constitutive model is described using a time-independent constitutive law, where the constituents can be described independently. The strain rate and the spin are given by

$$\dot{\epsilon}_{ij} = \frac{1}{2}(v_{i,j} + v_{j,i}), \quad \omega_{ij} = \frac{1}{2}(v_{i,j} - v_{j,i}) \quad (6)$$

where $v_{i,j}$ are the velocity gradients. The rate of nominal stresses, \dot{i}_{ij} , is

$$\dot{i}_{ij} = \overset{\circ}{\tau}_{ij} + \omega_{jk}\tau_{ik} + \omega_{ik}\tau_{kj} - \tau_{ik}v_{i,k} \quad (7)$$

where τ_{ij} are Kirchhoff stresses and $\overset{\circ}{\tau}_{ij}$ are components of the Jaumann rate of Kirchhoff stresses determined by $\overset{\circ}{\tau}_{ij} = L_{ijkl}\epsilon_{kl}$. Combining the latter two equations, the relation between the rate of nominal stresses and velocity gradients is

$$\dot{i}_{ij} = C_{ijkl}v_{i,k} \quad (8)$$

where C_{ijkl} are components of nominal moduli

$$C_{ijkl} = L_{ijkl} - \frac{1}{2}\tau_{kj}\delta_{il} - \frac{1}{2}\tau_{ij}\delta_{lk} - \frac{1}{2}\tau_{il}\delta_{kj} + \frac{1}{2}\tau_{ik}\delta_{lj} \quad (9)$$

and δ_{ij} denotes Kronecker delta. The moduli L_{ijkl} are to be described using a time-independent constitutive law, e.g., J_2 -

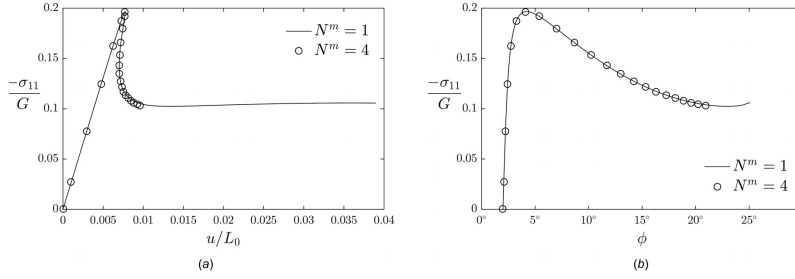


Fig. 6 Nondimensional stress versus normalized end displacement u/L_0 and fiber rotation ϕ for two simulations with 1 and 4 matrix element layers: (a) stress versus displacement and (b) stress versus fiber rotation

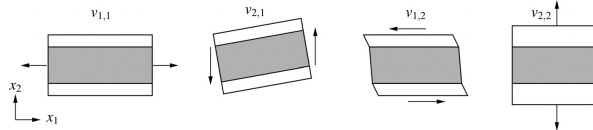


Fig. 7 Assumed deformation of the constituents based on overall deformations of the composite. For illustrative purpose, the gray constituent reacts stiffer, as in the case of a fiber embedded in a polymer matrix.

deformation and J_2 -flow theory. The moduli are to comply to the symmetries

$$L_{ijkl} = L_{jikl} = L_{ijlk} \quad (10)$$

as required by moment equilibrium $\tau_{ij} = \tau_{ji}$ and symmetry of the strain rates $\dot{\epsilon}_{ij} = \dot{\epsilon}_{ji}$. The relation between Kirchhoff stresses τ_{ij} and Cauchy stresses σ_{ij} is

$$\tau_{ij} = J \sigma_{ij} \quad (11)$$

where J is the Jacobian giving the volume ratio $J = V/V_0$. The relation between the rate of Cauchy stresses and the rate of nominal stresses is

$$\dot{\sigma}_{ij} = \dot{t}_{ij} - \sigma_{ij} v_{k,k} + v_{i,k} \sigma_{kj} \quad (12)$$

3.2 Constitutive Model by Christoffersen and Jensen. The constitutive model is based on the assumption that material lines parallel with the fibers are subjected to a common stretching and rotation as shown in the first two geometries in Fig. 7. In addition, the strains in the normal direction are averages of the constituent strains which can be written using velocity gradients

$$\begin{aligned} v_{1,1} &= v_{1,1}^f = v_{1,1}^m, & v_{2,1} &= v_{2,1}^f = v_{2,1}^m, \\ v_{1,2} &= c^f v_{1,2}^f + c^m v_{1,2}^m, & v_{2,2} &= c^f v_{2,2}^f + c^m v_{2,2}^m \end{aligned} \quad (13)$$

where c^f and c^m are, respectively, volume fractions of fiber and matrix complying to $c^f + c^m = 1$. A lack of superscript refers to overall composite quantities. It is required that the fibers are aligned with the x_1 -axis prior to deformation. Additionally, the constitutive model is based on that the constituents transmit identical traction normal to the fibers and together with overall equilibrium leads to

$$\begin{aligned} \dot{t}_{21} &= \dot{t}_{21}^f = \dot{t}_{21}^m, & \dot{t}_{22} &= \dot{t}_{22}^f = \dot{t}_{22}^m \\ \dot{t}_{11} &= c^f \dot{t}_{11}^f + c^m \dot{t}_{11}^m, & \dot{t}_{12} &= c^f \dot{t}_{12}^f + c^m \dot{t}_{12}^m \end{aligned} \quad (14)$$

By assuming a relationship between the rate of nominal stresses and velocity gradients in the form of Eq. (8) for both the constituents and composite, Christoffersen and Jensen [17] showed that the composite behavior could be described according to

$$\begin{aligned} C_{\alpha\beta\gamma\delta} &= c^f C_{\alpha\beta\gamma\delta}^f + c^m C_{\alpha\beta\gamma\delta}^m \\ &\quad - c^f c^m (C_{\alpha\beta 2\epsilon}^f - C_{\alpha\beta 2\epsilon}^m) H_{\epsilon\delta} (C_{2\gamma\delta}^f - C_{2\gamma\delta}^m) \\ M_{\alpha\beta} &= c^m C_{2\alpha 2\beta}^f + c^f C_{2\alpha 2\beta}^m \end{aligned} \quad (15)$$

where $H_{\alpha\beta}$ is the inverse of $M_{\alpha\beta}$ complying to

$$H_{\alpha\gamma} M_{\gamma\beta} = \delta_{\alpha\beta} \quad (16)$$

The velocity gradients $v_{i,2}^f$ for the constituents can be calculated using the velocity gradients $v_{i,j}$ for the composite

$$\begin{aligned} v_{i,2}^f &= -c^m H_{\epsilon\delta} (C_{2\epsilon 1\delta}^f - C_{2\epsilon 1\delta}^m) v_{\delta,1} + H_{\epsilon\delta} C_{2\epsilon 2\delta}^m v_{\delta,2} \\ v_{i,2}^m &= c^f H_{\epsilon\delta} (C_{2\epsilon 1\delta}^f - C_{2\epsilon 1\delta}^m) v_{\delta,1} + H_{\epsilon\delta} C_{2\epsilon 2\delta}^f v_{\delta,2} \end{aligned} \quad (17)$$

Equation (14) further entails the equalities

$$c^f \sigma_{11}^f + c^m \sigma_{11}^m = \sigma_{11}, \quad \sigma_{12}^f = \sigma_{12}^m = \sigma_{12}, \quad \sigma_{22}^f = \sigma_{22}^m = \sigma_{22} \quad (18)$$

3.3 Constituent Behavior. The behavior of the matrix constituent is described using a J_2 -deformation theory introduced by Støren and Rice [22]. The tensor of instantaneous moduli, L_{ijkl} , is given by

$$L_{ijkl} = G_s(\delta_{ik}\delta_{jl} + \delta_{il}\delta_{jk}) + \left(K - \frac{2}{3}G_s\right)\delta_{ij}\delta_{kl} - \frac{4}{3}(G_s - G_t)m_{ij}m_{kl} \quad (19)$$

where m_{ij} are

$$m_{ij} = \frac{1}{2\sigma_{\text{eq}}}s_{ij} \quad (20)$$

Here, σ_{eq} is the equivalent von Mises stress and s_{ij} are components of the deviatoric stress tensor

$$\sigma_{\text{eq}} = \sqrt{3J_2}, \quad J_2 = \frac{1}{2}s_{ij}s_{ij}, \quad s_{ij} = \sigma_{ij} - \delta_{ij}\frac{\sigma_{kk}}{3} \quad (21)$$

The bulk modulus K , the shear secant modulus G_s , and the tangent shear modulus G_t presented in Eq. (19) are calculated based on

$$G_s = \left(\frac{3}{E_s} - \frac{1-2\nu}{E}\right)^{-1}, \quad G_t = \left(\frac{3}{E_t} - \frac{1-2\nu}{E}\right)^{-1} \quad (22)$$

$$K = \frac{E}{3(1-2\nu)}$$

where ν is Poisson's ratio and E is Young's modulus. The tangent modulus E_t and the secant modulus E_s are calculated using the Ramberg–Osgood relation

$$E_t = E \left(1 + \frac{3n}{7} \left(\frac{\sigma_{\text{eq}}}{\sigma_y}\right)^{n-1}\right)^{-1} \quad (23)$$

$$E_s = E \left(1 + \frac{3}{7} \left(\frac{\sigma_{\text{eq}}}{\sigma_y}\right)^{n-1}\right)^{-1}$$

where σ_y is a reference yield stress. The material parameters used for the matrix constituent in the constitutive model are identical with parameters used in the FE-model. Additionally, a restriction is set on the Ramberg–Osgood curve, so the tangent modulus does not become smaller than a specified value $E_{t,\text{min}}$. The limit stress, σ_L , and strain, ε_L , where the minimum tangent modulus is reached, are

$$\varepsilon_L = \frac{\sigma_L}{E} + \frac{3\sigma_y}{7E} \left(\frac{\sigma_L}{\sigma_y}\right)^n \quad (24)$$

$$\sigma_L = \sigma_y \left[\left(\frac{E}{E_{t,\text{min}}} - 1\right) \frac{7}{3n} \right]^{\frac{1}{n-1}}$$

For an equivalent uni-axial stress $\sigma_{\text{eq}} < \sigma_L$, the moduli given by Eq. (23) are to be used and

$$E_t = E_{t,\text{min}},$$

$$E_s = \frac{\sigma_{\text{eq}}}{\varepsilon_{\text{eq}}}, \quad (25)$$

$$\varepsilon_{\text{eq}} = \frac{\sigma_{\text{eq}} - \sigma_L}{E_{t,\text{min}}} + \varepsilon_L$$

are to be used for $\sigma_{\text{eq}} > \sigma_L$. The fiber constituent is assumed to behave linear elastic and can therefore be described by the generalized Hooke's law

$$L_{ijkl} = \frac{E}{1+\nu} \left(\frac{1}{2}(\delta_{ik}\delta_{jl} + \delta_{il}\delta_{jk}) + \frac{\nu}{1-2\nu}\delta_{ij}\delta_{kl} \right) \quad (26)$$

3.4 Kink Band Propagation. In Jensen and Christoffersen [4], the authors created a semi-analytical kink band model to investigate the critical compressive stress of fiber-reinforced

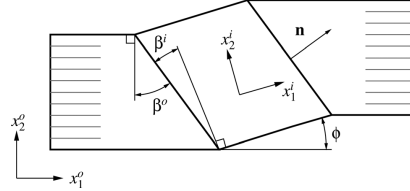


Fig. 8 Kink band geometry with two coordinate systems, one inside the band and one outside represented with $(\bullet)^i$ and $(\bullet)^o$ respectively

composite using the constitutive model from Christoffersen and Jensen [17]. The semi-analytical kink band model was further developed in Jensen [23] to investigate steady-state kink band broadening. The formulation of the kink band model will be repeated here for completeness.

It is assumed that a kink band has formed where the fibers inside the band have rotated relative to the fibers outside the band. The material inside and outside the kink band is represented with two different coordinate systems as shown in Fig. 8, where $(\bullet)^i$ and $(\bullet)^o$ represent quantities associated with the material inside and outside the band, respectively. The stress state outside and inside the band is updated according to

$$\dot{\sigma}_{\alpha\beta} = C_{\alpha\beta\gamma\delta} v_{\delta,\gamma} - \sigma_{\alpha\beta} v_{\gamma,\gamma} + v_{\alpha,\gamma} \sigma_{\gamma\beta} \quad (27)$$

which corresponds to Eq. (12). Here, $\dot{\sigma}_{ij}$ or v_{ij} or a combination of these can be given by external loading. The band orientation is updated according to

$$\dot{\beta} = -v_{\alpha,\beta} n_\alpha t_\beta \quad (28)$$

Here, n_α and t_α are the unit normal and unit tangent to the band, respectively,

$$[n_1^i, n_2^i] = [\cos(\beta^o), \sin(\beta^o)], \quad [t_1^i, t_2^i] = [-\sin(\beta^o), \cos(\beta^o)],$$

$$[n_1^o, n_2^o] = [\cos(\beta^i), \sin(\beta^i)], \quad [t_1^o, t_2^o] = [-\sin(\beta^i), \cos(\beta^i)] \quad (29)$$

The band orientations β^o and β^i are displayed in Fig. 8. The band orientation inside the band can also be written as $\beta^i = \beta^o - \phi$. The fiber volume fractions are updated according to

$$\varepsilon^{f,o} = \varepsilon^{f,o} e^{m,o} \left(\frac{f_{2,2}^{f,o}}{2.2} - v_{2,2}^{m,o} \right), \quad n_\alpha^i e_\alpha^i \frac{e^{f,i}}{A^{f,i}} = n_\alpha^o e_\alpha^o \frac{e^{f,o}}{A^{f,o}}, \quad (30)$$

where e_α are components of a unit vector parallel with the fibers. $A^{f,i}$ and $A^{f,o}$ are areas of fibers inside and outside the band, respectively.

In the current simulation, the fiber rotation increment, $\dot{\phi}$, is a prescribed quantity. Continuity of tractions and displacements is required during the increment $\dot{\phi}$. The fibers are aligned with the x_1 -axis initially and during rotation which leads to

$$v_{2,1}^o = 0, \quad v_{2,1}^i = 0 \quad (31)$$

Continuity of displacements across the boundary requires

$$w_{\alpha,\beta}^i v_\alpha^i t_\beta^i = v_{\alpha,\beta}^o v_\alpha^o t_\beta^o, \quad w_{\alpha,\beta}^i n_\alpha^i t_\beta^i = v_{\alpha,\beta}^o n_\alpha^o t_\beta^o \quad (32)$$

where $w_{\alpha,\beta}^i$ is the velocity gradients seen from a system that stays stationary during deformation

$$w_{\alpha,\beta}^j = v_{\alpha,\beta}^j + \Omega_{\alpha\beta}, \quad \Omega_{21} = -\Omega_{12} = \dot{\phi}, \quad \Omega_{11} = \Omega_{22} = 0 \quad (33)$$

Continuity of traction rates across the kink band boundary requires that

$$\begin{aligned} C_{\alpha\beta;\gamma\delta}^j w_{\delta,\gamma}^i n_x^j n_\beta^i &= C_{\alpha\beta;\gamma\delta}^o v_{\delta,\gamma}^o n_x^o n_\beta^o, \\ C_{\alpha\beta;\gamma\delta}^j w_{\delta,\gamma}^i n_x^j l_\beta^i &= C_{\alpha\beta;\gamma\delta}^o v_{\delta,\gamma}^o n_x^o l_\beta^o \end{aligned} \quad (34)$$

Equations (31) and (32) together with the latter equation yield six boundary conditions. The last two boundary conditions used in the simulation are

$$v_{1,2}^o = 0, \quad \dot{\phi}_{22}^o = 0 \quad (35)$$

which implicitly lead to the boundary condition $\dot{\sigma}_{12}^o = 0$.

After the initiation of the kink band, the fibers locks-up in a given angle and the easiest way of further deformation is by steady-state broadening of the developed kink band, which is seen in Fig. 3, stages (4) and (5). When the kink band broadens, the end shortening is increased as well. The work done per unit volume by external forces during propagation is

$$W^E = S_{\alpha\beta}^o \Delta E_{\alpha\beta}^* \quad (36)$$

where $\Delta E_{\alpha\beta}^*$ denotes the difference in Lagrangian strain inside and outside the kink band evaluated in the base material. The stresses $S_{\alpha\beta}^o$ are the work conjugate of the evaluated strains. It is assumed that the problem is primarily mechanical and thereby the steady-state can be found by a balance of mechanical work. In addition, it is assumed that the final stress state can be described using a deformation theory. Based on the assumptions, the work done per unit volume in the kink band is

$$W^I = \int_{\varepsilon^o}^{\varepsilon^i} \sigma_{\alpha\beta} d\varepsilon_{\alpha\beta} \quad (37)$$

where ε^o and ε^i are strain states outside and inside the kink band, respectively. The external work given by Eq. (36) and the internal work by Eq. (37) are evaluated for every increment $\dot{\phi}$ and when the equality

$$W^E = W^I \quad (38)$$

is satisfied, the propagation state is obtained. The evaluation of the internal and external work is shown in Fig. 9 as a function of fiber rotation, ϕ . In the example shown, the band orientation is fixed in an angle $\beta^o = 20$ deg. A steady-state lock-up angle $\phi^{ss} = 41$ deg is achieved. The current formulation includes finite extension of the fibers and volumetric changes of the composite, which are in contrast with many of the previous studies of kink band propagation. No prior restrictions are set regarding, e.g., the relation between the fiber rotation, ϕ , and the band orientation, β .

4 Analytical Model

An analytical model is proposed to estimate the steady-state propagation parameters. The model is based on some of the same assumptions made for the model presented in Sec. 3. In the current section, the fibers are assumed to be inextensible and incompressible, which are distinct from the assumptions for the two previous models. In Fig. 10, an illustration of a kink band that broadens with rigid fibers is shown. During a broadening increment, a material piece with length, l , rotates around a point, A. This leads to an end shortening of $u = l(1 - \cos \phi)$. The work done per unit volume by the external forces is

$$W^E = -\sigma_{11}^o (1 - \cos \phi) \quad (39)$$

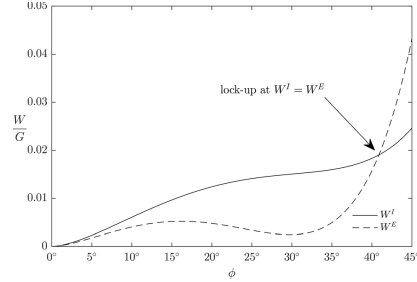


Fig. 9 External W^E and internal work W^I per unit volume as a function of fiber rotation ϕ for the semi-analytical model. The band orientation is set to $\beta = 20$ deg in the current simulation. The lock-up condition, $W^I = W^E$, is marked in the figure.

Continuity of stresses across the band requires that

$$\sigma_{\alpha\beta}^i n_x^i n_\beta^i = \sigma_{\alpha\beta}^o n_x^o n_\beta^o, \quad \sigma_{\alpha\beta}^i n_x^i l_\beta^i = \sigma_{\alpha\beta}^o n_x^o l_\beta^o \quad (40)$$

Assuming that only σ_{11}^i is present in the base material, the latter equations can be written explicitly as

$$\begin{aligned} \sigma_{11}^i \cos(\beta^o - \phi)^2 + 2\sigma_{12}^i \cos(\beta^o - \phi)\sin(\beta^o - \phi) \\ + \sigma_{22}^i \sin(\beta^o - \phi)^2 &= \sigma_{11}^o \cos(\beta^o)^2 \\ -\sigma_{11}^i \cos(\beta^o - \phi)\sin(\beta^o - \phi) + \sigma_{12}^i (\cos(\beta^o - \phi)^2 - \sin(\beta^o - \phi)^2) \\ + \sigma_{22}^i \cos(\beta^o - \phi)\sin(\beta^o - \phi) &= -\sigma_{11}^o \cos(\beta^o)\sin(\beta^o) \end{aligned} \quad (41)$$

Using the latter equations, the stresses σ_{11}^i and σ_{11}^o can be written in terms of the other quantities

$$\begin{aligned} \sigma_{11}^i &= -\sigma_{12}^i [\cot \phi + \tan(\beta^o - \phi)] - \sigma_{22}^i \cot \phi \tan(\beta^o - \phi), \\ \sigma_{11}^o &= -\sigma_{12}^i [\cot \phi + \tan \beta^o] - \sigma_{22}^i [\cot \phi \tan \beta^o - 1] \end{aligned} \quad (42)$$

The work per unit volume done by external forces can thereby be written in terms of σ_{12}^i and σ_{22}^i as

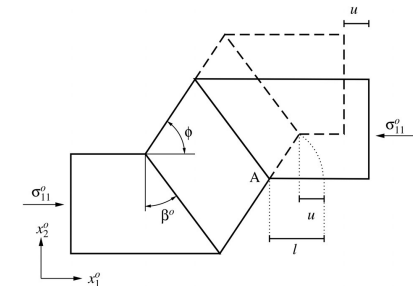


Fig. 10 Illustration of steady-state kink band propagation in the case of inextensible fibers. The geometry with dashed lines represents a propagated configuration.

$$W^E = \sigma_{12}^i [\cot\phi + \tan\beta^o](1 - \cos\phi) + \sigma_{22}^i [\cot\phi \tan\beta^o - 1](1 - \cos\phi) \quad (43)$$

The work per unit volume done by the stresses in the kink band is in the general case given by Eq. (37). It is assumed that only σ_{11}^i is present in the base material, and when the fibers are rigid, no straining and thereby no work is done by the base material. This leads to the simplification

$$W^I = \int_0^{\epsilon} \sigma_{\alpha\beta} d\epsilon_{\alpha\beta} \quad (44)$$

Further, the fibers are assumed rigid within the kink band and does no work. The inextensible fibers lead to $v_{1,1}^i = v_{1,1}^m = 0$. The internal work can be simplified to

$$W^I = 2c^m \int_0^{\epsilon} \sigma_{12}^m d\epsilon_{12}^m + c^m \int_0^{\epsilon} \sigma_{22}^m d\epsilon_{22}^m \quad (45)$$

Here, the superscript $(\cdot)^i$ is omitted since only stresses and strains inside the band are included in the equation. When regarding rigid fibers, continuity of displacements given by Eq. (32) can be simplified to

$$w_{\alpha,\beta}^i t_{\alpha}^i t_{\beta}^i = 0, \quad w_{\alpha,\beta}^m n_{\alpha}^m t_{\beta}^i = 0 \quad (46)$$

Expanding the repeated indices and utilizing $v_{2,1}^i = 0$ and $v_{1,1}^i = 0$ leads to

$$v_{1,2}^i \sin(\beta^o - \phi) \cos(\beta^o - \phi) + v_{2,2}^i \cos(\beta^o - \phi)^2 = 0, \quad (47)$$

$$v_{1,2}^i \cos(\beta^o - \phi)^2 + v_{2,2}^i \cos(\beta^o - \phi) \sin(\beta^o - \phi) = \dot{\phi}$$

and solving for $v_{1,2}^i$ and $v_{2,2}^i$ yields

$$v_{1,2}^i = \dot{\phi}, \quad v_{2,2}^i = \dot{\phi} \tan(\beta^o - \phi) \quad (48)$$

The same kinematics was obtained by Budiansky and Fleck [24] when the shear strain rate in the base material is zero. The strain rates are then

$$\dot{\epsilon}_{12}^i = \frac{\dot{\phi}}{2}, \quad \dot{\epsilon}_{22}^i = \dot{\phi} \tan(\beta^o - \phi) \quad (49)$$

Integrating the latter equation with respect to ϕ , and assuming a fixed band orientation β^o , yields the total logarithmic strain in the kink band

$$\epsilon_{12}^i = \frac{\phi}{2}, \quad \epsilon_{22}^i = \ln\left(\frac{\cos(\beta^o - \phi)}{\cos\beta^o}\right) \quad (50)$$

Figure 11 gives an illustrative example of a material point that propagates from a stage outside the band and into the band. On the configuration to the right, the stage inside the band is rotated to an amount of ϕ to show the total deformation. In the illustration, where $\phi = 60$ deg and $\beta = 20$ deg, the composite will be compressed going from stage (1) to (2). When $\phi = 2\beta$, no volumetric straining will be present. $\phi = 2\beta$ is the lock-up condition used in many of the previous studies of kink-band propagation, while the present study uses $W^I = W^E$.

The transverse strain and the shear strain of the composite are assumed to be an average of the constituents

$$\epsilon_{12} = c^m \epsilon_{12}^m + c^f \epsilon_{12}^f, \quad \epsilon_{22} = c^m \epsilon_{22}^m + c^f \epsilon_{22}^f \quad (51)$$

Based on the assumption of rigid fibers (i.e., $\epsilon_{12}^f = \epsilon_{22}^f = 0$), the matrix strain can be determined based on the overall strain according to

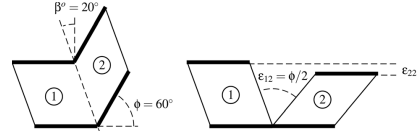


Fig. 11 Strain state outside (state 1) and inside the kink band (state 2). The strain state inside the kink band is rotated 60 deg on the configuration to the right.

$$\epsilon_{12}^m = \frac{\epsilon_{12}}{c^m}, \quad \epsilon_{22}^m = \frac{\epsilon_{22}}{c^m} \quad (52)$$

In the general case, the determination of the stress state depends on the total strain field and the strain history. For simplicity, it is assumed that the shear stress only depends on the shear strain $\sigma_{12}^m(\epsilon_{12}^m)$ and the transverse stress only depends on the transverse strain $\sigma_{22}^m(\epsilon_{22}^m)$, which is motivated by the findings from the FE-model. This is in general not true, but as shown in Sec. 5, this assumption leads to promising results. It is assumed that the transverse response is linear elastic, then the stress σ_{22}^m can be obtained using Eq. (26)

$$\sigma_{22}^m = \frac{E^m(1 - \nu^m)}{(1 + \nu^m)(1 - 2\nu^m)} \epsilon_{22}^m \quad (53)$$

Plane strain conditions, $\epsilon_{33}^m = 0$, and inextensible fibers, $\epsilon_{11}^m = 0$, are assumed in the calculations. The shear stress, σ_{12}^m , is assumed to follow a bilinear curve according to

$$\sigma_{12}^m = 2G_1 \epsilon_{12}^m \quad \text{for} \quad \epsilon_{12}^m < \epsilon_{12}^{m,y}$$

$$\sigma_{12}^m = 2G_2 \epsilon_{12}^m + \sigma_{12}^{m,y} \left(1 - \frac{G_2}{G_1}\right) \quad \text{for} \quad \epsilon_{12}^m > \epsilon_{12}^{m,y} \quad (54)$$

where G_1 and G_2 are the shear moduli before and after yielding, respectively, $G = E/(2(1 + \nu))$. The relation between the shear yield stress, σ_{12}^m , and the uni-axial yield stress $\sigma^{y,m}$ is

$$\sigma_{12}^{m,y} = \sqrt{\frac{1}{3}} \sigma^{y,m} \quad (55)$$

where a von Mises yield criterion is assumed. The uni-axial stress-strain relationship for the matrix material in the FE-model and the semi-analytical model follow a Ramberg-Osgood relation. For comparison with the other models, the first modulus is set to $E_1 = E^m$ and the second modulus is $E_2 = E_{t,\min}^m$. The yield stress used in the analytical model is based on

$$\sigma^{y,m} = E_1 \frac{\sigma_L - E_2 \epsilon_L}{E_1 - E_2} \quad (56)$$

Here, σ_L and ϵ_L are calculated using Eq. (24). The quantities are displayed in Fig. 12.

The traction continuity required in the constitutive model entailed Eq. (18). In line with the constitutive model, $\sigma_{22}^m = \sigma_{22}$ and $\sigma_{12}^m = \sigma_{12}$ are viable assumptions. Equations (53) and (54) together with Eq. (43) yield

$$W^E = (2C_2\phi + C_3)[\cot\phi + \tan\beta^o](1 - \cos\phi) + 2C_4 \ln\left(\frac{\cos(\beta^o - \phi)}{\cos\beta^o}\right)[\cot\phi \tan\beta^o - 1](1 - \cos\phi) \quad (57)$$

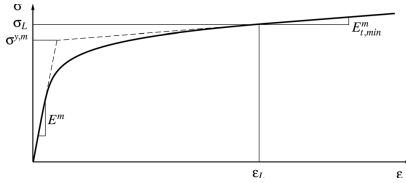


Fig. 12 Stress-strain relation for the semi-analytical and analytical models. The bilinear curve represents the response used for the analytical model.

where the constants are introduced

$$C_2 = \frac{G_2}{2c^m}, \quad C_3 = \sigma_{12}^{m,y} \left(1 - \frac{G_2}{G_1} \right), \quad (58)$$

$$C_4 = \frac{E^m(1-\nu^m)}{2c^m(1+\nu^m)(1-2\nu^m)}$$

The work done per unit volume by internal forces can be rewritten using the stresses σ_{12}^m and σ_{22}^m given by Eqs. (53) and (54) together with the strain increments $d\epsilon_{12}^m$ and $d\epsilon_{22}^m$ given by Eq. (49)

$$W^I = \int_0^{\phi^y} \frac{G_1}{c^m} \phi d\phi + \int_{\phi^y}^{\phi} \frac{G_2}{c^m} \phi + \sigma_{12}^{m,y} \left(1 - \frac{G_2}{G_1} \right) d\phi + \int_0^{\phi} \frac{E^m(1-\nu^m)}{c^m(1+\nu^m)(1-2\nu^m)} \ln \left(\frac{\cos(\beta^o - \phi)}{\cos \beta} \right) \tan(\beta^o - \phi) d\phi \quad (59)$$

where ϕ^y is the fiber angle when matrix yielding happens and is given by

$$\phi^y = \frac{2c^m \sigma_{12}^{m,y} (1+\nu^m)}{E^m \sqrt{3}} \quad (60)$$

Solving the integrals in Eq. (59) yields

$$W^I = C_1 (\phi^y)^2 + C_2 (\phi^2 - (\phi^y)^2) + C_3 (\phi - \phi^y) + C_4 \ln \left(\frac{\cos(\beta^o - \phi)}{\cos \beta} \right)^2 \quad (61)$$

where the constant has been introduced

$$C_1 = \frac{G_1}{2c^m} \quad (62)$$

The two equations derived for the external and internal work per unit volume, W^E and W^I , given by Eqs. (57) and (61) are analytical expressions, where the only variable is the fiber rotation ϕ . An evaluation of equations is shown in Fig. 13, where a fixed band orientation $\beta^o = 20$ deg is chosen. By comparing Figs. 9 and 13, good agreement is seen in the approximation of the external work, the internal work, and the intersection point between the curves. It does not seem possible to solve the transcendental equation $W^I(\phi) = W^E(\phi)$ for the steady-state lock-up angle ϕ^{ss} analytically based on the current formulation. The steady-state fiber angle ϕ^{ss} can be found either by using a nonlinear solver or by increasing ϕ and evaluating $W^I(\phi) - W^E(\phi)$ a sufficient number of times until $W^I(\phi) - W^E(\phi) \approx 0$.

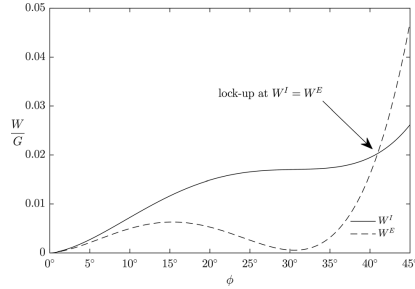


Fig. 13 External, W^E , and internal work W^I done per unit volume as a function of the fiber rotation ϕ for the analytical model. The band orientation is set to $\beta = 20$ deg. The lock-up condition, $W^I = W^E$, is marked in the figure.

5 Results

The three models presented in Secs. 2-4 will be used to estimate the steady-state kink band propagation stress σ_{11}^{ss} and lock-up angle ϕ^{ss} . The band orientation β is regarded as a fixed value in all of the three models. In several of the previous studies, the lock-up criteria $\phi = 2\beta$ were used in the calculations of the steady-state stress based on experimental observations of $\phi \approx 2\beta$. Vogler and Kyriakides [5] observed fiber rotations of $\phi > 2\beta$ under stress, and when the stress was removed, the fibers relaxed to $\phi \approx 2\beta$. Also, early experimental studies of kink band broadening conducted by Evans and Adler showed $\phi > 2\beta$. In Fig. 14 is the lock-up angle ϕ^{ss} shown as a function of the band orientation β_0 .

Results obtained using the three models are displayed in the figure, and all of the models predict a larger fiber rotation than 2β . The conventional lock-up angle $\phi = 2\beta$ is also displayed in the figure for comparison. The predictions of the fiber angles go asymptotically toward the conventional lock-up angle for large band orientations β . The steady-state broadening stress, $-\sigma_{11}^{ss}/G$, as a function of band orientation, β , shown in Fig. 15, predicts that the propagation stress lowers with increasing band orientations. Jensen [13] showed that the propagation stress σ_{11}^{ss} is sensitive to the minimum tangent modulus $E_{t,min}^m$, which was introduced in Sec. 3.3. The modulus $E_{t,min}^m/E^m = 1/100$ is used for the

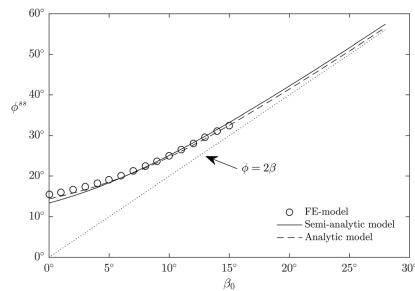


Fig. 14 Steady-state lock-up angle ϕ^{ss} as a function of initial kink band orientation β_0 . Results are shown for the three models presented. Additionally, the conventional assumption of fiber lock-up $\phi = 2\beta$ is included for comparison.

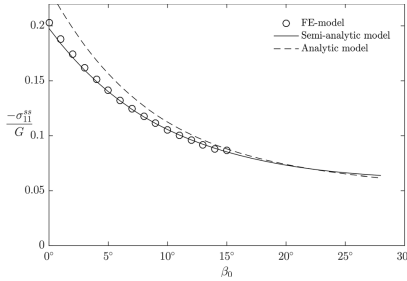


Fig. 15 Normalized steady-state kink band propagation stress $-\sigma_{11}^{ss}/G$ as a function of initial kink band orientation β_0 . Results are shown for the three models presented.

semi-analytical and analytical models. Beyond that, the material parameters given by Eq. (4) are used.

High correlation is seen between the three models despite the significant difference in model setup. The relatively high fiber stiffness $E^f/E^m = 35$ is used for the FE-model, and semi-analytical model and inextensible fibers are assumed for the analytical model. This is one of the explanations for the deviations seen in Fig. 15 between the models for small band orientations. It was only possible to obtain steady-state results between $\beta_0 = 0$ deg – 15 deg using the FE-model due to convergence problems at higher kink band orientations.

Figure 16 indicates that the lock-up angle ϕ^{ss} is sensitive to Poisson's ratio of the matrix material ν^m . The figure shows the results obtained for $\beta_0 = 10$ deg varying from $\nu^m = 0$ to $\nu^m = 0.5$. In the limit of $\nu^m = 0.5$, the matrix constituent becomes incompressible. All the models tend toward $\phi = 2\beta$ when the matrix constituent becomes incompressible, which agrees with assumptions made by previous authors.

Figure 17 argues that also the propagation stress σ_{11}^{ss} is sensitive to Poisson's ratio of the matrix. The highest stress is obtained for a nearly incompressible matrix. Previous authors have used the assumption of an incompressible composite (i.e., $\nu^m = 0.5$). Based on the current results, the propagation stresses predicted by previous authors are nonconservative for $\nu^m < 0.5$. The broadening stress $-\sigma_{11}^{ss}/G = 0.1$ for $\nu^m = 0.35$ is predicted using the FE-model, which is 80% of the stress predicted using $\nu^m \approx 0.5$.

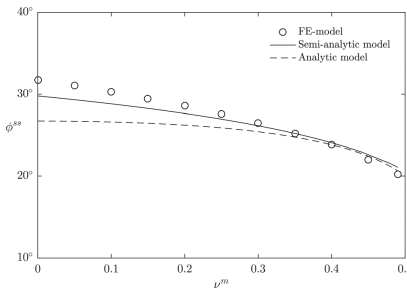


Fig. 16 Steady-state lock-up angle ϕ^{ss} as a function of Poisson's ratio for the matrix constituent ν^m . The initial band orientation is $\beta_0 = 10$ deg. Results are shown for the three models presented.

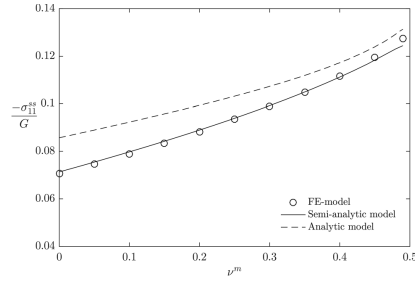


Fig. 17 Normalized steady-state kink band propagation stress $-\sigma_{11}^{ss}/G$ as a function of Poisson's ratio for the matrix constituent ν^m . The initial band orientation is $\beta_0 = 10$ deg. Results are shown for the three models presented.

Finally, the propagation stress as a function of the minimum tangent modulus $E_{t,min}^m/E^m$ is illustrated in Fig. 18 for the most critical band orientation, β_0 . When the kink band is fully formed and locked-up, the shear strain within the matrix is in the order $\epsilon_{12}^m = 20\% - 110\%$ depending on the initial band orientation β_0 . For such high strains, the Ramberg–Osgood curve predicts unrealistic low tangent moduli. The tangent modulus is restricted with the results shown in Fig. 18 following the method introduced in Sec. 3.3. The Ramberg–Osgood curves obtained using $E_{t,min}^m = 0.02 - 0.1$ all agree with the measurements of Kyriakides et al. [16] for small strains. The broadening stress is seen to be sensitive to the minimum tangent modulus, which is in line with the results shown in Jensen [13]. It was not possible to make a restriction on the minimum tangent modulus using the build in J_2 -deformation theory in ABAQUS, and results from the FE-model are, therefore, not shown in Fig. 18. A user material could have been used together with ABAQUS to restrict the tangent modulus $E_{t,min}^m$, but this has not been in the scope. The analytical model predicts critical band orientations in the range $\beta_0 = 28$ deg – 32 deg, where the semi-analytical model predicts orientations in the range $\beta_0 = 20$ deg – 26 deg. The higher band orientations, β_0 , predicted by the analytical model result in lower steady-state stresses which is in line with the results shown in Fig. 15.

Evans and Adler [6] observed several kink bands with orientations in the range $\beta = 20$ deg – 25 deg and fiber rotation between $\phi = 45$ deg and 60 deg for a carbon/carbon composite, which is in

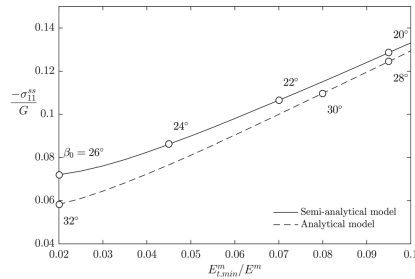


Fig. 18 Normalized steady-state kink band propagation stress $-\sigma_{11}^{ss}/G$ as a function of normalized minimum tangent modulus for the matrix constituent $E_{t,min}^m/E^m$. Results are shown for the semi-analytical and analytical models.

the range predicted by the three models. Moran et al. [7] observed $\beta = 20 \text{ deg} - 25 \text{ deg}$ and $\phi = 40 \text{ deg} - 45 \text{ deg}$ for a IM7/PEEK composite. They observed a propagation stress in the range $-\sigma_{11}^s/G = 0.052 - 0.086$ which corresponds to a band inclination $\beta = 20 \text{ deg} - 30 \text{ deg}$ according to the predictions in Fig. 15 using the proposed models. A recent experimental study of kink band propagation was conducted by Nizolek et al. [12] using a Cu/Nb nanolaminate composite with a band orientation $\beta \approx 27 \text{ deg}$ and a fiber rotation of $\phi \approx 60 \text{ deg}$. The relation of $\phi > 2\beta$ predicted by the three models correlates with their findings. It has not been possible to compare the steady-state propagation stress with the study done by Nizolek et al. [12] since the necessary material data for the current models were not present in the paper.

6 Conclusions

Steady-state kink band propagation in layered materials or fiber-reinforced composites has been analyzed. Three substantially different models have been used to investigate the phenomenon and two of the models have been developed during this study. A two-dimensional finite element model has been developed that includes inclined periodic boundary conditions to investigate a propagating infinite kink band. Steady-state was obtained using the FE-model, when the fiber rotation inside the kink band stopped rotating and overall band broadening was observed instead. An analytical model resulting in one transcendental equation for the propagation state has been proposed. The analytical model is based on the assumptions of inextensible fibers and a simple stress-strain relation inspired by observations from the FE-model. In contrast to models proposed by several previous authors, no assumptions regarding the fiber lock-up kinematics have been utilized. The condition for fiber lock-up is based on a balance of external and internal work in line with the methodology proposed by Jensen [13]. The two introduced models are used together with the constitutive model introduced by Jensen [13].

The three models have been used to investigate the steady-state lock-up angle and the propagation stress based on different parameters. Initially, the influence of the band orientation, β_0 , has been investigated, which is a prescribed quantity using the proposed models. The rotation of the fibers at lock-up exceeds the linear relation assumed by previous authors and the current findings correlate with experimental observations. It can be concluded that including compressibility of the matrix constituent has a large influence on the lock-up angle and the propagation stress. In line with the findings by Jensen [13], the matrix properties at large strains have a large influence of the propagation stress especially the tangents modulus and Poisson's ratio.

Funding Data

- Thomas B. Thriges fund.

References

- [1] Fleck, N., 1997, "Compressive Failure of Fibre Composites," *Adv. Appl. Mech.*, **33**, pp. 43-117.
- [2] Bishara, M., Vogler, M., and Rolles, R., 2017, "Revealing Complex Aspects of Compressive Failure of Polymer Composites—Part II: Failure Interactions in Multidirectional Laminates and Validation," *Compos. Struct.*, **169**, pp. 116-128.
- [3] Budiansky, B., 1983, "Micromechanics," *Comput. Struct.*, **16**(1-4), pp. 3-12.
- [4] Jensen, H. M., and Christoffersen, J., 1997, "Kink Band Formation in Fiber Reinforced Materials," *J. Mech. Phys. Solids*, **45**(7), pp. 1121-1136.
- [5] Vogler, T., and Kyriakides, S., 1997, "Initiation and Axial Propagation of Kink Bands in Fiber Composites," *Acta Mater.*, **45**(6), pp. 2443-2454.
- [6] Evans, A. G., and Adler, W. F., 1978, "Kinking as a Mode of Structural Degradation in Carbon Fiber Composites," *Acta Metall.*, **26**(5), pp. 725-738.
- [7] Moran, P. M., Liu, X. H., and Shih, C. F., 1995, "Kink Band Formation and Band Broadening in Fiber Composites Under Compressive Loading," *Acta Metall. Mater.*, **43**(8), pp. 2943-2958.
- [8] Vogler, T. J., and Kyriakides, S., 1999, "On the Axial Propagation of Kink Bands in Fiber Composites—Part I: Experiments," *Int. J. Solids Struct.*, **36**(4), pp. 557-574.
- [9] Hsu, S.-Y., Vogler, T. J., and Kyriakides, S., 1999, "On the Axial Propagation of Kink Bands in Fiber Composites—Part II: Analysis," *Int. J. Solids Struct.*, **36**(4), pp. 575-595.
- [10] Attwood, J. P., Fleck, N. A., Wadley, H. N. G., and Deshpande, V. S., 2015, "The Compressive Response of Ultra-High Molecular Weight Polyethylene Fibres and Composites," *Int. J. Solids Struct.*, **71**, pp. 141-155.
- [11] Bykov, E., Christoffersen, J., Dencker Christensen, C., and Sand Poulsen, J., 2002, "Kinkband Formation in Wood and Fiber Composites: morphology and Analysis," *Int. J. Solids Struct.*, **39**(13-14), pp. 3649-3673.
- [12] Nizolek, T., Begley, M., McCabe, R., Avallone, J., Mara, N., Beyerlein, I., and Pollock, T., 2017, "Strain Fields Induced by Kink Band Propagation in Cu-Nb Nanolaminate Composites," *Acta Mater.*, **133**, pp. 303-315.
- [13] Jensen, H. M., 1999, "Analysis of Compressive Failure of Layered Materials by Kink Band Broadening," *Int. J. Solids Struct.*, **36**(23), pp. 3427-3441.
- [14] Prabhakar, P., and Waas, A. M., 2013, "Interaction Between Kinking and Splitting in the Compressive Failure of Unidirectional Fiber Reinforced Laminated Composites," *Compos. Struct.*, **98**, pp. 85-92.
- [15] Skovgaard, S. P. H., and Jensen, H. M., 2018, "Constitutive Model for Imperfectly Bonded Fibre-Reinforced Composites," *Compos. Struct.*, **192**, pp. 82-92.
- [16] Kyriakides, S., Arseculeratne, R., Perry, E. J., and Liechti, K. M., 1995, "On the Compressive Failure of Fiber Reinforced Composites," *Int. J. Solids Struct.*, **32**(6-7), pp. 689-738.
- [17] Christoffersen, J., and Jensen, H. M., 1996, "Kink Band Analysis Accounting for the Microstructure of Fiber Reinforced Materials," *Mech. Mater.*, **24**(4), pp. 305-315.
- [18] Sørensen, K. D., Mikkelsen, L. P., and Jensen, H. M., 2009, "User Subroutine for Compressive Failure of Composites," *Simulia Customer Conference*, London, May 18-21, pp. 618-632.
- [19] Davidson, P., and Waas, A. M., 2014, "Mechanics of Kinking in Fiber-Reinforced Composites Under Compressive Loading," *Math. Mech. Solids*, **21**(6), pp. 667-684.
- [20] Wind, J. L., Steffensen, S., and Jensen, H. M., 2014, "Comparison of a Composite Model and an Individually Fiber and Matrix Discretized Model for Kink Band Formation," *Int. J. Non-Linear Mech.*, **67**, pp. 319-325.
- [21] Fleck, N. A., and Budiansky, B., 1991, "Compressive Failure of Fibre Composites Due to Microbuckling," *Third Symposium on Inelastic Deformation of Composite Materials*, Troy, NY, May 29-June 1, pp. 235-273.
- [22] Stören, S., and Rice, J. R., 1975, "Localized Necking in Thin Sheets," *J. Mech. Phys. Solids*, **23**(6), pp. 421-441.
- [23] Jensen, H. M., 1999, "Models of Failure in Compression of Layered Materials," *Mech. Mater.*, **31**(9), pp. 553-564.
- [24] Budiansky, B., and Fleck, N., 1993, "Compressive Failure of Fibre Composites," *J. Mech. Phys. Solids*, **41**(1), pp. 183-211.

Chapter 9

P4

A general approach for the study of kink band broadening in fibre composites and layered materials

9.1 Motivation

Kink band formation is the dominant compressive failure mechanism for many fibre-reinforced plastics. The stress at steady-state kink band broadening can be seen as a lower bound for the compressive strength in composites. Three substantially different models were developed in Skovsgaard and Jensen (2018c) to study kink band broadening. In the latter article, the emphasis was given to a carbon fibre-reinforced thermoplastic. Kink band broadening is observed in different composites at different length scales e.g. Nizolek et al. (2017) observed broadening in a Cu/Nb nanolaminate and Attwood et al. (2015) observed kink band broadening, that was developed between plies within a composite made from ultra-high molecular weight polyethylene.

In the current publication, the three models developed in [P3] are used within two case studies with different composite material behaviour to study steady-state kink band broadening and to compare with experimental results. The original source of the publication is: (Skovsgaard and Jensen, 2019).

9.2 Method

The unit cell finite element model, the semi-analytical model and the analytical model are used, that are described in Chapter 2, 3 and 4, respectively.

The finite element model consists of three layers: one matrix layer and two half fibre layers; or one elastic-plastic layer and two half elastic layers. Periodic boundary conditions are applied on a skewed mesh to get a band inclination β . An arc-length solver is used to solve the non-linear problem. The semi-analytical model is based on a kink band model developed by Jensen and Christoffersen (1997) with a homogenised constitutive formulation from Christoffersen and Jensen (1996). The analytical model, as described in Chapter 4, results in one transcendental equation for the steady-state propagation state and is derived by evaluating the internal and external work at the steady-state.

9.3 Contribution

The contributions to the publication comprise: the use of the three models in two case studies; changing the constitutive relations for the semi-analytical model to be used on the ply-level; conducting the simulations and writing the paper.

9.4 Main findings

The three models, initially introduced in [P3], were in the current publication reformulated and presented in a format that emphasises that the models can, equivalently, be used for layered materials and for fibre composites. Furthermore, the results indicate that the models can be used across different length scales to study kink band broadening.

In the first case study, a carbon fibre-reinforced PEEK composite is used to study the effect of fibre diameters upon kink band broadening using the unit cell FE-model. The predictions for the steady-state propagation stress, using the FE-model, approach the prediction by the semi-analytical model with decreasing fibre diameters. The semi-analytical model does not include intrinsic size effects.

In the second case study, the semi-analytical model and the analytical model are used to study kink band broadening for a composite made from ultra-high molecular weight polyethylene. The two models predict steady-state quantities that are in good agreement with the experimental observations done by Attwood et al. (2015) and Liu et al. (2014).

European Journal of Mechanics / A Solids 74 (2019) 394–402



Contents lists available at ScienceDirect

European Journal of Mechanics / A Solids

journal homepage: www.elsevier.com/locate/ejmsol

A general approach for the study of kink band broadening in fibre composites and layered materials[☆]

Simon P.H. Skovsgaard^{*}, Henrik Myhre Jensen

Department of Engineering, Aarhus University, Inge Lehmanns Gade 10, 8000, Aarhus C, Denmark

ARTICLE INFO

Keywords:

Kink band broadening
Maxwell construction
Propagating instability
Strain localisation
Size effects

ABSTRACT

The progressive non-linear mode of deformation known as steady-state kink band broadening is analysed for fibre composites and layered materials. The mode of deformation is investigated using an analytical, a semi-analytical model and a finite-element model. The semi-analytical model is based on a constitutive model, where independent material behaviour can be given for two constituents. The analytical model assumes rigid fibres and results in a transcendental equation for the kink band broadening state. Both the analytical and semi-analytical model use a Maxwell construction to determine the steady-state, which is done by equating the internal and external work. The influence of size-effects are explored and two case studies are performed; in the first case study the finite element model and semi-analytical model are used upon a carbon fibre-reinforced PEEK composite. The second case study is on a layered composite made from ultra high molecular-weight polyethylene fibres with a kink band developing on ply level.

1. Introduction

Laminates built from unidirectional fibre-reinforced composites will have an anisotropic material behaviour, where the amount of anisotropy mainly depends on the difference in fibre/matrix material properties and the fibre to matrix bonding. There can be a large difference in the tension, shear and transverse moduli in fibre-reinforced composites and together with the heterogeneities, this creates many possible material failures. Fibre-reinforced composites have high stiffness and strength in tension but can become unstable in compression and the compressive strength is often only 50–60% of their tensile strength. A frequently observed failure is kink band formation, where a band of material has rotated relative to the surrounding base material. The formation of kink bands has been observed in several experiments with compressive loading in the direction of the fibres including Kyriakides et al. (1995) and Piggott and Harris (1980) and others.

As described by Liu et al. (1996), the formation of a kink band can be divided into different stages; the linear response, incipient kinking, peak stress, transient kinking and steady-state kink band broadening. So far, the main focus has been to estimate the peak compressive stress for design purposes either by the use of experimental, numerical or analytical approaches. The compressive strength in unidirectional fibre composites is largely influenced by imperfections in the form of fibre

misalignments interacting with matrix plasticity as described in Fleck and Budiansky (1991) and Fleck et al. (1995).

Steady-state kink band broadening is a propagating instability on the material scale and can be put into the same category as neck propagation in polymers during stretching e.g. (1983) G'Sell (1983) and channelling cracks in layered materials e.g. Beuth (1992). The stress at band broadening can be seen as the lower bound of the compressive strength in fibre composites and is independent of fibre misalignments. The broadening stress can thus be used as a fail-safe compressive strength for structural applications and it does only depend on the material behaviour. Kink band broadening has been observed in different composites. In the early work of Evans and Adler (1978), they observed band broadening in a carbon fibre composite. Liu et al. (1996) observed band broadening in a IM7/PEEK carbon fibre composites, where the fibres stayed intact during broadening. Kink band broadening and transverse kink propagation was studied by Budiansky et al. (1998). Later, Byskov et al., (2002) performed a compressive study on wood (Norway Spruce) where kink band broadening was observed. Kink band broadening was observed to propagate on ply level in a composite made of ultra-high molecular-weight polyethylene (UHMWPE) fibres by Attwood et al. (2015). In a recent study conducted by Nizolek et al. (2017) they observed band broadening in a Cu–Nb nanolaminate composite.

[☆] This article was presented at the IUTAM Symposium on Size-Effects in Microstructure and Damage Evolution at Technical University of Denmark (2018).

^{*} Corresponding author.

E-mail addresses: sphs@eng.au.dk (S.P.H. Skovsgaard), hmj@eng.au.dk (H.M. Jensen).

<https://doi.org/10.1016/j.euromechsol.2018.12.007>

Received 18 September 2018; Received in revised form 18 December 2018; Accepted 21 December 2018

Available online 29 December 2018

0997-7538/© 2018 Elsevier Masson SAS. All rights reserved.

In the current study, three different models are used to investigate kink band broadening in a general framework, including a finite element model, a semi-analytical model and an analytical model. Two case studies with two different material compositions are presented. In the first case study, the size effects upon kink band broadening are investigated using the finite element model and the semi-analytical model. The analytical and semi-analytical models are used in a second case study using material parameters of an ultra high molecular-weight polyethylene fibre composite to predict some kink band broadening parameters. The theoretical predictions are compared with experiments performed by Attwood et al. (2015) on a composite made from UHMWPE fibres. This article is contributing to the further understanding of the compressive mechanics of fibre composites and layered materials. The analytical and semi-analytical model developed in Jensen (1999) and Skovsgaard and Jensen (2018c) are modified to predict the propagation stress and fibre lock-up angle for a composite made from UHMWPE fibres. The modifications lies in the implementation of the constitutive behaviour of the UHMWPE fibres. Furthermore, the fact that band broadening was observed to develop on ply level is taken into account. In this article it is further emphasized that the models developed in Jensen (1999) and Skovsgaard and Jensen (2018c) can be used for both layered materials and fibre reinforced composites with arbitrary material constituents.

2. Semi-analytical model for kink band initiation and broadening

The methodology introduced in Jensen (1999) is used to investigate kink band broadening using the homogenisation methodology developed in Christoffersen and Jensen (1996). Originally, the model was used to study a fibre reinforced composite with two constituents, a matrix and fibre composition. The latter model will be known as the semi-analytical model and is presented with two arbitrary constituents with the superscripts $(\bullet)^a$ and $(\bullet)^b$. The theory behind the approach will be outlined here.

2.1. General relations

The strain rate and spin are given by

$$\dot{\epsilon}_{ij} = \frac{1}{2}(v_{i,j} + v_{j,i}) \omega_{ij} = \frac{1}{2}(v_{i,j} - v_{j,i}) \quad (1)$$

where $v_{i,j}$ are the velocity gradients. Latin indices i.e. i, j, k take values 1,2,3, and Greek indices i.e. α, β, γ take values 1,2. A comma denotes partial derivative. The relation between the rate of nominal stresses \dot{i}_{ij} and velocity gradients are

$$\dot{i}_{ij} = C_{ijkl} v_{l,k} \quad (2)$$

where C_{ijkl} are components of nominal moduli

$$C_{ijkl} = L_{ijkl} - \frac{1}{2}\tau_{kj} \delta_{il} - \frac{1}{2}\tau_{ij} \delta_{lk} - \frac{1}{2}\tau_{li} \delta_{kj} + \frac{1}{2}\tau_{lk} \delta_{ij} \quad (3)$$

and δ_{ij} denote Kronecker delta and τ_{ij} are the current Kirchhoff stresses. The moduli L_{ijkl} describe the relation between the Jaumann rate of Kirchhoff stresses and strain rates $\dot{\epsilon}_{ij} = L_{ijkl} \dot{\epsilon}_{kl}$ and are to be described using a time-independent constitutive law e.g. J_2 -deformation and J_2 -flow theory. Moment equilibrium $\tau_{ij} = \tau_{ji}$ and strain symmetry $\dot{\epsilon}_{ij} = \dot{\epsilon}_{ji}$ require the symmetries

$$L_{ijkl} = L_{jikl} = L_{ijlk} \quad (4)$$

The relation between Cauchy stresses and Kirchhoff stresses are

$$\tau_{ij} = J \sigma_{ij} \quad (5)$$

where J is the Jacobian giving the volume ratio $J = V/V_0$. The relation between the rate of Cauchy stresses and the rate of nominal stresses is

$$\dot{\sigma}_{ij} = \dot{i}_{ij} - \sigma_{ij} v_{k,k} + v_{i,k} \sigma_{kj} \quad (6)$$

2.2. Constitutive model

The constitutive model introduced in Christoffersen and Jensen (1996) homogenises the material properties of two individually described constituents. The model is based on the kinematic assumption that material lines parallel with the x_1 -direction are subjected to a common stretching and rotation. The strains in the x_2 -direction are averages of the two constituent strains. The kinematics can be described using velocity gradients

$$v_{\alpha,1}^a = v_{\alpha,1}^b = v_{\alpha,1}^a v_{\alpha,2}^b = c^a v_{\alpha,2}^a + c^b v_{\alpha,2}^b \quad (7)$$

where c^a and $c^b = 1 - c^a$ are volume fractions of the constituents in the layered material or fibre composite. Superscripts $(\bullet)^a$ and $(\bullet)^b$ corresponds to values associated with the two arbitrary constituents. A lack of superscript refers to overall composite quantities. Additionally, the model is based on the assumption that planes with outward normal parallel with the x_2 -axis transmit identical tractions. This assumption together with overall equilibrium entails

$$\dot{i}_{2\alpha} = \dot{i}_{2\alpha}^a = \dot{i}_{2\alpha}^b \quad i_{1\alpha} = c^a i_{1\alpha}^a + c^b i_{1\alpha}^b \quad (8)$$

Christoffersen and Jensen (1996) introduced a matrix format to describe the relations for convenience. This matrix format is not repeated in the current article, instead the usual index notation is kept. Using the latter relations and under the assumption of plane strain, Christoffersen and Jensen (1996) showed that the composite behaviour could be described according to

$$C_{\alpha\beta\gamma\delta} = c^a C_{\alpha\beta\gamma\delta}^a + c^b C_{\alpha\beta\gamma\delta}^b - c^a c^b (C_{\alpha\beta 2\alpha}^a - C_{\alpha\beta 2\alpha}^b) H_{\alpha\gamma} (C_{2\beta\gamma}^a - C_{2\beta\gamma}^b) \quad (9)$$

where,

$$H_{\alpha\gamma} M_{\beta\delta} = \delta_{\alpha\beta} \quad M_{\beta\delta} = c^b C_{2\alpha 2\beta}^a + c^a C_{2\alpha 2\beta}^b \quad (10)$$

The moduli $M_{\alpha\beta}$ are initially calculated and then the inverse $H_{\alpha\beta}$ is determined so the equality $H_{\alpha\gamma} M_{\beta\delta} = \delta_{\alpha\beta}$ is satisfied. The moduli $C_{\alpha\beta\gamma\delta}^c$ for the constituents are initially calculated using Eq. (3) using the tangent moduli $L_{\alpha\beta\gamma\delta}^c$. The homogenisation methodology with two constituents was later extended to include information about imperfect bonding for a fibre composite in Skovsgaard and Jensen (2018b) and was extended to a three-dimensional version in Skovsgaard and Jensen (2018a). The constitutive model introduced by Jensen (1999), assuming plane strain conditions, was used in Tojaga et al. (2018) as a user subroutine UMAT in Abaqus to investigate the development of kink bands in open-hole fibre composites. The deformations for the individual constituents $v_{\alpha,\beta}^c$ are calculated based on the overall velocity gradients $v_{\alpha,\beta}$ in every increment. Furthermore, the stresses for the constituents are updated in every increment. Thereby, individual and independent constitutive relations can be used for the constituents through the moduli $L_{\alpha\beta\gamma\delta}^c$ with arbitrary elastic-plastic constitutive behaviour.

2.3. Kink band propagation

A semi-analytical kink band model was created in Jensen and Christoffersen (1997) using the constitutive formulation. The kink band model assumes that the kink band formation and propagation can be simplified into two material states; one inside the localised band and one outside the band (base material) see Fig. 1. It has previously been shown that the assumptions lead to good agreement with experimental results (Jensen and Christoffersen 1997 and Skovsgaard and Jensen (2018a)). The key equations and assumptions are introduced and for further details see Christoffersen and Jensen (1996) and Jensen (1999). Fig. 1 shows the kink band geometry and the local coordinates for the material states. Superscripts $(\bullet)^a$ and $(\bullet)^b$ refer to quantities associated with the outer base material and the inner band material, respectively. The angle ϕ gives the relative angle between the orientation of fibres

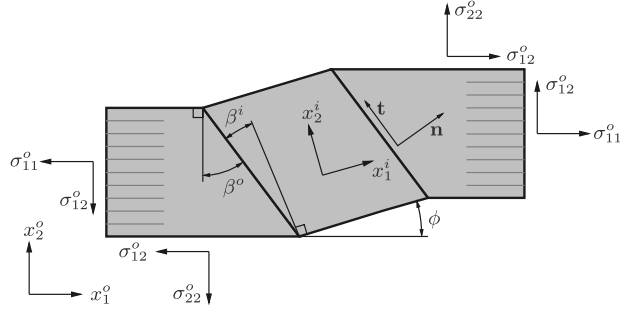


Fig. 1. Kink band geometry with two coordinate systems, one inside the band and one outside represented with $(\cdot)^i$ and $(\cdot)^o$ respectively.

inside and outside the band. The angles β^o and β^i are the relative band orientations seen from the two systems. The outward normal \mathbf{n} and tangent \mathbf{t} are shown on the band boundary.

The x_i -coordinate is aligned with the fibres, or layers in the case of a layered material, prior to deformation. This applies both for the state inside and outside the band. A Jaumann frame of reference is used, so the coordinate systems rotate with the deformation during an increment. The stresses in the two material states, inside and outside the kink band, are updated according to

$$\dot{\sigma}_{\alpha\beta}^o = C_{\alpha\beta\gamma\delta} v_{\delta,\gamma}^o - \sigma_{\alpha\beta}^o v_{\gamma,\gamma}^o + v_{\alpha,\gamma}^o \sigma_{\gamma\beta}^o \quad (11)$$

The relative band orientations are updated using

$$\dot{\beta}^o = -v_{\alpha,\beta}^o n_{,\alpha} t_{,\beta} \quad (12)$$

In the case of a material composition with different bulk moduli, then the volume fraction of the constituents are updated according to

$$\dot{c}^a = c^a c^b (v_{2,2}^a - v_{2,2}^b) \quad (13)$$

Due to the choice of a Jaumann frame of reference, then the coordinate systems rotate with the fibres, leading to

$$v_{2,1}^o = 0 \quad v_{2,1}^i = 0 \quad (14)$$

To ensure continuity of tractions and displacements the normal and tangent to the band are needed and are formulated relative to the individual frames

$$\begin{aligned} [n_1^o, n_2^o] &= [\cos(\beta^o), \sin(\beta^o)] [t_1^i, t_2^i] = [-\sin(\beta^o), \cos(\beta^o)] \\ &= [\cos(\beta^i), \sin(\beta^i)] [t_1^i, t_2^i] = [-\sin(\beta^i), \cos(\beta^i)] \end{aligned} \quad (15)$$

Continuity of displacements across the band boundary entails the two equations

$$w_{\alpha,\beta}^i t_{,\alpha}^i t_{,\beta}^o = v_{\alpha,\beta}^o t_{,\alpha}^o t_{,\beta}^i \quad w_{\alpha,\beta}^i n_{,\alpha}^i t_{,\beta}^o = v_{\alpha,\beta}^o n_{,\alpha}^o t_{,\beta}^o \quad (16)$$

where,

$$w_{\alpha,\beta}^i = v_{\alpha,\beta}^i + \Omega_{\alpha\beta}^i \Omega_{21} = -\Omega_{12} = \dot{\phi} \Omega_{11} = \Omega_{22} = 0 \quad (17)$$

The components $w_{\alpha,\beta}^i$ are the velocity gradients seen from a system that stays stationary during deformation i.e. does not follow the fibres during deformation. The relative spin $\dot{\phi}$ is included in the spin tensor Ω_{ij} . Equilibrium of tractions across the band entails

$$C_{\alpha\beta\gamma\delta}^i w_{\delta,\gamma}^i n_{,\alpha}^i n_{,\beta}^o = C_{\alpha\beta\gamma\delta}^o v_{\delta,\gamma}^o n_{,\alpha}^o n_{,\beta}^i \quad C_{\alpha\beta\gamma\delta}^i w_{\delta,\gamma}^i n_{,\alpha}^i t_{,\beta}^o = C_{\alpha\beta\gamma\delta}^o v_{\delta,\gamma}^o n_{,\alpha}^o t_{,\beta}^o \quad (18)$$

The kink band model is a two dimensional model with plain strain condition. The deformations in every material state are fully defined by the use of the four components of the velocity gradients. Since the kink band model only includes two material states, eight components of the velocity gradients are to be determined in every increment. Continuity

of velocities Eq. (16) and equilibrium of tractions Eq. (18) give the first four equations. The requirement of Eq. (14) gives further two equations. The last two boundary conditions used in the simulations are

$$v_{1,2}^o = 0 \quad \dot{\sigma}_{22}^o = 0 \quad (19)$$

which entails no shear straining and transverse stress in the base material. The kink band model was used to study the effect of varying initial imperfections ϕ_0 on the critical compressive strength σ_{11}^c in Jensen and Christoffersen (1997). The model can be used to study kink band broadening in composites as well using a Maxwell condition. In the case of steady-state broadening, it is assumed that a kink band has formed and locked up in a given orientation β^{ss} and with a fibre rotation ϕ^{ss} , where the superscript $(\cdot)^{ss}$ refers to a steady-state quantity. From this point, the easiest way of further deformation is to broaden the already developed band. In this state the band will broaden (or propagate) under a constant applied stress i.e. the work done by the external stresses and strains on a unit volume equals the work done by an unit volume transitioning from the base state to the band state $W^E = W^I$. The external work per unit volume is

$$W^E = S_{\alpha\beta}^o \Delta E_{\alpha\beta}^o \quad (20)$$

where $\Delta E_{\alpha\beta}^o$ is the difference in Green-Lagrangian strain inside and outside the band expressed in the base material and $S_{\alpha\beta}^o$ denotes the work conjugate Second Piola-Kirchhoff stress in the base material. The work done per unit volume in the band material is

$$W^I = \int_{\phi^o}^{\phi^i} \sigma_{\alpha\beta} d\varepsilon_{\alpha\beta} \quad (21)$$

where ε^o and ε^i are strain states outside and inside the band, respectively. The inner and outer work are evaluated in every increment i.e. for every fibre rotation ϕ . In the simulations, the band orientation β is seen as a fixed value and the fibre lock-up angle is search for where the Maxwell condition $W^E = W^I$ is satisfied. This methodology is in contrast to the approach done by several previous authors, where the kinematic relation $\phi = 2\beta$ is used, which have been observed in experiments.

3. Analytical model for kink band broadening

In Skovsgaard and Jensen (2018c) an analytical model was developed to evaluate the external and internal work per unit volume during kink band formation. This resulted in a transcendental equation in the form $W^E(\phi) = W^I(\phi)$, with fibre rotation ϕ being the only unknown. The model is inspired by the semi-analytical model regarding the two material states and the continuity requirements. The semi-analytical model is formulated in a general framework with arbitrary behaviour of the constituents. In contrast, the analytical model makes several prior

S.P.H. Skovsgaard, H.M. Jensen

European Journal of Mechanics / A Solids 74 (2019) 394–402

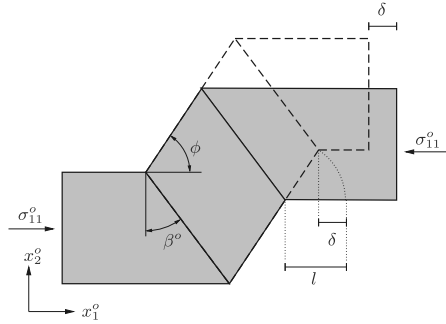


Fig. 2. Illustration of steady-state kink band propagation in the case of inextensible fibres. The geometry with dashed lines shows a propagated configuration.

assumption to the material behaviour e.g. large difference in elastic moduli between the constituents, which is the case for many fibre reinforced composites.

The model assumes that one of the constituents can be regarded as being rigid and incompressible, which is a valid assumption for many composites when evaluating the work e.g. carbon and glass fibre composites. A case study is presented later using an ultra high molecular-weight polyethylene fibre composite. It has been observed experimentally that these UHMWPE fibre composites have a three order of magnitude difference in moduli in compression and shear (Liu et al. (2014)). This make them ideal for this analytical model assuming rigid fibres. The kinematic constraint $\phi = 2\beta$ has not been used in the current study as in many of the previous studies. Some interesting results can be seen when this unnecessary kinematic constraint is relieved.

In Fig. 2 the geometry is seen that describes the analytical kink band broadening model. At a certain point during localisation the easiest way of further deformation is through kink band broadening. Assuming rigid fibres and a locked up geometry as seen in the figure, an infinitesimal fibre piece of length l will rotate into the localised band. This will result in an end shortening of $\delta = l(1 - \cos\phi)$. Since mechanical work is force times displacement, the external work per unit volume is

$$W^E = -\sigma_{11}^0(1 - \cos\phi) \quad (22)$$

where σ_{11}^0 is the external applied stress. Moran et al. (1995) came to the same result for the external work and was presented in a similar manner. No straining and thereby no work is done by the base material, due to the assumption of rigid fibres. Furthermore, no shear and transverse stresses are applied to the base material in the current analytical model. The work done per unit volume by the stresses in the kink band is

$$W^I = 2 \int_0^{\delta} \sigma_{12} d\epsilon_{12} + \int_0^{\delta} \sigma_{22} d\epsilon_{22} \quad (23)$$

Stress equilibrium across the band requires

$$\sigma_{\alpha\beta}^i n_\alpha^i t_\beta^i = \sigma_{\alpha\beta}^o n_\alpha^o t_\beta^o \quad (24)$$

where again n_α and t_α are the unit normal and tangent to the band plane expressed in either the inner or outer material system. Using the latter equation together with Eq. (15) yields

$$\begin{aligned} \sigma_{11}^i &= -\sigma_{12}^i [\cot\phi + \tan(\beta^0 - \phi)] - \sigma_{22}^i \cot\phi \tan(\beta^0 - \phi) \\ \sigma_{11}^o &= -\sigma_{12}^o [\cot\phi + \tan\beta^0] - \sigma_{22}^o [\cot\phi \tan\beta^0 - 1] \end{aligned} \quad (25)$$

which express the stresses σ_{11}^i and σ_{11}^o in terms of the inner stresses σ_{12}^i and σ_{22}^i . Continuity of velocities in the case of rigid fibres and no shear

and transverse straining in the base material require that

$$w_{\alpha,\beta}^i t_\alpha^i t_\beta^i = 0 \quad w_{\alpha,\beta}^o n_\alpha^o t_\beta^o = 0 \quad (26)$$

where $w_{\alpha,\beta}^i$ is given by Eq. (17). The velocity gradients integrates into the finite logarithmic strains

$$\epsilon_{12}^i = \frac{\phi}{2} \epsilon_{22}^i = \ln\left(\frac{\cos(\beta^0 - \phi)}{\cos\beta^0}\right) \quad (27)$$

which was shown by Skovsgaard and Jensen (2018c). The same kinematics were obtained by Budiansky and Fleck (1993). It is assumed that the transverse stresses can be expressed through transverse strains only, which is a simplification compared to a general elastic-plastic constitutive law. It is assumed that the transverse behaviour is purely elastic and plane strain conditions prevail, which yields the relation

$$\sigma_{22} = \frac{E(1-\nu)}{(1+\nu)(1-2\nu)} \epsilon_{22} \quad (28)$$

The shear stresses are assumed to dependent only on the shear strains, and follow a bilinear elastic-plastic relation

$$\begin{aligned} \sigma_{12} &= 2G_1 \epsilon_{12} \text{ for } \epsilon_{12} < \epsilon_{12}^y \\ \sigma_{12} &= 2G_2 \epsilon_{12} + \sigma_{12}^y \left(1 - \frac{\epsilon_{12}}{\epsilon_{12}^y}\right) \text{ for } \epsilon_{12} < \epsilon_{12} \end{aligned} \quad (29)$$

where G_1 is the shear modulus prior to yielding and G_2 is the shear modulus beyond yielding, the quantity ϵ_{12}^y is the shear strain where yielding takes place.

By introducing the constants

$$C_1 = \frac{G_1}{2} \quad C_2 = \frac{G_2}{2} \quad C_3 = \sigma_{12}^y \left(1 - \frac{G_2}{G_1}\right) \quad C_4 = \frac{E(1-\nu)}{2(1+\nu)(1-2\nu)} \quad (30)$$

then it was shown by Skovsgaard and Jensen (2018c) that the external and internal work done per unit volume can be expressed explicitly as

$$\begin{aligned} W^E &= (2C_2\phi + C_3)[\cot\phi + \tan\beta^0](1 - \cos\phi) \\ &+ 2C_4 \ln\left(\frac{\cos(\beta^0 - \phi)}{\cos\beta^0}\right)[\cot\phi \tan\beta^0 - 1](1 - \cos\phi) \end{aligned} \quad (31)$$

$$W^I = C_1(\phi^y)^2 + C_2(\phi^2 - (\phi^y)^2) + C_3(\phi - \phi^y) + C_4 \ln\left(\frac{\cos(\beta^0 - \phi)}{\cos\beta^0}\right)^2 \quad (32)$$

where the yield rotation,

$$\phi^y = \frac{\sigma_{12}^y}{G_1} \quad (33)$$

is introduced. The condition for steady-state broadening requires the work balance condition $W^E = W^I$ to be satisfied. The two equations, Eq. (31) and Eq. (32), giving the external and internal work do only depend on the rotation ϕ . It does not seem possible to solve the balance $W^E = W^I$ analytically with respect to ϕ and thereby gives a transcendental equation for the Maxwell condition of the steady-state kink band broadening.

4. Size effects upon kink band broadening

4.1. Finite element model

The influence of size effects upon kink band broadening will be investigated using a finite element model and will be compared with the results obtained using the semi-analytical kink band model. A case study is created for a fibre reinforced PEEK composite. The full elastic-plastic behaviour of the constituents for the later composite was thoroughly investigated in Kyriakides et al. (1995) and is thereby chosen for the current investigation. The finite element model was initially presented in Skovsgaard and Jensen (2018c). An illustration of the model

S.P.H. Skovsgaard, H.M. Jensen

European Journal of Mechanics / A Solids 74 (2019) 394–402

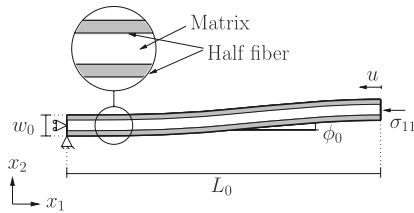


Fig. 3. Geometry of the micromechanical finite element model with two constituents. The darker regions represents the fibre constituent in the current case study.

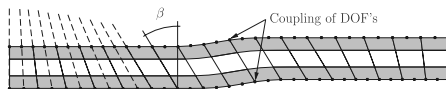


Fig. 4. Illustration of mesh used in the finite element simulations. The coupling of the nodes locks the deformation in an orientation β .

geometry and boundary conditions are shown in Fig. 3. The FE-model is a micromechanical model where the fibre and matrix constituents are modelled individually. The initial length of the geometry is L_0 . To simulate an infinite extent of the kink band, periodic boundary conditions (PBC) are utilized on the top and bottom of the geometry. The PBCs make it possible to model only one full layer of a constituent and two half layers. The middle layer will in the current model represent the PEEK constituent and the two half layers are fibres. The commercial software Abaqus 6.14 was used for the simulations. An implicit finite element solver was chosen together with an arc-length solver since the equilibrium path is non-linear. A special methodology for applying the periodic boundary conditions is introduced as can be seen in Fig. 4. In the middle of the geometry the elements are skewed and together with the chose of node coupling, this locks the formation and the kink band broadening at a given angle β . The mentioned periodic boundary conditions, where the band is locked during deformation, resemble the boundary conditions introduced for the analytical and semi-analytical model.

An imperfection in the form of a waviness was introduced in the geometry initially where the deformed coordinates are given by

$$\begin{aligned}
 x_2 &= \frac{1}{2} \phi_0 \left(\frac{-b_0}{2 \cos \beta} - X_2 \tan \beta \right) \quad \text{for } X_1 < X_{1,min} \\
 x_2 &= \frac{1}{2} \phi_0 \left[\frac{b_0}{2 \pi \cos \beta} \sin \left(\frac{2 \pi \cos \beta}{b_0} (X_1 + X_2 \tan \beta) \right) + X_1 \right] \quad \text{for } X_{1,min} < X_1 < X_{1,max} \\
 x_2 &= \frac{1}{2} \phi_0 \left(\frac{b_0}{2 \cos \beta} - X_2 \tan \beta \right) \quad \text{for } X_1 > X_{1,max}
 \end{aligned} \tag{34}$$

where x_i are deformed coordinates and X_i are initial coordinates expressed in a coordinate system placed in the geometry centre. The angle ϕ_0 is the angle of the largest fibre misalignment, which is in the centre of the geometry. The parameter b_0 is the extent of the imperfection in the x_1 -direction. Furthermore the parameters

$$X_{1,min} = \frac{-b_0}{2 \cos \beta} - X_2 \tan \beta \quad X_{1,max} = \frac{b_0}{2 \cos \beta} - X_2 \tan \beta \tag{35}$$

are introduced which give the start and end coordinate for the imperfection. Simplified imperfections can also be implemented but the imperfection used has shown to give consistent and stable results. The

fibre constituent is assumed to have a linear-elastic response. The PEEK constituent behaves elastic-plastic and is fitted to a Ramberg-Osgood relationship. The built-in plastic flow rule was chosen in Abaqus with isotropic hardening with a von-Mises yield criterion. The material parameters are normalized quantities of the one presented in Kyriakides et al. (1995). The material parameters and geometries used in the models are

$$\begin{aligned}
 c^f &= 0.6 & E^f/E^m &= 35 & \nu^f &= 0.263 \\
 \nu^m &= 0.356 & \sigma^{y,m}/E^m &= 0.013 & n^m &= 4 \\
 L_0 &= 1 & b_0 &= 0.5 & \phi_0 &= \Gamma & \beta &= 15^\circ
 \end{aligned} \tag{36}$$

where c^f is the fibre volume fraction, E^e and ν^e are the elastic parameters Young's modulus and Poisson's ratio. The plastic parameters $\sigma^{y,m}$ and n^m are the reference yield stress and the hardening exponent used in the Ramberg-Osgood relationship for the PEEK constituent.

The finite element model is substantially different from both the semi-analytical model and the analytical model. Although the differences in formation, the models give remarkable similar results as confirmed in Skovsgaard and Jensen (2018c). There are many differences in the numerical foundation. One of the more profound differences is that a fibre rotation increment ϕ is applied in the semi-analytical model and a compressive displacement u is applied in the FE-model.

4.2. Size effects and validation

The normalized fibre diameter d^f/L_0 is changed in the current study using the FE-model. Results showing the normalized compressive stress $-\sigma_{11}/G$ as a function of normalized end-displacement u/L_0 are presented in Fig. 5. Furthermore, deformed geometries at a normalized end-displacement $u/L_0 = 0.04$ are shown in Fig. 6. Results from six simulations are presented in the figures with different normalized fibre diameters. In the two simulations with large fibre diameters (0.1 – 0.05), here the boundary condition in the left and right together with a large bending stiffness prevents the geometries from reaching a steady-state. As the fibre diameter decreases the end effects decrease as well. As the fibre diameter decrease the compressive stress at steady-state σ^{ss} converges towards the same value for the simulations. Furthermore, the transition in the geometry going from the base material to the kinked area sharpens with decreasing fibre diameters. A sharp transition between the base and kink band material is consistent with the assumptions used in the analytical and semi-analytical model. The result from a simulation generated with the semi-analytical model (SA - model) is shown as a dashed line in Fig. 5. The result is presented as a horizontal line, since it is not possible to extract the compressive stress as a function of end-displacement from the semi-analytical model. The same material behaviour is chosen for the constituents in both the FE-model and the semi-analytical model.

5. Case study: kink band broadening in UHMWPE fibre composites

A case study is created using the analytical and semi-analytical model to show the usability of the models on a layered material. The compressive response of a composite made from ultra high molecular weight polyethylene fibres was investigated by Attwood et al. (2015). The composite was composed of plies with alternating 0° and 90° fibre orientation. A kink band was observed to develop during compression. Due to a notch initially present in the geometry, the transition to a kink band happened gradually and the deformation ended in a state with kink band broadening. Kink bands have frequently been observed to develop in a single ply on a fibre-matrix level. In the current case the kink band developed on a ply level between the 0° - 90° layers. Previously, the models have been used to investigate kink band formation in composites on the fibre-matrix scale, but the models will in the current case study be modified to develop on ply-level. In the case study, material parameters obtained for UHMWPE fibre composites will

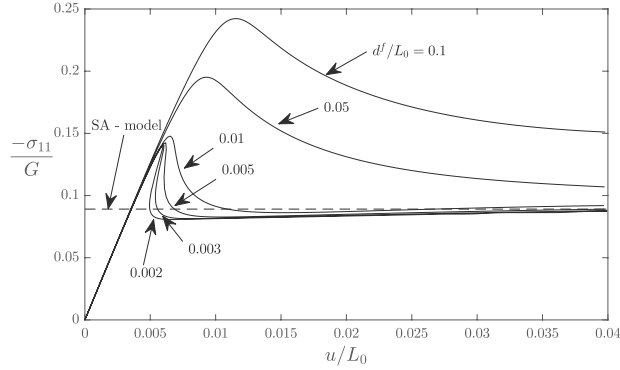


Fig. 5. Normalized compressive stress $-\sigma_{11}/G$ as a function of normalized end-displacement u/L_0 for different normalized fibre diameters d'/L_0

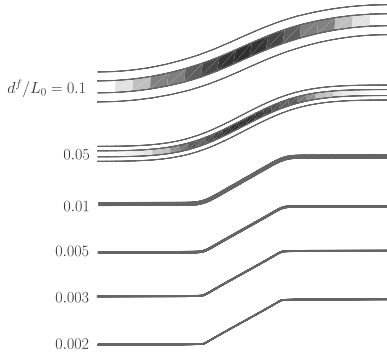


Fig. 6. Illustration of deformed geometries from the finite element simulations with different normalized fibre diameters d'/L_0 . The band orientation is chosen arbitrarily to be $\beta = 15^\circ$. The darker zones are areas of high shear straining.

be used. The material behaviour of the constituents for the semi-analytical and analytical model will be explained in the following.

5.1. Behaviour of plies for semi-analytical model

Different material behaviours are given to the 0° and 90° plies. The behaviour of the 90° plies are described using a J_2 -deformation theory introduced by Ståren and Rice (1975). The tensor of instantaneous moduli L_{ijkl} are given by

$$L_{ijkl} = G_s (\delta_{ik} \delta_{jl} + \delta_{il} \delta_{jk}) + \left(K - \frac{2}{3} G_s \right) \delta_{ij} \delta_{kl} - \frac{4}{3} (G_s - G_t) m_{ij} m_{kl}, \quad (37)$$

where,

$$m_{ij} = \frac{1}{2} \frac{s_{ij}}{\alpha_{eq}}. \quad (38)$$

The stress α_{eq} is the equivalent Von Mises stress and s_{ij} are components of the deviatoric stress tensor

$$\alpha_{eq} = \sqrt{3} J_2, \quad J_2 = \frac{1}{2} s_{ij} s_{ij}, \quad s_{ij} = \sigma_{ij} - \delta_{ij} \frac{\sigma_{kk}}{3}. \quad (39)$$

The bulk modulus K , the shear secant modulus G_s and the tangent shear modulus G_t introduced in the instantaneous moduli (Eq. (37)) are calculated based on

$$G_s = \left(\frac{3}{E_s} - \frac{1-2\nu}{E} \right)^{-1}, \quad G_t = \left(\frac{3}{E_t} - \frac{1-2\nu}{E} \right)^{-1}, \quad K = \frac{E}{3(1-2\nu)} \quad (40)$$

where ν denotes Poisson's ratio and E is Young's modulus. The tangent modulus E_t and secant modulus E_s are calculated using the Ramberg-Osgood relation

$$E_t = E \left(1 + \frac{3n}{7} \left(\frac{\sigma}{\sigma^y} \right)^{n-1} \right)^{-1} \\ E_s = E \left(1 + \frac{3}{7} \left(\frac{\sigma}{\sigma^y} \right)^{n-1} \right)^{-1} \quad (41)$$

where σ^y is a reference yield stress. The material parameters for the 90° plies are taken from Liu et al. (2014) and are given by

$$E^{90} = 150 \text{ [MPa]}, \quad \nu^{90} = 0.3, \quad \sigma^{y,90} = 3.12 \text{ [MPa]} \\ n^{90} = 10, \quad E_{t,min}^{90} = E^{90}/1000 \quad (42)$$

Superscripts $(\cdot)^{90}$ corresponds to values associated with the 90° plies. The parameters $\sigma^{y,90}$ and n^{90} are the reference yield stress and hardening exponent for the constituent. The reference yield stress is chosen based on the shear yield stress $\tau^y = 1.8$ [MPa] measured in the experiments by Russel et al. (2013) and assuming a von Mises yield criterion entails the yield stress $\sigma^y = \sqrt{3} \tau^y$. The uni-axial response is described using a Ramberg-Osgood relation according to

$$\epsilon = \frac{\sigma}{E} + \frac{3}{7E} \left(\frac{\sigma}{\sigma^y} \right)^n \quad (43)$$

where σ and ϵ are the uni-axial stress and strain. Furthermore, a restriction is set on the Ramberg-Osgood curve, so the tangent modulus does not become smaller than a specified value $E_{t,min}$. The limit stress σ_L and strain ϵ_L where the minimum tangent modulus is reached are

$$\epsilon_L = \frac{\sigma_L}{E} + \frac{3}{7E} \left(\frac{\sigma_L}{\sigma^y} \right)^n \\ \sigma_L = \sigma^y \left[\left(\frac{E}{E_{t,min}} - 1 \right) \frac{7}{3n} \right]^{\frac{1}{n-1}} \quad (44)$$

These values are illustrated on Fig. 7. For an equivalent uni-axial stress $\alpha_{eq} < \sigma_L$ then the moduli given by Eq. (41) are to be used and

S.P.H. Skovsgaard, H.M. Jensen

European Journal of Mechanics / A Solids 74 (2019) 394–402

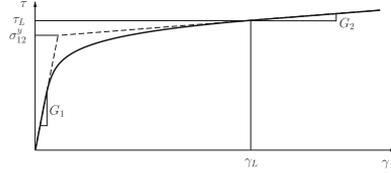


Fig. 7. Shear stress-strain relation for the semi-analytical and analytical model. The bi-linear curve represents the response used for the analytical model.

$$\begin{aligned}
 E_t &= E_{t,min} \\
 E_s &= \frac{\sigma_{eq}}{\epsilon_{eq}} \\
 \epsilon_{eq} &= \frac{\sigma_{eq} - \sigma_t}{E_{t,min}} + \epsilon_t
 \end{aligned} \tag{45}$$

are to be used for $\sigma_{eq} > \sigma_t$.

The 0° plies are assumed to behave orthotropic and linear elastic and can thereby be described using Hooke's Law for an orthotropic material. The relation between stresses and strains presented in a matrix format is given by

$$\begin{pmatrix} \sigma_{11} \\ \sigma_{22} \\ \sigma_{33} \\ \sigma_{12} \\ \sigma_{13} \\ \sigma_{23} \end{pmatrix} = \begin{pmatrix} \frac{1-\nu_{23}\nu_{32}}{E_2 E_3 \Delta} & \frac{\nu_{21}+\nu_{31}\nu_{23}}{E_2 E_3 \Delta} & \frac{\nu_{31}+\nu_{21}\nu_{32}}{E_2 E_3 \Delta} & 0 & 0 & 0 \\ \frac{\nu_{12}+\nu_{13}\nu_{32}}{E_1 E_3 \Delta} & \frac{1-\nu_{11}\nu_{13}}{E_3 E_1 \Delta} & \frac{\nu_{32}+\nu_{11}\nu_{12}}{E_3 E_1 \Delta} & 0 & 0 & 0 \\ \frac{\nu_{13}+\nu_{12}\nu_{23}}{E_1 E_2 \Delta} & \frac{\nu_{23}+\nu_{13}\nu_{21}}{E_1 E_2 \Delta} & \frac{1-\nu_{12}\nu_{21}}{E_1 E_2 \Delta} & 0 & 0 & 0 \\ 0 & 0 & 0 & 2G_{12} & 0 & 0 \\ 0 & 0 & 0 & 0 & 2G_{13} & 0 \\ 0 & 0 & 0 & 0 & 0 & 2G_{23} \end{pmatrix} \begin{pmatrix} \epsilon_{11} \\ \epsilon_{22} \\ \epsilon_{33} \\ \epsilon_{12} \\ \epsilon_{13} \\ \epsilon_{23} \end{pmatrix} \tag{46}$$

where,

$$\Delta = \frac{1 - \nu_{12}\nu_{21} - \nu_{23}\nu_{32} - \nu_{31}\nu_{13} - 2\nu_{12}\nu_{23}\nu_{31}}{E_1 E_2 E_3} \tag{47}$$

The moduli of the orthotropic constitutive relation comply to the symmetries $L_{ijkl} = L_{klij}$, this entails the relations

$$\nu_{21} = \nu_{12} \frac{E_2}{E_1} \quad \nu_{31} = \nu_{13} \frac{E_3}{E_1} \quad \nu_{32} = \nu_{23} \frac{E_3}{E_2} \tag{48}$$

The material parameters for the 0° plies are again taken from Liu et al. (2014) and Russel et al. (2013) and are given by

$$\begin{aligned}
 E_1 &= 68 \text{ [GPa]} & E_2 &= 150 \text{ [MPa]} & E_3 &= 150 \text{ [MPa]} \\
 G_{12} &= G_{13} = 60 \text{ [MPa]} & G_{23} &= E_2/(1 + \nu_{23}), \\
 \nu_{12} &\approx 0 & \nu_{13} &\approx 0 & \nu_{23} &\approx 0.5
 \end{aligned} \tag{49}$$

The material behaviour is highly anisotropic, which can be seen in the three order of magnitude difference between the moduli in tension E_1 and shear G_{12} .

5.2. Behaviour of plies for the analytical model

The original analytical model was created for kink band broadening on the fibre/matrix scale. In the case of UHMWPE fibres, kink bands are seen to develop on ply level. In the model presented in Skovsgaard and Jensen (2018c) a matrix volume fraction c^m was used due to the large difference in transverse and shear properties of the constituents. In the case of UHMWPE fibres it is assumed that the shear and transverse properties for the two constituents (0° and 90° plies) are the same.

To make a better comparison with the semi-analytical model, then the yield stress used is

$$\sigma_y^0 = G_1 \frac{\tau_L - G_2 \gamma_L}{G_1 - G_2} \tag{50}$$

where,

$$\begin{aligned}
 \gamma_L &= \frac{\tau_L}{G_1} + \frac{3\tau^y}{7G_1} \left(\frac{\tau_L}{\tau^y} \right)^n \\
 \tau_L &= \tau^y \left[\left(\frac{G_1}{G_2} - 1 \right) \frac{\tau}{3n} \right]^{\frac{1}{n-1}}
 \end{aligned} \tag{51}$$

where τ_L and γ_L is the shear stress and strain where the tangent is equal to G_2 for a curve following a Ramberg-Osgood relation. The quantities are shown in Fig. 7. The material parameters used for the analytical kink band model are

$$\begin{aligned}
 E &= 150 \text{ [MPa]} & G_1 &= 60 \text{ [MPa]} & G_2 &= G_1/1000 \\
 \nu &= 0.3 & n &= 10 & \tau^y &= 1.8 \text{ [MPa]}
 \end{aligned} \tag{52}$$

5.3. Results

Two different models that can predict the steady-state broadening state are used to estimate the response of a composite made from ultra-high molecular-weight polyethylene fibres. The two models, a semi-analytical and an analytical model, were initially presented in Jensen (1999) and Skovsgaard and Jensen (2018c) with normalized material values. The influence of the band orientation β upon the steady-state stress σ^{ss} and fibre rotation ϕ^{ss} are investigated for UHMWPE fibres in the present case study. The results are compared and discussed with respect to previously conducted experiments.

The lock-up angle ϕ^{ss} of the plies within the kink band at steady-state as function of initial kink band orientation β is presented in Fig. 8. The conventionally assumed relationship between the lock-up angle and the band orientation $\phi = 2\beta$ is also illustrated in the figure. Different arguments are given in the literature on how to determine the band orientation β at steady-state for a given composite. Moran et al. (1995) argue that the energetically favourable mode sets the band orientation i.e. the band orientations that will result in the lowest broadening stress σ^{ss} . The two models used predict that the lock-up angle asymptotically approaches the linear relationship $\phi = 2\beta$ as the angle β increases. For small values of β the two models deviate from the linear relation. Similar deviation was seen by Hsu et al. (1999) for a carbon fibre composite where they used a micro-mechanical finite element model with fixed band orientations. In the experiments conducted by Attwood et al. (2015), they investigated the compressive response of UHMWPE fibres. In the experiments a kink angle $\beta \approx 36^\circ$ and a lock up angle of $\phi^{ss} \approx 60^\circ$ was observed. The experimental observation, that $\phi < 2\beta$, disagrees with the predictions from the two models, which can be due to the fact, that the models do not take decohesion into account. Furthermore, it is unclear if the angles were measured upon loaded or unloaded specimens. There will be a change of geometry going from a loaded to an unloaded specimens due to

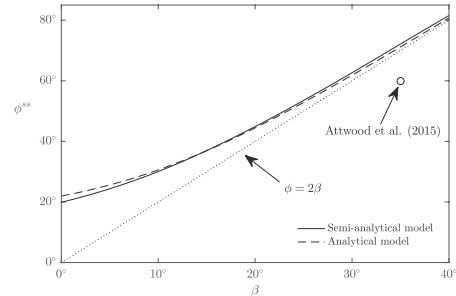


Fig. 8. Steady-state lock-up angle ϕ^{ss} as a function of initial kink band orientation β . Results are shown for the two models. Additionally, the conventional assumption of fibre lock-up $\phi = 2\beta$ is included for comparison.

S.P.H. Skovsgaard, H.M. Jensen

European Journal of Mechanics / A Solids 74 (2019) 394–402

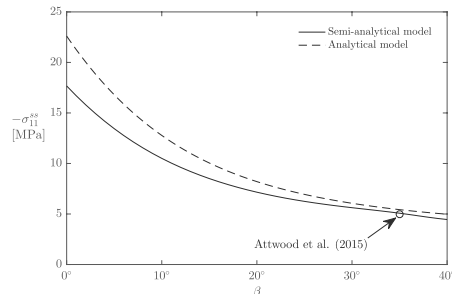


Fig. 9. Steady-state kink band propagation stress $-\sigma_{11}$ [MPa] as a function of initial kink band orientation β . Results are shown for the two models.

elasticity and relaxation/creep.

In the experiments performed by Liu et al. (2014) they investigated the collapse of a composite beam made from UHMWPE fibres. A transition from a shear dominated failure to a plastic hinge failure was observed, going from short to long beams. In the short shear dominated beams, the failure was similar to the formation of a kink band. Even though the kink failure investigated in the present study is based on pure compressive loading σ_{11} in the direction if 0° plies, then interesting similarities can be drawn. The band orientation in the shear dominated failure was in the range $\beta = 0^\circ - 5^\circ$ and the fibre rotation was approximately $\phi \approx 20^\circ$. These angles are determined based on the figures presented in Liu et al. (2014). The angles are in good agreement with the predictions from the two models presented in Fig. 8. These similarities argue that the kink band angle β^* at steady-state broadening can be influenced by the boundary conditions.

The steady-state stress σ_{11}^* applied to the base material as a function of initial band orientation β is presented in Fig. 9. The results in the figure argue that the broadening stress lowers with increasing band orientation. In the study conducted by Jensen (1999) similar results were predicted using material data for a carbon fibre-reinforced PEEK composite. The results from the two models presented in Fig. 9 predict a steady-state stress of $\sigma_{11} \approx 5 - 6$ [MPa] for a kink band orientation $\beta = 30 - 35^\circ$. This is in very good agreement with the experimental results presented in Fig. 10(a) in Attwood et al. (2015). The results from the analytical and semi-analytical model deviate for small band orientations, which also was observed in Skovsgaard and Jensen (2018c) for a carbon fibre-reinforced polymer composite.

6. Conclusions

Steady-state kink band broadening has been investigated for fibre reinforced composites and layered materials. The emphasis was given to the explanation of a semi-analytical and analytical approach to study the propagation instability. The models are formulated in a general framework and the constitutive behaviour for the constituents are needed as input. Two different composites are used in two case studies. The case studies both validate and show the usability of the used models.

In the first case study a carbon fibre-reinforced PEEK composite is investigated due to its well known constitutive behaviour of the constituents. The effect of the fibre diameter was investigated upon kink band broadening using a micromechanical finite element model. As the fibre diameter decreases the bending stiffness reduces, which leads to a sharp transition from kinked to unkinked area. This sharp transition is consistent with the assumptions made for the two simplified models. The results obtained using the FE-model approach the result obtained

using the semi-analytical model with decreasing fibre diameters.

In the second case study the analytical and semi-analytical approach were used to study kink band broadening in a composite made from ultra high molecular-weight polyethylene fibres. The study was made for UHMWPE fibre composites with a $0/90^\circ$ ply lay-up. Kink band formation and broadening have been observed to develop due to shearing between different plies instead of shearing between fibres and the surrounding matrix material. The 0° - and the 90° plies were treated as two different constituents. The 0° plies were modelled as been linear elastic and orthotropic in the semi-analytical model. Furthermore, the 90° plies were given an elastic-plastic behaviour and were assumed to behave isotropic. The analytical model assumed rigid fibres, which for the UHMWPE fibres are a valid assumption due to the three order of magnitude difference in the tension and shear moduli. A simple stress-strain relationship was used in the analytical model, which results in a transcendental equation to extract the stress and fibre lock-up angle at steady-state kink band broadening. The influence of the band orientation, β on the steady-state stress and lock-up angle was investigated in the case study. The two models predict steady-state quantities that are in good agreement with the experimental observations done by Attwood et al. (2015) and Liu et al. (2014). The results presented and experimental observations argue that the kink band orientation at steady-state broadening can be influenced by the boundary conditions.

Acknowledgements

This work was supported by the Thomas B. Thriges fund.

References

- Attwood, J.P., Fleck, N.A., Wadley, H.N.G., Deshpande, V.S., 2015. The compressive response of ultra-high molecular weight polyethylene fibres and composites. *Int. J. Solid Struct.* 71, 141–155. <https://doi.org/10.1016/j.ijsolstr.2015.06.015>.
- Beuth, J.L., 1992. Cracking of thin bonded films in residual tension. *Int. J. Solid Struct.* 29 (13), 1657–1675. [https://doi.org/10.1016/0020-7683\(92\)90015-L](https://doi.org/10.1016/0020-7683(92)90015-L).
- Budiansky, B., Fleck, N., 1993. Compressive failure of fibre composites. *J. Mech. Phys. Solid.* 41 (1), 183–211. [https://doi.org/10.1016/0022-5096\(93\)90068-Q](https://doi.org/10.1016/0022-5096(93)90068-Q).
- Budiansky, B., Fleck, N., Amazigo, J., 1998. On kink-band propagation in fiber composites. *J. Mech. Phys. Solid.* 46, 1637–1653. [https://doi.org/10.1016/S0022-5096\(97\)00042-2](https://doi.org/10.1016/S0022-5096(97)00042-2).
- Byskov, E., Christoffersen, J., Dencker Christensen, C., Sand Poulsen, J., 2002. Kink band formation in wood and fiber composites—morphology and analysis. *Int. J. Solid Struct.* 39 (13–14), 3649–3673. [https://doi.org/10.1016/S0020-7683\(02\)00174-9](https://doi.org/10.1016/S0020-7683(02)00174-9).
- Christoffersen, J., Jensen, H.M., 1996. Kink band analysis accounting for the micro-structure of fiber reinforced materials. *Mech. Mater.* 24 (4), 305–315. [https://doi.org/10.1016/S0167-6636\(96\)00052-X](https://doi.org/10.1016/S0167-6636(96)00052-X).
- Evans, A.G., Adler, W.F., 1978. Kinking as a mode of structural degradation in carbon fiber composites. *Acta Metall.* 26 (5), 725–738. [https://doi.org/10.1016/0001-6160\(78\)90023-8](https://doi.org/10.1016/0001-6160(78)90023-8).
- Fleck, N.A., Budiansky, B., 1991. Compressive failure of fibre composites due to micro-buckling. *Proc. 3rd Symp. on Inelastic Deformation of Composite Materials* 235–273.
- Fleck, N.A., Deng, L., Budiansky, B., 1995. Prediction of kink width in compressed fiber composites. *J. Appl. Mech.* 62, 329–337.
- G'sell, C., Aly-Helal, N.A., Jonas, J.J., 1983. Effect of stress triaxiality on neck propagation during the tensile stretching of solid polymers. *J. Mater. Sci.* 18 (6), 1731–1742. <https://doi.org/10.1007/BF00542069>.
- Hsu, S.-Y., Vogler, T., Kyriakides, S., 1999. On the axial propagation of kink bands in fiber composites : Part II analysis. *Int. J. Solid Struct.* 36, 575–595. [https://doi.org/10.1016/S0020-7683\(98\)00030-4](https://doi.org/10.1016/S0020-7683(98)00030-4).
- Jensen, H.M., 1999. Analysis of compressive failure of layered materials by kink band broadening. *Int. J. Solid Struct.* 36 (23), 3427–3441. [https://doi.org/10.1016/S0020-7683\(98\)00158-9](https://doi.org/10.1016/S0020-7683(98)00158-9).
- Jensen, H.M., Christoffersen, J., 1997. Kink band formation in fiber reinforced materials. *J. Mech. Phys. Solid.* 45 (7), 1121–1136. [https://doi.org/10.1016/S0022-5096\(96\)00126-3](https://doi.org/10.1016/S0022-5096(96)00126-3).
- Kyriakides, S., Arsecularatne, R., Perry, E.J., Liechti, K.M., 1995. On the compressive failure of fiber reinforced composites. *Int. J. Solid Struct.* 32 (6–7), 689–738. [https://doi.org/10.1016/0020-7683\(94\)00157-R](https://doi.org/10.1016/0020-7683(94)00157-R).
- Liu, X.H., Moran, P.M., Shih, C.F., 1996. The mechanics of compressive kinking in unidirectional fiber reinforced ductile matrix composites. *Compos. B Eng.* 27 (6), 553–560. [https://doi.org/10.1016/S1359-8368\(96\)00008-X](https://doi.org/10.1016/S1359-8368(96)00008-X).
- Liu, G., Thouless, M.D., Deshpande, V.S., Fleck, N.A., 2014. Collapse of a composite beam made from ultra high molecular-weight polyethylene fibres. *J. Mech. Phys. Solid.* 63

S.P.H. Skovsgaard, H.M. Jensen

European Journal of Mechanics / A Solids 74 (2019) 394–402

- (1), 320–335. <https://doi.org/10.1016/j.jmps.2013.08.021>. <https://doi.org/10.1016/j.jmps.2013.08.021>.
- Moran, P.M., Liu, X.H., Shih, C.F., 1995. Kink band formation and band broadening in fiber composites under compressive loading. *Acta Metall. Mater.* 43 (8), 2943–2958. [https://doi.org/10.1016/0956-7151\(95\)00001-C](https://doi.org/10.1016/0956-7151(95)00001-C).
- Nizolek, T., Begley, M., McCabe, R., Avallone, J., Mara, N., Beyerlein, I., Pollock, T., 2017. Strain fields induced by kink band propagation in Cu-Nb nanolaminate composites. *Acta Mater.* 133, 303–315. <https://doi.org/10.1016/j.actamat.2017.04.050>. <http://www.sciencedirect.com/science/article/pii/S1359645417303427>.
- Piggott, M.R., Harris, B., 1980. Compression strength of carbon, glass and kevlar-49 fiber reinforced polyester resins. *J. Mater. Sci.* 15 (10), 2523–2538. <https://doi.org/10.1007/BF00550757>.
- Russell, B.P., Karthikeyan, K., Deshpande, V.S., Fleck, N.A., 2013. The high strain rate response of Ultra High Molecular-weight Polyethylene: from fibre to laminate. *Int. J. Impact Eng.* 60, 1–9. <https://doi.org/10.1016/j.ijimpeng.2013.03.010>. <https://doi.org/10.1016/j.ijimpeng.2013.03.010>.
- Skovsgaard, S.P.H., Jensen, H.M., 2018a. Steady-state kink band propagation in layered materials. *J. Appl. Mech.* 85 (6). <https://doi.org/10.1115/1.4039573>. <http://appliedmechanics.asmedigitalcollection.asme.org/article.aspx?doi=10.1115/1.4039573>.
- Skovsgaard, S.P.H., Jensen, H.M., 2018b. Constitutive model for imperfectly bonded fibre-reinforced composites. *Compos. Struct.* 192, 82–92. <https://doi.org/10.1016/j.compstruct.2018.02.053>. February. <http://linkinghub.elsevier.com/retrieve/pii/S0263822317332002>.
- Skovsgaard, S.P.H., Jensen, H.M., 2018c. International Journal of Solids and Structures Three-dimensional constitutive model for elastic-plastic behaviour of fibre-reinforced composites. *Int. J. Solid Struct.* 139–140, 150–162. <https://doi.org/10.1016/j.ijsolstr.2018.01.032>. <https://doi.org/10.1016/j.ijsolstr.2018.01.032>.
- Stören, S., Rice, J.R., 1975. Localized necking in thin sheets. *J. Mech. Phys. Solid.* 23 (6), 421–441. [https://doi.org/10.1016/0022-5096\(75\)90004-6](https://doi.org/10.1016/0022-5096(75)90004-6).
- Tojaga, V., Skovsgaard, S.P.H., Jensen, H.M., 2018. Micromechanics of kink band formation in open-hole fibre composites under compressive loading. *Composites Part B* 149 (March), 66–73. <https://doi.org/10.1016/j.compositesb.2018.05.014>. <https://doi.org/10.1016/j.compositesb.2018.05.014>.

Chapter 10

P5

Load transfer at a bolted joint in a laminate made from ultra-high molecular weight polyethylene fibres

10.1 Motivation

Composites are used in several applications for different purposes. Carbon- and glass fibre-reinforced composites are often used to achieve structures with high strength and low weight. Composite plates made from ultra-high molecular weight polyethylene (UHMWPE) fibres are used in the industries of personnel and vehicle armour (See e.g. the bulletproof vest in Fig. 1.1b). UHMWPE was initially commercialised by the company DSM in the 1970s under the trade name Dyneema®. Fibres made from UHMWPE possess an incredible strength up to 3 GPa due to a gel-spinning/hot drawing process. Composite plates made from UHMWPE fibre laminates are in most cases composed of an equal amount of 0° and 90° plies. Even though the fibres possess high strength, the composite shear strength is of the order of 2 MPa i.e. three orders of magnitude difference from the fibre strength. This mismatch in composite shear and fibre strength and stiffness make the composite plates ideal for applications where ballistic energy absorption is important. It is challenging to measure the mechanical properties of laminates made from UHMWPE due to this stiffness mismatch. Furthermore, it is difficult to transfer load into the composite plates which give rise to special geometries in experimental set-ups.

The current article regards the transfer of loading at a bolted joint in a laminate made from UHMWPE fibres. The article is based on the work performed at the Engineering Department

at the University of Cambridge, which is the reason for the sudden change in research field from kink band formation to the one described in the following article.

10.2 Method

The article is mainly based on experimental work on the load transfer into plates made from UHMWPE. Specimens including holes were machined. The specimens were clamped in the bottom and a high steel bolt was placed through the top hole and displaced to measure and observe the pull-through behaviour.

A displacement controlled screw-driven test machine was used. The displacement was measured using a laser extensometer, the reaction force was measured by the load cell of the test machine. Furthermore, the influence of pre-clamping was investigated. The amount of transverse pre-clamping and the development of the loading was measured through an in-house made load cell composed of two strain gauges mounted on an aluminium tube. In the experiments, the specimen dimensions and the initial pre-clamping were varied.

Based on the experimental observations, a simple analytical model based on line-field theory was developed that adequately catches the main mechanism of load transfer. The analytical model gives an upper bound solution to the load transfer strength.

10.3 Contribution

The contributions to the article comprise: the development of the experimental set-up; performing the experiments; creating an analytical model; creating a failure map and writing the article.

10.4 Main findings

One of the main contributions to the field is the development of a failure map for the load transfer mechanism that distinguish between three failure mechanisms based on the specimen geometry. The mechanism of load transfer is determined based on the deformation pattern of the 0° and 90° plies obtained through a combination of X-ray tomography and optical images. It can be concluded, that the load transfer strength in UHMWPE composite plates is dominated by the inter-laminar shear yield strength between the 0° and 90° plies. Through the experiments and the analytical model, it can be confirmed that the inter-laminar shear yield strength depends linearly upon the out-of-plane pressure, similarly to Coulomb's law of friction.

ARTICLE IN PRESS

JID: SAS

[m5G;August 29, 2019;10:6]

International Journal of Solids and Structures xxx (xxxx) xxx



Contents lists available at ScienceDirect

International Journal of Solids and Structures

journal homepage: www.elsevier.com/locate/ijssolstr

Load transfer within the bolted joint of a laminate made from ultra-high molecular weight polyethylene fibres

S.P.H. Skovsgaard^{a,b}, H.M. Jensen^b, N.A. Fleck^{a,*}^a Department of Engineering, University of Cambridge, Trumpington Street, Cambridge, UK^b Department of Engineering, Aarhus University, Inge Lehmanns Gade 10, Aarhus C, Denmark

ARTICLE INFO

Article history:

Received 19 February 2019

Revised 29 July 2019

Accepted 14 August 2019

Available online xxx

Keywords:

UHMWPE fibres

Joint failure

Failure map

Pressure dependent shear strength

ABSTRACT

The mechanism of load transfer within the bolted joint of a laminate sheet made from ultra-high molecular weight polyethylene (UHMWPE) plies is investigated both experimentally and by an analytical model. The nature of load transfer and the active failure mechanisms are obtained as a function of joint geometry and of the lateral clamping force on the faces of the laminate (by pre-tensioning of the bolt). A combination of X-ray tomography and optical microscopy reveal that the dominant failure mechanism in the clamped joint is shear failure involving splits of the 0° plies and sliding at the interface between the 0° and 90° plies. A simple analytical model is developed for this shear failure mechanism and, upon noting the competing failure mechanisms of bearing failure, bolt shear and of tensile failure of the 0° plies, a failure mechanism map is constructed in terms of the geometry of the bolted joint, for the case of no pre-tension of the bolt. The analytical model for shear failure suggests that the enhancement in joint strength with increased pre-tensioning of bolt is due to the fact that the shear strength of the UHMWPE increases with increasing hydrostatic pressure.

© 2019 Published by Elsevier Ltd.

1. Introduction

Ultra-high molecular weight polyethylene (UHMWPE) fibres embedded in a polyurethane matrix have a high specific modulus and a high specific strength, and are commonly used for personnel and vehicle armour. Additionally, UHMWPE fibres are used for ropes, nets, footwear, cut resistant gloves and for air cargo containers. The company DSM¹ commercialized fibres made from UHMWPE in the late 1970s under the trade name Dyneema®. UHMWPE has extremely long molecular chains and, when fibres are produced using a gel-spinning/hot drawing process, the fibres possess a high strength on the order of 3 GPa, (Russell et al. 2013). The fibres are coated in a polyurethane (PU) resin solution and are then formed into [0/90/0/90] stacks. The PU solvent is removed during a drying process and the stacks are then hot pressed.

Several studies have been performed to determine the mechanical properties of UHMWPE fibres and composite plates. In the early work of Wilding and Ward (1978), the creep and recovery of ultra-high modulus polyethylene fibres were determined. Smith and Lemstra (1980) conducted one of the early studies

that lead to the choice of fibres used in Dyneema®. They measured the effect of draw ratio upon the tensile modulus and strength, and concluded that an extension ratio of $\lambda = 32$ by hot drawing led to a fibre strength of 3.0 GPa and a Young's modulus of 90 GPa. More recently, Govaert and Lemstra (1992) and Govaert and Peijs (1995) explored the sensitivity of the tensile response of UHMWPE fibres to temperature and to strain-rate.

Over the past decade, several authors have developed models to predict the ballistic performance of UHMWPE composite plates; for example, Grujicic et al. (2009) have developed a continuum-damage based constitutive model and implemented it within a finite element (FE) code. Iannucci and Pope (2011) have developed a model for the impact response of sheets made from high performance polymer fibres. Koh et al. (2010) investigated the behaviour of UHMWPE yarns by both quasi-static and dynamic tests. Additionally, Karthikeyan et al. (2013) performed quasi-static and dynamic impact tests on composite plates made from either UHMWPE fibres or carbon fibre-reinforced polymers. They observed that composites of high indentation strength in the quasi-static tests also had a high failure impulse. Russell et al. (2013) created a series of test methods for the mechanical performance of fibres, yarns and laminates made from UHMWPE. They highlighted the need to develop new geometries for tensile testing due to the difficulties in transferring load into laminates made from UHMWPE. A practical means of exploring load transfer in the

* Corresponding author.

E-mail address: naf1@eng.cam.ac.uk (N.A. Fleck).¹ DSM, Het Overloon 1, 6411 HE Heerlen, The Netherlands.

ARTICLE IN PRESS

JID: SAS

[m5G;August 29, 2019;10:6]

2

S.P.H. Skovsgaard, H.M. Jensen and N.A. Fleck / International Journal of Solids and Structures xxx (xxxx) xxx

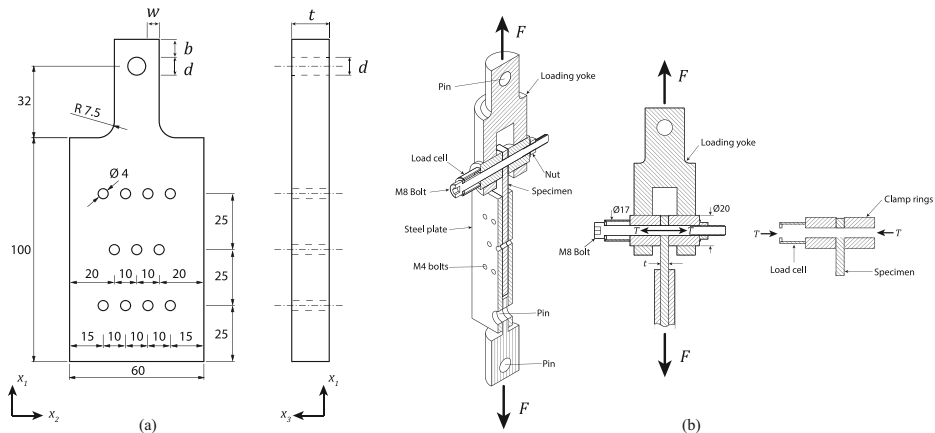


Fig. 1. (a). Specimen geometry. All dimensions are in mm. (b). Experimental set-up. A three-dimensional view is shown on the left. A sectional view of the top part is shown on the right. All dimensions are in mm.

presence of confinement is to transfer load via bolted joints: this motivates the current study.

We emphasise that it is difficult to measure the mechanical properties of laminates made from UHMWPE using conventional test methods due to the very low shear strength of both fibres and matrix. Consequently, indirect test methods have been developed. For example, Attwood et al. (2014) developed an out-of-plane compression test to determine the pressure sensitivity of UHMWPE laminates. The inter-layer strength was measured by Liu et al. (2014) via tests on an end-loaded cantilever beam. They extracted the elastic and plastic properties by varying the load level and by suitable positioning of the loading pin; a FE-model was used to aid interpretation of their results. The compressive response of UHMWPE fibres, and composite plates made from UHMWPE, was determined experimentally by Attwood et al. (2015) and was compared with fibre-kinking theory. In a recent study, Liu et al. (2018) determined the Mode I and II fracture toughness of a UHMWPE laminate. They performed a penetration experiment with a sharp-tipped punch and compared the measurements with a FE-model based upon a crystal plasticity model for the ply behaviour. Karthikeyan et al. (2013) performed both quasi-static loading and dynamic impact tests on end-clamped UHMWPE beams. They found that the method of confinement had a large influence on both the quasi-static and dynamic behaviours.

Several investigations have been performed on the mechanics of mechanically fastened joints in fibre-reinforced polymers. A failure mechanism map for single-lap bolted joints in CFRP laminates was constructed by Smith et al. (1986) on the basis of a set of tests on multidirectional CFRP laminates. Failure was by net-section tension, bearing or by shear-out along splits within the 0° plies. A similar methodology is followed in the present study. Camanho and Matthews (1997) distinguished five failure modes of composite joints: tension, shear, cleavage, bearing and a pull-through failure mode. A decade later, Thoppul et al. (2009) made a thorough review of the state-of-the-art methods to study the failure of composite joints. The focus in these previous studies was on glass and carbon fibre-reinforced polymers. In the present study,

we shall explore the extent to which these failure mechanisms persist in UHMWPE laminates of high in-plane strength but of very low shear strength.

2. Test method

We investigated the mechanism of load transfer into a bolted joint comprising HB26 Dyneema® [$0^\circ/90^\circ$] plates with and without transverse clamping. The plates had equal volume fractions of 0° and 90° plies and a ply thickness of $h = 60 \mu\text{m}$. Specimens of overall thickness $t = 6.5 \text{ mm}$ and ply layout $(0^\circ, 90^\circ)_{54}$ were machined to the geometry as depicted in Fig. 1(a), with bolt diameter $d = 8 \text{ mm}$, ligament width $w = 6 \text{ mm}$ and ligament height $b = 2, 4, 6$ or 8 mm . The lower part of each specimen was clamped between two hardened steel plates using eleven M4 (Grade 12.9²) steel bolts. The need for a large number of small bolts to introduce load into the specimen without local joint failure at each of the small bolts is traced to the fact that UHMWPE laminates have a high tensile strength but a low shear strength. Special measures must be taken to ensure load introduction into the specimen, as discussed by Russell et al. (2013). The variables b and w for the ligament dimensions are used in the present study in order to emphasise their role. They are closely related to the overall width of the joint $W = 2w + d$ and to the end-distance from the centre of the bolt to the free edge of the plate $e = b + d/2$.

An in-plane bearing load F was imposed on each specimen via a steel bolt (Grade2 12.9) of diameter d and thick washers (that is, clamping rings) of diameter $d_w = 25 \text{ mm}$; this was achieved by the loading arrangement of Fig. 1(b). In addition, the effect of the clamping pre-load T_0 in the bolt upon the shear response was investigated by suitable torquing of the bolt. The bolt was displaced in the x_1 direction relative to the composite panel using a screw-driven test machine with a displacement rate of 1 mm/min . The bolt displacement u was measured by a laser extensometer and the reaction force F was determined by the load cell of the test

² ASTM F568M

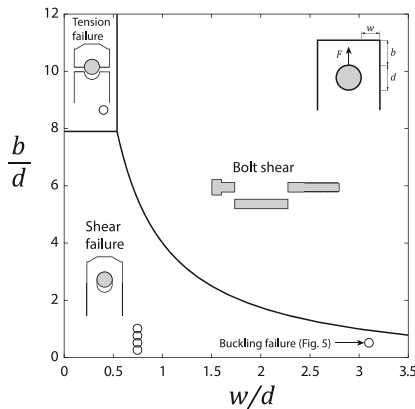


Fig. 2. Failure map for the choice $T_0 = 0$. Laminate thickness $t/d = 0.8$ and ply thickness $h/d = 0.0075$.

machine. The transverse clamping force T was measured via an in-house load cell consisting of two 120Ω strain gauges mounted on the opposing walls of an aluminium alloy tube. The strain gauges were of dimension $3 \text{ mm} \times 1 \text{ mm}$ and of gauge factor 2.15, and a Wheatstone quarter bridge circuit was used for strain measurement. The load cell was of length 20 mm , outer diameter 17 mm and wall thickness 1.3 mm . The degree of bending of the load cell was determined by the difference in axial strain between the gauges and was found to be less than 20% of the mean value throughout each test. We conclude that bending of the load cell was negligible. The mean response of the gauges was used to calculate the transverse clamping force T of the specimens, and this transverse force was recorded by a data-logger. The clamping pre-load T_0 and the evolution of the load T during the test were measured and are reported below.

3. Observed failure modes

We begin by summarising the observed failure modes. The active failure mode of the bolted joint as a function of joint geometry and of clamping pre-load was determined by a combination of visual observation and X-ray CT microscopy.³ A failure map was created for a bolted joint with zero clamping pre-load, $T_0 = 0$, as shown in Fig. 2; the location of the boundaries between failure mechanisms are derived in a subsequent section. The competing failure mechanisms for $T_0 = 0$ are shear of the bolt, tensile failure of the 0° plies at the sides of the hole and shear failure of the laminate; these are sketched in the inserts of Fig. 2. For the case of pin loading with clamping washers absent, the shear mode of failure was replaced by a bearing mode of failure. Fig. 2 is valid for clamped specimens of low d/t ratio. The failure map was constructed for the choice $d = 8 \text{ mm}$ and $t = 6.5 \text{ mm}$. Further work is needed in order to determine the failure map for the clamped specimen at large d/t to determine whether bearing failure intervenes. This is beyond the scope of the present study. The failure map in Fig. 2 is consistent with that of Smith et al. (1986) for 0/90

³ Nikon X-Tek XT H 225ST, at an operating voltage of 50kV

Table 1
Dimensions, confinement and observed failure modes.

| t, mm | d, mm | b, mm | w, mm | Bolt pre-load T_0 , kN | Failure mode |
|-------|-------|-------|-------|--------------------------|--------------|
| 12 | 6 | 15 | 7 | free | Bolt shear |
| 6.5 | 6 | 40 | 3 | 0 | Tension |
| 6.5 | 6 | 4 | 25 | 0 | Buckling |
| 12 | 8 | 4 | 6 | 0 | Shear |
| 12 | 8 | 4 | 6 | free | Shear |
| 6.5 | 8 | 4 | 6 | 0 | Shear |
| 6.5 | 8 | 4 | 6 | 0.84 | Shear |
| 6.5 | 8 | 4 | 6 | 2.89 | Shear |
| 6.5 | 8 | 4 | 6 | 3.67 | Shear |
| 6.5 | 8 | 4 | 6 | 4.75 | Shear |
| 6.5 | 8 | 4 | 6 | 6.59 | Shear |
| 6.5 | 8 | 4 | 6 | 7.67 | Shear |
| 6.5 | 8 | 4 | 6 | 8.92 | Shear |
| 6.5 | 8 | 2 | 6 | free | Shear |
| 6.5 | 8 | 4 | 6 | free | Shear |
| 6.5 | 8 | 6 | 6 | free | Shear |
| 6.5 | 8 | 8 | 6 | free | Shear |
| 6.5 | 8 | 2 | 6 | 0 | Shear |
| 6.5 | 8 | 4 | 6 | 0 | Shear |
| 6.5 | 8 | 6 | 6 | 0 | Shear |
| 6.5 | 8 | 8 | 6 | 0 | Shear |
| 6.5 | 8 | 2 | 6 | 8.92 | Shear |
| 6.5 | 8 | 4 | 6 | 8.92 | Shear |
| 6.5 | 8 | 6 | 6 | 8.92 | Shear |
| 6.5 | 8 | 8 | 6 | 8.92 | Shear |

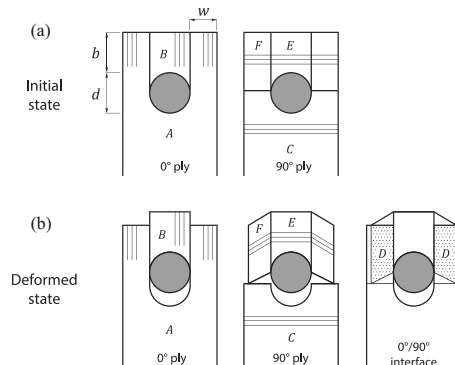


Fig. 3. The load transfer mechanism for shear failure of the bolted joint, with $T_0 \geq 0$. D denotes delamination between the $[0^\circ/90^\circ]$ plies.

CFRP laminates; they also found that shear failure dominates the map for low values of w/d and b/d .

An additional failure mechanism was observed in the present study, that of a transverse plate-buckling mode for plates of large ligament width w , and this is detailed below. Table 1 gives an overview of the dimensions, confinement and the corresponding failure modes observed in the experiments.

3.1. Shear failure

The shear mode of failure occurs for the clamped case, $T_0 \geq 0$, in specimens of small ligament width and height. Interrupted tests and X-ray CT observations were performed in order to reveal the deformation within the 0° plies, 90° plies and the delamination between plies. An idealised view of this deformation mode is sketched in Fig. 3; the accompanying interrupted test (and CT images) are reported in Fig. 4 for the clamped case with $T_0 = 0$, and

ARTICLE IN PRESS

JID: SAS

[m5G; August 29, 2019; 10:6]

4

S.P.H. Skovsgaard, H.M. Jensen and N.A. Fleck / International Journal of Solids and Structures xxx (xxxx) xxx

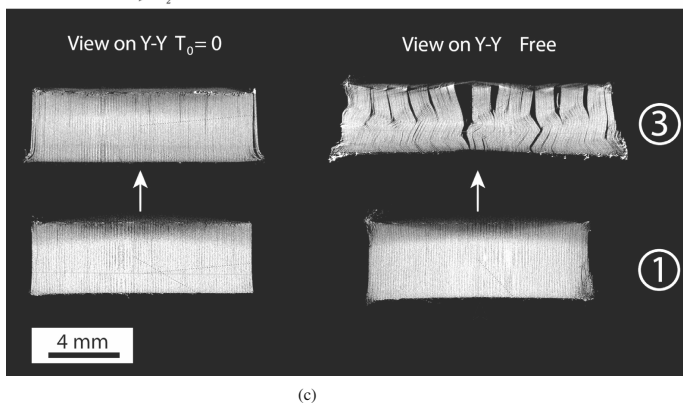
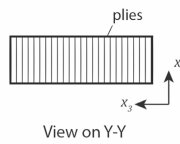
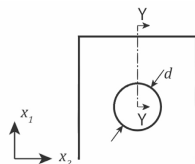
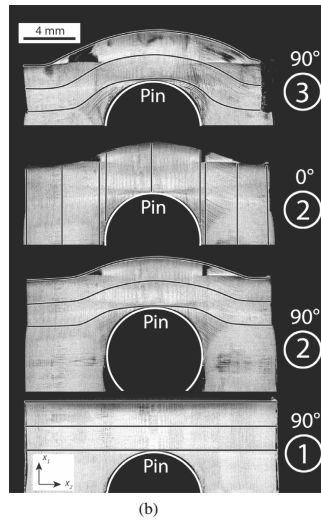
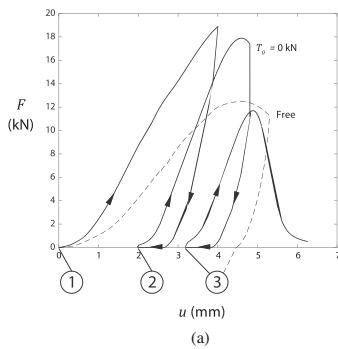


Fig. 4. (a). Axial force F versus axial displacement u for the choice $T_0 = 0$ and the unconstrained case (Free). For both tests, $b = 4$ mm, $w = 6$ mm and $t = 12$ mm. (b). CT images of selected 90° or 0° plies near the mid-plane of the specimen, for the choice $T_0 = 0$. Plan view along the x_3 direction of Fig. 1. (c). Transverse views of the shear failure of the plies above the pin for the clamped case with $T_0 = 0$, and for the pin-loaded case, labelled free.

Please cite this article as: S.P.H. Skovsgaard, H.M. Jensen and N.A. Fleck, Load transfer within the bolted joint of a laminate made from ultra-high molecular weight polyethylene fibres, International Journal of Solids and Structures, <https://doi.org/10.1016/j.ijsolstr.2019.08.014>

ARTICLE IN PRESS

JID: SAS

[m5G;August 29, 2019;10:6]

S.P.H. Skovsgaard, H.M. Jensen and N.A. Fleck/International Journal of Solids and Structures xxx (xxxx) xxx

5

of geometry $b = 4$ mm, $w = 6$ mm and $t = 12$ mm. The initial undeformed state of a representative 0° ply and 90° ply is sketched in Fig. 3(a) and is labelled as (1) in the CT images of Fig. 4(b) and also in the CT image of Fig. 4(c). The specimen was loaded to peak load and then fully unloaded, to obtain the point (2) on the force F versus displacement u curve of the joint in Fig. 4(a); CT scans of representative 0° plies and 90° plies are given in Fig. 4(b) (again labelled (2)). Reloading and subsequent unloading brought the specimen to state (3) as marked in Fig. 3, with the observed deformation state given in Fig. 4. The bolt washers prevent thickening of the specimen adjacent to the bolt, and shear failure of the 0° plies occurs. This is clear from the transverse section of the specimen in Fig. 4(c).

A simple kinematic representation of this failure mode is given in Fig. 3(b), and is described as follows. A portion B of 0° ply material translates by the same displacement u as that of the loading bolt. The remainder of the ply (labelled portion A) remains stationary, and so the collapse mechanism of the 0° ply comprises sliding by a displacement u along two splits (located at the boundary between portions A and B). The deformation state of the 90° ply is slightly more complex. A portion C is undeformed, whereas the portion E of the 90° ply remains bonded to the adjacent portion B in the 0° ply, and is thereby displaced by the displacement u . The portion F of the 90° ply contains the same fibres as portion E , and undergoes in-plane shear as sketched, and as shown in Fig. 4(b). The portion F delaminates and slides with respect to the adjacent portion A of the 0° ply, thereby creating a delamination patch D .

Now consider the case of pin loading with the clamping washers absent, for the same geometry of $b = 4$ mm, $w = 6$ mm and $t = 12$ mm. The force F versus displacement u curve of the joint is included in Fig. 4(a), and labelled 'free'. A bearing failure occurs for this case of unconstrained out-of-plane expansion of the laminate, see the cross-section of state (3) in Fig. 4(c). The portion B of 0° plies and portion E of 90° plies (as defined in Fig. 3) undergo out-of-plane microbuckling with intermittent delamination, see Fig. 4(c).

3.2. Competing collapse modes for the clamped case, $T_0 \geq 0$

An alternative failure mode is tensile failure of the 0° plies adjacent to the loaded bolt. This has been reported previously by Attwood et al. (2014). Bolt shear intervenes for a joint of high aspect ratio b/d and w/d . A more surprising mode that is observed in the present study is out-of-plane plate-buckling for large w/d , as shown in Fig. 5. The buckling failure mode dictates the peak load and occurs shortly before the load maximum, see the dashed line in Fig. 7(b). It is conjectured that this is due to the build-up of a large tensile stress in the 90° plies above the hole leading to

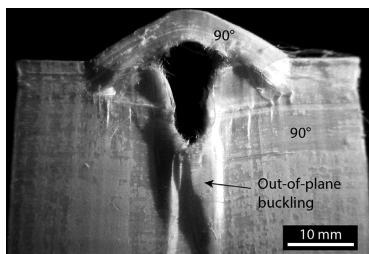


Fig. 5. Optical image of specimen of width $w = 25$ mm, $b = 4$ mm, $t = 6.5$ mm, showing failure by buckling of plate beneath the pin.

compression stress beneath the hole during the later stages of bolt pull-out in the shear failure mode.

4. Sensitivity of joint strength to geometry and clamping

4.1. Effect of initial clamping

The effect of initial clamping pre-load T_0 upon the axial force F versus bolt displacement u is given in Fig. 6(a) for the choice $b = 4$ mm, $w = 6$ mm and $t = 6.5$ mm. This choice of geometry ensures that the shear mode of failure is active. The evolution of transverse clamping force T in each test is summarised in Fig. 6(b). The main features are as follows. Delamination between the 0° and 90° plies, as labelled zone D of Fig. 3(b), occurs at a very low load of below 2 kN, and the subsequent response is linear up to the peak load, labelled F_m . The magnitude F_m increases (linearly) with the pre-load T_0 as shown in Fig. 6(c). This is explained by the pressure dependence of UHMWPE fibre composites, as discussed by Attwood et al. (2014). The clamping force T also increases to a peak value of T_m with increasing bolt displacement u . The clamping force resists out-of-plane swelling of the laminate, and for completeness Fig. 6(c) contains a plot of F_m versus T_m : again the relationship is linear. We note in passing that the peak load F_m occurs at the same value of bolt displacement, and the shift in clamping force ($T_m - T_0$) is constant for all specimens of a given geometry. This is consistent with the notion that the kinematics of the shear failure is insensitive to the level of clamping force.

4.2. Effect of ligament height

The effect of ligament height b upon the bolt force F versus bolt displacement u characteristic is summarised in Fig. 7(a) for 4 values of $b = 2, 4, 6$ and 8 mm, $w = 6$ mm, $t = 6.5$ mm and $T_0 = 0$. In all cases, shear failure occurred. The associated evolution of clamping force T during each test is given in Fig. 7(b). Out-of-plane swelling of the laminate leads to an increase in clamping force with increasing bolt displacement u , and a peak in the clamping force is attained at the same instant that F attains its peak value of F_m . The peak load F_m increases with increasing b , as emphasised by the plot of F_m versus b in Fig. 7(c). For completeness, this figure also contains the sensitivity of F_m to b for $T_0 = 8.9$ kN, for the case of a freely supported bolt (absent clamping) for which bearing failure occurs; it is clear that F_m also increases with the degree of clamping. Likewise, the peak value T_m increases with increasing degree of clamping, and increases in an almost linear manner with increasing b , see Fig. 7(d).

5. Analytical model for shear failure

An analytical model is now proposed for the observed shear failure of the bolted joint. The model assumes a collapse mechanism and thereby gives an upper bound solution for the shear failure force. First, a relation between the axial force as function of axial bolt displacement is derived for the case of relative sliding of the interface between the 0° and 90° plies. Second, the additional force due to in-plane shearing is derived, and it is shown that this dissipation is sufficiently small for the increase in shear force to be negligible.

5.1. Plastic dissipation by inter-laminar shearing

The portion F delaminates and slides with respect to the portion A of the 0° ply, thereby creating a delamination patch D , see Fig. 3(b). The delamination patch D is divided into two zones $D1$ and $D2$, see Fig. 8. The axial bolt displacement u is related to the

ARTICLE IN PRESS

JID: SAS

[m5G; August 29, 2019; 10:6]

6

S.P.H. Skovsgaard, H.M. Jensen and N.A. Fleck / International Journal of Solids and Structures xxx (xxxx) xxx

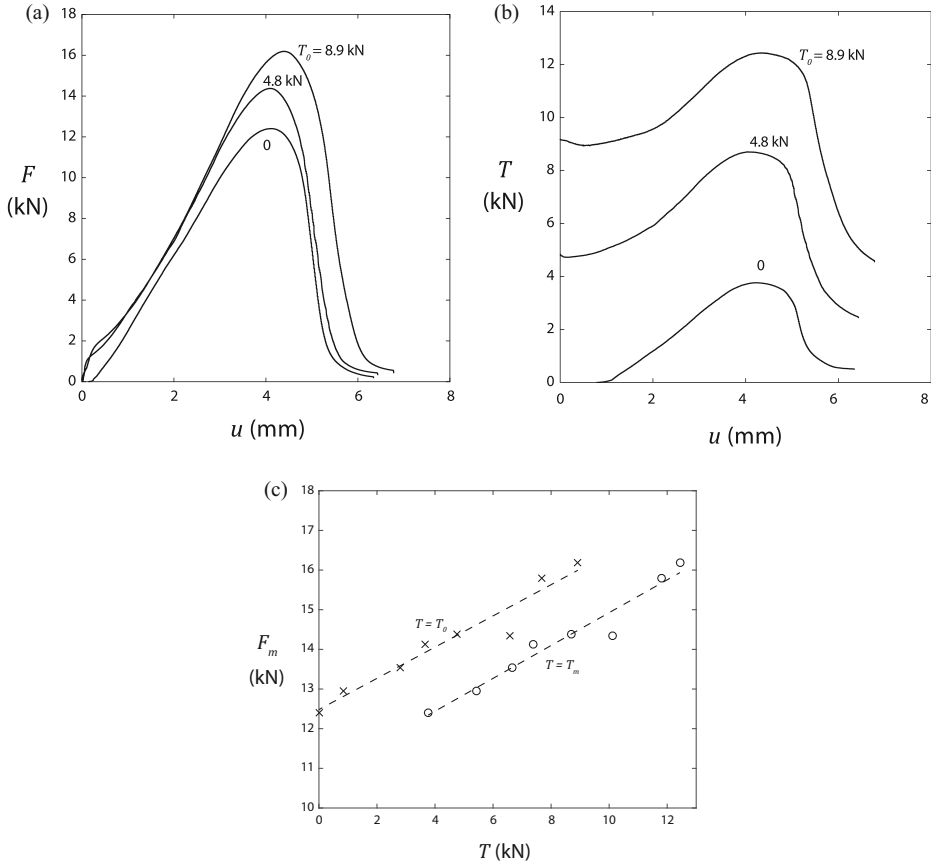


Fig. 6. (a). Axial force F versus axial displacement u . (b). Transverse force T versus axial displacement u . (c). Maximum axial force F_m versus initial transverse force T_0 and maximum value T_m . Dashed lines are best fits to the data. Throughout, specimen ligament height $b = 4$ mm, width $w = 6$ mm and laminate thickness $t = 6.5$ mm.

rotation ϕ of the 90° plies by

$$u = w \sin \phi \tag{1}$$

and the fibres are taken to be inextensible. The delamination patches D1 and D2 are of area A_1 and A_2 , respectively, where

$$A_1 = w \cos \phi \left(b + \frac{d}{2} - u \right) \tag{2}$$

$$A_2 = \frac{1}{2} w \cos \phi u$$

The total number of ply interfaces n_l , over which inter-laminar sliding occurs, is

$$n_l = \frac{t}{h} - 1 \tag{3}$$

where t is the specimen thickness and h is the ply thickness. Now, the principle of virtual work requires that

$$F \delta u = 2 n_l \tau_y \left(A_1 \frac{\delta u}{2} + A_2 \frac{\delta u}{3} \right) \tag{4}$$

where δu is a virtual displacement. Here, a simple rigid-plastic constitutive relation is assumed such that τ_y is the inter-laminar shear yield strength. The factors of $1/2$ and $1/3$ arise from the fact that the assumed displacement field varies across the width of the delamination patch. Upon making use of Eqs. (1) and (2), the virtual work statement (4) reduces to

$$F = n_l \tau_y w \cos \phi \left(b + \frac{d}{2} - \frac{2}{3} w \sin \phi \right) \tag{5}$$

Please cite this article as: S.P.H. Skovsgaard, H.M. Jensen and N.A. Fleck, Load transfer within the bolted joint of a laminate made from ultra-high molecular weight polyethylene fibres, International Journal of Solids and Structures, <https://doi.org/10.1016/j.ijsolstr.2019.08.014>

ARTICLE IN PRESS

JID: SAS

[m5G; August 29, 2019; 10:6]

S.P.H. Skovsgaard, H.M. Jensen and N.A. Fleck / International Journal of Solids and Structures xxx (xxxx) xxx

7

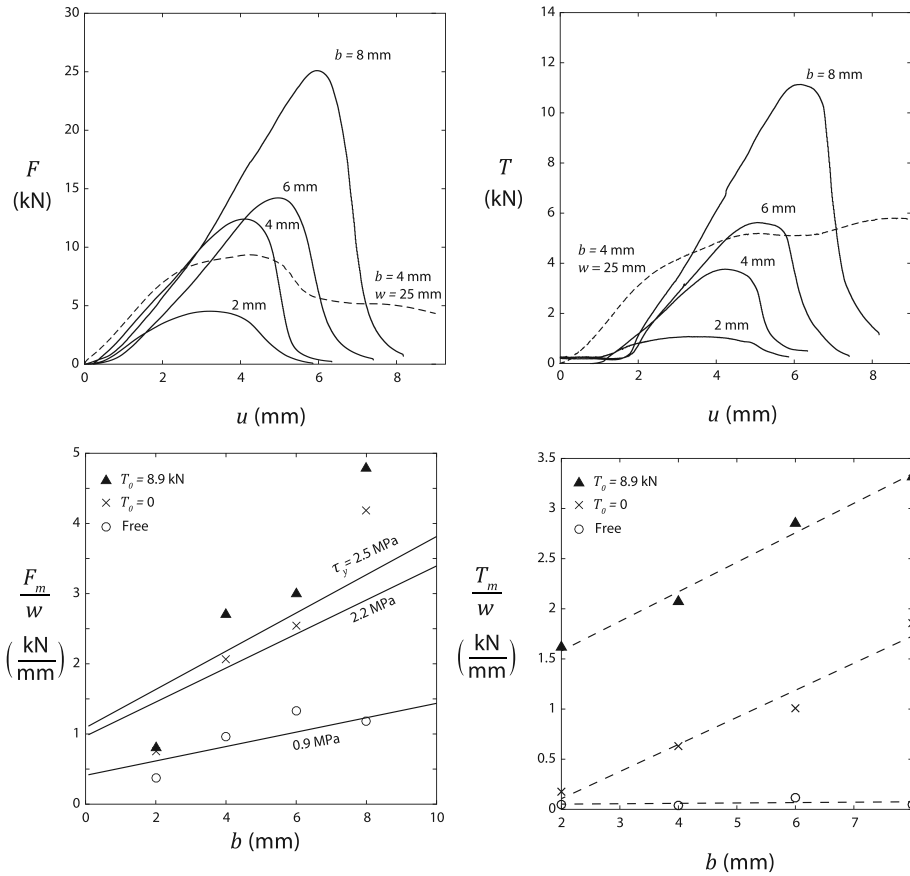


Fig. 7. (a). Axial force F versus axial displacement u for the choice $T_0 = 0$. (b). Transverse force T versus axial displacement u for the choice $T_0 = 0$. (c). Maximum axial force F_m/w versus ligament height b . Solid lines show predictions by the analytical model. (d). Maximum transverse force T_m/w versus ligament height b . Dashed lines show best fit to the data. Throughout, specimen $w = 6$ mm, thickness $t = 6.5$ mm besides an experiment showing buckling with $w = 25$ mm (dashed line).

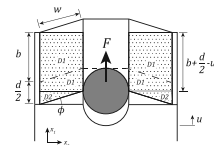


Fig. 8. Sketch of the geometry for analytical model.

with peak value F_{pc} for the plastic collapse mode achieved at $\phi = 0$, such that

$$F_{pc} = n_t \tau_y w \left(b + \frac{d}{2} \right) \quad (6)$$

5.2. Additional plastic dissipation due to in-plane shearing

The additional force ΔF due to in-plane shearing is now deduced. The portion F in Fig. 3 undergoes in-plane shearing. The portion F has an in-plane area of

$$A_F = 2 \left(b + \frac{d}{2} \right) w \cos \phi \quad (7)$$

The virtual displacement δu is related to the virtual rotation $\delta \phi$ by

$$\delta u = w \cos \phi \delta \phi \quad (8)$$

Using the displacement-rotation relation, Eq. (1). During a virtual displacement, the area A_F shears an amount $\delta \phi$. Then, the

ARTICLE IN PRESS

JID: SAS

[m5G;August 29, 2019;10:6]

8

S.P.H. Skovsgaard, H.M. Jensen and N.A. Fleck / International Journal of Solids and Structures xxx (xxxx) xxx

additional term in the principle of virtual work for in-plane shearing is of the form

$$\Delta F \delta u = A_F h \delta \phi \tau_y n_{90} \quad (9)$$

where n_{90} is the number of 90° plies. Again, a simple rigid-plastic constitutive relation is used, where the in-plane shear yield strength τ_y is identical to the inter-laminar yield strength. The relation (9) is simplified via Eqs. (7) and (8) to read

$$\Delta F = 2 \left(b + \frac{d}{2} \right) \tau_y n_{90} h \quad (10)$$

Upon normalising the additional axial force ΔF due to in-plane shearing by the peak load Eq. (6) due to inter-laminar shearing we obtain

$$\frac{\Delta F}{F_{pc}} = \frac{2 \left(b + \frac{d}{2} \right) n_{90} h}{\left(b + \frac{d}{2} \right) n_l w} \quad (11)$$

Now, the number of interfaces n_l is twice the number of 90° plies n_{90} . Consequently, the additional force arriving from in-plane shearing scales as

$$\frac{\Delta F}{F_{pc}} = \frac{h}{w} \quad (12)$$

Recall that the ply thickness h equals 60 μm and the ligament width w equals 6 mm for the majority of the test specimens. Thus, in-plane shearing will increase the axial force by only 1% and this is deemed negligible.

6. Comparison of shear failure prediction with observation

The analytical model of shear failure is now compared with the experimental results by treating the inter-laminar shear strength τ_y as a free parameter that depends upon the degree of clamping. The predictions of Eq. (6) are compared with the measured values of maximum force F_m in Fig. 7(c), assuming that $\tau_y = 0.95$ MPa for clamping-free, $\tau_y = 2.2$ MPa for $T_0 = 0$ and $\tau_y = 2.5$ MPa for $T_0 = 8.9$ kN. Recall that the measured inter-laminar shear strength is $\tau_y = 2$ MPa as obtained by Liu et al. (2014) and Attwood et al. (2014); they used a double-notch shear test. The agreement is satisfactory.

The out-of-plane clamping pressure increases the inter-laminar yield strength as follows. Attwood et al. (2014) studied the out-of-plane compressive response of UHMWPE laminates. They observed a pressure sensitivity of the form

$$\tau_y = \tau_0 + \mu p \quad (13)$$

where τ_y is the shear yield strength, τ_0 is the strength in the absence of pressure, p is the pressure and μ is a non-negative pressure sensitivity coefficient. Attwood et al. (2014) found that a coefficient $\mu = 0.05$ gave good agreement with experimental results. The increased inter-laminar yield strength as observed in the current study can be explained by the pressure sensitivity of UHMWPE. To illustrate this, consider a specimen of ligament width $w = 6$ mm, ligament height $b = 8$ mm and bolt diameter $d = 8$ mm. An initial pre-load of $T_0 = 8.9$ kN results in an average pressure $p = 43$ MPa beneath the clamping ring. Upon substituting an initial yield strength, $\tau_0 = 0.95$ MPa, a pressure sensitivity coefficient $\mu = 0.05$ and $p = 43$ MPa into Eq. (13) the predicted yield strength is $\tau_y = 3.1$ MPa. This is in reasonable agreement with the inferred value of $\tau_y = 2.5$ MPa.

7. Failure mechanism map

The background to the construction of the failure map of Fig. 2 is now given. We consider each mechanism in turn. Introduce the non-dimensional geometric parameters

$$\tilde{t} = \frac{t}{d} \quad \tilde{b} = \frac{b}{d} \quad \tilde{w} = \frac{w}{d} \quad (14)$$

along with the non-dimensional force on the bolt

$$\tilde{F} = \frac{F}{d t \tau_y} \quad (15)$$

where d is the bolt diameter, t the plate thickness and τ_y is the inter-laminar shear yield strength.

7.1. Shear failure

The load maximum for the shear failure is given by Eq. (6) using the simple analytical model. The non-dimensional force at shear failure (plastic collapse) is

$$\tilde{F}_{pc} = \frac{F_{pc}}{d t \tau_y} = n_l \tilde{w} \left(\tilde{b} + \frac{1}{2} \right) \frac{1}{\tilde{t}} \quad (16)$$

7.2. Bolt shear

The bolt carries a transverse shear force $V = F/2$ at two locations. Assume that the bolt shears plastically when the shear stress on the section attains the shear strength τ_{bf} . High strength bolts are almost elastic, ideally plastic in their response, with a tensile strength of $\sigma_{bf} = 1200$ MPa, and a shear strength $\tau_{bf} = 1200/\sqrt{3}$ MPa = 693 MPa by the von Mises yield criterion. Consequently, bolt shear occurs at a load

$$F_{bf} = \frac{\pi}{2} d^2 \tau_{bf} \quad (17)$$

and, upon introducing the non-dimensionalisation we obtain

$$\tilde{F}_{bf} = \frac{F_{bf}}{d t \tau_y} = \frac{\pi}{2} \frac{\tau_{bf}}{\tau_y} \frac{1}{\tilde{t}} \quad (18)$$

7.3. Tensile failure of the laminate

Tensile failure of the fibres within the 0° plies occurs at an axial stress of $\sigma_f = 3000$ MPa within the fibres. Recall that the strength of the composite normal to the fibre direction is three orders of magnitude lower than in the direction of the fibres and is thereby negligible. The strength of the composite in tension is

$$\sigma_t = \frac{1}{2} \sigma_f c^f \quad (19)$$

where $c^f = 0.83$ is the volume fraction of fibres (Liu et al. (2014)). A factor of 1/2 is introduced due to the equal volume fraction of 0° and 90° plies, and the fact that the 90° plies provide a negligible contribution to the strength. The smallest cross sectional area normal to the force F is $2 w t$, see Fig. 1. Consequently, the force at tensile failure is

$$F_t = 2 w t \sigma_t \quad (20)$$

and so the non-dimensional force \tilde{F}_t at tension failure is

$$\tilde{F}_t = \frac{F_t}{d t \tau_y} = 2 \frac{\sigma_t}{\tau_y} \tilde{w} \quad (21)$$

ARTICLE IN PRESS

JID: SAS

[m5G;August 29, 2019;10:6]

S.P.H. Skovsgaard, H.M. Jensen and N.A. Fleck/*International Journal of Solids and Structures* xxx (xxxx) xxx

9

7.4. Construction of failure map

A failure map for $T_0 = 0$ is constructed with geometric axes b/d and w/d in order to identify regimes of dominance of the competing failure modes, see Fig. 2. The active mode has the lowest failure load from the relations Eqs. (16), (18) and (21). The boundaries are located by equating the failure load of competing mechanisms. The precise boundary between shear failure and out-of-plane plate buckling is unknown; consequently, the boundary is not drawn in the failure map.

8. Concluding remarks

The present study highlights the dominance of the shear mode of joint failure in a bolted joint made from a UHMWPE laminate, and subjected to out-of-plane clamping by the bolt. The 0° plies split such that the central portion of 0° plies (adjacent to the bolt) is sheared-out from the joint by movement of the bolt. The 90° plies that are stacked with the central portion of 0° plies are also dragged-out of the joint by the bolt displacement. This leads to tensile pull-through of the 90° plies and to delamination of the 0° plies.

The strength at shear failure is increased substantially by increasing clamping force, and this is explained in terms of the pressure sensitivity of the shear strength of the UHMWPE composite. A simple analytical model highlights the importance of slip between the plies in providing the resistance to a shear failure. Also, a failure map is constructed and provides useful guidelines for joint strength as a function of geometry. In order to predict the plate buckling mode at large ligament width w , a 3D finite element model would be required and this is beyond the scope of the present study.

Acknowledgements

The research work was supported by the Thomas B. Thriges Fond; Aage og Johanne Louis-Hansens Fond; Knud Højgaard's Fond; Augustinus Fonden; Reinholdt W Jorck og Hustrus Fond; Marie & M. B. Richters Fond; and the Graduate School of Science and Technology (Aarhus University). The authors are grateful for fi-

nancial support for this work in the form of an ERC MULTILAT grant 669764, and to DSM for providing the Dyneema® composites used in this study.

References

- Attwood, J.P., Fleck, N.A., Wadley, H.N.G., Deshpande, V.S., 2015. The compressive response of ultra-high molecular weight polyethylene fibres and composites. *Int. J. Solids Struct.* 71, 141–155. doi:10.1016/j.ijsolstr.2015.06.015.
- Attwood, J.P., Khaderi, S.N., Karthikeyan, K., Fleck, N.A., Omasta, M.R., Wadley, H.N.G., Deshpande, V.S., 2014. The out-of-plane compressive response of Dyneema® composites. *J. Mech. Phys. Solids* 70, 200–226. doi:10.1016/j.jmps.2014.05.017.
- Camanho, P., Matthews, F., 1997. Stress analysis and strength prediction of mechanically fastened joints in FRP: a review. *Compos. Part A Appl. Sci. Manuf.* 28, 529–547. doi:10.1016/S1359-835X(97)00004-3.
- Govaert, L.E., Lemstra, P.J., 1992. Deformation behavior of oriented UHMWPE fibers. *Colloid Polym. Sci.* 270, 455–464. doi:10.1007/BF00665989.
- Govaert, L.E., Peijs, T., 1995. Tensile strength and work of fracture of oriented polyethylene fibre. *Polymer (Guildf)* 36, 4425–4431. doi:10.1016/0032-3861(95)96948-3.
- Grujicic, M., Arakere, G., He, T., Bell, W.C., Glomski, P.S., Cheeseman, B.A., 2009. Multi-scale ballistic material modeling of cross-plyed compliant composites. *Compos. Part B Eng.* 40, 468–482. doi:10.1016/j.compositesb.2009.02.002.
- Iannucci, L., Pope, B., 2011. High velocity impact and armour design. *Express Polym. Lett.* 5, 262–272. doi:10.3144/expresspolymlett.2011.26.
- Karthikeyan, K., Russell, B.P., Fleck, N.A., Omasta, M., Wadley, H.N.G., Deshpande, V.S., 2013. The soft impact response of composite laminate beams. *Int. J. Impact Eng.* 60, 24–36. doi:10.1016/j.ijimpeng.2013.04.002.
- Koh, A.C.P., Shim, V.P.W., Tan, V.B.C., 2010. Dynamic behaviour of UHMWPE yarns and addressing impedance mismatch effects of specimen clamps. *Int. J. Impact Eng.* 37, 324–332. doi:10.1016/j.ijimpeng.2009.10.008.
- Liu, B.G., Kandan, K., Wadley, H.N.G., Deshpande, V.S., 2018. Deep penetration of ultra-high molecular weight polyethylene composites by a sharp-tipped punch. *J. Mech. Phys. Solids* doi:10.1016/j.jmps.2018.06.001.
- Liu, G., Thouless, M.D., Deshpande, V.S., Fleck, N.A., 2014. Collapse of a composite beam made from ultra high molecular-weight polyethylene fibres. *J. Mech. Phys. Solids* 63, 320–335. doi:10.1016/j.jmps.2013.08.021.
- Russell, B.P., Karthikeyan, K., Deshpande, V.S., Fleck, N.A., 2013. The high strain rate response of ultra high molecular-weight polyethylene: from fibre to laminate. *Int. J. Impact Eng.* 60, 1–9. doi:10.1016/j.ijimpeng.2013.03.010.
- Smith, P., Lemstra, P.J., 1980. Ultra-high strength polyethylene filaments by solution spinning/drawing. 3. Influence of drawing temperature. *Polym. (U. K.)* 21, 1341–1343. doi:10.1016/0032-3861(80)90205-0.
- Smith, P.A., Pascoe, K.J., Polak, C., Stroud, D.O., 1986. The behaviour of single-lap bolted joints in CFRP laminates. *Compos. Struct.* 6, 41–55. doi:10.1016/0263-8223(86)90067-X.
- Thoppul, S.D., Finegan, J., Gibson, R.F., 2009. Mechanics of mechanically fastened joints in polymer-matrix composite structures - a review. *Compos. Sci. Technol.* 69, 301–329. doi:10.1016/j.compscitech.2008.09.037.
- Wilding, M.A., Ward, I.M., 1978. Tensile creep and recovery in ultra-high modulus linear polyethylenes. *Polymer (Guildf)* 19, 969–976. doi:10.1016/0032-3861(78)90208-2.

Chapter 11

C1

Micromechanics of kink band formation in open-hole fibre composites under compressive loading

11.1 Motivation

One of the main methodologies to transfer load between two structures is through bolted joints. Structural applications made in fibre-reinforced composites may include open-holes for different reasons. Experiments suggest that kink band formation is the dominant failure mechanism for open hole fibre composites with a soft and ductile resin material. It has been observed that fibre kinking is initiated from the hole edge and is followed by other failure mechanisms e.g. delamination and fibre breakage.

The current publication deals with the investigation of compressive failure of open-hole fibre composites by kink band formation. Despite the many contributions to the problem, different aspects of the phenomenon still remain unknown. The original source of the publication is: (Tojaga et al., 2018).

11.2 Method

The investigation of kink band formation is challenging since the simulations must include large deformations and rotations together with non-linear elastic-plastic material behaviour. Furthermore, often arc-length solvers are required since the equilibrium path includes snap-back and snap-through behaviour.

The finite element software Abaqus/CAE 6.14 together with a user subroutine (UMAT) written in Fortran 77 are used to solve the problem. The constitutive model by Christoffersen and Jensen (1996) is implemented in the UMAT. The model by Christoffersen and Jensen (1996) is described in Section 3.2. Two versions of the constitutive model are implemented: a version with perfect bonding and one with no bonding between the fibre and matrix constituent. Material parameters from Kyriakides et al. (1995) are used in the study.

11.3 Contribution

The contributions to the publication comprise: changes made on a user subroutine initially created by Sørensen et al. (2009) to have better convergence. Further contributions include participations in supervision of Vedad Tojaga, discussion of the article content and proofreading.

11.4 Main findings

Illustrations of the different fields (e.g. stress and strain fields) prior to the peak stress are presented. These graphical illustrations give valuable insight into the initiation of kink bands. The influence of fibre orientations relative to the loading direction is investigated for an open-hole unidirectional fibre composite. Furthermore, the influence of perfect fibre/matrix bonding and no bonding are investigated where the realistic compressive strength lies between the two boundaries.

One of the main strengths behind the current publication, compared to previous studies on open-hole compression of composites, is the constitutive relation that includes information about the current stress and strain state for the constituents during loading.

Composites Part B 149 (2018) 66–73



Contents lists available at ScienceDirect

Composites Part B

journal homepage: www.elsevier.com/locate/compositesb

Micromechanics of kink band formation in open-hole fibre composites under compressive loading



Vedad Tojaga*, Simon P.H. Skovsgaard, Henrik Myhre Jensen

Department of Engineering, Aarhus University, Inge Lehmanns Gade 10, 8000 Aarhus C, Denmark

ARTICLE INFO

Keywords:

Laminates
Microstructures
Plastic deformation
Micro-mechanics

ABSTRACT

The micromechanics of kink band formation in open-hole fibre composites under compressive loading is described. The objective being the development of a methodology for designing of structural components with open-holes. Our results explain why failure by kink band formation propagates from the edges of an open-hole in a direction almost perpendicular to the loading direction and why the 0 plies govern the compressive failure of an open-hole laminate. The proposed design methodology accounts for the microstructure, including the fibre/matrix bonding, and the nonlinear behaviour of the constituents, enabling it to prevent local failure at the hole edges, or global failure, by kink banding of a laminate containing stress concentrations.

1. Introduction

The compressive strength of a unidirectional fibre composite is often less than 60 % of its tensile strength; hence, in many cases, the compressive strength dictates the design. An important mechanism of compressive failure in fibre composites is a localized imperfection-sensitive material instability known as plastic microbuckling, leading to the formation of one or more kink bands by localization of plastic deformation. Both terminologies, i.e. plastic microbuckling and kink band formation, are adopted in this paper. Manufacturing and curing of a composite inevitably introduce fibre misalignments. The matrix provides lateral stability to the fibres and prevents, or postpones, the occurrence of plastic microbuckling, inducing a complex strain field in the matrix. After a small amount of fibre rotation under a remote compressive stress, geometric softening associated with the fibre rotation outweighs the plastic strain hardening of the matrix, and a microbuckle nucleates and then propagates through the composite. The remote compressive stress, at which the composite fails by the formation of kink bands, i.e. the critical stress, is sensitive to fibre misalignments since the load carrying capacity of the material is lost locally. The latter description emphasizes the importance of accounting for the nonlinear behaviour of the constituents and the microstructure of a composite when investigating plastic microbuckling. In the early work on kink band formation, Argon [1] and Budiansky [2] identified that fibre misalignments and plastic shear deformation in the matrix govern the critical stress. Christoffersen and Jensen [3] developed a homogenized constitutive model accounting for the microstructure of a unidirectional fibre composite and allowing all cases of time-independent elastic-

plastic behaviour of the constituents, making it suitable for analysing plastic microbuckling. Sørensen et al. [4] implemented the model [3] as a user subroutine (UMAT) into the finite element program ABAQUS. Jensen [5] extended the latter formulation to account for full decohesion between the matrix and the fibres. The models in Refs. [3] and [5] do not take the fibre bending rigidity into account; however, the fibre bending rigidity decreases with the fibre diameter and in most real-life applications, fibre composites contain many thin fibres embedded in a matrix. A constitutive model for imperfectly bonded fibre-reinforced polymer composites by Skovsgaard and Jensen [6] describes the transition between these two models. Recently, Skovsgaard and Jensen [7] developed a three-dimensional constitutive model for elastic-plastic behaviour of fibre-reinforced composites inspired by the two-dimensional model [3]. Depending on the given structural component and how well controlled the fibre misalignments are, due to manufacturing, the critical stress may not be suitable for engineering applications. Beyond the critical stress, in the post-critical region, the kink band may propagate (under steady-state conditions) through the material at a constant stress known as the steady-state kinking stress. At steady-state, the fibres in the kink band stop rotating, i.e. lock-up, forcing the kink band to spread into the base material. A semi-analytical model by Jensen [8] predicts the steady-state kinking stress. Recently, Skovsgaard and Jensen [9] developed an analytical model for steady-state kinking. Liu et al. [10] suggest that, for unidirectional fibre composites containing stress concentrations, e.g. holes and notches, a lower bound for the critical stress can be estimated by the steady-state kinking stress. Structural applications of fibre composites may include components with open-holes. The ability to predict compressive failure of open-hole

* Corresponding author.

E-mail addresses: vt@eng.au.dk (V. Tojaga), sphs@eng.au.dk (S.P.H. Skovsgaard), hmj@eng.au.dk (H.M. Jensen).<https://doi.org/10.1016/j.compositesb.2018.05.014>

Received 14 March 2018; Received in revised form 1 May 2018; Accepted 9 May 2018

Available online 12 May 2018

1359-8368/ © 2018 Elsevier Ltd. All rights reserved.

fibre composites is a problem of considerable importance to the Aerospace Engineering community. It provides useful information about how a composite performs in an open-hole application and how resistant it is to defects from fabrication or in-service. Open-hole compression tests on fibre composites suggest that the dominant mechanism of compressive failure is plastic microbuckling [11–20], provided that the matrix displays ductile material behaviour. Plastic microbuckling starts progressively from the edges of a hole and propagates in a direction normal to the loading direction. Modelling of compressive failure interactions in an open-hole T300/914 laminate using a homogenized description of the material separated by interfaces reveals, in accordance with the latter experimental observations, that plastic microbuckling starts progressively from the edges of a hole [22]. Experimental studies by Soutis and Fleck [13], Soutis et al. [14–16] and Ahn and Waas [28] suggest that plastic microbuckling, in the 0° plies, governs the compressive failure of an open-hole carbon/epoxy laminate.

Whitney and Nuismer [23] developed an average stress and a point stress failure criterion for notched laminates. The point stress failure criterion predicts failure when the stress at a distance d_0 away from the hole reaches the unnotched strength. The average stress failure criterion predicts failure when the average stress over a distance a_0 reaches the unnotched strength. The distance parameters a_0 and d_0 vary with hole size and stacking sequence among other factors [24]. After observing that plastic microbuckling, in the 0° plies, governs the compressive failure of an open-hole laminate, Soutis et al. [15] developed a cohesive zone model for predicting the open-hole compression strength. In the cohesive zone model, plastic microbuckling initiates when a remote compressive stress multiplied by a stress concentration factor reaches the unnotched strength. A crack replaces the microbuckled zone and when the crack obtains a critical length such that the remote compressive stress attains a maximum value, catastrophic failure takes place. For the simplicity of application, many textbooks adopt the latter failure criteria; however, these criteria depend on an accurate measurement of unnotched strength and compressive fracture toughness, which highly depend on the microstructure. Ahn and Waas [17] defined a global-local approach in which a micro-region around a hole is analysed. Boundary conditions to be applied on the micro-region are obtained from a global homogenous model. Extensions of this method are validated and used by airframe manufacturers to predict the open-hole compression strength of laminates [25–26]. These studies can capture kink band formation, which is the dominant failure mechanism in compression, and damage in the off-axis plies within a laminate.

Despite the many contributions, the micromechanics associated with kink band formation in open-hole fibre composites under compressive loading remains less understood. This paper aims to describe the micromechanics with the objective of developing a design methodology, accounting for the nonlinear behaviour of the constituents and the microstructure of the composite, for designing of structural components with open-holes. It is inspired by [27]. To accomplish the latter objective, the constitutive models in Refs. [3] and [5] are applied using finite element analysis. The semi-analytical model in Ref. [8] enables a verification of the findings in Ref. [10].

2. Constitutive relations

The constitutive relation

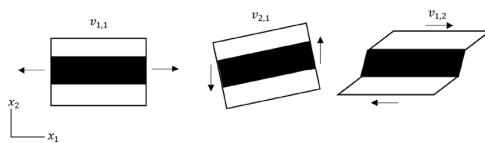


Fig. 1. Incremental deformation in a RVE of a unidirectional fibre composite with perfect fibre/matrix bonding.

$$\dot{\epsilon}_{ij} = C_{ijkl} v_{l,k} \tag{1}$$

relates the nominal stress rates $\dot{\epsilon}_{ij}$ to the velocity gradients $v_{l,j}$ through the nominal moduli C_{ijkl} . This paper adopts the index notation, the summation convention and Cartesian coordinates. Latin indices, e.g. i, j, k, l , take values 1,2,3 and Greek indices, e.g. α, β, γ , take values 1,2. Neglecting the incremental volume change of a material, i.e. $v_{k,k} = 0$, the relation between the nominal moduli C_{ijkl} and the instantaneous moduli L_{ijkl} is

$$C_{ijkl} = L_{ijkl} + \frac{1}{2} \sigma_{ik} \delta_{jl} - \frac{1}{2} \sigma_{il} \delta_{jk} - \frac{1}{2} \sigma_{kj} \delta_{li} \tag{2}$$

where the instantaneous moduli L_{ijkl} relate the Jaumann rate of the Cauchy stresses $\dot{\sigma}_{ij}$ to the strain rates $\dot{\epsilon}_{ij}$, i.e.

$$\dot{\sigma}_{ij} = L_{ijkl} \dot{\epsilon}_{kl} \quad , \quad \dot{\epsilon}_{ij} = \frac{1}{2} (v_{l,j} + v_{j,l}) \tag{3}$$

and consequently, they satisfy the minor symmetries, i.e.

$$L_{ijkl} = L_{jikl} = L_{ijlk} \tag{4}$$

The relation between the Jaumann rate of the Cauchy stresses $\dot{\sigma}_{ij}$ and the nominal stress rates $\dot{\epsilon}_{ij}$ is

$$\dot{\sigma}_{ij} = \dot{\epsilon}_{ij} - \omega_{jk} \sigma_{ik} - \omega_{ik} \sigma_{kj} - \sigma_{ij} v_{k,k} + \sigma_{jk} v_{i,k} \quad , \quad \omega_{ij} = \frac{1}{2} (v_{l,j} - v_{j,l}) \tag{5}$$

where ω_{ij} denote the spin.

3. Constitutive models

For convenience, the notation in Section 2 is adopted in the matrix form

$$\dot{\mathbf{t}}_{\alpha}^c = \mathbf{C}_{\alpha\beta}^c \mathbf{v}_{\beta}^c \tag{6}$$

equivalent to Eq. (1), where

$$\mathbf{v}^c = \begin{bmatrix} v_1^c \\ v_2^c \end{bmatrix}, \quad \mathbf{t}_i^c = \begin{bmatrix} t_{i1}^c \\ t_{i2}^c \end{bmatrix}, \quad \mathbf{t}_2^c = \begin{bmatrix} t_{21}^c \\ t_{22}^c \end{bmatrix} \tag{7}$$

from which it follows that

$$\mathbf{C}_{11}^c = \begin{bmatrix} C_{1111}^c & C_{1112}^c \\ C_{1211}^c & C_{1212}^c \end{bmatrix}, \quad \mathbf{C}_{12}^c = \begin{bmatrix} C_{1121}^c & C_{1122}^c \\ C_{1221}^c & C_{1222}^c \end{bmatrix},$$

$$\mathbf{C}_{21}^c = \begin{bmatrix} C_{2111}^c & C_{2112}^c \\ C_{2211}^c & C_{2212}^c \end{bmatrix}, \quad \mathbf{C}_{22}^c = \begin{bmatrix} C_{2121}^c & C_{2122}^c \\ C_{2221}^c & C_{2222}^c \end{bmatrix} \tag{8}$$

Superscript c refers to one of the constituents, i.e. fibre f or matrix m . The x_1 - and x_2 - axes are assumed to be parallel with and normal to the fibres prior to deformation, respectively. This section presents the constitutive models by Christoffersen and Jensen [3] and Jensen [5], assuming perfect fibre/matrix bonding and no fibre/matrix bonding, respectively, in the form

$$\dot{\mathbf{t}}_{\alpha} = \mathbf{C}_{\alpha\beta} \mathbf{v}_{\beta} \tag{9}$$

equivalent to Eq. (6). When superscripts are omitted, the quantities refer to the composite.

V. Tojaga et al.

Composites Part B 149 (2018) 66–73

3.1. Constitutive model with perfect fibre/matrix bonding

Assuming displacement continuity in a representative volume element (RVE) of a unidirectional fibre composite (Fig. 1), i.e.

$$\mathbf{v}_{,1}^f = \mathbf{v}_{,1}^m = \mathbf{v}_{,1} \tag{10}$$

$$c^f \mathbf{v}_{,2}^f + c^m \mathbf{v}_{,2}^m = \mathbf{v}_{,2} \tag{11}$$

where the sum of the fibre and matrix volume fractions is unity, i.e. $c^f + c^m = 1$, and overall equilibrium, i.e.

$$c^f \mathbf{i}_1^f + c^m \mathbf{i}_1^m = \mathbf{i}_1 \tag{12}$$

$$\mathbf{i}_2^f = \mathbf{i}_2^m = \mathbf{i}_2 \tag{13}$$

By combination of Eqs. (6), (10)–(13), one obtains

$$\mathbf{v}_{,2}^f = (c^m \mathbf{C}_{22}^f + c^f \mathbf{C}_{22}^m)^{-1} (c^m (\mathbf{C}_{21}^m - \mathbf{C}_{21}^f) \mathbf{v}_{,1} + \mathbf{C}_{22}^m \mathbf{v}_{,2}) \tag{14}$$

$$\mathbf{v}_{,2}^m = (c^m \mathbf{C}_{22}^f + c^f \mathbf{C}_{22}^m)^{-1} (c^f (\mathbf{C}_{21}^f - \mathbf{C}_{21}^m) \mathbf{v}_{,1} + \mathbf{C}_{22}^f \mathbf{v}_{,2}) \tag{15}$$

and the composite moduli

$$\mathbf{C}_{\alpha\beta}^c = c^f \mathbf{C}_{\alpha\beta}^f + c^m \mathbf{C}_{\alpha\beta}^m - c^f c^m (\mathbf{C}_{22}^f - \mathbf{C}_{22}^m) (c^m \mathbf{C}_{22}^f + c^f \mathbf{C}_{22}^m)^{-1} (\mathbf{C}_{2\beta}^f - \mathbf{C}_{2\beta}^m) \tag{16}$$

3.2. Constitutive model with no fibre/matrix bonding

In addition to Eqs. (10) and (12), assuming displacement continuity between the matrix and the composite (Fig. 2), i.e.

$$\mathbf{v}_{,2}^m = \mathbf{v}_{,2} \tag{17}$$

and that the tractions normal to the fibres are not transmitted to the fibres, i.e.

$$\mathbf{i}_2^f = 0 \tag{18}$$

such that the overall tractions \mathbf{i}_2 , acting on the composite, are an average of the local tractions in the matrix \mathbf{i}_2^m , i.e.

$$\mathbf{i}_2 = c^m \mathbf{i}_2^m \tag{19}$$

we obtain

$$\mathbf{v}_{,2}^f = -(\mathbf{C}_{22}^f)^{-1} \mathbf{C}_{21}^f \mathbf{v}_{,1} \tag{20}$$

and the composite moduli

$$\mathbf{C}_{\alpha\beta}^c = c^f \mathbf{C}_{\alpha\beta}^f + c^m \mathbf{C}_{\alpha\beta}^m - c^f \mathbf{C}_{\alpha 2}^f (\mathbf{C}_{22}^f)^{-1} \mathbf{C}_{2\beta}^f \tag{21}$$

4. Implementation

Sørensen et al. [4] implemented the constitutive model in Subsection 3.1 as a user subroutine (UMAT) into ABAQUS. The current implementation of the constitutive models in Section 3, in which a superscript refers to the constituents and no superscript refers to the composite, contains the following steps:

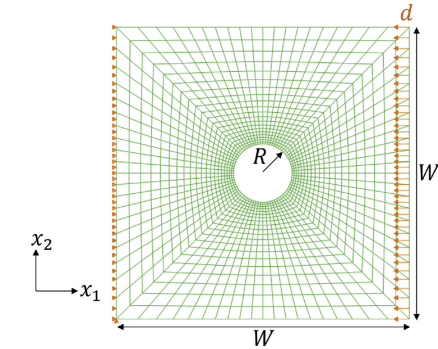


Fig. 3. Finite element mesh, with 1600 fully integrated biquadratic elements in plane strain and ratio $R/W = 0.1$.

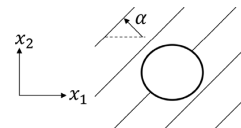


Fig. 4. Initial fibre orientation α .

Table 1 AS4/PEEK material parameters.

| σ_y^f [MPa] | E^f [MPa] | ν^f | n^f | c^f | σ_y^m [MPa] | E^m [MPa] | ν^m | n^m |
|--------------------|-------------|---------|-------|-------|--------------------|-------------|---------|-------|
| 4.140 | 214.000 | 0.263 | 1.9 | 0.6 | 82.1 | 6.140 | 0.356 | 4 |

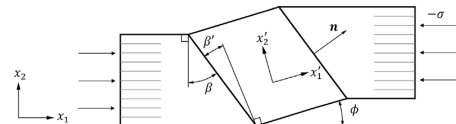


Fig. 5. Kink band geometry, with an inclination angle β . The fibres in the kink band are rotated at an angle ϕ .

- 1) Load $c^f, \sigma_y^f, I_{ij}^f, \mathbf{C}_{\alpha\beta}^f, \mathbf{C}_{\alpha\beta}^c, \alpha_{\alpha\beta}$ from previous time step
- 2) Calculate $\nu_{\alpha,\beta}$ from

$$\nu_{\alpha,\beta} = (c_{\alpha\gamma} \epsilon_{\gamma\eta} F_{\eta\eta}^k - F_{\alpha\zeta}^k) F_{\beta\zeta}^k{}^{-1} \tag{22}$$

where $F_{\alpha\beta}^k$ and $F_{\alpha\beta}^0$ denote the deformation gradients at the end and in the beginning of the increment, respectively, and $\epsilon_{\alpha\beta}$ denotes the incremental directional cosines. A rigid body rotation contributes to the

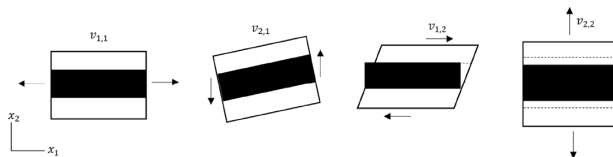


Fig. 2. Incremental deformation in a RVE of a unidirectional fibre composite with no fibre/matrix bonding.

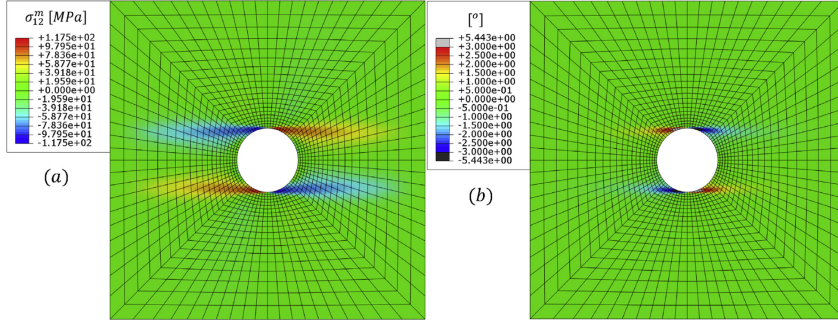


Fig. 6. (a) Matrix shear stress σ_{12}^m . (b) Local fibre orientations. For comparison, the initial fibre orientation α is 0° .

components of the velocity gradient $v_{1,1}$ and $v_{2,2}$ unless $F_{\alpha\beta}^A$ and $F_{\alpha\beta}^0$ refer to the same frame of reference; hence, the first expression in the parenthesis refers to the frame of reference in the beginning of the increment.

- 3) Calculate $v_{\alpha,\beta}^c$ from Eqs. (10), (14) and (15) or (10), (17), (20)
- 4) Update $\sigma_{\alpha\beta}$ from Eq. (5)
- 5) Update σ_{ij}^c from Eq. (3)
- 6) Update c^f from Ref. [8]

$$\dot{c}^f = c^f e^m (v_{2,2}^f - v_{2,2}^m) \quad (23)$$

- 7) Update L_{ijkl}^f from the J_2 flow theory of plasticity with isotropic hardening, i.e.

$$L_{ijkl}^c = \frac{E^c}{1+\nu^c} \left[\frac{1}{2} (\delta_{ik}\delta_{jl} + \delta_{il}\delta_{jk}) + \frac{\nu^c}{1-2\nu^c} \delta_{ij}\delta_{kl} - \beta^c \frac{3}{2} \frac{E^c/E^f - 1}{E^c/E^f - (1-2\nu^c)/3} \frac{s_{ij}^c s_{kl}^c}{(s_{ij}^c)^2} \right] \quad (24)$$

where E^c denotes the Young's modulus, ν^c denotes the Poisson's ratio, E^f denotes the tangent modulus, s_{ij}^c denotes the deviatoric part of the Cauchy stress σ_{ij}^c , σ_e^c denotes the effective von Mises stress, i.e.

$$\sigma_e^c = \sqrt{\frac{3}{2} s_{ij}^c s_{ij}^c} \quad (25)$$

δ_{ij} denotes the Kronecker delta and β^c contains the conditions for plastic flow

$$\beta^c = \begin{cases} 1 & \text{for } \sigma_e^c = (\sigma_e^c)_{\max} \text{ and } \dot{\sigma}_e^c \geq 0 \\ 0 & \text{for } \sigma_e^c < (\sigma_e^c)_{\max} \text{ or } \dot{\sigma}_e^c < 0 \end{cases} \quad (26)$$

The Ramberg-Osgood relation yields the tangent modulus

$$E_t^c = \frac{E^c}{\frac{3}{7} n^c \left(\frac{\sigma_e^c}{\sigma_y^c} \right)^{n^c-1} + 1} \quad (27)$$

where σ_y^c and n^c denote the yield stress and the hardening index, respectively.

- 8) Update $C_{\alpha\beta}^c$ from Eq. (2) followed by (8)
- 9) Update $C_{\alpha\beta}$ from Eq. (16) or (21)
- 10) Update $L_{\alpha\beta\gamma}$ from Eq. (8) followed by (2)
- 11) Return $L_{\alpha\beta\gamma}$, $\sigma_{\alpha\beta}$ and the state variables in step 1 to ABAQUS

The implementation of the constitutive model in Subsection 3.2 and steps 2, 6 – 10 are new or modified compared to Sørensen et al. [4].

5. Finite element analysis

The finite element model (Fig. 3) of an open-hole plate, which is simply supported along its left edge and subjected to a compressive displacement d , incrementally, along its right edge, is implemented in ABAQUS. α (Fig. 4) denotes the initial fibre orientation. Plane strain conditions apply; hence (Fig. 3), resembles a ply of an open-hole laminate under compressive loading. The user subroutine (UMAT) loads the AS4/PEEK material parameters (Table 1) from Kyriakides et al. [28].

6. Localization of deformation

The semi-analytical model by Jensen [8] considers the kink band geometry (Fig. 5), with an initial band inclination β_0 and an initial fibre rotation $\phi_0 = 0^\circ$. In the procedure, we then prescribe a fibre rotation increment ϕ such that the fibres in the kink band rotate relative to the fibres in the base material, i.e.

$$v_{2,1} = 0, \quad v_{2,1}' = \phi \quad (28)$$

where superscript ' refers to kink band coordinates.

Continuity of velocities across the boundary between the base material and the kink band requires that

$$v_{\alpha,\beta}' q_{\alpha}' n_{\beta}' = v_{\alpha,\beta} q_{\alpha} n_{\beta}, \quad v_{\alpha,\beta}' q_{\alpha}' n_{\alpha}' = v_{\alpha,\beta} q_{\alpha} n_{\alpha} \quad (29)$$

where n_{α} and q_{α} denote the unit normal and the unit tangent to the band boundary in the base material coordinates, respectively, and n_{α}' and q_{α}' in the kink band coordinates, i.e.

$$(n_1, n_2) = (\cos \beta, \sin \beta), \quad (q_1, q_2) = (-\sin \beta, \cos \beta), \\ (n_1', n_2') = (\cos \beta', \sin \beta'), \quad (q_1', q_2') = (-\sin \beta', \cos \beta') \quad (30)$$

where β and β' denote the inclination angle of the kink band relative to the base material and the kink band, respectively, from which it follows that the band inclination is updated according to

$$\dot{\beta} = -v_{\alpha,\beta} q_{\beta} n_{\alpha}, \quad \dot{\beta}' = -v_{\alpha,\beta}' q_{\beta}' n_{\alpha}' \quad (31)$$

Continuity of traction rates across the boundary between the base material and the kink band requires that

$$n_{\alpha}' C_{\alpha\beta\gamma}' v_{\beta}' n_{\gamma}' = n_{\alpha} C_{\alpha\beta\gamma} v_{\beta} n_{\gamma}, \quad n_{\alpha}' C_{\alpha\beta\gamma}' v_{\beta}' q_{\gamma}' = n_{\alpha} C_{\alpha\beta\gamma} v_{\beta} q_{\gamma} \quad (32)$$

Continuity of unit area $A = A^f/c^f$ across the boundary between the two regions requires that

$$n_{\alpha} e_{\alpha} \frac{c^f}{A} = n_{\alpha}' e_{\alpha}' \frac{c^f}{A'} \quad (33)$$

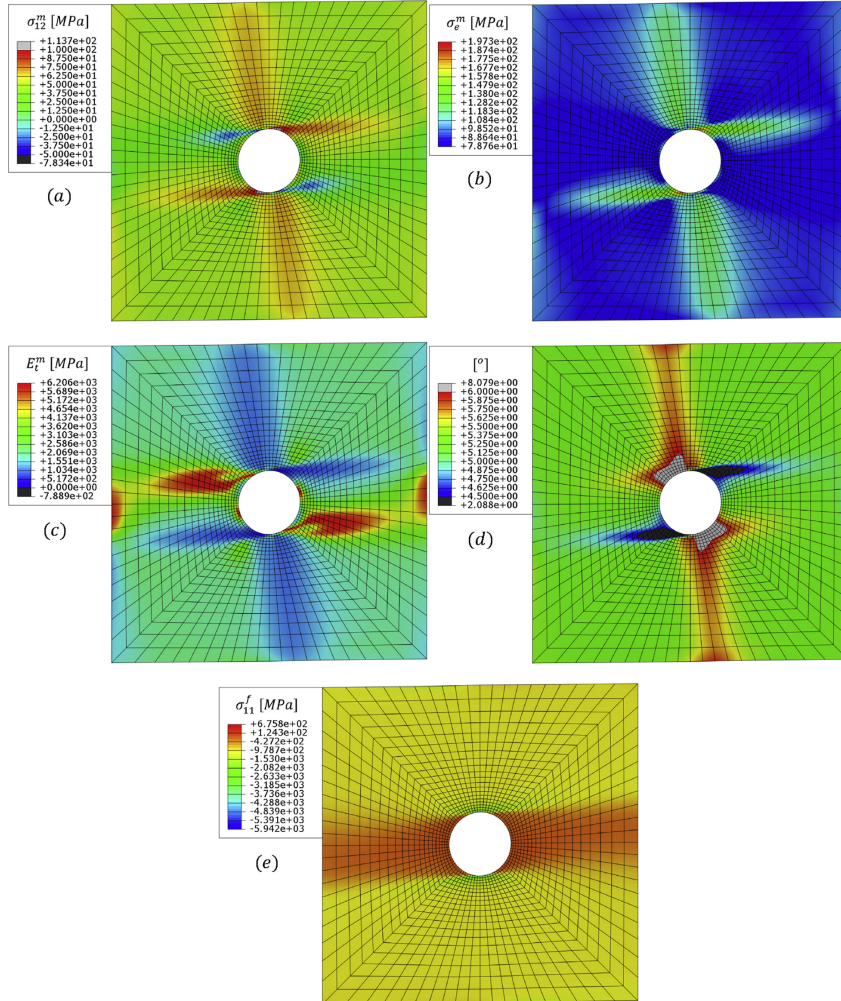


Fig. 7. (a) Matrix shear stress σ_{12}^m . (b) Effective matrix von Mises stress σ_e^m . For comparison, the matrix yield stress σ_y^m is 82.1 MPa. (c) Tangent matrix modulus E_t^m . For comparison, the Young's modulus E^m is 6.140 MPa. (d) Local fibre orientations. For comparison, the initial fibre orientation α is 5°. (e) Longitudinal fibre stress σ_{11}^f .

where e_x and e'_x denote a unit vector parallel with the fibres in the base material and the kink band, respectively. c^f is the fibre volume fraction in the base material from Eq. (23). Due to different stress states inside and outside the kink band, Eq. (33) yields the fibre volume fraction in the kink band, denoted c'^f . At steady-state, many previous studies use the lock-up condition $\phi = 2\beta_0$, neglecting the volumetric straining of the matrix between rigid fibres. Experimental studies by Poulsen et al. [29] and Vogler and Kyriakides [30] suggest that this lock-up condition

underestimates the fibre rotation ϕ . In the present study, at steady-state, the work done per unit volume by the stresses in the kink band W_I equals the work done per unit volume by the external loads W_E , i.e.

$$W_I = W_E \tag{34}$$

where

V. Tojaga et al.

Composites Part B 149 (2018) 66–73

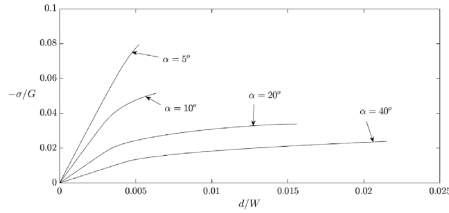


Fig. 8. Normalized applied stress $-\sigma/G$ as a function of normalized applied displacement d/W from initial to critical stress for $\alpha = 5^\circ, 10^\circ, 20^\circ, 40^\circ$. The elastic shear modulus of the composite G normalizes the applied stress $-\sigma$ and the initial width of the plate W normalizes the applied displacement d .

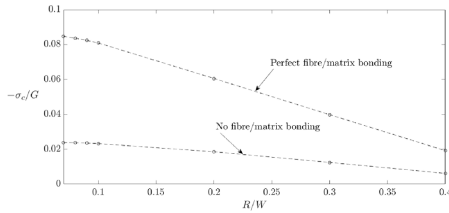


Fig. 9. Normalized (converged) critical stress $-\sigma_c/G$ as a function of normalized hole radius R/W associated with perfect fibre/matrix bonding and full decohesion for $\alpha = 5^\circ$. The elastic shear modulus of the composite G normalizes the critical stress $-\sigma_c$ and the initial width of the plate W normalizes the hole radius R .

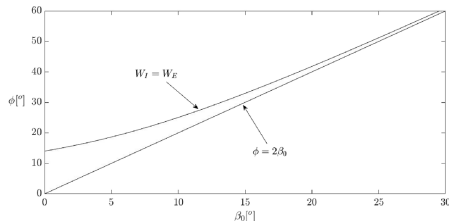


Fig. 10. Fibre rotation ϕ_s , at steady-state, as a function of initial band inclination β_0 .

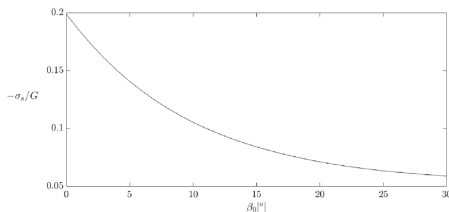


Fig. 11. Normalized steady-state kinking stress $-\sigma_s/G$ as a function of initial band inclination β_0 . The elastic shear modulus of the composite G normalizes the steady-state kinking stress $-\sigma_s$.

$$W_I = \int_{\epsilon} \sigma'_{\alpha\beta} d\epsilon'_{\alpha\beta}, \quad W_E = S_{\alpha\beta} \Delta E_{\alpha\beta} \tag{35}$$

ϵ' and ϵ denote the strain states inside and outside the kink band, respectively, $\Delta E_{\alpha\beta}$ denote the difference in Lagrangian strains inside and outside the kink band expressed in the base material and $S_{\alpha\beta}$ denote the work conjugated second Piola-Kirchhoff stresses. At steady-state, i.e. when $W_I = W_E$, the applied stress, denoted $-\sigma$ (Fig. 5), is the steady-state kinking stress, denoted $-\sigma_s$, Equations (28)–(35), together with the constitutive model in Subsection 3.1 and the constitutive relations in Sections 2 and 4, comprise an incremental procedure for determining the steady-state kinking stress of the AS4/PEEK composite (Table 1).

7. Results and discussion

Fibre misalignments together with plastic shear deformation in the matrix govern the critical stress of a unidirectional fibre composite; consequently, in Subsection 7.1, these factors are subsequently analysed at the critical stress. In Subsection 7.2, a suitable design methodology of structural components with open-holes is investigated. Unless otherwise stated, the constitutive model in Subsection 3.1 applies.

7.1. Micromechanics

For $\alpha=0^\circ$, the matrix shear stress σ''_2 (Fig. 6a) and the local fibre orientations (Fig. 6b) resemble the numerical results by Fleck et al. [20], where they used a constitutive model taking the fibre bending rigidity into account. In the present case, the fibre bending rigidity is negligible if the fibre diameter is much smaller than the size of the hole. The carbon fibres used in Ref. [28] were 7 micrometres in diameter. For comparison, a typical clearance hole for a M10 bolt is 11 millimetres in diameter.

For $\alpha = 5^\circ$, the matrix shear stress σ''_2 (Fig. 7a) is no longer symmetrical around the hole. The effective matrix von Mises stress σ''_m (Fig. 7b) indicates that the matrix yields at the locations where the matrix shear stress σ''_2 is highest (Fig. 7a). Since the uniaxial stress-strain relation follows the Ramberg-Osgood relation, i.e. Eq. (27), a significant reduction in the tangent matrix modulus E''_m (Fig. 7c) is seen at the locations where the effective matrix von Mises stress σ''_m is highest (Fig. 7b). The local fibre orientations (Fig. 7d) show the formation of a kink band due to an increase in matrix flexibility (Fig. 7c), suggesting that plastic microbuckling propagates in a direction almost normal to the loading direction corresponding to the experimental observations [11–21]. In addition (Fig. 7d), shows elastic microbuckling in the regions near the hole where the matrix does not yield (Fig. 7c). Wind et al. [31] showed that the fibres do not rotate significantly from the initial to the critical stress when considering a unidirectional fibre composite with fibre misalignments. This finding leads to the conclusion that the deformation of the open-hole causes the fibres to rotate severely near the hole and in the regions where they are less supported by the matrix, making the open-hole a severe imperfection. The longitudinal fibre stress σ''_1 (Fig. 7e) indicates that the highest compressive stresses are at the top and bottom edges of the hole where the fibres rotate the most (Fig. 7d), suggesting that plastic microbuckling propagates from the top and bottom edges of the hole corresponding to the experimental observations [11–21].

In a laminate under compressive loading, the 0° plies are stiffer than the off-axis plies and carry most of the load. Due to the stiffness provided by the fibres, no severe deformation of these plies takes place prior to failure, as (Fig. 8), showing the applied stress $-\sigma$ as a function of the applied displacement d for various values of α , indicates. In the off-axis plies, the fibres are more prone to rotate, causing the matrix to shear in between the fibres, which (Fig. 8) also indicates. (Fig. 8) suggests, in accordance with the experimental observations by Soutis et al. [13–17], that plastic microbuckling, in the 0° plies, governs the compressive failure. This observation leads to the conclusion that one

V. Tojaga et al.

Composites Part B 149 (2018) 66–73

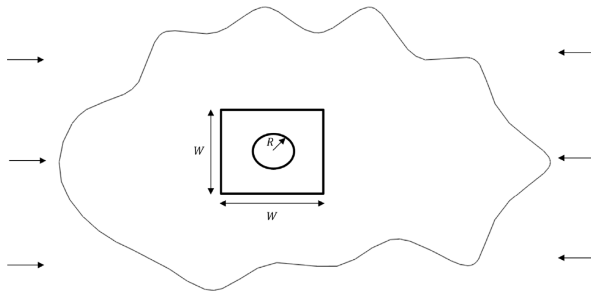


Fig. 12. Cut-out open-hole composite, with radius R and outer dimensions W .

should monitor the applied stresses acting on these plies to prevent laminate failure, provided that the number of 0° plies is high in comparison with the number of off-axis plies.

The constitutive model in Subsection 3.2 verifies these findings; however, the fibres are not supported laterally by the matrix in this model; hence, it provides a lower bound for the critical stress, with the situation in practice somewhere in between, as (Fig. 9), showing the critical stress, denoted $-\sigma_c$, as a function of the hole radius R , illustrates. The applied theory of plasticity ignores the dilatational stress, which makes it suitable for fibres but less suitable for polymeric materials; hence, it may overpredict matrix failure. The lower bound (Fig. 9) compensates for this uncertainty. In this regard, it is emphasized that the constitutive models in Section 3 allow all cases of time-independent elastic-plastic behaviour of the constituents.

7.2. Design

At steady state, (Fig. 10), showing the fibre rotation ϕ as a function of the initial band inclination β_0 , indicates, in accordance with the experimental studies [29–30], that $\phi > 2\beta_0$.

(Fig. 11) shows the steady-state kinking stress $-\sigma_s$ as a function of the initial band inclination β_0 , with the minimum normalized steady-state kinking stress $-\sigma_{s,min}/G = 0,059$; where G denotes the elastic shear modulus of the composite. A comparison with (Fig. 9) indicates that a lower bound for the critical stress of a unidirectional open-hole fibre composite can be estimated by the minimum steady-state kinking stress, provided that the hole is small in proportion to the composite, in which case one avoids global failure. Still, local failure, at the hole edges, may take place. To avoid failure at the hole edges, the applied stress, acting on a cut-out of the composite surrounding the hole (Fig. 12), must be within the range (Fig. 9). In this regard, the ratio $\frac{R}{W}$ must remain low, desirably close to 0.1; otherwise, the free edges, i.e. the top and bottom edges (Fig. 3), will interact to a higher degree with the open-hole, in which case (Fig. 9) underestimates the local load bearing capacity. If the number of 0° plies, in a laminate, is high in comparison with the number of off-axis plies, these plies govern the compressive failure of the laminate (Subsection 7.1); hence, the latter design approaches also apply for laminates.

(Fig. 10) and (Fig. 11) correspond to [8].

8. Conclusion

A non-empirical approach is introduced for determining the micro-mechanics of kink band formation in open-hole fibre composites under compressive loading. Our results explain and predict, in accordance with experimental observations, that a kink band propagates from the edges of an open-hole in a direction almost perpendicular to the loading direction and the 0° plies govern the compressive failure of

an open-hole laminate. These findings lead to the conclusion that the constitutive models (Section 3) are applicable to describe the micro-mechanics using a homogenized description of the composite. This homogenization takes the microstructure, including the fibre/matrix bonding, and the nonlinear behaviour of the constituents into account. A non-empirical approach is introduced for designing of structural components with open-holes. Using the mentioned homogenization to describe the behaviour of the composite, the semi-analytical model (Section 6) predicts, in accordance with experimental observations, that the kink band lock-up condition at steady-state, used by many previous studies, underestimates the rotation of the kink band relative to the base material. Our results indicate that the steady-state kinking stress can be estimated as a lower bound, provided that the hole is small in comparison to the laminate. This design approach is suitable to prevent global failure by kink banding of a laminate containing stress concentrations; however, to prevent local failure at the hole edges, the constitutive models in Section 3 predict the local compressive strength using finite element analysis. The present work suggests a convenient and useful predictive tool for design engineers.

Acknowledgements

Thomas B. Thriges fund supported this work.

References

- [1] Argon AS. Fracture of composites. *Treatise Mater Sci Technol* 1972;1:79–114.
- [2] Budiansky B. *Micromech Comp Struct* 1983;16:3–12.
- [3] Christoffersen J, Jensen HM. Kink band analysis accounting for the microstructure of fiber reinforced materials. *Mech Mater* 1996;24:305–15.
- [4] Sørensen KD, Mikkelsen LP, Jensen HM. User subroutine for compressive failure of composites. SIMULIA customer conference. London, May. 2009. p. 618–32.
- [5] Jensen HM. Models of failure in compression of layered materials. *Mech Mater* 1999;31:553–64.
- [6] Skovsgaard SPH, Jensen HM. Three-dimensional constitutive model for elastic-plastic behaviour of fibre-reinforced composites. *Int J Solid Struct* 2018;113–13.
- [7] Skovsgaard SPH, Jensen HM. Constitutive model for imperfectly bonded fibre-reinforced composites. *Compos Struct* 2018;192:82–92.
- [8] Jensen HM. Analysis of compressive failure of layered materials by kink band broadening. *Int J Solid Struct* 1999;36:3427–41.
- [9] Skovsgaard, S.P.H., Jensen, H.M., Steady state kink band propagation in layered materials, *J Appl Mech* 82, 061005.
- [10] Liu XH, Moran PM, Shih CF. The mechanics of compressive kinking in unidirectional fiber reinforced ductile matrix composites. *ComposPart B Eng* 1996;27:553–60.
- [11] Waas A, Babcock C. Observation of the initiation and progression of damage in compressively loaded composite plates containing a cutout NASA Progress Report, Grant NSG-1483 1986.
- [12] Givyn EG, Bradley WL, Elber W. Micromechanics of compression failure in open hole composite laminates. *STP1012. Compos Mater Fatig Fract* 1989;2:118–36.
- [13] Soutis C, Fleck NA. Static compression failure of carbon fibre T800/924C composite plate with a single hole. *J Compos Mater* 1990;24:536–58.
- [14] Soutis C, Fleck NA, Curtis PT. Hole-hole interaction in carbon fibre/epoxy laminates under uniaxial compression. *Composites* 1991;22:31–8.
- [15] Soutis C, Fleck NA, Smith PA. Failure prediction technique for compression loaded

V. Tojaga et al.

Composites Part B 149 (2018) 66–73

- carbon fibre-epoxy laminate with an open hole. *J Compos Mater* 1991;25:1476–98.
- [16] Soutis C, Curtis PT, Fleck NA. Compressive failure of notched carbon fibre composites. *Proc Math Phys Sci* 1993;440:241–56.
- [17] Ahn J, Waas AM. Prediction of compressive failure in laminated composites at room and elevated temperature. *AIAA J* 2002;40:346–58.
- [18] Khamseh AR, Waas AM. Failure mechanisms of uniply composite plates with a circular hole under static compressive loading. *J Eng Mater Technol* 1992;114:304–10.
- [19] Waas AM, Junghyun A, Khamseh AR. Compressive failure of notched uniply composite laminates. *ComposPart B Eng* 1998;29:75–80.
- [20] Fleck NA, Liu D, Shu JY. Microbuckle initiation from a hole and from the free edge of a fibre composite. *Int J Solid Struct* 2000;37:2757–75.
- [21] Suemasu H, Takahashi H, Ishikawa T. On failure mechanisms of composite laminates with an open hole subjected to compressive load. *Compos Sci Technol* 2006;66:634–41.
- [22] Allix O, Feld N, Baranger E, Guimard JM, Ha-Minh C. The compressive behavior of composites including fiber kinking: modelling across the scales. *Meccanica* 2014;49:2571–86.
- [23] Whitney JM, Nuismer RJ. Stress fracture criteria for laminated composites containing stress concentrations. *J Compos Mater* 1974;8:253–65.
- [24] Hodge AJ, Nettles AT, Jackson JR. Comparison of open-hole compression strength and compression after impact strength on carbon fiber/epoxy laminates for the ares 1 composite interstage. NASA/TP-2011-216460. 2011.
- [25] Davidson P, Pineda EJ, Heinrich C, Waas AM. A unified model for predicting the open-hole tensile and compressive strengths of composite laminates for aerospace applications. 54th AIAA/ASME/ASCE/ AHS/ASC Structures, Structural Dynamics, and Materials Conferences. Boston, Massachusetts. April, 2013.
- [26] Joseph APK, Waas AM, Wooseok J, Pineda EJ, Liguore S, Wanthal S. Progressive damage and failure prediction of open hole tension and open hole compression specimens. 56th AIAA/ASME/ASCE/ AHS/ASC Structures, Structural Dynamics, and Materials Conferences. Kissimmee, Florida. January, 2015.
- [27] Tojaga V. Methodology for modelling failure of open-hole fiber composites in compression Master's thesis Aarhus University; 2018.
- [28] Kyriakides S, Arseculeratne R, Perry EJ. On the compressive failure of fiber reinforced composites. *Int J Solid Struct* 1995;32:689–738.
- [29] Poulsen JS, Moran PM, Shih CF, Byskov E. Kink band initiation and band width broadening in clear wood compressive loading. *Mech Mater* 1997;25:67–77.
- [30] Vogler TJ, Kyriakides S. Initiation and axial propagation of kink bands in fiber composites. *Acta Mater* 1997;45:2443–54.
- [31] Wind JL, Steffensen S, Jensen HM. Comparison of composite model and an individually fiber and matrix discretized model for kink band formation. *Int J Non Lin Mech* 2014;67:319–25.

Appendix A

Jaumann rate of Cauchy stresses

From the definition of Cartesian tensors, a second order tensor A_{ij} transforms between arbitrary coordinate system by

$$A'_{ij} = R_{ik}R_{jl}A_{kl} \quad (\text{A.1})$$

Where R_{ij} are components of a proper orthogonal rotation tensor. An infinitesimal line element between to neighbouring points P and Q is denoted dx_j and dx'_j , when they are observed from the two coordinate systems x_i and x'_i , see Fig. A.1. The two systems coincide at time t , so dx_j and dx'_j are identical at this instant. During a rigid body rotation, at instant $t = t + dt$, the coordinate system x_i stays stationary and the system x'_i takes part of the rotation. The difference $dx_j - dx'_j$ observed from the two systems is equal to

$$dx_j - dx'_j = dv_j dt \quad (\text{A.2})$$

where dv_j denotes the relative velocity of point Q with respect to P. The relative velocity is

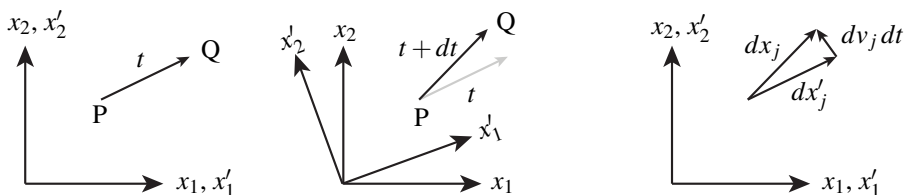


Figure. A.1 Illustration of the concept of rotating coordinate systems.

given by

$$dv_i = \frac{\partial v_i}{\partial x_j} dx_j \quad (\text{A.3})$$

The velocity gradient tensor $\partial v_i/\partial x_j$ can be divided into a symmetric and anti-symmetric part

$$\begin{aligned} \dot{\epsilon}_{ij} &= \frac{1}{2} \left(\frac{\partial v_i}{\partial x_j} + \frac{\partial v_j}{\partial x_i} \right) \\ \omega_{ij} &= \frac{1}{2} \left(\frac{\partial v_i}{\partial x_j} - \frac{\partial v_j}{\partial x_i} \right) \end{aligned} \quad (\text{A.4})$$

Where $\dot{\epsilon}_{ij}$ is the strain rate tensor and ω_{ij} is the spin tensor. When considering a rigid body rotation the relative velocity Eq. (A.3) can be written as

$$dv_j = \omega_{ji} dx'_i \quad (\text{A.5})$$

Combining Eqs. (A.2) and (A.5) yields

$$dx_j - dx'_j = \omega_{ji} dx'_i dt \quad (\text{A.6})$$

Which can be rewritten

$$dx_j = (\delta_{ij} + \omega_{ji} dt) dx'_i \quad (\text{A.7})$$

Since ω_{ij} is an anti-symmetric tensor $\omega_{ji} = -\omega_{ij}$ which leads to

$$dx_j = (\delta_{ij} - \omega_{ij} dt) dx'_i \quad (\text{A.8})$$

The expression in the parenthesis can be compared to the directional cosines given by Eq. (A.1). Let $\dot{\sigma}_{ij}$ and $\dot{\sigma}'_{ij}$ be the stress rates referred to the fixed x_i and the rotating x'_i coordinate system respectively. Using Eq. (A.8) the stress components at the time $t + dt$ of the rotating coordinates becomes

$$\sigma_{ij} + \dot{\sigma}_{ij} dt = (\delta_{ik} - \omega_{ik} dt) (\delta_{jl} - \omega_{jl} dt) (\sigma_{kl} + \dot{\sigma}_{kl} dt) \quad (\text{A.9})$$

By neglecting terms containing squares and cubes of dt , the equation can be expanded to

$$\sigma_{ij} + \dot{\sigma}_{ij} dt = \delta_{ik} \delta_{jl} \sigma_{kl} + \delta_{ik} \delta_{jl} \dot{\sigma}_{kl} dt - \delta_{ik} \omega_{jl} \sigma_{kl} dt - \delta_{jl} \omega_{ik} \sigma_{kl} dt \quad (\text{A.10})$$

Using the property, that Kronecker delta substitutes index, yields

$$\sigma_{ij} + \dot{\sigma}_{ij} dt = \sigma_{ij} + \dot{\sigma}_{ij} dt - \omega_{jl} \sigma_{il} dt - \omega_{ik} \sigma_{kj} dt \quad (\text{A.11})$$

The equation can be simplified to give the stress rate in the rotating coordinate system

$$\dot{\sigma}_{ij} = \dot{\sigma}_{ij} - \omega_{jk} \sigma_{ik} - \omega_{ik} \sigma_{kj} \quad (\text{A.12})$$

In some literatures the relation is written in the equivalent form

$$\dot{\sigma}_{ij} = \dot{\sigma}_{ij} - \omega_{ik} \sigma_{kj} + \sigma_{ik} \omega_{kj} \quad (\text{A.13})$$

This stress rate is known as the co-rotational Jaumann-Zaremba stress rate and is often used in constitutive relations since the stress rate is objective.

Appendix B

Nominal stresses

In this chapter the relation between the rate of nominal and Kirchhoff stresses is set-up.

The relative motion between two neighboring points can be described through the deformation gradient $F_{ij} = \partial x_i / \partial X_j$ where x_i are components of the current coordinates of material points and X_i are the reference coordinates. The inverse of the deformation gradient $F_{ij}^{-1} = \partial X_i / \partial x_j$ relates material lines of the reference configuration as a function of material lines in the current configuration

$$dX_i = \frac{\partial X_i}{\partial x_j} dx_j = F_{ij}^{-1} dx_j \quad (\text{B.1})$$

Due to conservation of mass, the product between the density and the volume remains constant

$$\rho ds_j dx_j = \rho_0 dS_i dX_i \quad (\text{B.2})$$

where ρ and ρ_0 are densities of material points in the current and reference configuration respectively. ds_i and dS_i are infinitesimal surfaces in the current and reference configuration. Combining Eqs. *refdefgrad* and (B.2) yields

$$\rho ds_j dx_j = \rho_0 dS_i \frac{\partial X_i}{\partial x_j} dx_j \quad (\text{B.3})$$

Which can be rewritten

$$\left(ds_j - \frac{\rho_0}{\rho} \frac{\partial X_i}{\partial x_j} dS_i \right) dx_j = 0 \quad (\text{B.4})$$

Since dx_j in general is non-zero, the equation embraced by the parenthesis must be zero, which gives the Nanson's formula

$$ds_j = \frac{\rho_0}{\rho} \frac{\partial X_i}{\partial x_j} dS_i \quad (\text{B.5})$$

Which relates surface vectors between the current and reference configuration.

To give a relation between Cauchy stresses σ_{ij} (true stress) and the nominal stresses t_{ij} an infinitesimal force df_j is introduced. The following relation between the stresses is introduced

$$df_j = t_{ij} dS_i = \sigma_{kj} ds_k \quad (\text{B.6})$$

Substitution of ds_k using Eq. (B.5) yields

$$t_{ij} dS_i = \sigma_{kj} \frac{\rho_0}{\rho} \frac{\partial X_i}{\partial x_k} dS_i \quad (\text{B.7})$$

Since dS_i is a common factor the relation between the nominal and Cauchy stresses is

$$t_{ij} = \frac{\rho_0}{\rho} \frac{\partial X_i}{\partial x_k} \sigma_{kj} = J F_{ik}^{-1} \sigma_{kj} \quad (\text{B.8})$$

The relation between Cauchy and Kirchhoff stress is given by

$$\tau_{ij} = J \sigma_{ij} \quad (\text{B.9})$$

Where J is the Jacobian, which represent the density ratio ($J = \rho_0/\rho$) from the initial to the current configuration. The relationship between nominal stress and Kirchhoff stress is thereby

$$t_{ij} = \frac{\partial X_i}{\partial x_k} \tau_{kj} = F_{ik}^{-1} \tau_{kj} \quad (\text{B.10})$$

To calculate the nominal stress rate the material derivative is utilised. The operator representing the material derivative of a spatial field is introduced

$$\frac{d(\bullet)}{dt} = \frac{\partial(\bullet)}{\partial t} + v_m \frac{\partial(\bullet)}{\partial x_m} = (\bullet)_{,t} + v_m (\bullet)_{,m} \quad (\text{B.11})$$

The first term in Eq. (B.11) denotes the spatial time derivative of the spatial field, while the second term is the convective rate of change of the spatial field. By using the product rule of

differentiation the material time derivate of Eq. (B.8) can be written as

$$\frac{d(t_{ij})}{dt} = \frac{\partial X_i}{\partial x_k} \frac{d(\tau_{kj})}{dt} + \frac{d}{dt} \left(\frac{\partial X_i}{\partial x_k} \right) \tau_{kj} \quad (\text{B.12})$$

Now focus is given to the material time derivative of the inverse of the deformation gradient. By using the operator Eq. (B.11) the derivative can be written as

$$\frac{d}{dt} \left(\frac{\partial X_i}{\partial x_k} \right) = X_{i,kt} + v_m X_{i,km} \quad (\text{B.13})$$

A term $v_{m,k} X_{i,m}$ is added and subtracted from the expression

$$\frac{d}{dt} \left(\frac{\partial X_i}{\partial x_k} \right) = X_{i,kt} + v_m X_{i,km} + v_{m,k} X_{i,m} - v_{m,k} X_{i,m} \quad (\text{B.14})$$

Using the product rule of differentiation the equation can be rewritten

$$\frac{d}{dt} \left(\frac{\partial X_i}{\partial x_k} \right) = (X_{i,t} + v_m X_{i,m})_{,k} - v_{m,k} X_{i,m} \quad (\text{B.15})$$

The term in the parenthesis is the material time derivative of the initial coordinates dX_i/dt . Since the initial coordinates do not change with time $dX_i/dt = 0$. The equation can be simplified into

$$\frac{d}{dt} \left(\frac{\partial X_i}{\partial x_k} \right) = -v_{m,k} X_{i,m} \quad (\text{B.16})$$

By using Eq. (B.16) the stress rate can be written as

$$\dot{t}_{ij} = F_{ik}^{-1} \dot{\tau}_{kj} - v_{m,k} F_{im}^{-1} \tau_{kj} \quad (\text{B.17})$$

This can be rewritten, using the fact that the repeated indices can be renamed, and that the Kirchoff stress tensor is symmetric

$$\dot{t}_{ij} = F_{im}^{-1} (\dot{\tau}_{mj} - \tau_{jk} v_{m,k}) \quad (\text{B.18})$$

If the initial state coincide with the current state then $\partial X_i / \partial x_m = \delta_{im}$.

$$\dot{t}_{ij} = \delta_{im} (\dot{\tau}_{mj} - \tau_{jk} v_{m,k}) \quad (\text{B.19})$$

Kronecker delta renames index

$$\dot{t}_{ij} = \dot{\tau}_{ij} - \tau_{jk} v_{i,k} \quad (\text{B.20})$$

The Jaumann rate of Kirchhoff stresses is given by

$$\overset{\circ}{\tau}_{ij} = \dot{\tau}_{ij} - \omega_{jk} \tau_{ik} - \omega_{ik} \tau_{kj} \quad (\text{B.21})$$

Combining Eqs. (B.20) and (B.21) yields

$$\dot{i}_{ij} = \overset{\circ}{\tau}_{ij} + \omega_{jk} \tau_{ik} + \omega_{ik} \tau_{kj} - \tau_{jk} v_{i,k} \quad (\text{B.22})$$

Replacing the spin tensor ω_{ij} using Eq. (3.3) yields

$$\dot{i}_{ij} = \overset{\circ}{\tau}_{ij} + \frac{1}{2} (v_{j,k} - v_{k,j}) \tau_{ik} + \frac{1}{2} (v_{i,k} - v_{k,i}) \tau_{kj} - \tau_{jk} v_{i,k} \quad (\text{B.23})$$

Expanding the parenthesis

$$\dot{i}_{ij} = \overset{\circ}{\tau}_{ij} + \frac{1}{2} v_{j,k} \tau_{ik} - \frac{1}{2} v_{k,j} \tau_{ik} + \frac{1}{2} v_{i,k} \tau_{kj} - \frac{1}{2} v_{k,i} \tau_{kj} - \tau_{jk} v_{i,k} \quad (\text{B.24})$$

The last and the fourth term on the right have the same components since the Cauchy stress tensor is symmetric the terms cancel out.

$$\dot{i}_{ij} = \overset{\circ}{\tau}_{ij} + \frac{1}{2} v_{j,k} \tau_{ik} - \frac{1}{2} v_{k,j} \tau_{ik} - \frac{1}{2} v_{i,k} \tau_{kj} - \frac{1}{2} v_{k,i} \tau_{kj} \quad (\text{B.25})$$

Reapeted index can be renamed

$$\dot{i}_{ij} = \overset{\circ}{\tau}_{ij} + \frac{1}{2} v_{j,k} \tau_{ik} - \frac{1}{2} v_{l,j} \tau_{il} - \frac{1}{2} v_{i,k} \tau_{kj} - \frac{1}{2} v_{l,i} \tau_{lj} \quad (\text{B.26})$$

Kronecker Delta is added and indices are substituted

$$\dot{i}_{ij} = \overset{\circ}{\tau}_{ij} + \frac{1}{2} v_{l,k} \tau_{ik} \delta_{jl} - \frac{1}{2} v_{l,k} \tau_{il} \delta_{jk} - \frac{1}{2} v_{l,k} \tau_{kj} \delta_{il} - \frac{1}{2} v_{l,k} \tau_{lj} \delta_{ik} \quad (\text{B.27})$$

The Jaumann stress rate can be calculated using an incremental stiffness tensor

$$\overset{\circ}{\tau}_{ij} = L_{ijkl} \dot{\epsilon}_{kl} \quad (\text{B.28})$$

The incremental stiffness tensor must satisfy the symmetries

$$L_{ijkl} = L_{jikl} = L_{ijlk} \quad (\text{B.29})$$

Using the symmetries of L_{ijkl} in Eq. (B.28) leads to

$$\begin{aligned}\hat{\tau}_{ij} &= L_{ijkl} \hat{\epsilon}_{kl} = L_{ijkl} \frac{1}{2} (v_{k,l} + v_{l,k}) = \frac{1}{2} (L_{ijkl} v_{k,l} + L_{ijkl} v_{l,k}) \\ &= \frac{1}{2} (L_{ijlk} v_{l,k} + L_{ijkl} v_{l,k}) = L_{ijkl} v_{l,k}\end{aligned}\quad (\text{B.30})$$

Combining Eq. (B.30) and (B.27) yields

$$\dot{i}_{ij} = L_{ijkl} v_{l,k} + \frac{1}{2} v_{l,k} \tau_{ik} \delta_{jl} - \frac{1}{2} v_{l,k} \tau_{il} \delta_{jk} - \frac{1}{2} v_{l,k} \tau_{kj} \delta_{il} - \frac{1}{2} v_{l,k} \tau_{lj} \delta_{ik} \quad (\text{B.31})$$

Isolating $v_{l,k}$ yields

$$\dot{i}_{ij} = \left(L_{ijkl} + \frac{1}{2} \tau_{ik} \delta_{jl} - \frac{1}{2} \tau_{il} \delta_{jk} - \frac{1}{2} \tau_{kj} \delta_{il} - \frac{1}{2} \tau_{lj} \delta_{ik} \right) v_{l,k} \quad (\text{B.32})$$

By moving around terms, the fourth order tensor in the parenthesis can written as

$$C_{ijkl} = L_{ijkl} - \frac{1}{2} \delta_{il} \tau_{kj} - \frac{1}{2} \delta_{ik} \tau_{lj} - \frac{1}{2} \tau_{il} \delta_{kj} + \frac{1}{2} \tau_{ik} \delta_{lj} \quad (\text{B.33})$$

Which is the tensor of nominal moduli relating nominal stress increments to velocity gradients through the Kirchhoff stress tensor.

Appendix C

Constitutive formulation

In this appendix the derivations behind the constitutive model developed by Christoffersen and Jensen (1996) is explained.

It is convenient to decompose the constitutive equations into a matrix representation for simplicity in the derivation, where the rate of nominal stresses are collected in the vectors

$$\mathbf{t}_1 = \begin{pmatrix} \dot{i}_{11} \\ \dot{i}_{12} \end{pmatrix} \quad \mathbf{t}_2 = \begin{pmatrix} \dot{i}_{21} \\ \dot{i}_{22} \end{pmatrix} \quad (\text{C.1})$$

The velocity components are collected in the vector

$$\mathbf{v} = \begin{pmatrix} v_1 \\ v_2 \end{pmatrix} \quad (\text{C.2})$$

The constitutive equation given by Eq. (3.26) can be written in the form

$$\mathbf{t}_\alpha = \mathbf{C}_{\alpha\beta} \mathbf{v}_{,\beta} \quad \alpha, \beta \in \{1, 2\} \quad (\text{C.3})$$

The matrix system written in the full form

$$\begin{pmatrix} \dot{i}_{11} \\ \dot{i}_{12} \\ \dot{i}_{21} \\ \dot{i}_{22} \end{pmatrix} = \begin{pmatrix} C_{1111} & C_{1112} & C_{1121} & C_{1122} \\ C_{1211} & C_{1212} & C_{1221} & C_{1222} \\ C_{2111} & C_{2112} & C_{2121} & C_{2122} \\ C_{2211} & C_{2212} & C_{2221} & C_{2222} \end{pmatrix} \begin{pmatrix} v_{1,1} \\ v_{2,1} \\ v_{1,2} \\ v_{2,2} \end{pmatrix} \quad (\text{C.4})$$

The components of $\mathbf{C}_{\alpha\beta}$ represents the matrices

$$\begin{aligned}\mathbf{C}_{11} &= \begin{pmatrix} C_{1111} & C_{1112} \\ C_{1211} & C_{1212} \end{pmatrix} \\ \mathbf{C}_{12} &= \begin{pmatrix} C_{1121} & C_{1122} \\ C_{1221} & C_{1222} \end{pmatrix} \\ \mathbf{C}_{21} &= \begin{pmatrix} C_{2111} & C_{2112} \\ C_{2211} & C_{2212} \end{pmatrix} \\ \mathbf{C}_{22} &= \begin{pmatrix} C_{2121} & C_{2122} \\ C_{2221} & C_{2222} \end{pmatrix}\end{aligned}\tag{C.5}$$

Eq. (3.22) can be rewritten using the introduced matrix notation

$$\mathbf{t}_2^f = \mathbf{t}_2^m = \mathbf{t}_2\tag{C.6}$$

\mathbf{t}_2^c for the constituents can be calculated using Eq. (C.3)

$$\mathbf{t}_2^c = \mathbf{C}_{2\beta}^c \mathbf{v}_{,\beta}^c = \mathbf{C}_{21}^c \mathbf{v}_{,1}^c + \mathbf{C}_{22}^c \mathbf{v}_{,2}^c\tag{C.7}$$

Using the first assumption given by Eq. (3.17) $\mathbf{v}_{,1}^c = \mathbf{v}_{,1}$ leads to

$$\mathbf{t}_2^c = \mathbf{C}_{21}^c \mathbf{v}_{,1} + \mathbf{C}_{22}^c \mathbf{v}_{,2}^c\tag{C.8}$$

Using the latter equation with Eq. (C.6) yields the equality

$$\mathbf{C}_{21}^f \mathbf{v}_{,1} + \mathbf{C}_{22}^f \mathbf{v}_{,2}^f = \mathbf{C}_{21}^m \mathbf{v}_{,1} + \mathbf{C}_{22}^m \mathbf{v}_{,2}^m\tag{C.9}$$

To find a relation between the velocity gradients of the constituents, Eq. (3.19) is used. The equation (3.19) can be written using the matrix notation

$$c^f \mathbf{v}_{,2}^f + c^m \mathbf{v}_{,2}^m = \mathbf{v}_{,2}\tag{C.10}$$

Isolating $\mathbf{v}_{,2}^f$ yields

$$\mathbf{v}_{,2}^f = \frac{1}{c^f} (\mathbf{v}_{,2} - c^m \mathbf{v}_{,2}^m)\tag{C.11}$$

Multiplying by \mathbf{C}_{22}^m on both sides yields

$$\mathbf{C}_{22}^m \mathbf{v}_{,2}^f = \frac{1}{c^f} (\mathbf{C}_{22}^m \mathbf{v}_{,2} - c^m \mathbf{C}_{22}^m \mathbf{v}_{,2}^m)\tag{C.12}$$

$\mathbf{C}_{22}^m \mathbf{v}_{,2}^m$ can be isolated from Eq. (C.9), and combined with the latter equation, which yields

$$\mathbf{C}_{22}^f \mathbf{v}_{,2}^f = \frac{1}{c^f} \left(\mathbf{C}_{22}^m \mathbf{v}_{,2} - c^m \left(\mathbf{C}_{21}^f \mathbf{v}_{,1} + \mathbf{C}_{22}^f \mathbf{v}_{,2}^f - \mathbf{C}_{21}^m \mathbf{v}_{,1} \right) \right) \quad (\text{C.13})$$

Moving c^f to the left and expanding the parenthesis yields

$$c^f \mathbf{C}_{22}^m \mathbf{v}_{,2}^f = \mathbf{C}_{22}^m \mathbf{v}_{,2} - c^m \mathbf{C}_{21}^f \mathbf{v}_{,1} - c^m \mathbf{C}_{22}^f \mathbf{v}_{,2}^f + c^m \mathbf{C}_{21}^m \mathbf{v}_{,1} \quad (\text{C.14})$$

Moving terms related to $\mathbf{v}_{,2}^f$ to the left and collecting terms related to $\mathbf{v}_{,\beta}$ yields

$$\left(c^m \mathbf{C}_{22}^f + c^f \mathbf{C}_{22}^m \right) \mathbf{v}_{,2}^f = c^m \left(\mathbf{C}_{21}^m - \mathbf{C}_{21}^f \right) \mathbf{v}_{,1} + \mathbf{C}_{22}^m \mathbf{v}_{,2} \quad (\text{C.15})$$

Introducing the matrix \mathbf{C}_{22}^*

$$\mathbf{C}_{22}^* = c^m \mathbf{C}_{22}^f + c^f \mathbf{C}_{22}^m \quad (\text{C.16})$$

the velocity gradients $\mathbf{v}_{,2}^f$ for the fibre can be isolated using the latter term

$$\mathbf{v}_{,2}^f = \mathbf{C}_{22}^{*-1} \left(c^m \left(\mathbf{C}_{21}^m - \mathbf{C}_{21}^f \right) \mathbf{v}_{,1} + \mathbf{C}_{22}^m \mathbf{v}_{,2} \right) \quad (\text{C.17})$$

The equation can also be written in the form

$$\mathbf{v}_{,2}^f = c^m \mathbf{C}_{22}^{*-1} \left(\mathbf{C}_{21}^m - \mathbf{C}_{21}^f \right) \mathbf{v}_{,1} + \mathbf{C}_{22}^{*-1} \mathbf{C}_{22}^m \mathbf{v}_{,2} \quad (\text{C.18})$$

In the same manner, the velocity gradients $\mathbf{v}_{,2}^m$ for the matrix can be determined as

$$\mathbf{v}_{,2}^m = c^f \mathbf{C}_{22}^{*-1} \left(\mathbf{C}_{21}^f - \mathbf{C}_{21}^m \right) \mathbf{v}_{,1} + \mathbf{C}_{22}^{*-1} \mathbf{C}_{22}^f \mathbf{v}_{,2} \quad (\text{C.19})$$

The terms in front of $\mathbf{v}_{,2}$ can be replaced. It is convenient to write the velocity gradients in the equivalent form

$$\begin{aligned} \mathbf{v}_{,2}^f &= -c^m \mathbf{C}_{22}^{*-1} \left(\mathbf{C}_{21}^f - \mathbf{C}_{21}^m \right) \mathbf{v}_{,1} - c^m \mathbf{C}_{22}^{*-1} \left(\mathbf{C}_{22}^f - \mathbf{C}_{22}^m \right) \mathbf{v}_{,2} + \mathbf{v}_{,2} \\ \mathbf{v}_{,2}^m &= c^f \mathbf{C}_{22}^{*-1} \left(\mathbf{C}_{21}^f - \mathbf{C}_{21}^m \right) \mathbf{v}_{,1} + c^f \mathbf{C}_{22}^{*-1} \left(\mathbf{C}_{22}^f - \mathbf{C}_{22}^m \right) \mathbf{v}_{,2} + \mathbf{v}_{,2} \end{aligned} \quad (\text{C.20})$$

In the latter equations the following identities were utilized

$$\begin{aligned} \mathbf{C}_{22}^{*-1} \mathbf{C}_{22}^m \mathbf{v}_{,2} &= -c^m \mathbf{C}_{22}^{*-1} \left(\mathbf{C}_{22}^f - \mathbf{C}_{22}^m \right) \mathbf{v}_{,2} + \mathbf{v}_{,2} \\ \mathbf{C}_{22}^{*-1} \mathbf{C}_{22}^f \mathbf{v}_{,2} &= c^f \mathbf{C}_{22}^{*-1} \left(\mathbf{C}_{22}^f - \mathbf{C}_{22}^m \right) \mathbf{v}_{,2} + \mathbf{v}_{,2} \end{aligned} \quad (\text{C.21})$$

The first identity will be proven in the following. The terms with coefficients of $\mathbf{v}_{,2}$ can be isolated in the right part of the equality

$$\mathbf{C}_{22}^{*-1} \mathbf{C}_{22}^m \mathbf{v}_{,2} = \left(-c^m \mathbf{C}_{22}^{*-1} \left(\mathbf{C}_{22}^f - \mathbf{C}_{22}^m \right) + \mathbf{I} \right) \mathbf{v}_{,2} \quad (\text{C.22})$$

Where \mathbf{I} is the identity matrix. The identity matrix can be replaced by $\mathbf{I} = \mathbf{C}_{22}^{*-1} \mathbf{C}_{22}^*$

$$\mathbf{C}_{22}^{*-1} \mathbf{C}_{22}^m \mathbf{v}_{,2} = \left(-c^m \mathbf{C}_{22}^{*-1} \left(\mathbf{C}_{22}^f - \mathbf{C}_{22}^m \right) + \mathbf{C}_{22}^{*-1} \mathbf{C}_{22}^* \right) \mathbf{v}_{,2} \quad (\text{C.23})$$

The matrix \mathbf{C}_{22}^{*-1} can be isolated and put outside the parenthesis, and \mathbf{C}_{22}^* can be expanded using Eq. (C.16)

$$\mathbf{C}_{22}^{*-1} \mathbf{C}_{22}^m \mathbf{v}_{,2} = \mathbf{C}_{22}^{*-1} \left(-c^m \left(\mathbf{C}_{22}^f - \mathbf{C}_{22}^m \right) + c^f \mathbf{C}_{22}^m + c^m \mathbf{C}_{22}^f \right) \mathbf{v}_{,2} \quad (\text{C.24})$$

The inner parenthesis is expanded

$$\mathbf{C}_{22}^{*-1} \mathbf{C}_{22}^m \mathbf{v}_{,2} = \mathbf{C}_{22}^{*-1} \left(-c^m \mathbf{C}_{22}^f + c^m \mathbf{C}_{22}^m + c^f \mathbf{C}_{22}^m + c^m \mathbf{C}_{22}^f \right) \mathbf{v}_{,2} \quad (\text{C.25})$$

The two terms $(c^m \mathbf{C}_{22}^f)$ cancel out

$$\mathbf{C}_{22}^{*-1} \mathbf{C}_{22}^m \mathbf{v}_{,2} = \mathbf{C}_{22}^{*-1} \left(c^m \mathbf{C}_{22}^m + c^f \mathbf{C}_{22}^m \right) \mathbf{v}_{,2} \quad (\text{C.26})$$

\mathbf{C}_{22}^m is isolated

$$\mathbf{C}_{22}^{*-1} \mathbf{C}_{22}^m \mathbf{v}_{,2} = \mathbf{C}_{22}^{*-1} \left(c^m + c^f \right) \mathbf{C}_{22}^m \mathbf{v}_{,2} \quad (\text{C.27})$$

using the property that the sum of the volume fractions is unity $c^f + c^m = 1$ yields

$$\mathbf{C}_{22}^{*-1} \mathbf{C}_{22}^m \mathbf{v}_{,2} = \mathbf{C}_{22}^{*-1} \mathbf{C}_{22}^m \mathbf{v}_{,2} \quad (\text{C.28})$$

Similarly, the second identity in Eq. (C.21) can be proven. The nominal stress rate for the components in the vector \mathbf{t}_1^c can be calculated using Eq. (C.3)

$$\mathbf{t}_1^c = \mathbf{C}_{1\beta}^c \mathbf{v}_{,\beta}^c = \mathbf{C}_{11}^c \mathbf{v}_{,1} + \mathbf{C}_{12}^c \mathbf{v}_{,2}^c \quad (\text{C.29})$$

Using Eqs. (C.20) the nominal stress rate vectors \mathbf{t}_1^f and \mathbf{t}_1^m can be determined

$$\begin{aligned} \mathbf{t}_1^f &= \mathbf{C}_{11}^f \mathbf{v}_{,1} + \mathbf{C}_{12}^f \left(-c^m \mathbf{C}_{22}^{*-1} \left(\mathbf{C}_{21}^f - \mathbf{C}_{21}^m \right) \mathbf{v}_{,1} - c^m \mathbf{C}_{22}^{*-1} \left(\mathbf{C}_{22}^f - \mathbf{C}_{22}^m \right) \mathbf{v}_{,2} + \mathbf{v}_{,2} \right) \\ \mathbf{t}_1^m &= \mathbf{C}_{11}^m \mathbf{v}_{,1} + \mathbf{C}_{12}^m \left(c^f \mathbf{C}_{22}^{*-1} \left(\mathbf{C}_{21}^f - \mathbf{C}_{21}^m \right) \mathbf{v}_{,1} + c^f \mathbf{C}_{22}^{*-1} \left(\mathbf{C}_{22}^f - \mathbf{C}_{22}^m \right) \mathbf{v}_{,2} + \mathbf{v}_{,2} \right) \end{aligned} \quad (\text{C.30})$$

Collecting terms related to \mathbf{v}, β

$$\begin{aligned}\dot{\mathbf{t}}_1^f &= \left(\mathbf{C}_{11}^f - c^m \mathbf{C}_{12}^f \mathbf{C}_{22}^{*-1} \left(\mathbf{C}_{21}^f - \mathbf{C}_{21}^m \right) \right) \mathbf{v}_{,1} + \left(\mathbf{C}_{12}^f - c^m \mathbf{C}_{12}^f \mathbf{C}_{22}^{*-1} \left(\mathbf{C}_{22}^f - \mathbf{C}_{22}^m \right) \right) \mathbf{v}_{,2} \\ \dot{\mathbf{t}}_1^m &= \left(\mathbf{C}_{11}^m + c^f \mathbf{C}_{12}^m \mathbf{C}_{22}^{*-1} \left(\mathbf{C}_{21}^f - \mathbf{C}_{21}^m \right) \right) \mathbf{v}_{,1} + \left(\mathbf{C}_{12}^m + c^f \mathbf{C}_{12}^m \mathbf{C}_{22}^{*-1} \left(\mathbf{C}_{22}^f - \mathbf{C}_{22}^m \right) \right) \mathbf{v}_{,2}\end{aligned}\quad (\text{C.31})$$

For overall equilibrium of nominal stress rates, Eq. (3.25) was introduced which can be rewritten using the matrix format

$$\dot{\mathbf{t}}_1 = c^f \dot{\mathbf{t}}_1^f + c^m \dot{\mathbf{t}}_1^m \quad (\text{C.32})$$

Combining this equation with Eq. (C.31) yields

$$\begin{aligned}\dot{\mathbf{t}}_1 &= c^f \left(\left(\mathbf{C}_{11}^f - c^m \mathbf{C}_{12}^f \mathbf{C}_{22}^{*-1} \left(\mathbf{C}_{21}^f - \mathbf{C}_{21}^m \right) \right) \mathbf{v}_{,1} + \left(\mathbf{C}_{12}^f - c^m \mathbf{C}_{12}^f \mathbf{C}_{22}^{*-1} \left(\mathbf{C}_{22}^f - \mathbf{C}_{22}^m \right) \right) \mathbf{v}_{,2} \right) + \\ &\quad c^m \left(\left(\mathbf{C}_{11}^m + c^f \mathbf{C}_{12}^m \mathbf{C}_{22}^{*-1} \left(\mathbf{C}_{21}^f - \mathbf{C}_{21}^m \right) \right) \mathbf{v}_{,1} + \left(\mathbf{C}_{12}^m + c^f \mathbf{C}_{12}^m \mathbf{C}_{22}^{*-1} \left(\mathbf{C}_{22}^f - \mathbf{C}_{22}^m \right) \right) \mathbf{v}_{,2} \right)\end{aligned}\quad (\text{C.33})$$

Moving around terms, the equation can be simplified into

$$\begin{aligned}\dot{\mathbf{t}}_1 &= \left(c^f \mathbf{C}_{11}^f + c^m \mathbf{C}_{11}^m - c^f c^m \left(\mathbf{C}_{12}^f - \mathbf{C}_{12}^m \right) \mathbf{C}_{22}^{*-1} \left(\mathbf{C}_{21}^f - \mathbf{C}_{21}^m \right) \right) \mathbf{v}_{,1} + \\ &\quad \left(c^f \mathbf{C}_{12}^f + c^m \mathbf{C}_{12}^m - c^f c^m \left(\mathbf{C}_{12}^f - \mathbf{C}_{12}^m \right) \mathbf{C}_{22}^{*-1} \left(\mathbf{C}_{22}^f - \mathbf{C}_{22}^m \right) \right) \mathbf{v}_{,2}\end{aligned}\quad (\text{C.34})$$

Next the focus is on the nominal stress rate vector $\dot{\mathbf{t}}_2^c$ for the constituents. Again the relation given by Eq. (C.3) is used

$$\dot{\mathbf{t}}_2^c = \mathbf{C}_{21}^c \mathbf{v}_{,1} + \mathbf{C}_{22}^c \mathbf{v}_{,2} \quad (\text{C.35})$$

Inserting $\mathbf{v}_{,2}^f$ and $\mathbf{v}_{,2}^m$ from Eq. (C.20) yields the nominal stress rates

$$\begin{aligned}\dot{\mathbf{t}}_2^f &= \mathbf{C}_{21}^f \mathbf{v}_{,1} + \mathbf{C}_{22}^f \left(-c^m \mathbf{C}_{22}^{*-1} \left(\mathbf{C}_{21}^f - \mathbf{C}_{21}^m \right) \mathbf{v}_{,1} - c^m \mathbf{C}_{22}^{*-1} \left(\mathbf{C}_{22}^f - \mathbf{C}_{22}^m \right) \mathbf{v}_{,2} + \mathbf{v}_{,2} \right) \\ \dot{\mathbf{t}}_2^m &= \mathbf{C}_{21}^m \mathbf{v}_{,1} + \mathbf{C}_{22}^m \left(c^f \mathbf{C}_{22}^{*-1} \left(\mathbf{C}_{21}^f - \mathbf{C}_{21}^m \right) \mathbf{v}_{,1} + c^f \mathbf{C}_{22}^{*-1} \left(\mathbf{C}_{22}^f - \mathbf{C}_{22}^m \right) \mathbf{v}_{,2} + \mathbf{v}_{,2} \right)\end{aligned}\quad (\text{C.36})$$

Collecting terms related to $\mathbf{v}_{,\beta}$ entail the two alternative expressions for \mathbf{t}_2 according to the second assumption Eq. (C.6)

$$\begin{aligned}\mathbf{t}_2 &= \left(\mathbf{C}_{21}^f - c^m \mathbf{C}_{22}^f \mathbf{C}_{22}^{*-1} \left(\mathbf{C}_{21}^f - \mathbf{C}_{21}^m \right) \right) \mathbf{v}_{,1} + \left(\mathbf{C}_{22}^f - c^m \mathbf{C}_{22}^f \mathbf{C}_{22}^{*-1} \left(\mathbf{C}_{22}^f - \mathbf{C}_{22}^m \right) \right) \mathbf{v}_{,2} \\ \mathbf{t}_2 &= \left(\mathbf{C}_{21}^m + c^f \mathbf{C}_{22}^m \mathbf{C}_{22}^{*-1} \left(\mathbf{C}_{21}^f - \mathbf{C}_{21}^m \right) \right) \mathbf{v}_{,1} + \left(\mathbf{C}_{22}^m + c^f \mathbf{C}_{22}^m \mathbf{C}_{22}^{*-1} \left(\mathbf{C}_{22}^f - \mathbf{C}_{22}^m \right) \right) \mathbf{v}_{,2}\end{aligned}\quad (\text{C.37})$$

The two expressions of \mathbf{t}_2 give the same result based on the second assumption. It is of interest to collect the two terms into one expression using the volume fractions, who obey the property $c^f + c^m = 1$.

$$\begin{aligned}\mathbf{t}_2 &= c^f \left(\left(\mathbf{C}_{21}^f - c^m \mathbf{C}_{22}^f \mathbf{C}_{22}^{*-1} \left(\mathbf{C}_{21}^f - \mathbf{C}_{21}^m \right) \right) \mathbf{v}_{,1} + \left(\mathbf{C}_{22}^f - c^m \mathbf{C}_{22}^f \mathbf{C}_{22}^{*-1} \left(\mathbf{C}_{22}^f - \mathbf{C}_{22}^m \right) \right) \mathbf{v}_{,2} \right) + \\ & \quad c^m \left(\left(\mathbf{C}_{21}^m + c^f \mathbf{C}_{22}^m \mathbf{C}_{22}^{*-1} \left(\mathbf{C}_{21}^f - \mathbf{C}_{21}^m \right) \right) \mathbf{v}_{,1} + \left(\mathbf{C}_{22}^m + c^f \mathbf{C}_{22}^m \mathbf{C}_{22}^{*-1} \left(\mathbf{C}_{22}^f - \mathbf{C}_{22}^m \right) \right) \mathbf{v}_{,2} \right)\end{aligned}\quad (\text{C.38})$$

Moving around terms, the equation can be simplified into

$$\begin{aligned}\mathbf{t}_2 &= \left(c^f \mathbf{C}_{21}^f + c^m \mathbf{C}_{21}^m - c^f c^m \left(\mathbf{C}_{22}^f - \mathbf{C}_{22}^m \right) \mathbf{C}_{22}^{*-1} \left(\mathbf{C}_{21}^f - \mathbf{C}_{21}^m \right) \right) \mathbf{v}_{,1} + \\ & \quad \left(c^f \mathbf{C}_{22}^f + c^m \mathbf{C}_{22}^m - c^f c^m \left(\mathbf{C}_{22}^f - \mathbf{C}_{22}^m \right) \mathbf{C}_{22}^{*-1} \left(\mathbf{C}_{22}^f - \mathbf{C}_{22}^m \right) \right) \mathbf{v}_{,2}\end{aligned}\quad (\text{C.39})$$

The matrix system may be written in the form given by Eq. (C.3), where the components of $\mathbf{C}_{\alpha\beta}$ is

$$\mathbf{C}_{\alpha\beta} = c^f \mathbf{C}_{\alpha\beta}^f + c^m \mathbf{C}_{\alpha\beta}^m - c^f c^m \left(\mathbf{C}_{\alpha 2}^f - \mathbf{C}_{\alpha 2}^m \right) \mathbf{C}_{22}^{*-1} \left(\mathbf{C}_{2\beta}^f - \mathbf{C}_{2\beta}^m \right) \quad (\text{C.40})$$

Based on the composite constitutive relation the nominal stress increments can be determined. By returning to the original index notation used in the dissertation, the moduli given by Eq. (C.40) can be written in the form introduced in Eq. (3.27). Going from the matrix notation to the index notation, the components of the matrix \mathbf{C}_{22}^* are equal to the components given by $M_{\alpha\beta}$. Similarly, the components of \mathbf{C}_{22}^{*-1} are equal to the components of $H_{\alpha\beta}$.

Volume fraction increment

The fibre c^f and matrix c^m volume fractions will change during deformation, due to the difference in the constituent properties. It is chosen to determine the fibre volume fraction increment \dot{c}^f . Based on this volume fraction increment, both volume fractions can be

determined. The volume fractions for the constituents are based on

$$c^f = \frac{V^f}{V} \quad c^m = \frac{V^m}{V} \quad (\text{C.41})$$

Where V is the total volume of a unit cell and V^c are volumes of the constituents in the unit cell. The volume increment for the constituents can be calculated using the velocity gradients

$$\dot{V}^c = V^c v_{k,k}^c \quad (\text{C.42})$$

Which can be expanded using Eq. (C.41)

$$\dot{V}^c = V c^c v_{k,k}^c \quad (\text{C.43})$$

The volume increment of a unit cell is a combination of the increments of both constituents

$$\dot{V} = V \left(c^f v_{k,k}^f + c^m v_{k,k}^m \right) \quad (\text{C.44})$$

The total fibre volume can be written as

$$V^f = c^f V \quad (\text{C.45})$$

The fibre volume increment can be determined using the product rule of differentiation

$$\dot{V}^f = \dot{c}^f V + c^f \dot{V} \quad (\text{C.46})$$

Isolating the term $\dot{c}^f V$ yields

$$\dot{c}^f V = \dot{V}^f - c^f \dot{V} \quad (\text{C.47})$$

\dot{V}^f and \dot{V} can be replaced using Eqs. (C.43) and (C.44)

$$\dot{c}^f V = V c^f v_{k,k}^f - c^f V \left(c^f v_{k,k}^f + c^m v_{k,k}^m \right) \quad (\text{C.48})$$

The volume V is a common factor and can be omitted

$$\dot{c}^f = c^f v_{k,k}^f - c^f \left(c^f v_{k,k}^f + c^m v_{k,k}^m \right) \quad (\text{C.49})$$

Multiplying the first part on the right by $(c^m + c^f)$ and expanding the parenthesis yields

$$\dot{c}^f = c^f c^f v_{k,k}^f + c^f c^m v_{k,k}^f - c^f c^f v_{k,k}^f - c^f c^m v_{k,k}^m \quad (\text{C.50})$$

This can be simplified into

$$\dot{c}^f = c^f c^m \left(v_{k,k}^f - v_{k,k}^m \right) \quad (\text{C.51})$$

Expanding the repeated indices yields

$$\dot{c}^f = c^f c^m \left(v_{1,1}^f + v_{2,2}^f + v_{3,3}^f - v_{1,1}^m - v_{2,2}^m - v_{3,3}^m \right) \quad (\text{C.52})$$

The constitutive model is two-dimensional and assumes plane strain conditions, thereby $v_{3,3}^c = 0$. The constitutive model is based on the assumption that material lines parallel with the fibres (parallel with x_1 axis) are subject to a common stretch, thereby $v_{1,1}^f = v_{1,1}^m$. The latter equation can thereby be simplified into

$$\dot{c}^f = c^f c^m \left(v_{2,2}^f - v_{2,2}^m \right) \quad (\text{C.53})$$

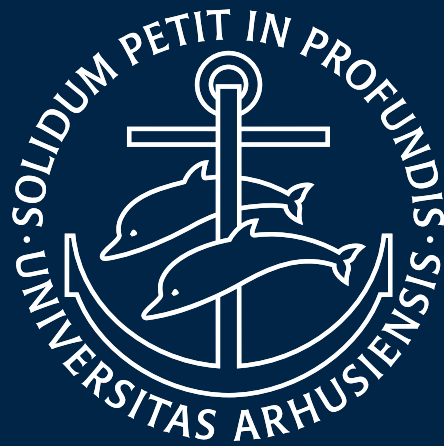
Bibliography

- Argon, A. S. (1972). *Fracture of composites*, volume 1. ACADEMIC PRESS, INC.
- Ashby, M., Evans, T., Fleck, N., Hutchinson, J., Wadley, H., and Gibson, L. (2000). *Metal Foams: A Design Guide*. Elsevier Science.
- Attwood, J. P., Fleck, N. A., Wadley, H. N. G., and Deshpande, V. S. (2015). The compressive response of ultra-high molecular weight polyethylene fibres and composites. *International Journal of Solids and Structures*, 71:141–155.
- Beuth, J. L. (1992). Cracking of thin bonded films in residual tension. *International Journal of Solids and Structures*, 29(13):1657–1675.
- Budiansky, B. (1983). Micromechanics. *Computers & Structures*, 16(1-4):3–12.
- Budiansky, B. and Fleck, N. (1993). Compressive failure of fibre composites. *Journal of the Mechanics and Physics of Solids*, 41(1):183–211.
- Chater, E. and Hutchinson, J. W. (1984). On the Propagation of Bulges and Buckles. *Journal of Applied Mechanics*.
- Christoffersen, J. and Jensen, H. M. (1996). Kink band analysis accounting for the microstructure of fiber reinforced materials. *Mechanics of Materials*, 24(4):305–315.
- Corneliussen, A. H. and Shield, R. T. (1961). Finite deformation of elastic membranes with application to the stability of an inflated and extended tube. *Archive for Rational Mechanics and Analysis*, 7(1):273–304.
- Ericksen, J. L. (1975). Equilibrium of bars. *Journal of Elasticity*, 5(3):191–201.
- Evans, A. G. and Adler, W. F. (1978). Kinking as a mode of structural degradation in carbon fiber composites. *Acta Metallurgica*, 26(5):725–738.
- Fleck, N. (1997). Compressive failure of fibre composites.
- Fleck, N. A. and Budiansky, B. (1991). Compressive failure of fibre composites due to microbuckling. *Proc. 3rd Symp. on Inelastic Deformation of Composite Materials*, pages 235–273.
- Fleck, N. A. and Shu, J. Y. (1995). Microbuckle initiation in fibre composites : A finite element study. *Journal of the Mechanics and Physics of Solids*, 43(12):1887–1918.

- Guggenheim, E. A. (1959). *Thermodynamics, Classical and Statistical*, pages 1–118. Springer Berlin Heidelberg, Berlin, Heidelberg.
- Hsu, S.-Y., Vogler, T., and Kyriakides, S. (1999). On the axial propagation of kink bands in fiber composites : Part II analysis. *International Journal of Solids and Structures*, 36:575–595.
- Hsu, S.-Y., Vogler, T. J., and Kyriakides, S. (1998). Compressive Strength Predictions for Fiber Composites. *Journal of Applied Mechanics*, 65(1):7.
- Huang, Z.-M. (2018). On micromechanics approach to stiffness and strength of unidirectional composites. *Journal of Reinforced Plastics and Composites*, page 073168441881193.
- Hutchinson, J. W. and Koiter, W. T. (1970). Postbuckling theory. *Applied mechanics reviews*, 23(12):1353–1366.
- Hutchinson, J. W. and Neale, K. W. (1978). Sheet Necking-II. Time-Independent Behavior.
- Hutchinson, J. W. and Neale, K. W. (1983). Neck propagation. *Journal of the Mechanics and Physics of Solids*, 31(5):405–426.
- Hutchinson, J. W. and Suo, Z. (1991). Mixed Mode Cracking in Layered Materials. *Advances in Applied Mechanics*.
- Jäger, J., Sause, M. G., Burkert, F., Moosburger-Will, J., Greisel, M., and Horn, S. (2015). Influence of plastic deformation on single-fiber push-out tests of carbon fiber reinforced epoxy resin. *Composites Part A: Applied Science and Manufacturing*, 71:157–167.
- Jensen, H. M. (1988). Collapse of hydrostatically loaded cylindrical shells. *International Journal of Solids and Structures*, 24(1):51 – 64.
- Jensen, H. M. (1999a). Analysis of compressive failure of layered materials by kink band broadening. *International Journal of Solids and Structures*, 36(23):3427–3441.
- Jensen, H. M. (1999b). Models of failure in compression of layered materials. *Mechanics of Materials*, 31:553–564.
- Jensen, H. M. and Christoffersen, J. (1997). Kink band formation in fiber reinforced materials. *Journal of the Mechanics and Physics of Solids*, 45(7):1121–1136.
- Jensen, H. M. and Thouless, M. D. (1995). Buckling Instability of Straight Edge Cracks. *Journal of Applied Mechanics*, 62(3):620–625.
- Ji, W., Waas, A. M., and Bazant, Z. P. (2013). On the Importance of Work-Conjugacy and Objective Stress Rates in Finite Deformation Incremental Finite Element Analysis. *Journal of Applied Mechanics*, 80(4):041024.
- Jones, R. (1975). *Mechanics of Composite Materials*. International student edition. Scripta Book Company.
- Kyriakides, S. (1993). Propagating Instabilities in Structures. *Advances in Applied Mechanics*, 30:67 – 189.
- Kyriakides, S. (1998). *Propagating Instabilities in Solids*. APS March Meeting Abstracts.

- Kyriakides, S., Arseculeratne, R., Perry, E. J., and Liechti, K. M. (1995). On the compressive failure of fiber reinforced composites. *International Journal of Solids and Structures*, 32(6-7):689–738.
- Kyriakides, S. and Yu-Chung, C. (1991). The initiation and propagation of a localized instability in an inflated elastic tube. *International Journal of Solids and Structures*, 27(9):1085 – 1111.
- Lager, J. R. and June, R. R. (1969). Compressive Strength of Boron-Epoxy Composites. *Journal of Composite Materials*, 6:48–56.
- Liu, G., Thouless, M. D., Deshpande, V. S., and Fleck, N. A. (2014). Collapse of a composite beam made from ultra high molecular-weight polyethylene fibres. *Journal of the Mechanics and Physics of Solids*, 63(1):320–335.
- Liu, X. H., Moran, P. M., and Shih, C. F. (1996). The mechanics of compressive kinking in unidirectional fiber reinforced ductile matrix composites. *Composites Part B: Engineering*, 27(6 SPEC. ISS.):553–560.
- Mesloh, R. E., Sorenson, J. E., and Atterbury, T. J. (1973). Buckling—and offshore pipelines. *Gas*, 49(7):40 – 43.
- Moran, P. M., Liu, X. H., and Shih, C. F. (1995). Kink band formation and band broadening in fiber composites under compressive loading. *Acta Metallurgica Et Materialia*, 43(8):2943–2958.
- Naya, F., Herraiez, M., Gonzalez, C., Lopes, C., der Veen, S. V., and Pons, F. (2017). Computational micromechanics of fiber kinking in unidirectional FRP under different environmental conditions. *Composites Science and Technology*, 144:26–35.
- Nizolek, T., Begley, M., McCabe, R., Avallone, J., Mara, N., Beyerlein, I., and Pollock, T. (2017). Strain fields induced by kink band propagation in Cu-Nb nanolaminate composites. *Acta Materialia*, 133:303–315.
- Palmer, A. C. and Martin, J. H. (1972). Buckle propagation in submarine pipelines. *Nature*, 254:46 – 48.
- Paterson, M. S. and Weiss, L. E. (1966). Experimental deformation and folding in phyllite. *Bulletin of the Geological Society of America*, 77(4):343–374.
- Poulios, K. and Niordson, C. F. (2016). Homogenization of long fiber reinforced composites including fiber bending effects. *Journal of the Mechanics and Physics of Solids*, 94:433–452.
- Prabhakar, P. and Waas, A. M. (2013). Interaction between kinking and splitting in the compressive failure of unidirectional fiber reinforced laminated composites. *Composite Structures*, 98:85–92.
- Rice, J. R. (1976). The Localization of plastic deformation. *Theoretical and Applied Mechanics*, pages 207–220.
- Rosen, B. W. (1965). Mechanics of composite strengthening. *Fiber Composite Seminar of the American Society for Metals*, pages 37–75.

- Sammis, C. G. and Ashby, M. F. (1986). The failure of brittle porous solids under compressive stress states. *Acta Metallurgica*, 34(3):511–526.
- Schreyer, S. L. and Masur, E. F. (1966). Buckling of shallow arches. *Journal of the Engineering Mechanics Division*, 92:1 – 20.
- Shaffer, G. D. (2006). An Archaeomagnetic Study of a Wattle and Daub Building Collapse. *Journal of Field Archaeology*.
- Skovsgaard, S. P. H. and Jensen, H. M. (2018a). Constitutive model for imperfectly bonded fibre-reinforced composites. *Composite Structures*, 192(February):82–92.
- Skovsgaard, S. P. H. and Jensen, H. M. (2018b). International Journal of Solids and Structures Three-dimensional constitutive model for elastic-plastic behaviour of fibre-reinforced composites. *International Journal of Solids and Structures*, 139-140:150–162.
- Skovsgaard, S. P. H. and Jensen, H. M. (2018c). Steady-State Kink Band Propagation in Layered Materials. *Journal of Applied Mechanics*, 85(6):061005.
- Skovsgaard, S. P. H. and Jensen, H. M. (2019). A general approach for the study of kink band broadening in fibre composites and layered materials. *European Journal of Mechanics - A/Solids*, 74(September 2018):394–402.
- Slaughter, W. S., Fleck, N. A., and Budiansky, B. (1993). Compressive failure of fibre composites: the roles of multi-axial loading and creep. *Journal of Engineering Materials and Technology*, 115(3):308 – 313.
- Sørensen, K. D., Mikkelsen, L. P., and Jensen, H. M. (2009). User subroutine for compressive failure of composites. *2009 Simulia Customer Conference*, (1965):618–632.
- Sutcliffe, M. and Fleck, N. (1997). Microbuckle propagation in fibre composites. *Acta Materialia*, 45(3):921–932.
- Timoshenko, S. and Young, D. (1962). *Elements of Strength of Materials. Fourth Edition*. D. Van Nostrand Company.
- Tojaga, V., Skovsgaard, S. P. H., and Jensen, H. M. (2018). Micromechanics of kink band formation in open-hole fibre composites under compressive loading. *Composites Part B*, 149(March):66–73.
- Vogler, T. and Kyriakides, S. (1997). Initiation and axial propagation of kink bands in fiber composites. *Acta Materialia*, 45(6):2443–2454.
- Wind, J. L., Steffensen, S., and Jensen, H. M. (2014). Comparison of a composite model and an individually fiber and matrix discretized model for kink band formation. *International Journal of Non-Linear Mechanics*, 67:319–325.



PhD Dissertation

Author: Simon Peter Hald Skovsgård

Supervisor: Henrik Myhre Jensen

Department of Engineering

Aarhus University, Denmark